



**HAL**  
open science

# Quantum Hall Ferromagnetism in Multicomponent Systems

Angelika Hildegard Knothe

► **To cite this version:**

Angelika Hildegard Knothe. Quantum Hall Ferromagnetism in Multicomponent Systems. Mesoscopic Systems and Quantum Hall Effect [cond-mat.mes-hall]. Université Paris Saclay (COmUE); Albert-Ludwigs-Universität (Freiburg im Breisgau, Allemagne), 2017. English. NNT: 2017SACLS595 . tel-01760011

**HAL Id: tel-01760011**

**<https://theses.hal.science/tel-01760011>**

Submitted on 5 Apr 2018

**HAL** is a multi-disciplinary open access archive for the deposit and dissemination of scientific research documents, whether they are published or not. The documents may come from teaching and research institutions in France or abroad, or from public or private research centers.

L'archive ouverte pluridisciplinaire **HAL**, est destinée au dépôt et à la diffusion de documents scientifiques de niveau recherche, publiés ou non, émanant des établissements d'enseignement et de recherche français ou étrangers, des laboratoires publics ou privés.

NNT : 2017SACLS595

DISSERTATION  
zur Erlangung des Doktorgrades  
der Fakultät für Mathematik und Physik  
der Albert-Ludwigs-Universität Freiburg im Breisgau  
und der Université Paris-Saclay

THÈSE DE DOCTORAT  
DE ALBERT-LUDWIGS-UNIVERSITÄT FREIBURG IM BREISGAU  
ET DE  
L'UNIVERSITÉ PARIS-SACLAY  
PRÉPARÉE À L'UNIVERSITÉ PARIS-SUD

ECOLE DOCTORALE N° 564  
« Physique en Île de France »

Spécialité de doctorat: Physique

Vorgelegt von / Par

**Mme Angelika Hildegard Knothe**

Quantum Hall Ferromagnetism in Multicomponent Systems

**Ort und Tag der mündlichen Prüfung: Freiburg, den 10. Oktober 2017**

**Thèse présentée et soutenue à Freiburg, le 10 octobre 2017**

Dekan (Universität Freiburg): Prof. Dr. Gregor Herten

Président (Université Paris Saclay): M. Gilles Bloch

**Mitglieder der Jury / Composition du Jury:**

M. Roche, Patrice	Directeur de Recherche CEA SPEC Saclay	Vorsitzender / Président
M. Fal'ko, Vladimir	Professor University of Manchester	Gutachter / Rapporteur
M. Sinova, Jairo	Professor Universität Mainz	Gutachter / Rapporteur
M. Dittmaier, Stefan	Professor Universität Freiburg	Prüfer / Examineur
M. Jolicœur, Thierry	Directeur de Recherche LPTMS Orsay	Betreuer der Arbeit / Directeur de thèse
M. Buchleitner, Andreas	Professor Universität Freiburg	Betreuer der Arbeit / Directeur de thèse



# Quantum Hall Ferromagnetism in Multicomponent Systems

---

Dissertation

**Angelika Hildegard Knothe**

Physikalisches Institut  
Fakultät für Mathematik und Physik  
Albert-Ludwigs-Universität Freiburg im Breisgau

and

Laboratoire de Physique Théorique et Modèles Statistiques (LPTMS), Orsay  
Université Paris Sud/ Paris Saclay  
École Doctorale de Physique en Île de France

October 12, 2017



Seht ihr den Mond dort stehen? Er ist nur halb zu sehen, und ist doch rund und schön!  
So sind wohl manche Sachen, die wir getrost belachen, weil unsre Augen sie nicht sehn.

**Matthias Claudius, "Der Mond ist aufgegangen"**

Il y a des fleurs partout pour qui veut bien les voir.

**Henri Matisse**

Aprende las reglas como un profesional, para que puedas romperlas como un artista.

**Pablo Picasso**

Я хочу понять вас, Я учусь свой неясный язык.

Александр Пушкин

If you are lucky enough to have lived in Paris as a young man, then wherever you go for  
the rest of your life, it stays with you, for Paris is a moveable feast.

**Ernest Hemingway, "A moveable feast"**



---

## Dank — Remerciements — Acknowledgements

---

**B**EDANKEN möchte ich mich bei Herrn Prof. Dr. Andreas Buchleitner, der den Ideen einer binationalen Promotion und der deutsch-französischer Zusammenarbeit vom ersten Moment an offen gegenüberstand und damit meinen Wechsel nach Frankreich und meine Zeit in Paris möglich gemacht hat.

Je remercie Thierry Jolicœur qui a accepté, de loin et sans me connaître, de prendre part à ce voyage parfois incertain. Pendant mes deux ans en France et même au-delà, il m'a guidée le long mon parcours scientifique d'une main sûre et éprouvée.

I want to express gratitude explicitly to all the members of the jury for accepting the task and investing a considerable amount of time and effort into this final stage of my thesis.

Diese Arbeit wurde unterstützt durch ein Jahresstipendium für Doktoranden des Deutschen Akademischen Austauschdienstes DAAD (10/2014 - 09/2015) sowie durch ein Promotionsstipendium der Studienstiftung des deutschen Volkes (10/2015 - 09/2017).

*Für meine liebe Mama und meinen lieben Papa  
Freiburg, August 2017*



## Abstract

The present thesis deals with two-dimensional quantum Hall systems in which the electrons may be endowed with multiple discrete degrees of freedom. *Quantum Hall ferromagnetism* provides a framework to treat these electronic degrees of freedom as effective spins and isospins of the electrons. Different orderings of the electronic spins and isospins then characterise different possible phases of the system. Using this analogy, various aspects of the two-dimensional systems in the quantum Hall regime are explored theoretically by studying the corresponding spin and isospin structure.

The work consists of three parts in which different two-dimensional materials are investigated in the quantum Hall regime. In any of the three projects presented within this thesis, *Hartree Fock* theory is employed to study the multicomponent spin and isospin system at the mean field level. All our considerations are stimulated directly by experimental results. We draw our main motivation from the key idea that purely theoretical investigations of abstract models may allow us to obtain deeper insights into the physical processes and mechanisms that determine the properties of the materials. This, in turn, we hope to allow conclusions about the experiments by providing possible explanations of the phenomena observed, as well as prospects for future investigations.

The first project deals with a finite piece of *monolayer graphene*: The electron spin and isospin properties are studied in the presence of an edge terminating the atomic graphene lattice and breaking translational invariance in space. In monolayer graphene, the electrons carry also an additional isospin degree of freedom besides the electronic spin. This is called the "valley isospin". By tracing the evolution of the system as a function of space from the bulk to the edge we analyse how the structure of ground and excited states is influenced by the presence of a boundary with respect to the properties of the translationally invariant bulk. We find novel phases in the vicinity of the edge which have not been observed before in the bulk of the system. The properties of the resulting edge state structure and their possible relation to conductance measurements are discussed. In particular, we challenge the commonly applied explanation of experimentally observed transitions between regimes of different conductance properties of monolayer graphene in terms of transitions between different bulk phases. We suggest an alternate explanation based solely on transitions between different edge phases.

In the second part, we turn our interest to *bilayer graphene*, where for an infinite system in the absence of boundaries, the dependence of spin and isospin properties on external magnetic and electric fields is investigated. For the graphene bilayer, where an additional "orbital" isospin degree of freedom comes into play due to a degeneracy between the  $n = 0$  and the  $n = 1$  Landau level, we identify the various different ground state spin and isospin phases which may emerge as functions of the electric and magnetic field strengths and provide the corresponding phase diagrams. We investigate the properties of phases, especially of those that exhibit non-trivial coherence properties of the isospin degrees of freedom and compare to the literature about experimentally observed phase transitions in bilayer graphene.

Finally, in the most recent project, we give an outlook on the possibility of extending the ideas above to analyse the two-dimensional surface states of three-dimensional crystals in the quantum Hall regime. The example of the *(111) surface of elemental bismuth* is discussed: in this case, we are confronted with a multi-valley system featuring six degenerate, anisotropic valleys. We make an attempt to model the dispersion of this system by approximating the valleys as elliptic bands and accounting for the effect of local strain. First, preliminary results on possible valley ordering of different ground state phases are presented.

## Zusammenfassung

Die vorliegende Arbeit beschäftigt sich mit zweidimensionalen Quanten-Hall Systemen, in welchen die Elektronen über mehrere diskrete Freiheitsgrade verfügen können. *Quanten-Hall Ferromagnetismus* stellt einen Rahmen dar, um diese elektronischen Freiheitsgrade als effektive Spins und Isospins der Elektronen zu beschreiben. Verschiedene Anordnungen der Spins und Isospins charakterisieren dann verschiedene mögliche Phasen des Systems. Unter Ausnutzung dieser Analogie werden unterschiedliche Aspekte der zweidimensionalen Systeme im Quanten-Hall Regime theoretisch untersucht, indem die jeweilige Spin und Isospin Struktur analysiert wird.

Die Arbeit besteht aus drei Teilen, in denen jeweils unterschiedliche zweidimensionale Systeme im Quanten-Hall Regime studiert werden. In jedem der drei Projekte, welche in dieser Arbeit vorgestellt werden, wird die *Hartree-Fock-Theorie* genutzt, um die Spin- und Isospin-Systeme mit mehreren Komponenten auf der Basis von Molekularfeldnäherung zu untersuchen. Alle unsere Überlegungen wurden angeregt durch experimentelle Ergebnisse. Wir beziehen unsere Hauptmotivation aus der zentralen Idee, dass aus rein theoretischen Untersuchungen abstrakter Modelle tiefgreifende Einsichten bezüglich der physikalischen Prozesse und Mechanismen gewonnen werden können, welche dem Verhalten des Systems zu Grunde liegen. Dies wiederum, so unsere Hoffnung, soll Rückschlüsse auf die Experimente zulassen, sowohl um Erklärungen für die beobachteten Phänomene zu liefern, als auch um Anregungen für zukünftige Untersuchungen zu geben.

Das erste Projekt beschäftigt sich mit einer endlichen Probe aus *einlagigem Graphen*: Untersucht werden die Eigenschaften von Spin und Isospin der Elektronen in der Nähe eines Randes des atomistischen Graphengitters, durch welchen die Translationsinvarianz des Raumes gebrochen wird. In einlagigem Graphen tragen die Elektronen nebst dem Elektronenspin einen weiteren Isospin-Freiheitsgrad, genannt der "Valley Isospin". In einer ortsabhängigen Untersuchung, welche die Materialeigenschaften als Funktion des Raumes vom Inneren bis zum Rand nachvollzieht, analysieren wir, wie die Struktur des Grundzustands und der angeregten Zustände beeinflusst wird in der Gegenwart eines Randes des Gitters im Vergleich zu den Eigenschaften des translationsinvarianten Inneren. Wir finden neuartige Phasen in der Nähe des Randes, welche nicht im Inneren des Systems auftreten. Die Eigenschaften der entstehenden Randzustände und ihre mögliche Beziehung zu Leitfähigkeitsmessungen werden diskutiert. Insbesondere stellen wir die allgemein übliche Erklärung für die experimentell beobachteten Übergänge zwischen

Bereichen verschiedener Leitfähigkeitseigenschaften in Frage, welche eine direkte Verbindung zu Übergängen zwischen verschiedenen Phasen im Inneren annimmt. Wir stellen eine alternative Erklärungsmöglichkeit vor, der Übergänge zwischen Phasen lediglich im Randbereich der Probe zu Grunde liegen.

Im zweiten Teil wenden wir uns *zweilagigem Graphen* zu. In einem unendlichen System ohne Ränder sind die Abhängigkeiten der Eigenschaften von Spin und Isospin von äußeren magnetischen und elektrischen Feldern Gegenstand unserer Untersuchungen. In zweilagigem Graphen kommt ein weiterer "orbitaler" Isospin-Freiheitsgrad ins Spiel, aufgrund einer Entartung der Landauniveaus mit Quantenzahlen  $n = 0$  und  $n = 1$ . Wir identifizieren die verschiedenen Spin- und Isospin-Phasen des Grundzustandes, die als Funktion der elektrischen und magnetischen Feldstärken aufkommen können und legen die dazugehörigen Phasendiagramme vor. Darüber hinaus untersuchen wir die Eigenschaften der Phasen, insbesondere derer, welche nichttriviale Kohärenzeigenschaften der Isospin-Freiheitsgrade aufweisen und vergleichen mit der Literatur zu experimentell beobachteten Phasenübergängen in zweilagigem Graphen.

Im Rahmen des neuesten Projektes schließlich geben wir einen Ausblick auf mögliche Erweiterungen der oben vorgestellten Ideen, wie zweidimensionale Oberflächenzustände von dreidimensionalen Kristallen im Quanten-Hall Regime untersucht werden können. Das Beispiel der *(111) Fläche von elementarem Wismut* wird vorgestellt: In diesem Fall sehen wir uns einem System gegenüber, welches sechs entartete, anisotrope Valleys aufweist. Wir machen einen Vorschlag, wie die Dispersion durch ein Modell angenähert werden könnte, in dem die Valleys als elliptische Energiebänder beschrieben werden und welches den Effekt von lokaler Spannung beinhaltet. Erste vorläufige Ergebnisse zu möglichen Ordnungszuständen des Valley Freiheitsgrades verschiedener Grundzustandsphasen werden vorgestellt.

## Résumé

Cette thèse traite des systèmes de Hall quantiques en deux dimensions, dans lesquels les électrons peuvent porter plusieurs degrés de liberté discrets différents. Le ferromagnétisme de Hall quantique fournit une manière de traiter ces degrés de liberté électroniques comme des spins et isospins effectifs des électrons. Les différentes phases du système correspondent alors à différents ordres de spin ou d'isospin. En exploitant cette analogie, nous explorons différents aspects des systèmes bi-dimensionnels dans le régime de Hall quantique en étudiant la structure correspondante des spins et isospins. Ce travail consiste en trois parties qui analysent différents matériaux bi-dimensionnels dans le régime de l'effet Hall quantique. Dans chaque projet, nous utilisons la théorie de Hartree-Fock pour étudier le système à plusieurs composantes de spin et d'isospin dans l'approximation de champ moyen. Toutes nos considérations sont directement stimulées par des résultats expérimentaux. Notre motivation principale est d'obtenir une compréhension plus profonde des processus physiques et des mécanismes qui déterminent les propriétés des matériaux à partir d'investigations exclusivement théoriques de modèles abstraits. Nous espérons que cela permettra par la suite de tirer des conclusions sur les expériences, de donner des explications aux phénomènes observés ainsi que de donner des perspectives pour des investigations futures.

Le premier projet est consacré à un morceau fini d'une monocouche de graphène : nous étudions les propriétés de spin et d'isospin des électrons en présence d'un bord qui brise la symétrie de translation dans l'espace. Dans les monocouches de graphène, les électrons portent, en plus du spin réel, un degré de liberté supplémentaire qui s'appelle «l'isospin de vallée». Nous analysons comment la structure de l'état fondamental ainsi que celle des états excités est influencée par la présence du bord, en comparaison avec les propriétés de l'intérieur du système qui conserve la symétrie de translation. Nous observons près du bord des états nouveaux qui ne peuvent pas être trouvés dans l'intérieur. Nous discutons les propriétés de la structure des états de bord ainsi que leurs relations éventuelles avec des mesures de conductivité. En particulier nous remettons en question l'explication habituelle des transitions entre régimes de conductivités différentes observées dans des études expérimentales d'une couche simple de graphène, qui est fondée sur des transitions entre des différentes phases dans l'intérieur du système. Nous proposons une explication alternative basée uniquement sur des transitions entre différentes phases près du bord.

Dans la deuxième partie, nous nous intéressons aux bicouches de graphène et nous analysons, pour des systèmes infinis sans bords, la dépendance des propriétés de spin et d'isospin sur les champs magnétiques et électriques extérieurs. Dans les bicouches de graphène, il existe un degré de liberté «orbital» supplémentaire à cause d'une dégénérescence entre les niveaux de Landau avec les nombres quantiques  $n = 0$  et  $n = 1$ . Nous identifions les multiples états fondamentaux différents en fonction des intensités des champs électrique et magnétique et nous présentons les diagrammes de phases correspondants. Nous analysons les propriétés des phases, notamment celles pour lesquelles les degrés de liberté d'isospin présentent une cohérence non-triviale et nous faisons la comparaison avec la littérature expérimentale sur les transitions de phase dans les bicouches de graphène.

Enfin, dans notre projet le plus récent, nous donnons un aperçu de la possibilité d'étendre les idées précédentes pour analyser des surfaces bi-dimensionnelles de cristaux en trois dimensions dans le régime de Hall quantique. Nous discutons l'exemple d'une surface (111) de bismuth élémentaire : dans ce cas, on est confronté à un système de plusieurs vallées dégénérées et anisotropes. Nous essayons de trouver un modèle de dispersion dans ce système en approximant les vallées par des bandes elliptiques et en considérant l'effet de contraintes locales. On présente des résultats préliminaires sur l'ordre du degré de liberté de vallée des états fondamentaux.

---

## Contents

---

<b>List of Symbols</b>	<b>19</b>
<b>I Introduction</b>	<b>21</b>
I.1 Introduction . . . . .	21
I.2 The General Picture . . . . .	22
I.2.1 Diving into the Physics of the Quantum Hall Regime . . . . .	22
I.2.2 Two Dimensions in Physics . . . . .	30
I.3 Experimental Motivation . . . . .	34
I.3.1 Monolayer Graphene - From the Bulk, can we understand the Edges? . . . . .	35
I.3.2 Bilayer Graphene - How many Different Phases are there? . . . . .	36
I.3.3 Bismuth(111) - Does the Ground State break Symmetries? . . . . .	38
<b>II Theoretical Background</b>	<b>41</b>
II.1 Theoretical Description of the Materials . . . . .	41
II.1.1 Mono- and Bilayer Graphene: Band Structure and Landau Level Quantisation . . . . .	41
II.1.2 Bismuth(111): Approximate Description of the Dispersion and Anisotropic Landau Level Quantisation . . . . .	61
II.2 Quantum Hall Ferromagnetism and Hartree Fock Theory . . . . .	64
II.2.1 The SU(N) Quantum Hall Ferromagnet . . . . .	64
II.2.2 Hartree Fock Decoupling of a Two-Particle Interaction . . . . .	68
<b>III Edge State Structure of Graphene Monolayers in the <math>\nu = 0</math> Quantum Hall State</b>	<b>73</b>
III.1 Edge State Structure of Monolayer Graphene - Introduction . . . . .	73
III.1.1 Theoretical Framework and Model Hamiltonian . . . . .	75

III.2	Edge State Structure of Monolayer Graphene	
	- Results and Discussion . . . . .	87
III.2.1	Choice of Parameters . . . . .	87
III.2.2	Ground State Properties . . . . .	89
III.2.3	Mean Field Spectrum and Excited States . . . . .	95
III.2.4	Edge State Structure of Monolayer Graphene	
	- Conclusions and Remarks . . . . .	116
<b>IV</b>	<b>Phase Diagram of a Graphene Bilayer in the Zero-Energy Landau Level</b>	<b>119</b>
IV.1	Bilayer Graphene in the Zero-Energy Landau Level - Introduction . . . . .	119
IV.1.1	Theoretical Framework and Model Hamiltonian . . . . .	121
IV.2	Bilayer Graphene in the Zero-Energy Landau Level - Results (I):	
	Hartree Fock Phase Diagrams . . . . .	132
IV.2.1	Overview over the Phases . . . . .	133
IV.2.2	Individual Presentation of the Phases . . . . .	134
IV.2.3	Properties of the Phases - Comparative Discussion . . . . .	167
IV.2.4	Negative against Positive Filling Factors . . . . .	169
IV.2.5	Phase Diagrams - Summary and Conclusion . . . . .	170
IV.3	Bilayer Graphene in the Zero-Energy Landau Level - Results (II):	
	Physical Properties of the Phases . . . . .	177
IV.3.1	Octet Polarisation and Hund's Rules . . . . .	177
IV.3.2	Layer Polarisation . . . . .	178
IV.3.3	Extrapolation to Zero Magnetic Field . . . . .	182
IV.3.4	Properties of the Phases - Summary . . . . .	186
IV.3.5	Relation to Experiment and to Theoretical Studies . . . . .	186
IV.4	Bilayer Graphene in the Zero-Energy Landau Level	
	- Conclusions and Remarks . . . . .	192
<b>V</b>	<b>Valley Order of the Bi(111) Surface States in the Quantum Hall Regime</b>	<b>197</b>
V.1	Quantum Hall States on the (111) Surface of Bismuth - Introduction . . . . .	197
V.1.1	Theoretical Model of Bi(111) Quantum Hall States . . . . .	199
V.1.2	Theoretical Treatment and Hartree Fock Routine . . . . .	207
V.2	Quantum Hall States on the (111) Surface of Bi	
	- First Results: Ground State Valley Occupation . . . . .	208
V.2.1	Bi(111) at $\nu = \frac{1}{6}$ . . . . .	208
V.2.2	Bi(111) at $\nu = \frac{2}{6}$ . . . . .	212
V.2.3	Bi(111) at $\nu = \frac{3}{6}$ . . . . .	214
V.2.4	Bi(111) at $\nu = \frac{4}{6}$ . . . . .	215
V.2.5	Bi(111) at $\nu = \frac{5}{6}$ . . . . .	217

V.3	Quantum Hall States on the (111) Surface of Bi	
	- Discussion and Preliminary Conclusion . . . . .	220
V.3.1	General Behaviour of the Model . . . . .	220
V.3.2	Discussion of the Physically Relevant Regime . . . . .	221
V.3.3	Preliminary Summary . . . . .	224
<b>VI</b>	<b>Final Discussion</b>	<b>225</b>
VI.1	Conclusion . . . . .	225
VI.1.1	Monolayer Graphene - From the Bulk, can we understand the Edges? . . . . .	226
VI.1.2	Bilayer Graphene - How many Different Phases are there? . . . . .	226
VI.1.3	Bismuth(111) - Does the Ground State break Symmetries? . . . . .	227
VI.1.4	Summary: Understanding a Material - Bulk versus Edge Phenomena . . . . .	227
VI.2	Outlook . . . . .	228
<b>A</b>	<b>Monolayer Graphene: The Kinetic Energy effective Edge Potential</b>	<b>231</b>
A.1	Landau Levels in the Presence of a Boundary . . . . .	231
A.1.1	Low-Energy Dirac Hamiltonian . . . . .	231
A.1.2	Terminating Edge: Boundary Conditions . . . . .	234
<b>B</b>	<b>Monolayer Graphene: Parametrisation of the Ground State Wave Function</b>	<b>243</b>
B.1	The Minimal Set of Parameters . . . . .	243
B.1.1	Parametrising a General Antisymmetric Matrix . . . . .	244
B.1.2	Parametrising the Energy Functional . . . . .	248
<b>C</b>	<b>Bilayer Graphene: Exchange Interaction Matrix Elements</b>	<b>253</b>
C.1	Explicit Form of the Exchange Integrals . . . . .	253
C.2	Energetic Scales . . . . .	255
<b>D</b>	<b>Bismuth(111): Decomposition of the Coulomb Interaction</b>	<b>257</b>
D.1	Coulomb Interaction for Anisotropic Quantum Hall States . . . . .	257
D.1.1	Form Factors for Lowest Landau Level Interaction . . . . .	258
D.1.2	Estimation of Different Scattering Processes . . . . .	260
	<b>Synthèse en Français</b>	<b>265</b>



---

## List of Symbols

---

$c$	The speed of light
$e$	The elementary charge of the electron
$m$	The mass of the electron
$\epsilon$	The dielectric constant
$\varepsilon_F$	The Fermi energy
$\hbar$	Planck's constant
$\rho_{xx}$	The longitudinal, dissipative resistivity
$\rho_{xy}$	The transversal Hall resistivity
$\sigma_{xx}$	The longitudinal conductivity
$\sigma_{xy}$	The transversal conductivity
$\ell_B = \sqrt{\frac{\hbar c}{eB}}$	The magnetic length
$\nu$	The filling factor
$\omega_c$	The cyclotron frequency
$N_{LL}$	The Landau level degeneracy
$\mathbf{A}$	The vector potential
$\mathbf{B}$	The magnetic field
$\mathbf{E}$	The electric field
$\Delta_B$	The bias potential
$\mathbf{S}, \mathbf{T}, \mathbf{L}$	The spin, the valley isospin, and the orbital isospin



---

## Introduction

---

### I.1 Introduction

The main motivation for the work presented in this dissertation stems from the complex and involved, yet overwhelmingly rich and fascinating area of condensed matter physics, where pure theory meets real life experiments. We have decided to embark on a journey to investigate theoretically the properties of quite a special class of materials: *two-dimensional electron systems in the quantum Hall regime where the electrons may carry multiple discrete degrees of freedom*. There are several different key aspects which add richness and complexity to this kind of systems: understanding the variety of *quantum Hall effects* has evolved into one of the most important and most influential areas of condensed matter physics all since the revolutionary discovery of the integer quantum Hall effect by Klaus von Klitzing on February 5th, 1980 [[v. Klitzing et al., 1980](#); [v. Klitzing, 1985](#)]. Hence, the effects of strong external magnetic fields on the most elementary properties of electrons in two spatial dimensions must be accounted for carefully in any type of quantum Hall system. On the other side, the properties of the material itself which hosts the two-dimensional electron system may very well be of crucial importance: today, the class of possible two-dimensional materials goes far beyond the conventional two-dimensional electron gas in semiconductor heterostructures in which the quantum Hall effects were first discovered and this family is still growing. We may encounter situations in which the electrons are endowed with more than just the common spin degree of freedom: while the spin is an intrinsic feature of the fermionic electron itself, further properties might be dictated by the material's characteristics, such as its symmetries, or degeneracies of the band structure. This gives rise to so-called *multi-component systems*. It is therefore an

involved, yet utmost intriguing endeavour to study *quantum Hall physics in novel two-dimensional materials*: where the many different aspects meet and merge to create intricate, exceptionally rich settings. Many aspects of the mutual influence of quantum Hall effects and the properties, symmetries, and topologies of various different kinds of materials yet have to be understood. This bears major interest in several ways. On the one hand, the investigation of novel materials always naturally includes the possibility to be of relevance for new kinds of applications and technologies. This kind of research carries over the insights of physics into the real, everyday world. On the other hand, novel systems pose novel, fundamental questions that stimulate the most basic kind of research. Materials as those investigated in this work most certainly still hold a huge variety of challenges and surprises for the world of pure solid state physics.

The main aim of this introductory chapter is to place the work of this thesis in a larger, general context by summarising some of the main concepts of multicomponent quantum Hall systems. We start by introducing the basic phenomenology of quantum Hall physics. Second, we discuss different physical examples of two-dimensional electron systems as they will be studied within the three projects that constitute this work. Finally, as this research is directly related to experiments carried out on the respective materials, we present some of the most important experimental observations which stimulated the key questions in these three different projects.

## I.2 The General Picture

### I.2.1 Diving into the Physics of the Quantum Hall Regime

Naturally, limited by the scope of this thesis, we can only give a very brief introduction to the vast field of quantum Hall physics. We make the attempt to provide the minimum background information needed to understand the remainder of the text. For more detailed explanations we refer the reader to appropriate, more extensive literature, *e.g.*, [Yoshioka, 2010; MacDonald, 1994; Janssen et al., 1994; Jain, 2007].

#### The Quantum Hall Effect - Phenomenology

What is the quantum Hall effect? The quantum Hall effect occurs in two-dimensional electron systems in the limit of strong perpendicular magnetic fields. Let us imagine a conduction measurement on a setup as sketched in figure I.1: there is a current  $I$  running through a two-dimensional sample to which a perpendicular magnetic field has been applied. We are interested in studying the *longitu-*

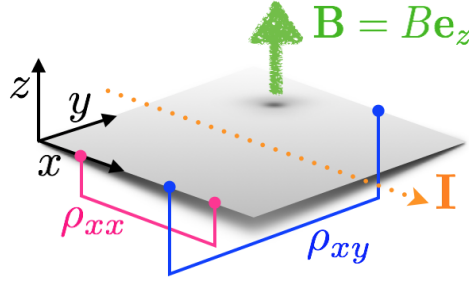


Figure I.1

Sketch of the setup to determine the longitudinal, dissipative resistivity  $\rho_{xx}$  and the transversal Hall resistivity  $\rho_{xy}$  in a quantum Hall measurement.

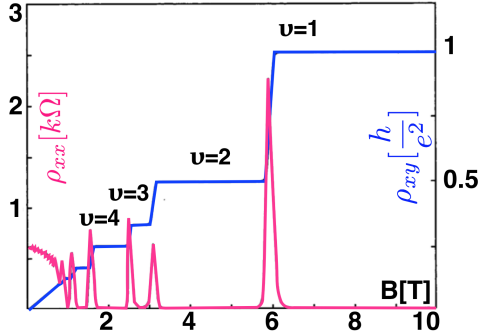


Figure I.2

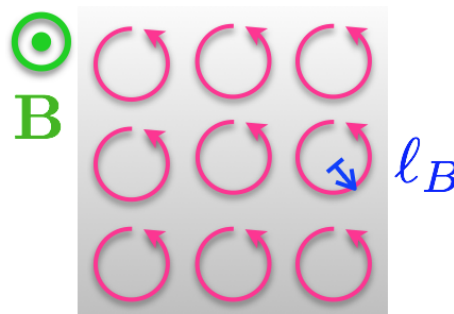
The dependence of  $\rho_{xx}$  and  $\rho_{xy}$  on the magnetic field. Figure from reference [Tsui, 1998] (edited).

dinal, dissipative resistivity  $\rho_{xx}$  in the direction of the current and the transversal Hall resistivity  $\rho_{xy}$  perpendicular to the current. As Edwin Hall described in 1879 [Hall, 1879] there is indeed a non-zero voltage drop in the perpendicular direction across the sample, due to the action of the Lorentz force which the electrons as charged particles experience in the presence of a magnetic field. This perpendicular voltage is referred to as the *Hall-Voltage*  $V_H$ . A description in terms of classical Drude scattering theory predicts  $\rho_{xx}$  to be independent of the strength of the magnetic field  $B$  while  $\rho_{xy}$  should depend linearly on  $B$  [MacDonald, 1994]:

$$\rho_{xx}^{class} = \text{const}, \quad \rho_{xy}^{class} \propto B. \quad (\text{I.1})$$

The outcome of a careful measurement in high quality samples with sufficiently high electron mobility, however, shows dramatically different behaviour. Figure I.2 shows the dependence of  $\rho_{xx}$  and  $\rho_{xy}$  on the magnetic field strengths as presented in reference [Tsui, 1998]. For sufficiently small magnetic fields  $B \lesssim 0.5$  T the predictions of Drude theory seem to work fairly well. For higher values of  $B$ , however, the following behaviour is observed:

- The Hall resistivity  $\rho_{xy}$  shows a *plateau structure*, being almost constant over certain finite intervals of the magnetic field. Within these intervals, the dissipative resistivity  $\rho_{xx}$  becomes very small. Non-zero values of  $\rho_{xy}$  can only be observed in a distinct *peak structure* with sharp sparks exactly at the values of  $B$  when  $\rho_{xy}$  changes between plateaus.

**Figure I.3**

Classical picture of the motion of charged particles in a perpendicular magnetic field: the electrons move in cyclotron orbits of radius  $\ell_B$ .

- The value at which the Hall resistivity stagnates within the plateaus is given by exactly  $\frac{h}{e^2}$  divided by an integer. These are the numbers  $\nu$  labelling the features in figure I.2. We will find these numbers to correspond to the filling factors of the *integer quantum Hall effect*. Hence, there is *quantisation* of the Hall resistivity. Accordingly, the *Hall conductivity*  $\sigma_{xy} = -\frac{1}{\rho_{xy}}$  is quantised into integer multiples of  $\frac{e^2}{h}$ . This quantisation has been established to be of universal nature, *i.e.*, not to depend on the kind of sample, nor on its geometry or size.

This anomalous behaviour of the resistivity of two-dimensional electron systems, discovered by Klaus von Klitzing on February 5th, 1980 [v. Klitzing, 1985], is commonly referred to as the *quantum Hall effect*.

### Landau Level Quantisation

What is the origin of the quantisation  $\sigma_{xy} = -j\frac{e^2}{h}$ ? To see this, we consider the quantum mechanical solution of a free electron in two spatial dimensions subject to a magnetic field. The Hamiltonian for an electron moving in two dimensions in a perpendicular magnetic field is given by

$$H = \frac{\boldsymbol{\pi}^2}{2m}, \quad (\text{I.2})$$

where  $m$  is its mass. We denote by  $\boldsymbol{\pi} = m\mathbf{v} = \mathbf{p} - \frac{e\mathbf{A}}{c}$  the dynamical momentum for velocity  $\mathbf{v}$  and the vector potential  $\mathbf{A}$  as in  $B = \mathbf{e}_z \cdot (\nabla \times \mathbf{A})$  for a uniform, perpendicular magnetic field. Hence,  $H$  of equation (I.2) is identified to have the form of a generalised harmonic oscillator, because it is quadratic both in the spatial coordinates and in the canonical momentum  $\mathbf{p}$ . It can be solved conveniently using the algebraic method similar to the conventional harmonic oscillator treatment

in second quantisation:

The components of the kinetic momentum form a pair of canonically conjugate variables as they fulfil

$$[\pi_x, \pi_y] = -i \frac{\hbar^2}{\ell_B^2}. \quad (\text{I.3})$$

In the equation above,  $\ell_B = \sqrt{\frac{\hbar c}{eB}}$  is a quantity with the unit of a spatial length and denotes the *magnetic length*. We will see it to represent the characteristic length scale of quantum Hall systems.

Introducing a set of ladder operators as

$$\mathbf{a} := \frac{1}{\sqrt{2}} \frac{\ell_B}{\hbar} (\pi_x - i\pi_y), \quad \mathbf{a}^\dagger := \frac{1}{\sqrt{2}} \frac{\ell_B}{\hbar} (\pi_x + i\pi_y), \quad (\text{I.4})$$

which fulfil  $[\mathbf{a}, \mathbf{a}^\dagger] = 1$ , allows to rewrite the Hamiltonian of equation (I.2) as

$$\mathbf{H} = \hbar\omega_c \left( \mathbf{a}^\dagger \mathbf{a} + \frac{1}{2} \right), \quad (\text{I.5})$$

with the characteristic *cyclotron frequency*  $\omega_c = \frac{eB}{mc}$ .

It follows that the eigenenergies of a free, charged particle in a two-dimensional configuration with a perpendicular magnetic field are given by the discretised values  $E_n = \hbar\omega_c(n + \frac{1}{2})$  like a harmonic oscillator. These discrete energy levels are referred to as the *Landau levels*.

In the classical picture, the electrons as charged particles in a magnetic field are forced into the circular motion of a *cyclotron orbit* of radius  $\ell_B$ , as sketched in figure I.3. Let this classical intuition guide us when we dissect the position operator  $\mathbf{r} = \mathbf{R} + \mathbf{r}_c$  into the *cyclotron orbit guiding centre operator*  $\mathbf{R}$  for the centre coordinate for the position of each cyclotron orbit and the *cyclotron coordinate*  $\mathbf{r}_c$  identifying the cyclotron motion with  $r_x^c = \frac{\ell_B^2}{\hbar} \pi_y$  and  $r_y^c = -\frac{\ell_B^2}{\hbar} \pi_x$ . We see that the energies  $E_n$  are independent of the guiding centre coordinate  $\mathbf{R}$ . Hence, we expect each of these quantum energies  $E_n$  to be degenerate in the position of the cyclotron orbit.

This degeneracy can be made explicit by constructing the ladder operators associated with the guiding centre operators: for  $[x, y] = 0$  to hold for the components of  $\mathbf{r} = (x, y)$ , the components of  $\mathbf{R} = (X, Y)$  necessarily have to fulfil  $[X, Y] = i\ell_B^2$ ; Hence  $X$  and  $Y$  again form a canonical pair and we may define corresponding

ladder operators by

$$\mathbf{b} = \frac{1}{2\ell_B}(X + iY), \quad \mathbf{b}^\dagger = \frac{1}{2\ell_B}(X - iY), \quad (\text{I.6})$$

which implies  $[\mathbf{b}, \mathbf{b}^\dagger] = 1$  and  $[\mathbf{a}, \mathbf{b}] = [\mathbf{a}^\dagger, \mathbf{b}] = [H, \mathbf{b}] = 0$ .

The guiding centre ladder operators  $\mathbf{b}, \mathbf{b}^\dagger$  produce a set of degenerate eigenstates of the one-body kinetic energy operator  $H$ . In each Landau level, there hence is a whole set of states degenerate in the cyclotron orbit guiding centre coordinates.

The full quantum state of an electron in two spatial dimensions in the presence of a perpendicular magnetic field hence carries two quantum numbers  $n, m$  labelling the Landau level and the guiding centre quantum number, respectively. The full set of eigenstates generically can be generated successively using the raising operators on the ground state  $|0, 0\rangle$ :

$$|n, m\rangle = \frac{1}{\sqrt{n!m!}}(\mathbf{a}^\dagger)^n(\mathbf{b}^\dagger)^m|0, 0\rangle. \quad (\text{I.7})$$

This degeneracy in the guiding centre coordinate implies that we can put several, energetically degenerate, electrons into the same Landau level  $n$ . The number of possible states per Landau level,  $N_{LL}$ , can be estimated by comparing the surface occupied by each cyclotron orbit to the total surface of the sample  $A$

$$N_{LL} = \frac{A}{2\pi\ell_B^2}. \quad (\text{I.8})$$

For a total number of electrons  $N_e$  in the system, to quantify the fraction of Landau level states occupied by electrons, we define at this point the *filling factor*  $\nu$  as

$$\nu = \frac{N_e}{N_{LL}} = 2\pi\ell_B^2 n_e, \quad (\text{I.9})$$

in terms of the electronic density  $n_e = \frac{N_e}{A}$ .

### The Edge State Picture

Understanding and explaining the full beauty of the quantum Hall effect in all its details goes far beyond the scope of this introductory text. We can only make an attempt to sketch some aspects that give an idea about one way of perceiving how quantisation and transport come about in quantum Hall systems.

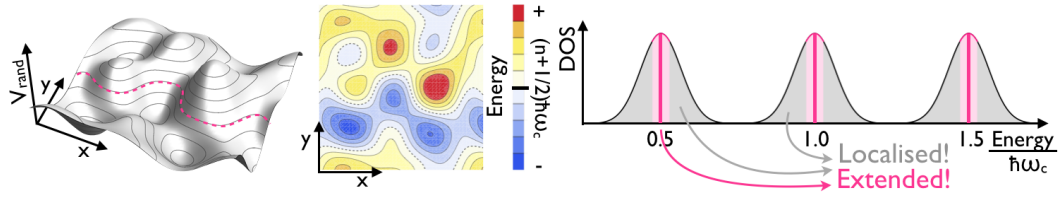


**Figure I.4**

Effect of a disorder potential  $V_{rand}$ , as in the left and centre plot, on the density of states (DOS) of the electrons in the quantum Hall system. Disorder leads to a broadening of the density of states around the discrete Landau level energies, where the trajectories at energies above and below the Landau levels are localised by the hills and valleys of the disordered landscape and extended states connecting two sides of the sample can be found only in the centre of the lobes, at the Landau level energies (magenta, dashed line in the left sketch).

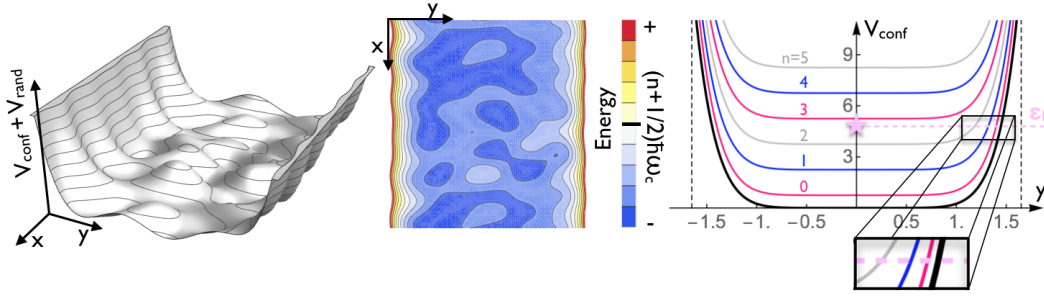
The key idea is to consider a less idealised, Landau level quantised two-dimensional electron system, in the presence of the following two amendments:

#### A weak disorder potential

The presence of imperfections and impurities will be unavoidable in any real sample. In fact, disorder turns out to be a crucial ingredient of the quantum Hall effect. We consider a disorder potential  $V_{rand}$  as a perturbation to the system which we require to be weak, *i.e.*, much smaller than the Landau level spacing  $\hbar\omega_c$ , smooth as a function of space, and symmetric, *i.e.*,  $\langle V_{rand} \rangle = 0$ . Such a disorder potential turns out to lead to broadening of the density of states around the discrete delta peaks of the Landau levels [Janssen et al., 1994]. Charged particles in the presence of electric and magnetic fields prefer to move along the equipotential lines of the electrostatic potential. Therefore, the states above and below the Landau level energies will be localised around the hills and valleys of the disorder potential. Only trajectories at energies sufficiently close to a Landau level form extended states which can connect two sides of the sample. This mechanism is illustrated in figure I.4. As a consequence, the density of states will consist of broad lobes of mainly localised states with one extended state at the centre of each lobe, at each Landau level energy.

#### A confinement potential

Any real sample in experiment will be of finite size and the two-dimensional electron gas will be confronted with some sort of confinement at its edges. The effect of a confinement potential  $V_{conf}$  is sketched in figure I.5. The Landau levels will bend at the sample's boundaries and follow the confining po-


**Figure I.5**

The effect of confinement by a confinement potential  $V_{conf}$  on the quantum Hall system: the Landau levels bend (magenta, blue, and gray lines in the right plot) and follow the confinement potential  $V_{conf}$  (black line). While the electron trajectories in the bulk are localised by disorder, close to the boundaries extended, current-carrying edge states are formed. The number of edge states is given by the number of Landau levels fully occupied below the Fermi energy  $\epsilon_F$ .

tential. In the bulk of the sample, the states will continue to be localised due to the presence of disorder. Sufficiently close to the boundaries, however, the confinement potential will outweigh the bumps of  $V_{rand}$  — it is here, in the vicinity of the boundaries, that extended states form which connect two sides of the sample. These *edge states* can carry current and lead to transport across the sample. As we require the disorder to be sufficiently weak it does not induce mixing between Landau levels and the bulk states remain gapped. Therefore, the number of current-carrying edge states is given by the number of fully occupied Landau levels below the Fermi energy  $\epsilon_F$  as the highest energy of a single electron in the system.

Now, due to the interplay between disorder and confinement in a Landau level quantised two-dimensional quantum Hall system, the emergent picture is the following: while the states in the bulk of the system are localised, extended, current-carrying states form along the edges of the sample. This gives rise to *gapped* bulk states which by definition represent an *incompressible* state: a finite input of energy is needed to alter the electron density by an infinitesimal amount. Simultaneously, a set of *gapless* edge states exists: the absence of a gap in the single particle spectrum, *i.e.*, the *compressibility* of the system at the edges implies metallic, *i.e.*, conducting behaviour of the edge states. As explained above, the number of edge channels is given by the number of occupied Landau levels in the bulk. As each extended edge state contributes a quantum of  $\sigma_{xy,LL} = -\frac{e^2}{h}$  to the Hall conductance, the total Hall conductance of the system is given by the quantised value  $\sigma_{xy,tot} = -\nu\frac{e^2}{h}$ . It remains constant while the Fermi energy is varied, but remains

between two Landau levels in the bulk, while it changes in a discontinuous jump when the number of occupied Landau levels in the bulk changes.

The edge states hence represent a system of metallic, one-dimensional transport channels: they carry a current which runs in opposite directions at either of the sample sides, a property for which they are endowed with the title *counter propagating* or *chiral* edge states.

### Energy Scales

How do we define the *quantum Hall regime*? Let us compare the energy scales that characterise a quantum Hall system. The theory of quantum Hall effects treats as its subject the physics of two-dimensional electron systems in the limit where the magnetic field is sufficiently strong such that the mixing of Landau levels can be considered as a weak perturbation. In other words, we would like to restrict ourselves to the scenario in which any effect distorting the *ideal* Landau levels, *i.e.*, the Landau levels in the absence of disorder or interactions, is small compared to the gap between adjacent Landau levels. The most prominent effects altering the ideal Landau levels will be the presence of disorder and mutual interactions between the electrons.

Hence, a crucial energy scale of a quantum Hall system is given by the Landau level splitting  $\Delta E$ :

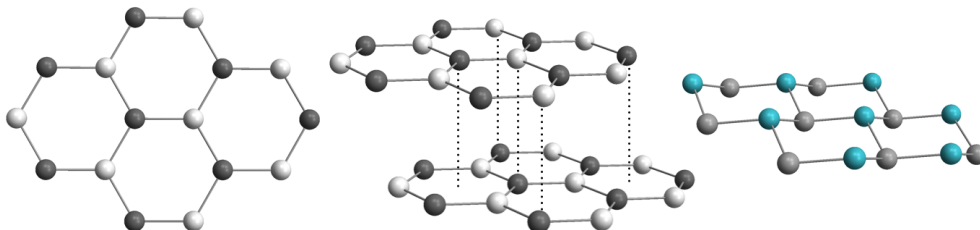
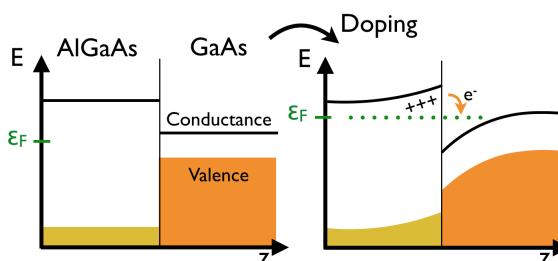
$$\Delta E = \hbar\omega_c = \hbar\frac{eB}{mc}. \quad (\text{I.10})$$

It has to be noted, however, that the ideal Landau levels are flat and of zero width within the bulk of a quantum Hall system. That is, the energies of disorder and interactions will be the *only* energy scales deciding the behaviour of the system, as there is no other scale, such as a kinetic energy term or a bandwidth, to compete with. As an essential consequence, although disorder and interaction may be small compared to  $\Delta E$ , generally in a quantum Hall system, their very presence itself cannot be treated within a perturbative approach.

Above, we have expounded how the emergence of gapless edge states from gapped bulk states yields an explanation for the quantised value of conductance and resistance observed as the quantum Hall effect. Hence, generally, the physics of a quantum Hall system crucially depends on the existence of a gap in the ideal energy spectrum. In the case where the interactions are weaker than the disorder, we may effectively work in a single particle picture and the gaps to be considered are these already present in the single particle Landau level spectrum  $E_n = \hbar\omega_c(n + \frac{1}{2})$  as follows from equation (I.2). This gives rise to the *integer*

**Figure I.6**

Two-dimensional electron gases form at the interface between a doped insulator (AlGaAs) and a semiconductor (GaAs) in a heterostructure.

**Figure I.7**

Examples of two-dimensional electron systems which will be studied as quantum Hall materials throughout this thesis: monolayer graphene, bilayer graphene, and the (111) surface of elemental Bismuth.

*quantum Hall effect*, which we addressed above starting from the experimental observations of plateaus of the Hall resistivity at integer values of  $\nu$  as in figure I.2. The regime when the disorder potential dominates, therefore, is referred to as the *integer quantum Hall regime*. It is the regime considered within this thesis. In the opposite case of the *fractional quantum Hall regime*, the physics is dominated by interactions and many-particle effects. In this case, additional gaps are opened by the mutual electron-electron interactions and, as a consequence, generally at higher values of the magnetic field than for the integer case, additional plateaus appear in the curve of  $\rho_{xy}$  at fractional values of  $\nu$ . This is known as the *fractional quantum Hall effect* [Tsui et al., 1982]. We shall not discuss further the properties of fractional quantum Hall systems within this thesis.

## I.2.2 Two Dimensions in Physics

### Two-Dimensional Materials

The quantum Hall effect has first been discovered in two-dimensional electron gases in doped semiconductor heterostructures. However, as we saw in the sketch of an explanation above, its origin is rooted solely in the fact that we are considering two-dimensional electronic systems in the quantum Hall regime. In par-

ticular, its occurrence is independent of many details of the sample hosting the electron gas, such as shape or geometry. As a consequence, we may expect quantum Hall phenomena in basically any two-dimensional electron system under the right conditions. As a matter of fact, quantum Hall effects have been observed in a variety of two-dimensional systems to this day. Let us summon some key features of several of these materials as they will be discussed throughout this work.

### The two-dimensional electron gas

Two-dimensional electron gases can be realised, for instance, at the interface between a doped insulator and a semiconductor due the mechanism illustrated in figure I.6: both compounds exhibit a gap between the valence and the conduction band, which is larger in the insulator than in the semiconductor material. Without any doping, when both materials are charge neutral, the Fermi energy of the heterojunction lies within the gap for both compounds. The level scheme for the undoped case is shown in the left plot of figure I.6. If now the insulator is n-doped, there will be excess electrons compared to the neutral, undoped case. The Fermi level on the insulator side is raised above the conduction band of the semiconductor. Therefore, the electrons of the donors will tend to lower their energy by migrating across the interface into the conduction band of the semiconductor. They leave behind the positively charged donors, creating charge polarisation and depleting the energy levels - as a consequence, the electrons are bound to the interface by this positive charge. The final configuration of the energy bands once this process has equilibrated is shown in the right plot of figure I.6.

This mechanism creates an electron gas at the interface between the insulator and the semiconductor. It is effectively two-dimensional as the  $z$ -component perpendicular to the plane is frozen due to the confinement by the deformed conduction band. Most importantly, this electron gas can be considered to be a "free" gas of electrons: the electrons that constitute the electron gas are excess charges due to the n-doping, so they are not bound by the crystal structure. As a consequence, they can be assumed to be governed by the free, parabolic dispersion which enters equation (I.2).

### Two-dimensional atomic crystals: graphene

Since the isolation of *graphene* [Novoselov et al., 2004; Geim and Novoselov, 2007], a single layer of carbon atoms forming a two-dimensional hexagonal lattice, exploration of quantum Hall effects has become possible in a different kind of systems: truly two-dimensional crystals of the thickness of one atomic layer. Graphene is certainly the most prominent example as the trailblazer in the field, but by now there are many more examples of

two-dimensional crystals in which quantum Hall phenomena have been observed<sup>\*</sup>. These atomic crystals offer several technical advantages compared to bulk materials or conventional two-dimensional electron gases: for example, in systems as thin as a few atomic layers, there are pronounced electric-field effects, as the electric field is not screened like in the bulk. As a consequence, in atomically thin films it is possible to control the carrier density in the sheet simply by applying gate voltage [Novoselov et al., 2004]. Furthermore, a two-dimensional electron gas generally needs to be confined by external, artificial potentials. As these confinement potentials naturally cannot be made arbitrarily steep, this leads to the effect of *edge reconstruction* [Chklovskii et al., 1992; Chamon and Wen, 1994; Yang, 2003]: as a consequence of the interplay of interaction energy and the energy of a sufficiently shallow confinement potential, the ground state turns out to energetically prefer to form an inhomogeneous stripe phase around the edge. However, unlike the two-dimensional energy gas, where this inhomogeneous charge distributions spoils all possibility of observing pure edge phenomena of the idealised system [Chang et al., 1996; Grayson et al., 1998], in atomic crystals the boundaries of the lattices are atomically sharp. This should allow observation of quantum Hall edge state physics without complications from edge reconstruction [Hu et al., 2011; Li et al., 2013].

At the most fundamental level, the quantum Hall effect is inherent to any two-dimensional electron system in the quantum Hall regime. There are, however, important differences when comparing a crystal system to the free electron gas of the semiconductor heterostructures [Barlas et al., 2012]. Most strikingly, the electrons in a crystal are not "free", they are bound by the crystal structure. Therefore, their energetics is determined by the band structure of the underlying crystal. Landau level quantisation in the quantum Hall regime will quantise this energy structure instead of the free parabolic dispersion that enters equation (I.2). Furthermore, possible symmetries of the crystal lattice may translate to the quantum Hall regime and introduce additional degeneracies or degrees of freedom.

Generally speaking, the particular properties of the specific crystal, such as, *e.g.*, the properties and symmetries of the underlying lattice, or the shape and symmetry properties of the corresponding band structure have to be taken into account when describing an electron gas on any two-dimensional lattice in the quantum Hall regime.

---

<sup>\*</sup> We name Silicene, a two-dimensional layer of Silicium atoms or two-dimensional Germanium, out of curiosity [Ezawa, 2012; Liu et al., 2011].

### Bilayer quantum Hall systems

Already in the case of two-dimensional electron gases, multi-layer systems have been of interest: in bilayer quantum Hall systems made of two sheets on top of each other we may introduce an additional "which-layer degree of freedom" that can assume the two distinct configurations "top" and "bottom" when the electrons reside on the top or the bottom layer, respectively. Furthermore, in the bilayer geometry the electronic interactions are altered depending on whether electrons interact within the same or across the two different sheets. As a consequence, these systems give rise to a plethora of novel quantum Hall phenomena [Ezawa, 2008; Sarma and Pinczuk, 1996; Ezawa et al., 2005].

Naturally, graphene is a prime example for forming multilayer systems: as a descendant of the graphite crystal, it comes with an entire family of multilayer cousins. Among these, bilayer graphene, built from two layers of monolayer graphene, is just one example [Barlas et al., 2012].

### Two-dimensional surface states

Recently, attention has been raised also by certain three dimensional crystals: their surfaces naturally are two-dimensional systems and hence surface states confined to these surfaces represent yet another possibility for electrons to live in two spatial dimensions. Examples which have been discussed include the SnTe material class or elemental bismuth [Li et al., 2016; Feldman et al., 2016; Sodemann et al., 2017]. Depending on the symmetries of both, the bulk material as well as the surface, these surface crystal states may have exotic, novel properties. Again, just as in the case of truly two-dimensional lattices, the properties of the crystal have to be translated to the quantum Hall regime when considering the system subject to a magnetic field and carefully be taken into account in a quantum Hall description.

The specific examples for the two-dimensional materials studied in the quantum Hall regime within this thesis are monolayer graphene, bilayer graphene, and the (111) surface of elemental bismuth. These systems are sketched in figure I.7.

### Length Scales

In the previous section we saw that the decisive length scale of a quantum Hall system is given by the magnetic length  $\ell_B = \sqrt{\frac{\hbar c}{eB}}$ . It defines the size of the cyclotron orbits as sketched in figure I.3. The stronger the magnetic field, the smaller the radius of the orbits. The magnetic length is the lattice constant for the lattice of Landau quantised cyclotron orbits.

Now, when considering the case of an electron gas in a crystal material, the characteristic length scale of this material is given by the lattice constant  $a$  of the host lattice. The question arises how  $\ell_B$  compares to  $a$ .

Within this thesis we work within a *continuum approximation*, assuming the lattice constant of the underlying atomic lattice to be much smaller than the magnetic length on the range of magnetic field strengths considered:

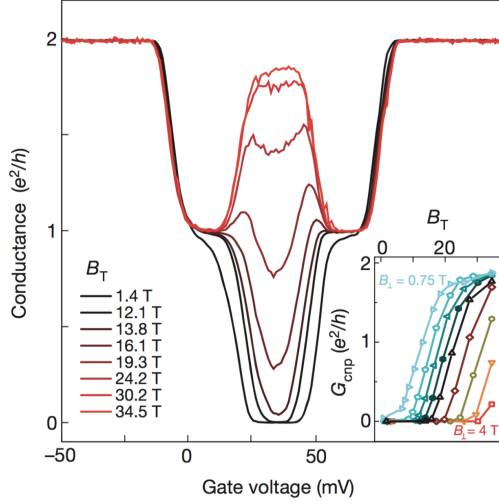
$$a \ll \ell_B. \tag{I.11}$$

Physically this amounts to assuming that the electrons in the two-dimensional host crystal, while being influenced by the lattice structure through the band structure and possible symmetries, do not feel the lattice at the atomic scale. That is, the electrons do not get localised or scattered by the atoms of the crystal. They rather behave like a "pseudo-free" gas with a different dispersion and maybe some other additional properties specific to the particular crystal geometry, such as energetic degeneracies due to the symmetries of the lattice band structure.

### I.3 Experimental Motivation

There have been numerous experimental investigations of a variety of different two-dimensional electron systems in the quantum Hall regime. The picture they draw of the physics that may happen is extraordinarily rich and beautifully manifold: characterising the system in terms of physically observable, but most elementary properties, such as conductance, they reveal the existence of a plethora of different possible features and behaviours. These features will depend on the specific type of host material for the electrons, but also on experimentally tuneable parameters, such as the filling factor, or external magnetic and electric fields. Therefore, these systems represent a huge playground for the exploration of novel quantum Hall phenomena.

Within this thesis, we present three projects on quantum Hall phenomena: in monolayer graphene, bilayer graphene, and the (111) surface states of elemental Bismuth, respectively. This section reviews the experimental findings that stimulated our research on either of the materials. At the same time, we give a brief outlook on what our intent is to help understand these phenomena in each of the cases.

**Figure I.8**

Conductance measurements on monolayer graphene in tilted magnetic fields. Figure from reference [Young et al., 2014].

### I.3.1 Monolayer Graphene - From the Bulk, can we understand the Edges?

Monolayer graphene samples in strong magnetic fields exhibit integer and fractional quantum Hall effects similar to two-dimensional electron gases as, *e.g.*, in semiconductor heterostructures [Bolotin et al., 2009; Dean et al., 2011]. We focus on charge-neutral monolayer graphene. As we will see in the following chapter, charge neutrality in monolayer graphene corresponds to the case when there are two electrons per orbital in the  $\nu_{MLG} = 0$  monolayer graphene Landau level. The experimental phenomenology of this particular quantum Hall system is the following: while the system proves to be strongly insulating for any value of the magnetic field as long as this field is applied perpendicularly to the sample, the following change of the conductance behaviour has been observed for tilted magnetic fields. Upon rotation of the sample with respect to the field, the system can be tuned from a perfect insulator to a good conductor [Young et al., 2014]. This transition is demonstrated in figure I.8. Here we quote results of reference [Young et al., 2014], where the Hall conductance of the  $\nu_{MLG} = 0$  monolayer graphene quantum Hall state,  $G_{cnp} = \sigma_{xy}(\nu_{MLG} = 0)$ , of charge-neutral monolayer graphene on hexagonal boron nitride substrates was measured: the total value of the magnetic field  $B_T$  is increased while the the component of the field perpendicular to the graphene sample is held fixed at  $B_{\perp} = 1.4$  T. While the system is insulating for perpendicular magnetic fields, upon tilting of the magnetic field the conductance of the charge neutrality point  $G_{cnp}$  is found to gradually increase, until it saturates at a value  $G_{cnp} \approx 1.8 \frac{e^2}{h}$ , at strongly inclined fields. This is close to the quantised value of  $2 \frac{e^2}{h}$  expected for the Hall conductivity of a quantum Hall system featur-

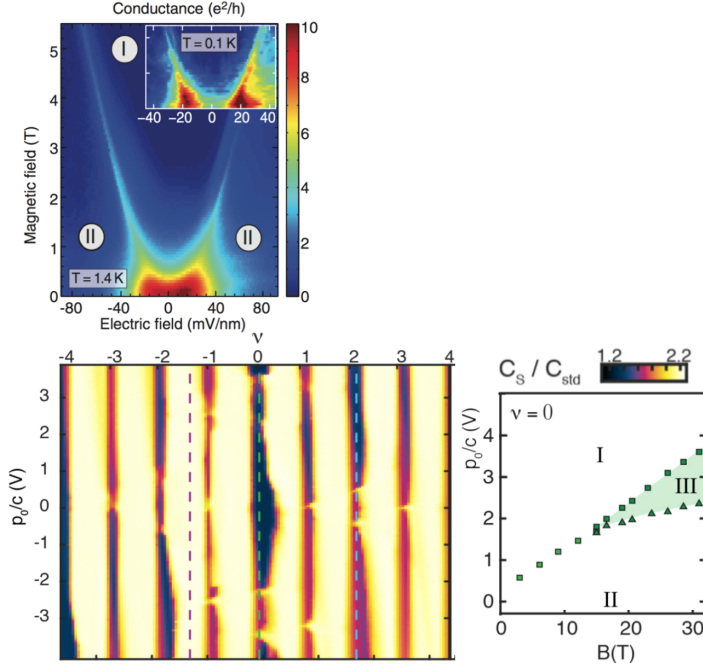
ing two electrons per orbital. In the same reference the authors demonstrate that the bulk of the sample remains in an incompressible, insulating state for all values and tilting angles of the magnetic field.

As we tried to motivate in the previous section, conductance properties of quantum Hall systems are inherently related to the properties of the current-carrying edge states. Within this project on monolayer graphene we ask the following question: starting from the properties of bulk monolayer graphene as indicated by experiment and supported also by earlier theoretical works, can we understand the influence of a boundary in a finite piece of monolayer graphene? We make statements about the edge state properties, including the ground state structure and the conductance properties of monolayer graphene by investigating the changes on the states of the system when approaching from the bulk an edge that terminates the monolayer graphene lattice. We find novel edge state phases that exhibit properties which are not observed in the bulk of the system. Furthermore, our results indicate the possibility to relate tuning between insulating and conducting behaviour of monolayer graphene to pure edge phenomena, *i.e.*, to transitions that occur within a regime spatially close to the edge, only, without affecting the bulk properties.

### I.3.2 Bilayer Graphene - How many Different Phases are there?

The quantum Hall physics of bilayer graphene in external magnetic and electric fields has proven to be a particularly rich and multi-faceted field. We quote the experimental results of references [Weitz et al., 2010; Kim et al., 2011; Bao et al., 2012; Velasco Jr et al., 2012; Maher et al., 2013; Velasco Jr et al., 2014; Lee et al., 2014; Maher et al., 2014; Shi et al., 2016; Hunt et al., 2016].

Conductance measurements on bilayer graphene in external fields draw the following picture: while the system is insulating over a wide range of values of the magnetic and electric fields applied, sudden changes of the conductivity can be observed for certain particular magnitudes of the electric or magnetic fields: examples of experimental data demonstrating this behaviour are shown in figure I.9. The upper plot, taken from reference [Weitz et al., 2010], shows conductance measured in suspended bilayer graphene at charge neutrality (which, for bilayer graphene, corresponds to the bilayer graphene filling factor  $\nu_{BLG} = 0$ ) for different values of a magnetic and an electric field applied perpendicularly to the sample. Clear spikes of enhanced conductance separate between broad insulating regimes. The lower plots, extracted from reference [Hunt et al., 2016], hint at the complexity of the full picture: the left figure quotes results in bilayer graphene encapsulated


**Figure I.9**

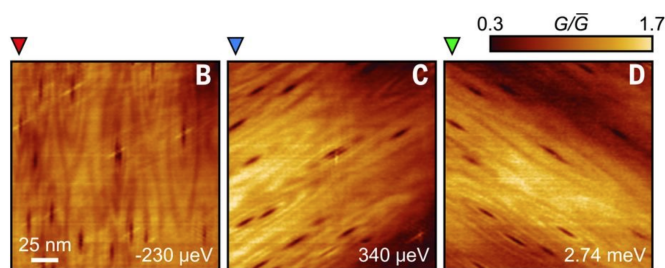
Conductance measurements on bilayer graphene at different filling factors  $\nu_{BLG}$  in perpendicular magnetic and electric fields. Upper figure from reference [Weitz et al., 2010], lower figures (edited) from reference [Hunt et al., 2016].

into hexagonal boron nitride, where normalised capacitance has been measured for different values of the filling factor  $\nu_{BLG}$ , which corresponds to a different number of electrons in the system. The parameter that has been varied is the rescaled ideal layer polarisation,  $\frac{p_0}{c}$ , which is proportional to the electric field applied. At a magnetic field of  $B = 31\text{ T}$ , as function of the electric field, a variety of spikes in capacity is observed: for each value of the filling factor, these spikes occur differently many times at different values of the field. From this and similar measurements the authors of reference [Hunt et al., 2016] extract the phase diagram shown in the lower right plot of figure I.9: here, for the system at charge neutrality  $\nu_{BLG} = 0$ , they distinguish between three different phases in the plane spanned by the magnetic and electric field.

Measurements akin to the two examples shown in figure I.9 (see references [Weitz et al., 2010; Kim et al., 2011; Bao et al., 2012; Velasco Jr et al., 2012; Maher et al., 2013; Velasco Jr et al., 2014; Lee et al., 2014; Maher et al., 2014; Shi et al., 2016; Hunt et al., 2016]) indicate that in bilayer graphene under strong external fields multiple transitions between different phases can be induced by varying the magnetic and electric fields applied. Despite the extensive effort invested into experimental investigations of this system, in some cases the nature of the underlying quantum Hall state could not yet fully be clarified, neither as to the exact number of phases for particular values of the filling factor, nor as to the nature of the states in the

**Figure I.10**

Spatial conductance maps of the Bi(111) surface at  $B = 12.9$  T for different energies, *i.e.*, for different filling factors, revealing the anisotropic character of the quantum Hall states. Figure from [Feldman et al., 2016].



respective phases. For this project on bilayer graphene presented here, the leading question therefore is the following: by modelling bilayer graphene theoretically, what predictions can we make about the properties of the system? Based on earlier theoretical investigations as well as experimental suggestions, we derive a microscopical model of bilayer graphene in the quantum Hall regime. With this model we study for different filling factors the behaviour of the system as a function of external electric and magnetic fields. We derive the corresponding phase diagrams of bilayer graphene at different  $\nu_{BLG}$  in the plane spanned by the magnitude of the electric and the magnetic field, respectively, by identifying the number and the nature of the different phases. Novel ground state phases and phase transitions are observed and, by analysing in detail the physical properties of the respective phases, predictions are made for comparison with experimental results.

### I.3.3 Bismuth(111) -

#### Does the Ground State break Symmetries?

The quantum Hall effect for the surface states of the (111) surface of bismuth exhibits a novel feature with respect to the situation in monolayer or bilayer graphene or conventional semiconductor heterostructures: the geometry of the Fermi surface gives rise to an energetic structure with an overall rotational symmetry in momentum space but locally anisotropic structures [Du et al., 2016; Ast and Höchst, 2001]. The question arises as to the consequences for the nature and the symmetry properties of the corresponding quantum Hall states. Figure I.10, quoting reference [Feldman et al., 2016], gives hints for an anisotropic structure: for different energies, *i.e.*, for different filling factors, implying different numbers of electrons in the system, conductance maps in real space at a magnetic field of  $B = 12.9$  T reveal anisotropic, elliptical regions of reduced conductance, suggesting elliptical shape of the respective corresponding wave functions. The exact nature of the underlying quantum state yet remains elusive. This is the main question we would like to address within this our project on the quantum Hall states

of the Bi(111) surface: starting from a microscopical model of the energetic structure for the (111) surface of bismuth where we carefully take into account the consequences of its anisotropic structure, what are the symmetry properties of the ground state that we predict theoretically for different values of the system parameters? We wish to understand the symmetry structure of the respective states compared to the global rotational symmetry of the Fermi surface. The aim is to explain either the preservation of this symmetry, or its breaking, respectively from its origin in the anisotropies of the dispersion in momentum space, as well as the relation to the symmetries of the bismuth lattice in real space.



---

## Theoretical Background

---

### II.1 Theoretical Description of the Materials

For a single electron in a solid its energetics is described by its band structure, indicating the ranges of energies allowed or forbidden by quantum mechanics, respectively. In this chapter, we introduce the different materials which will be studied within this thesis. We start by discussing the physical nature and the lattice structure of either of these materials. Second, we elucidate their band structure as well as the possible ways to approximate the low-energy bands closest to the Fermi surface. In a subsequent step, we see how this energetic structure is affected in the presence of a magnetic field entailing quantisation of the continuous energy bands into discrete Landau levels.

#### II.1.1 Mono- and Bilayer Graphene: Band Structure and Landau Level Quantisation

##### Lattice and Crystal Structure

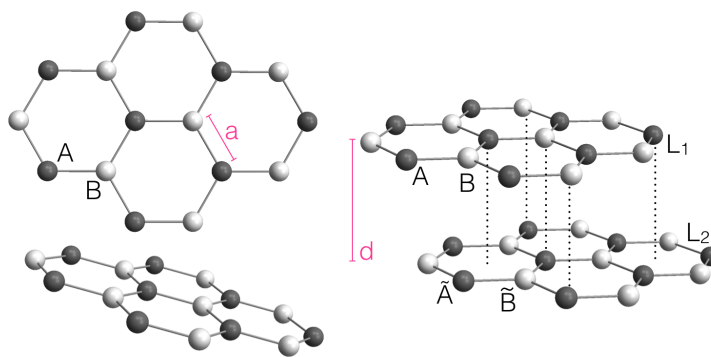
We show the crystallographic structure of the mono- and bilayer graphene lattice in figure II.1. The term *graphene* refers to single-layered graphite: carbon atoms form a two-dimensional, planar, hexagonal lattice. With *bilayer graphene* we denote two-layered graphite, *i.e.*, two monolayer graphene sheets grown on top of each other.\*

---

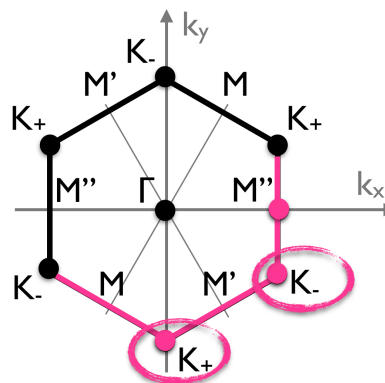
\* *Bilayer graphene* is to be distinguished from *double layer graphene*, where two individual graphene monolayers are artificially held in the vicinity of each other. Typically, the two monolayer graphene sheets in a double layer setup are separated by a dielectric such as hexagonal boron nitride, and the separation distance  $d_d$  is a variable system parameter.

**Figure II.1**

Lattice structure of monolayer graphene (left, seen from different angles) and bilayer graphene (right).


**Figure II.2**

Reciprocal lattice of the hexagonal lattice: the interior of the rotated hexagon and the part of the border marked in magenta are counted to the first Brillouin zone.



The honeycomb lattice is not a Bravais lattice<sup>†</sup>, therefore it is described as constructed from two triangular Bravais sub-lattices, or, equivalently, as a triangular Bravais lattice with multiple atoms per unit cell. In monolayer graphene we label the two inequivalent carbon atoms per unit cell by  $A$  and  $B$ , respectively (figure II.1). The bilayer graphene lattice is composed of two such monolayers, an upper layer  $L_1$  and a lower layer  $L_2$ , which are separated by an interlayer distance  $d$ . This yields a total of four inequivalent carbon atoms  $\{A, B, \tilde{A}, \tilde{B}\}$  per unit cell in bilayer graphene, where we distinguish between the atoms  $A$  and  $B$  on the upper layer and  $\tilde{A}$  and  $\tilde{B}$  on the lower layer (see figure II.1).

Obviously, for multilayer graphene systems with a number of layers  $n > 1$ , there are several possible ways to arrange the layers on top of each other. This is commonly referred to as the different possible *stackings* of the layers. In trilayer graphene, literature discusses at length the different properties for ABA compared

<sup>†</sup> In three spatial dimensions, a lattice is called a *Bravais lattice* if it can be generated by an infinite set of translations of three linear independent primitive vectors  $\mathbf{a}_i$ , *i.e.*, if every point of the lattice can be written as  $\mathbf{R} = \sum_{i=1}^3 n_i \mathbf{a}_i$  with  $n_i$  integer.

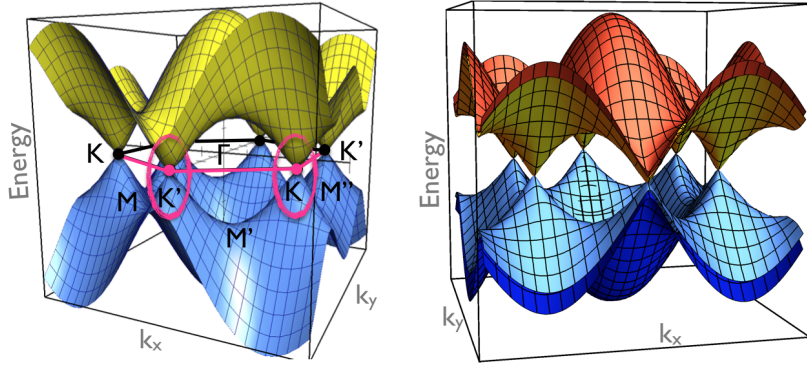


**Figure II.3**  
 Band structure of monolayer (left) and bilayer graphene (right) within the first Brillouin zone.

to ABC stacking [Bao et al., 2011; Lui et al., 2011], where the letters refer to the layers and indicate whether the sequence of arrangements repeats or not. In this sense, the configuration of bilayer graphene sketched in II.1 corresponds to an AB-stacked bilayer configuration. We extensively discuss this case of AB bilayer graphene, called *Bernal-stacked* bilayer graphene, in the following introductory section. We will not consider other cases such as AA-stacking [Liu et al., 2009] or twisting between the two layers [Lopes dos Santos et al., 2007; Mele, 2010; Luican et al., 2011; Lee et al., 2011; Kim et al., 2016].

In figure II.2 we show for the hexagonal structure the reciprocal lattice in momentum space: it in turn is given by a hexagon rotated by an angle of  $\frac{\pi}{3}$  with respect to the original real space lattice. The characteristic crystallographic points in momentum space are denoted as follows: the  $\Gamma$ -point is located at the centre of the Brillouin zone, the  $K$ -points indicate the corners, and we find an  $M$ -point in the centre of each line connecting the corners. In order to avoid double counting, the interior of the hexagon together with the border highlighted in magenta in figure II.2 are counted to the first Brillouin zone. The first Brillouin zone of the hexagonal lattice hence comprises the set of crystallographic inequivalent points  $\{\Gamma, M, M', M'', K, K'\}$ .

The characteristic length scales of the monolayer graphene and bilayer graphene lattice in real space are given by the lattice constant  $a \approx 0.142$  nm of the monolayer and the interlayer distance  $d \approx 0.34$  nm of the bilayer lattice. The lattice constant of the underlying triangular Bravais lattice is given by  $a_L = \sqrt{3}a \approx 0.246$  nm.

### Band Structure and Energetic Properties

Figure II.3 shows the band structure of monolayer and bilayer graphene in the first Brillouin zone. We sketch how this electronic dispersion can be obtained within the tight-binding formalism and discuss some of the most prominent features.

### Band Structure of Monolayer Graphene

We review the electronic properties of monolayer graphene within a tight-binding approximation. Let us start by understanding which are the electrons relevant for charge transport in graphene. Carbon, as an element of the fourth main group of the periodic table, possesses six electrons. The atomic shells to be filled are the 1s, 2s, and the 2p orbitals. Two electrons fill the innermost shell 1s. Three electrons are involved in the  $sp^2$  hybridisation, that is, they are in a superposition between the  $|2s\rangle$  and the  $|2p_x\rangle, |2p_y\rangle$  states. These make the planar  $\sigma$ -bonds between the carbon atoms responsible for the formation of a honeycomb structure. Energetically, these five electrons are far below the Fermi level and do not contribute to electronic transport. The remaining electrons, however, one electron per carbon atom occupying the  $p_z$ -orbital perpendicular to the plane, respectively, form  $\pi$ -bonds. Hence, each carbon atom has four bonds, one  $\sigma$  bond with each of its three neighbours and one  $\pi$ -bond that sticks out of plane. The  $\pi$ -electrons are the electrons responsible for the low-energy electronic properties of graphene.

The band structure theory for  $\pi$ -electrons on a honeycomb lattice was calculated originally within the tight-binding approximation in reference [Wallace, 1947].

Taking into account the onsite energy  $\varepsilon := \varepsilon_A = \varepsilon_B$ , nearest neighbour hopping with hopping parameter  $\gamma_0$ , as well as an overlap parameter  $s$  for orbitals on adjacent sites, the tight binding transfer and overlap matrices  $T$  and  $S$ , respectively, can be found to read [Saito et al., 1998; Goerbig, 2011; McCann and Koshino, 2013]

$$T_{ML} = \begin{bmatrix} \varepsilon & -\gamma_0 f(\mathbf{k}) \\ -\gamma_0 f^*(\mathbf{k}) & \varepsilon \end{bmatrix}, \quad S_{ML} = \begin{bmatrix} 1 & s f(\mathbf{k}) \\ s f^*(\mathbf{k}) & 1 \end{bmatrix}, \quad (\text{II.1})$$

where the function  $f(\mathbf{k})$  is given by

$$f(k_x, k_y) = \sqrt{4 \cos\left(\frac{1}{2}\sqrt{3}ak_x\right) \cos\left(\frac{ak_y}{2}\right) + 4 \cos^2\left(\frac{ak_y}{2}\right) + 1}. \quad (\text{II.2})$$

This directly yields the band structure of monolayer graphene given by the two bands [Saito et al., 1998]

$$\epsilon_\lambda(\mathbf{k}) = \frac{\varepsilon + \lambda\gamma_0 |f(\mathbf{k})|}{1 + \lambda s |f(\mathbf{k})|}, \quad \lambda = \pm 1, \quad (\text{II.3})$$

where for choosing  $\lambda = -1$  the lower lying valence band is obtained, while  $\lambda = +1$  yields the conduction band. The bandwidth is proportional to the hopping parameter  $\gamma_0$ .

If figure II.3 we plot the monolayer graphene band structure of equation (II.3), for the parameters  $\varepsilon = 0.22$  eV,  $\gamma_0 = 2$  eV, and  $s = 0.01$ .

### Band Structure of Bilayer Graphene

For bilayer graphene there are several possibilities how to arrange two hexagonal lattices upon each other; the most common type is the case of *Bernal stacking* which is shown in figure II.1: here, the carbon atoms of sub-layer  $A$  on the upper layer  $L_1$  fall on top of the atoms of sub-layer  $\tilde{B}$  of the lower layer  $L_2$ , while the carbon atoms of sub-layer  $B$  in  $L_1$  come to lie above the void in the centre of a hexagon of  $L_2$ . If two atoms lie on top of each other they are referred to as *dimer* sites as opposed to *non-dimer* sites when this is not the case.

For the case of Bernal stacked bilayer graphene the transfer matrix integral obtained from the so-called Slonczewski-Weiss-McClure [McClure, 1957; Slonczewski and Weiss, 1958] model of bulk graphite reads [McCann and Koshino, 2013]

$$T_{BL} = \begin{bmatrix} \delta_{AB} & -\gamma_3 f(\mathbf{k}) & -\gamma_4 f^*(\mathbf{k}) & -\gamma_0 f^*(\mathbf{k}) \\ -\gamma_3 f^*(\mathbf{k}) & \delta_{AB} & -\gamma_0 f(\mathbf{k}) & -\gamma_4 f(\mathbf{k}) \\ -\gamma_4 f(\mathbf{k}) & -\gamma_0 f^*(\mathbf{k}) & 0 & \gamma_1 \\ -\gamma_0 f(\mathbf{k}) & -\gamma_4 f^*(\mathbf{k}) & \gamma_1 & 0 \end{bmatrix}, \quad (\text{II.4})$$

where we introduced the tight-binding parameters as follows: the hoppings  $\gamma_0 = \gamma_{A \leftrightarrow B}$  describe intra-layer coupling, *i.e.*, for next neighbours in-plane hopping within one graphene layer, and  $\gamma_1 = \gamma_{\tilde{A} \leftrightarrow B}$  captures interlayer hopping via vertical coupling between the pairs of orbitals on the dimer sites. Furthermore, the skew interlayer couplings containing both in-plane and vertical components are denoted by  $\gamma_3 = \gamma_{A \leftrightarrow \tilde{B}}$  for coupling between two non-dimer orbitals, and  $\gamma_4 = \gamma_{A \leftrightarrow \tilde{A}}$  for coupling between one dimer and one non-dimer orbital. Due to different on-site energies in bilayer graphene, there also appears an energetic splitting  $\delta_{A,B}$  between the local energies between  $A$  and  $B$  sites on each layer.

The overlap parameters in bilayer graphene are small compared to the hopping integrals and the overlap integral matrix of bilayer graphene is generally treated as a unit matrix:  $S_{BL} \equiv \mathbb{1}$ . Therefore, the eigenvalues of the transfer matrix integral of equation (II.4) directly yield the four bands of the band structure of bilayer graphene as shown in figure II.3, for parameters  $\gamma_0 = 3.16$  eV,  $\gamma_1 = 0.381$  eV,  $\gamma_3 = 0.38$  eV,  $\gamma_4 = 0.14$  eV, and  $\delta_{AB} = 0.016$  eV.

*Discussion of the Band Structure*

We discuss the most important features of the band structure of monolayer and bilayer graphene as obtained from the above tight-binding treatment. The electronic dispersions are shown in figure II.3, respectively.

- There are two bands in the band structure of monolayer graphene, one valence and one conduction band, as there are two inequivalent atoms per unit cell. For bilayer graphene, due to the four-atomic basis, we obtain four bands, forming two valence bands and two conduction bands, respectively.
- Let us discuss the overall shape of the band structure of monolayer and bilayer graphene: the valence and conduction bands bend towards each other in tips, such that the gap between them vanishes at several special points of the Brillouin zone. These points where the two bands of monolayer graphene or the two inner-lying bands of bilayer graphene touch we denote with  $\mathbf{k}_D$ .<sup>‡</sup> In perfectly symmetric, undeformed graphene these touching points  $\mathbf{k}_D$  are located at the corners of the Brillouin zone of the honeycomb lattice, *i.e.*, at the crystallographic  $K$  points in momentum space. As there are two such inequivalent  $K$  corners counted for the first Brillouin zone of graphene (see figure II.2), there are two inequivalent  $\mathbf{k}_D$  points per graphene Brillouin zone, located at  $\mathbf{k}_D = K_+ = +K$  and  $\mathbf{k}_D = K_- = -K$ , respectively.
- As the Hamiltonians of equations (II.1) and (II.4) do not depend on the spin of the electrons, each of the bands in II.3 are doubly degenerate in the spin configurations  $\sigma = \uparrow, \downarrow$ .
- In charge neutral graphene every carbon atom contributes exactly one conduction electron as the  $\pi$ -electron in the  $p_z$  orbital. Therefore, as there are always two degenerate spin states available in each band, in the case of neutral monolayer and bilayer graphene the band structure is exactly half filled: the valence band is completely filled while the conduction band is completely empty. As a consequence, in the charge neutral case the Fermi surface is located exactly at the  $\mathbf{k}_D$  points where the valence and the conduction band touch. Therefore, the low-energy physics of the system, *i.e.*, the physics of the ground state or of low-energy excitations around the Fermi surface will figure predominantly the energetic structure in the vicinity of the  $\mathbf{k}_D$  points.

<sup>‡</sup> The index  $D$  is reminiscent from the case of monolayer graphene where these points  $\mathbf{k}_D$  are commonly referred to as "Dirac" points, as the band structure of monolayer graphene disperses linearly in their vicinity. This will be discussed in detail in the next section.

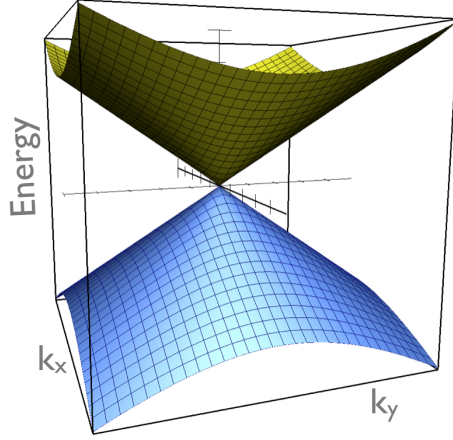


**Figure II.4**

Cone-like structure of the low-energy approximation to the dispersion of monolayer graphene in the vicinity of the  $K_+$  and  $K_-$  points.

### Low-Energy Approximation to the Band Structure in the Vicinity of the Dirac Points

An approximation which captures the energetic dispersion in the vicinity of the  $k_D$  points can facilitate the description of low-energy processes. In this context, the term "low-energy" refers to an energy much smaller than the bandwidth.

In order to obtain such an approximate low-energy description, the wave vector  $\mathbf{k}$  is decomposed as  $\mathbf{k} = \pm\mathbf{K} + \mathbf{p}$  with  $|\mathbf{p}| \ll |\mathbf{K}|$ . The electronic dispersion of monolayer and bilayer graphene, equations (II.1) and (II.4), are then expanded in  $|\mathbf{p}|a$  around the  $k_D$  points.

#### *Low-Energy Approximation: Monolayer Graphene*

In the case of monolayer graphene an expansion of the Hamiltonian to first order in the small parameter  $|\mathbf{p}|a$  around the Dirac points yields the effective low-energy Hamiltonian [Niemi and Semenoff, 1985; Goerbig, 2011]

$$\hat{H}_{eff}^{\tau}(\mathbf{q}) = \tau \hbar v_F (q_x \sigma^x + q_y \sigma^y), \quad (\text{II.5})$$

which is to act on the two-component spinors

$$\psi^{\tau=+} = \begin{pmatrix} \psi^{A,+} \\ \psi^{B,+} \end{pmatrix} \text{ and } \psi^{\tau=-} = \begin{pmatrix} \psi^{B,-} \\ \psi^{A,-} \end{pmatrix}, \quad (\text{II.6})$$

respectively. The above notation comprises the following information:

- The two-component spinor states of equation (II.6) in the space corresponding to the effective Hamiltonian of equation (II.5) consist of the probability amplitudes  $\psi^{A,B}$  of the particles on the two sub-lattices  $A$  and  $B$ .

- Reflecting spin degeneracy,  $\hat{H}_{eff}^\tau$  of equation (II.5) acts equally on spin-up or spin-down electrons. It can easily be translated to four-dimensional spin-valley space  $\mathcal{H} = \mathcal{H}_{spin} \otimes \mathcal{H}_{valley}$  by writing  $\hat{H}_{eff,full}^\tau = \sigma_z \otimes \hat{H}_{eff}^\tau$ , where  $\sigma_z$  denotes the third Pauli matrix. For simplicity, we will, however, suppress the spin index until it is needed explicitly.
- The index  $\tau = \pm 1$  accounts for the equivalence of the energetic dispersion of monolayer graphene around either of the Dirac points  $\mathbf{k}_D$ . This energetic degeneracy in the vicinity of either  $\mathbf{k}_D$  is referred to as the *valley degeneracy*.

Two such Dirac points are counted for the first Brillouin zone of monolayer graphene, located at the inequivalent points  $\mathbf{k}_D = \pm \mathbf{K}$  in momentum space. These are captured by the index  $\tau$  according to  $\tau = +1 \hat{=} +\mathbf{K}$  and  $\tau = -1 \hat{=} -\mathbf{K}$ . As will become clear in the following chapters, valley degeneracy in graphene can be in an excellent approximation treated as an SU(2) isospin with the two different possible configurations  $\tau = \pm 1$ . We will exploit this correspondence at length in our investigations of monolayer and bilayer graphene. See appendix D for more details.

- We denote by  $v_F = \frac{3|\gamma_0|a}{2\hbar}$  the Fermi velocity of monolayer graphene.
- Diagonalisation of the Hamiltonian in equation (II.5) yields the particle-hole symmetric eigenenergies

$$\epsilon_{ML,eff}^{\lambda,\tau}(\mathbf{q}) = \lambda \hbar v_F |\mathbf{q}|. \quad (\text{II.7})$$

This reflects the approximately linear dispersion of electrons in monolayer graphene in the low-energy description in the vicinity of the  $\mathbf{k}_D$  points. The resulting diabolo shape of this low-energy dispersion is shown in figure II.4. This low-energy energy structure is referred to as the *Dirac cone* structure. The association with Dirac stems from the resemblance of the low-energy effective Hamiltonian of monolayer graphene, equation (II.5), to the two-dimensional massless Dirac Hamiltonian  $H_D = v_F \mathbf{p} \cdot \boldsymbol{\sigma}$ , with momentum  $\mathbf{p} = \hbar \mathbf{q}$  and the Pauli vector  $\boldsymbol{\sigma} = (\sigma_x, \sigma_y)$ . The role of the real spin of the electrons is played by the two-valued "which layer" degree of freedom with configurations *A* and *B*.

- Valley degeneracy manifests itself in the independency of the effective low-energy dispersion of equation (II.7) of the valley index  $\tau$ .

### *Low-Energy Approximation: Bilayer Graphene*

A similar line of argument as for monolayer graphene also holds for bilayer graphene: the energetic structure around the  $\mathbf{k}_D$  points, where the valence and the conduction band touch, is of particular interest for a description of the low-energy physics around the Fermi surface.

In the vicinity of the  $\mathbf{k}_D$  point the effective low-energy Hamiltonian reads [McCann and Koshino, 2013]

$$H_\tau = \tau \begin{bmatrix} \frac{1}{2}\Delta_B + \frac{1}{2}\tau(1+\tau)\delta_{AB} & v_3\mathbf{p} & v_4\mathbf{p}^\dagger & v_0\mathbf{p}^\dagger \\ v_3\mathbf{p}^\dagger & -\frac{1}{2}\Delta_B + \frac{1}{2}\tau(1+\tau)\delta_{AB} & v_0\mathbf{p} & v_4\mathbf{p} \\ v_4\mathbf{p} & v_0\mathbf{p}^\dagger & -\frac{1}{2}\Delta_B + \frac{1}{2}\tau(1-\tau)\delta_{AB} & \gamma_1 \\ v_0\mathbf{p} & v_4\mathbf{p}^\dagger & \gamma_1 & \frac{1}{2}\Delta_B + \frac{1}{2}\tau(1-\tau)\delta_{AB} \end{bmatrix}, \quad (\text{II.8})$$

where we introduced the effective velocities  $v_i = \frac{3a|\gamma_i|}{2\hbar}$  and a bias potential  $\Delta_B = edE_\perp[\frac{mV}{nm}]$  induced by an electric field of strength  $E_\perp$  perpendicular to the bilayer graphene sample.

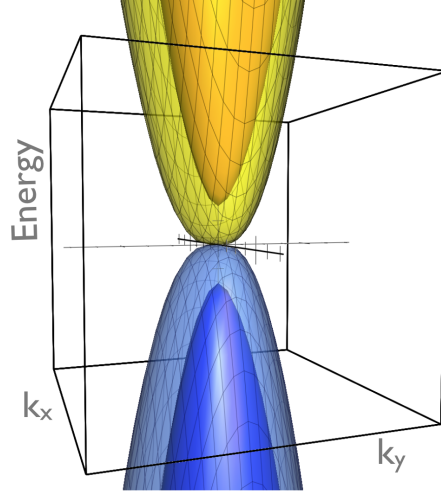
The Hamiltonian of equation (II.8) acts, respectively, on the four-component spinor fields

$$\psi_{K_+} = \begin{pmatrix} \psi_A \\ \psi_{\tilde{B}} \\ \psi_{\tilde{A}} \\ \psi_B \end{pmatrix} \quad \text{and} \quad \psi_{K_-} = \begin{pmatrix} \psi_{\tilde{B}} \\ \psi_A \\ \psi_B \\ \psi_{\tilde{A}} \end{pmatrix}. \quad (\text{II.9})$$

Where in the case of monolayer graphene we were dealing with two-component spinors for the probability amplitudes on the two sub-lattices  $A$  and  $B$ , equation (II.6), in bilayer graphene the single particle states of equation (A.2) are written in four component bases, where the electronic occupation on the four atoms  $A, \tilde{A}, B, \tilde{B}$  in the bilayer graphene unit cell is taken into account.

Again, as expounded for monolayer graphene, there is degeneracy in the real spin degree of freedom and the spin index in the effective bilayer graphene Hamiltonian of equation (II.8) is understood.

To perceive the implications of the low-energy approximation formulated in equation (II.8) we note the following: when neglecting the parameters  $v_4$  and  $\delta_{AB}$  the eigenenergies of the low-energy Hamiltonian of equation (II.8) can be found easily


**Figure II.5**

Energetic dispersion of bilayer graphene in the vicinity of the  $\mathbf{k}_D$  points within the low-energy approximation according to equation (II.10).

as

$$(\epsilon_{BL,eff}^{\alpha,\tau})^2(\mathbf{q}) = \frac{1}{4} \left[ \Delta_B^2 + 2[\gamma_1^2 + q^2(2v_0 + v_3^2)] + (-1)^\alpha f(\mathbf{q}) \right], \quad (\text{II.10})$$

where

$$f(\mathbf{q}) = 2\sqrt{\gamma_1^4 + 8\gamma_1 q_x(q_x^2 - 3q_y^2)v_0^2v_3 + q^2[2\gamma_1^2(2v_0^2 - v_3^2) + 4\Delta_B^2v_0^2] + q^4v_3^2(4v_0^2 + v_3^2)}. \quad (\text{II.11})$$

The approximate low-energy dispersion of equation (II.10) is plotted in figure II.5.

From this approximate equation for the dispersion of bilayer graphene we learn the following:

- Equation (II.10) shows that for  $v_4 = \delta_{AB} = 0$ , the Hamiltonian of equation (II.8) yields two valence and two conduction bands which are symmetric with respect to the Fermi level. Hence, the model is particle-hole symmetric at this level of approximation. Terms containing the parameters  $v_4$  and  $\delta_{AB}$  non-equal to zero, however, do break particle-hole symmetry.
- The dispersion relation associated with equation (II.10) contains terms of higher than linear order in  $\mathbf{q}$ . In the present case of bilayer graphene the bands therefore exhibit non-linear behaviour in the vicinity of their point of coalescence, in contrast to the linear behaviour observed for monolayer graphene. The band touching is therefore not linear as in the case of monolayer graphene. The low lying bands correspond to the index  $\alpha = 1$  in equation (II.10); It is instructive to consider them in the unbiased case, *i.e.*,  $\Delta_B = 0$

in equation (II.10), and neglect all terms proportional to  $v_3$ , for demonstration. In this case equation (II.10) further reduces to

$$\epsilon_{BL,eff}^{1,\tau}(\mathbf{q}) \approx \pm \sqrt{\frac{\gamma_1^2}{4} + v_0^2 q^2} - \frac{1}{2}\gamma_1. \quad (\text{II.12})$$

This simplified expression exhibits the following limiting behaviour:

- ★ Approximately linear for very large momenta, where  $q \gg \frac{\gamma_1}{v_0}$ :  $\epsilon_{BL,eff}^{1,\tau}(\mathbf{q}) \approx \pm v_0 q$ .
- ★ Extrapolation to approximately quadratic shape at very small momenta, *i.e.*, for  $q \ll \frac{\gamma_1}{v_0}$ :  $\epsilon_{BL,eff}^{1,\tau}(\mathbf{q}) \approx \pm \frac{v_0^2}{\gamma_1} q^2$ .

In bilayer graphene the band touching of the low-lying valence and conduction band is therefore approximately quadratic.

- Exactly at the touching point, at  $\mathbf{q} = 0$ , equation (II.10) reduces to

$$\epsilon_{BL,eff}^{1,\tau}(0) = \pm \frac{\Delta_B}{2}, \quad \epsilon_{BL,eff}^{2,\tau}(0) = \pm \frac{1}{2} \sqrt{\Delta_B^2 + 4\gamma_1^2}. \quad (\text{II.13})$$

Hence the band gap between the valence and the conduction band pairs in this approximation involves two parameters:

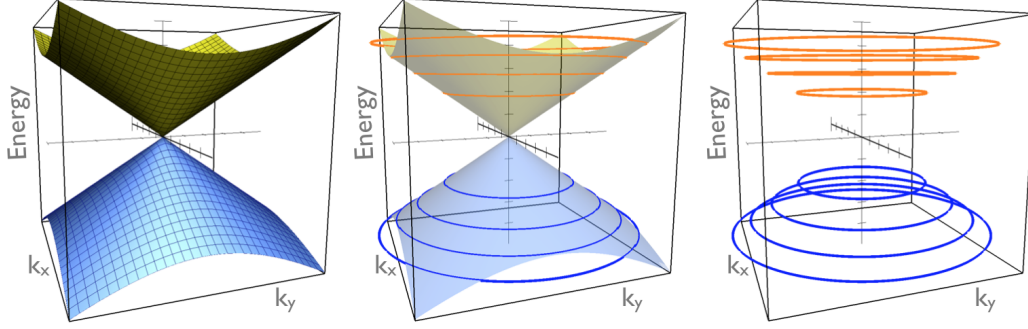
- ★ In the unbiased system,  $\Delta_B \equiv 0$ , the gap is controlled by the hopping parameter  $\gamma_1$ .
- ★ At non-zero bias, *i.e.*, for  $\Delta_B \neq 0$ , the splitting is further enhanced by the bias potential  $\Delta_B$ .

Hence, in bilayer graphene the band gap can be tuned by an external electric field inducing a variable bias  $\Delta_B$ .

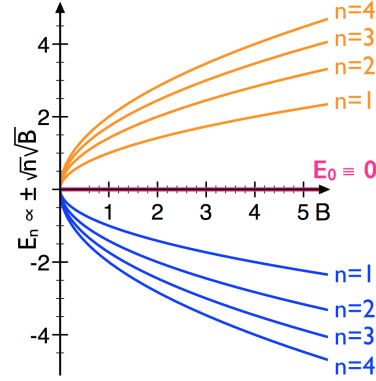
- As in the case of monolayer graphene the dispersion relation of equation (II.10) does not depend on the valley index  $\tau$ . We hence recover also in the case of bilayer graphene the same type of valley degeneracy as discussed already for monolayer graphene (see discussion following equation (II.5)).

### Energetic Dispersion in the Presence of a Magnetic Field: Landau Level Quantisation

We are concerned with the situation in which an external magnetic field is applied to the monolayer graphene or bilayer graphene system. It is well-known that a sufficiently strong magnetic field in a two-dimensional electron system leads to quantisation of the electronic dispersion: in the semiclassical picture, the electrons


**Figure II.6**

Quantisation of the low-energy dispersion of monolayer graphene into discrete Landau levels. For fixed  $B$ , the Landau level spacing in monolayer graphene is not equidistant but the energy of the  $n$ th Landau level rather scales with the square root of  $n$ :  $E_n \propto \pm\sqrt{n}\sqrt{B}$  (cf. equation (II.22)).


**Figure II.7**

Dispersion of any  $n$ th monolayer graphene Landau level proportional to the square root of the magnetic field strength  $B$ :  $E_n(B) \propto \pm\sqrt{n}\sqrt{B}$  (cf. equation (II.22)).

are forced by the Lorentz force to move in cyclotron orbits; When solving the problem quantum mechanically, a discrete level spectrum for the electronic energies is obtained, the so-called *Landau levels*.

We now consider Landau level quantisation for the case of monolayer and bilayer graphene.

#### *Landau Level Quantisation: Monolayer Graphene*

To treat the system of monolayer graphene subject to a magnetic field generated by the vector potential  $\mathbf{A}$  we employ *Peierls substitution* [Peierls, 1933]

$$\mathbf{p} \mapsto \boldsymbol{\pi} = \mathbf{p} + \frac{e}{c}\mathbf{A}(\mathbf{r}), \quad (\text{II.14})$$

which amounts to replace the kinetic momentum  $\mathbf{p} = \hbar\mathbf{q}$  by the canonical momentum  $\pi = \mathbf{p} + \frac{e}{c}\mathbf{A}(\mathbf{r})$  in the Hamiltonian  $H$  in equation (II.5)<sup>§</sup>.

This leads to the following Hamiltonian describing the low-energy regime of monolayer graphene in the presence of the magnetic field  $\mathbf{B} = \nabla \times \mathbf{A}$ :

$$H_{eff,B}^{\tau}(\pi) = \tau v_F (\pi_x \sigma^x + \pi_y \sigma^y). \quad (\text{II.15})$$

As the components of  $\pi$  fulfil the commutation relation  $[\pi_x, \pi_y] = -i\frac{\hbar^2}{\ell_B^2}$ , they form a canonical pair. In analogy to the quantisation of the one dimensional harmonic oscillator we hence introduce annihilation and creation operators  $a$  and  $a^\dagger$  as

$$a = \frac{\ell_B}{\sqrt{2}\hbar}(\pi_x - i\pi_y), \quad a^\dagger = \frac{\ell_B}{\sqrt{2}\hbar}(\pi_x + i\pi_y), \quad (\text{II.16})$$

respectively. In terms of these operators the Hamiltonian of equation (II.15) reads

$$H_{eff,B}^{\tau}(\pi) = \tau v_F \sqrt{2} \frac{\hbar}{\ell_B} \begin{pmatrix} 0 & a \\ a^\dagger & 0 \end{pmatrix}. \quad (\text{II.17})$$

Using the representation of the state as in equation (II.6), the eigenvalue equation to solve reads

$$H_B^{\tau}(\pi)\psi_n^{\tau} = E_n\psi_n^{\tau}. \quad (\text{II.18})$$

On the scout for solutions to equation (II.18) we make the generic spinor ansatz  $\psi_n^{\tau} = \begin{pmatrix} u_n \\ v_n \end{pmatrix}$  for the single particle wave function in the  $n$ th Landau level. Acting with the Hamiltonian  $H_B^{\tau}(\pi)$  of equation (II.17) on this state  $\psi_n^{\tau}$  as

$$H_B^{\tau}(\pi)\psi_n^{\tau} = \tau\sqrt{2}\frac{\hbar v_F}{\ell_B} \begin{pmatrix} a & v_n \\ a^\dagger & u_n \end{pmatrix} \stackrel{!}{=} E_n \begin{pmatrix} u_n \\ v_n \end{pmatrix}, \quad (\text{II.19})$$

yields the following coupled equations to be solved:

$$\tau\sqrt{2}\frac{\hbar v_F}{\ell_B} a v_n \stackrel{!}{=} E_n u_n \quad \text{and} \quad \tau\sqrt{2}\frac{\hbar v_F}{\ell_B} a^\dagger u_n \stackrel{!}{=} E_n v_n. \quad (\text{II.20})$$

---

<sup>§</sup> The Peierls substitution provides an approximate way to implement a magnetic field into a tight-binding Hamiltonian under the assumption that the vector potential  $\mathbf{A}$  varies slowly in space [Peierls, 1933]. In the present context, this is justified as the magnetic field is weak enough for the lattice spacing to be much smaller than the magnetic length:  $a \ll \ell_B = \sqrt{\frac{c\hbar}{eB}}$ . This is consistent with the comparison of length scales we discussed in the introductory chapter I, section I.2.2.

Acting with  $a$  from the left on the first of equations (II.20), we find the defining equation for  $v_n$ :

$$\begin{aligned} \tau\sqrt{2}\frac{\hbar v_F}{\ell_B} a^\dagger a v_n & \stackrel{!}{=} E_n \underbrace{a^\dagger u_n}_{E_n \frac{1}{\tau} \frac{\ell_B}{\sqrt{2}\hbar v_F} v_n} \\ \Leftrightarrow a^\dagger a v_n & = E_n^2 \frac{1}{\tau^2} \frac{\ell_B^2}{2\hbar^2 v_F^2} v_n, \end{aligned} \quad (\text{II.21})$$

from which  $v_n$  is deduced to be an eigenstate of the number operator  $N = a^\dagger a$ . Writing  $|n\rangle$  for the  $n$ th eigenstate of  $N$ , *i.e.*, the state containing  $n$  excitations,  $v_n$  is found to be proportional to  $|n\rangle$ ,  $v_n \propto |n\rangle$ . Therefore, it follows for the eigenenergies of the  $n$ th excited state:

$$\begin{aligned} N v_n & \propto N |n\rangle = n|n\rangle \\ \Rightarrow E_n^2 \frac{1}{\tau^2} \frac{\ell_B^2}{2\hbar^2 v_F^2} v_n & \propto E_n^2 \frac{1}{\tau^2} \frac{\ell_B^2}{2\hbar^2 v_F^2} |n\rangle, \\ \Rightarrow E_n & = \pm \sqrt{n} \frac{\sqrt{2}\hbar v_F}{\ell_B} \propto \pm \sqrt{n} \sqrt{B}, \end{aligned} \quad (\text{II.22})$$

where the last relation follows from the definition of the magnetic length  $\ell_B = \sqrt{\frac{\hbar c}{eB}}$ .

Equation (II.22) represents the quantised Landau level structure of electrons in monolayer graphene in the low-energy regime near the Dirac points. Due to the linear dispersion of the low-energy approximate description the Landau levels of monolayer graphene depend on the square-root of the Landau level index,  $\sqrt{n}$ , and they depend on the magnetic field as  $\sqrt{B}$ . Positive and negative energy solutions are obtained, labelled by  $\lambda = \pm 1$ , which reflects that the band structure of graphene consists of two bands, the valence and the conduction band. The dispersion of the monolayer graphene Landau levels is shown in figure II.7. The valley index labelled by  $\tau = \pm 1$  disappears when being squared and therefore does not influence the value of  $E_n$ ; we hence recover the energy degeneracy of the two inequivalent Dirac points.

The single particle Landau level wave function  $\psi_n^\tau$  corresponding to the single particle state of the  $\tau$  valley in the  $n$ th Landau level is obtained by combining the proportionality  $v_n \propto |n\rangle$  with the defining equations of II.20:

For a non-zero number of excitations,  $n \neq 0$ , acting with the annihilation operator  $a$  from the left yields

$$a v_n \propto \sqrt{n} |n-1\rangle$$

$$\stackrel{\text{eqn. (II.20)}}{=} E_n \frac{1}{\sqrt{2\xi}} \frac{\ell_B}{\hbar v_F} u_n = \sqrt{n} u_n. \quad (\text{II.23})$$

This relation implies the proportionality  $u_n \propto |n-1\rangle$ .

Hence, the state vector of the  $n$ th excited state reads

$$\psi_{n \neq 0}^{\lambda, \tau} = \mathcal{N} \begin{pmatrix} \alpha |n-1\rangle \\ \beta |n\rangle \end{pmatrix}, \quad (\text{II.24})$$

with the proportionality factors  $\alpha$  and  $\beta$  constrained by  $|\alpha| = |\beta|$  and a normalisation factor  $\mathcal{N}$ . When  $\alpha$  and  $\beta$  have the same sign,  $\text{sgn}(\alpha) = \text{sgn}(\beta)$ , we obtain the positive energy solution  $+E_n$ , whereas  $\text{sgn}(\alpha) = -\text{sgn}(\beta)$  implies the negative eigenenergy  $-E_n$ . We choose  $\alpha = 1$  and  $\beta = \lambda\tau$  which yields  $\beta = \pm 1$ , depending on the band index  $\lambda = \pm 1$  and the valley index  $\tau = \pm 1$ .

For the special case of the zero energy solution, there is no dependence on the band index  $\lambda$  and we find only one solution for each valley. For  $n = 0$ , due to the property  $a|0\rangle = 0$ , the state vector has only one non-zero component and reads:

$$\psi_{n=0}^{\tau} = \frac{1}{\sqrt{2}} \begin{pmatrix} 0 \\ \tau |0\rangle \end{pmatrix}. \quad (\text{II.25})$$

This implies the state in each valley to reside solely on one of the triangular sublattices.

Similarly to the case of Landau level quantisation of the free electron gas presented in chapter I, the cyclotron energy of the  $n$ th Landau level in monolayer graphene, equation (II.22), is independent of the guiding centre coordinate of the cyclotron orbit. The corresponding quantum number can be incorporated in the description of the state by following the exact same steps as for the free electron gas in chapter I: by decomposing the position operator  $\mathbf{r}$  into the position of the guiding centre and of the cyclotron coordinate as  $\mathbf{r} = \mathbf{R} + \mathbf{r}_c$  and introducing the ladder operators  $\mathbf{b} = \frac{1}{\sqrt{2\ell_B}}(X + iY)$  and  $\mathbf{b}^\dagger = \frac{1}{\sqrt{2\ell_B}}(X - iY)$ , where  $X$  and  $Y$  are the coordinates of the guiding centre:  $\mathbf{R} = (X, Y)$ . These ladder operators  $\mathbf{b}, \mathbf{b}^\dagger$  define the algebra of the guiding centre quantum number with eigenstates  $|m\rangle$  of the associated number operator given by  $\mathbf{b}^\dagger \mathbf{b} |m\rangle = m |m\rangle$  for  $m \in \mathbb{N}^0$ .

Hence the electronic state of the  $n$ th Landau level acquires the additional quantum number accounting for the degeneracy in the guiding centre coordinate and the full quantum states read:

$$\psi_{n \neq 0, m}^{\lambda, \tau} = \psi_{n \neq 0}^{\lambda, \tau} \otimes |m\rangle = \mathcal{N} \begin{pmatrix} \alpha |n-1, m\rangle \\ \beta |n, m\rangle \end{pmatrix}, \quad (\text{II.26})$$

$$\psi_{n=0, m}^{\tau} = \psi_{n=0}^{\tau} \otimes |m\rangle = \frac{1}{\sqrt{2}} \begin{pmatrix} 0 \\ \tau |0, m\rangle \end{pmatrix}. \quad (\text{II.27})$$

For many calculations it is useful to chose a specific gauge for the vector potential. Within the Landau gauge with  $\mathbf{A} = (0, Bx, 0)$  the real space representation of the electronic wave function in the  $n$ th Landau level reads

$$\phi_{n, k_y}(\mathbf{r}) = \langle \mathbf{r} | n, m \rangle = \frac{1}{L_y} e^{ik_y y} \frac{1}{\sqrt{2^n n! \sqrt{\pi} \ell_B}} e^{-\frac{(x - X_{k_y})^2}{2\ell_B^2}} H_n(x - X_{k_y}). \quad (\text{II.28})$$

Let  $k_y$  be  $y$ -component of the Landau gauge momentum with  $k_y = \frac{2\pi}{L_y} |m|$  for a system of extension  $L_y$  in  $y$ -direction, and  $X_{k_y} = k_y \ell_B^2$  the guiding centre coordinate. With  $H_n$  we denote the  $n$ th Hermite polynomial.

#### Landau Level Quantisation: Bilayer Graphene

★ Description in terms of an approximate two-band model:

To understand the properties of bilayer graphene in an external magnetic field it is instructive to consider a simplified model in which the highest and the lowest lying bands are incorporated effectively and the description is reduced to a picture in terms of only two effective bands [McCann and Fal'ko, 2006].

In the most simplified version, *i.e.*, for  $B = \Delta_B = v_4 = v_3 = \delta_{AB} = 0$  in equation (II.8), the the effective two-band Hamiltonian describing the low-energy physics of bilayer graphene in the vicinity of the Dirac points can be written in the form [McCann and Fal'ko, 2006; McCann and Koshino, 2013]

$$H_{BL,eff} = \frac{1}{2m^*} \begin{bmatrix} 0 & (q_x - iq_y)^2 \\ (q_x + iq_y)^2 & 0 \end{bmatrix}, \quad (\text{II.29})$$

in terms of the effective mass  $m^* = \frac{\gamma_1}{2v_0^2}$  derived from the approximately quadratic dispersion equation (II.12). The Hamiltonian in equation (II.29) is written in the

basis  $(A_2, B_1)$  for the  $K_-$  point or in the basis  $(B_1, A_2)$  for the  $K_+$  point, respectively.

In the presence of a magnetic field, the procedure to obtain the Landau levels for the Hamiltonian  $H_{BL,eff}$  is similar to the monolayer graphene case. After the Peierls substitution,  $\mathbf{p} \mapsto \pi = \mathbf{p} + \frac{e}{c}\mathbf{A}(\mathbf{r})$  as in equation (II.14), an equivalent calculation yields the approximate Landau level structure of bilayer graphene,

$$E_n = \pm \hbar \omega_c \sqrt{n(n-1)}, \quad (\text{II.30})$$

with characteristic frequency  $\omega_c = \frac{eB}{m^*}$  and corresponding eigenfunctions

$$\psi_{\tau,n \geq 2} = \tau \frac{1}{\sqrt{2}} \begin{pmatrix} |n\rangle \\ \pm |n-2\rangle \end{pmatrix} \text{ and } \psi_{\tau,n=1} = \begin{pmatrix} |1\rangle \\ 0 \end{pmatrix}, \psi_{\tau,n=0} = \begin{pmatrix} |0\rangle \\ 0 \end{pmatrix}. \quad (\text{II.31})$$

Like in the case of Landau level quantisation of the free electron gas or of monolayer graphene, these states are complemented to fully characterise the electronic quantum states in the  $n$ th Landau level by the guiding centre quantum number  $m$ :

$$\psi_{\tau,n \geq 2,m} = \psi_{\tau,n \geq 2} \otimes |m\rangle, \psi_{\tau,n=0,m} = \psi_{\tau,n=0} \otimes |m\rangle. \quad (\text{II.32})$$

We list some of the main features of this approximate description of bilayer graphene in the frame of the two-band model:

- We obtain a scaling of the Landau level energies for bilayer graphene of linear leading order in  $n$  for  $n \gg 1$  as a reminiscence of the approximately quadratic band structure of bilayer graphene at low energies.
- One of the major peculiarities of bilayer graphene is the approximate two-fold degeneracy of the zero-energy Landau level state. We see from equation (II.30) that for both, Landau level quantum number  $n = 0$  and  $n = 1$ , the Landau level energy vanishes:  $E_0 = E_1 = 0$ . Hence, within the description of the two-band model, there is exact degeneracy of the  $n = 0$  and the  $n = 1$  Landau level. We note, however, that there is no underlying, fundamental symmetry that protects this degeneracy.
- From equation (II.31) we deduce that for the zero-energy states of the two-band model there is a correspondence between the Landau level index and the sub-lattice which is occupied by the electrons: at the  $K_+$  valley the wave functions  $\psi_{K_+,n=1}$  and  $\psi_{K_+,n=0}$  fully reside on the layer  $L_2$ , while  $\psi_{K_-,n=1}$  and  $\psi_{K_-,n=0}$  occupy the lattice  $L_1$ , only.

★ Landau level quantisation within the four-band model:

Landau level quantisation in bilayer graphene in the full four-band model is somewhat more involved [Mucha-Kruczyński, 2013; Mucha-Kruczyński et al., 2008, 2009; Côté and Barrette, 2013]; We present the calculation at the level of approximation which is adopted throughout this work: we start from an exact, analytical calculation in which the smallest tight-binding parameters are neglected and re-include them subsequently as small perturbations.

In a first step, the main features can be demonstrated most conveniently for a simplified model in which the components proportional to the smallest parameters  $\delta_{AB}$ ,  $\gamma_3$ , and  $\gamma_4$  are neglected. In this case the action of the ladder operators  $\pi = \pi_x + \pi_y$  and  $\pi^\dagger = \pi_x - \pi_y$  in the Hamiltonian of equation (II.8), which act as lowering and raising operators in the basis of Landau functions, respectively, enforces the electronic state of the  $n$ th Landau Level in the valley  $K_+$  to be of the form (agreeing on  $|n\rangle \equiv 0$  for  $n < 0$ ):

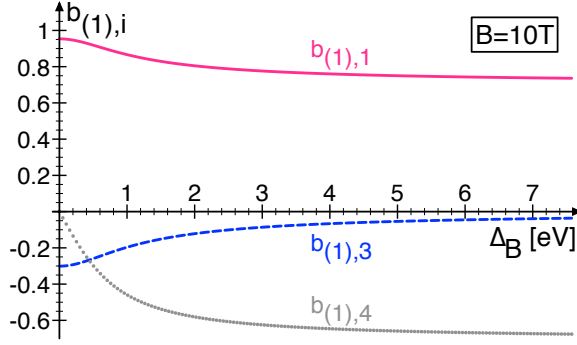
$$\psi_{K_+,n} = \begin{pmatrix} b_{(n),1}|n\rangle \\ b_{(n),2}|n-2\rangle \\ b_{(n),3}|n-1\rangle \\ b_{(n),4}|n-1\rangle \end{pmatrix}, \quad (\text{II.33})$$

where the coefficients  $b_{(n),i}$  are determined by the system of linear equations imposed by the eigenvalue equation  $H_{K_+}\psi_{K_+}^{(n)} = \epsilon_n\psi_{K_+}^{(n)}$ .

Again, above states of equation (II.33) are complemented with the guiding centre quantum number  $m$ ; for calculations where a real-space representation of the electronic state is employed, we refer to the akin monolayer graphene case of equation (II.28).

Of special interest are the cases  $n = 0$  and  $n = 1$  as in the following we focus on the physics of the zero-energy multiplet in bilayer graphene. Therefore, we note for further use the explicit properties of the states with  $n = 0$  and  $n = 1$ :

$$\psi_{K_+,0} = \begin{pmatrix} |0\rangle \\ 0 \\ 0 \\ 0 \end{pmatrix}, \quad \psi_{K_+,1} = \begin{pmatrix} b_{(1),1}|1\rangle \\ 0 \\ b_{(1),3}|0\rangle \\ b_{(1),4}|0\rangle \end{pmatrix}, \quad (\text{II.34})$$


**Figure II.8**

Evolution of the coefficients  $b_{(1),i}$  functions of  $\Delta_B$  at magnetic field strength  $B=10$  T.

with coefficients [Shizuya, 2012]

$$\begin{aligned} b_{(1),1} &= c_1, \\ b_{(1),3} &= -\frac{c_1}{g_1}(1 - M^2 z^2), \\ b_{(1),4} &= -c_1 z M. \end{aligned} \quad (\text{II.35})$$

In above relations,  $c_1 = \frac{1}{\sqrt{1 + \frac{1}{g_1^2}(1 - M^2 z^2)^2 + z^2 M^2}}$  denotes the normalisation constant in terms of the rescaled parameters  $g_1 = \frac{\gamma_1}{\hbar\omega_c}$  and  $2M = \frac{\Delta_B}{\hbar\omega_c}$ . The parameter  $z$  is determined as the solution to the equation

$$z = \frac{1}{g_1^2}(2 - z)(1 - M^2 z^2) \text{ in the range } 0 \leq z \leq 1, \quad (\text{II.36})$$

which implies that  $z$  is a function of the bias potential:  $z(\Delta_B)$ .

Figure II.8 shows the evolution of the coefficients  $b_{(1),1}$ ,  $b_{(1),3}$ , and  $b_{(1),4}$  as functions of the rescaled bias  $M$  for a magnetic field  $B = 10$  T.

The associated lowest energy eigenvalues of the  $n = 0$  and the  $n = 1$  mode are given by

$$\begin{aligned} E_{\tau,n=0} &= \tau \frac{1}{2} \Delta_B, \\ E_{\tau,n=1} &= \tau \frac{1}{2} \Delta_B - \tau \frac{1}{2} z \Delta_B, \end{aligned} \quad (\text{II.37})$$

where  $\tau$  denotes the valley index.

In a second step, we include the parameters neglected beforehand,  $\delta_{AB}$ ,  $\gamma_3$ , and  $\gamma_4$ , by estimating their influence when they are treated as small perturbations to the

system.

To this end we start with the Hamiltonian in the  $K_+$  valley in the absence of any external electric field, *i.e.*, for  $\Delta_B = 0$ , and write it as an expansion in the above parameters:

$$\begin{aligned}
 H_{K_+}^{\Delta_B=0} = & \underbrace{\hbar\omega_c \begin{bmatrix} 0 & 0 & 0 & a^\dagger \\ 0 & 0 & a & 0 \\ 0 & a^\dagger & 0 & g_1 \\ a & 0 & g_1 & 0 \end{bmatrix}}_{M_{1,K_+}} + \delta_{ab} \underbrace{\begin{bmatrix} 1 & 0 & 0 & 0 \\ 0 & 1 & 0 & 0 \\ 0 & 0 & 0 & 0 \\ 0 & 0 & 0 & 0 \end{bmatrix}}_{M_{\delta_{AB},K_+}} \\
 & + \hbar\omega_c \frac{\gamma_3}{\gamma_0} \underbrace{\begin{bmatrix} 0 & a & 0 & 0 \\ a^\dagger & 0 & 0 & 0 \\ 0 & 0 & 0 & 0 \\ 0 & 0 & 0 & 0 \end{bmatrix}}_{M_{\gamma_3,K_+}} + \hbar\omega_c \frac{\gamma_4}{\gamma_0} \underbrace{\begin{bmatrix} 0 & 0 & a^\dagger & 0 \\ 0 & 0 & 0 & a \\ a & 0 & 0 & 0 \\ 0 & a^\dagger & 0 & 0 \end{bmatrix}}_{M_{\gamma_4,K_+}}. \quad (\text{II.38})
 \end{aligned}$$

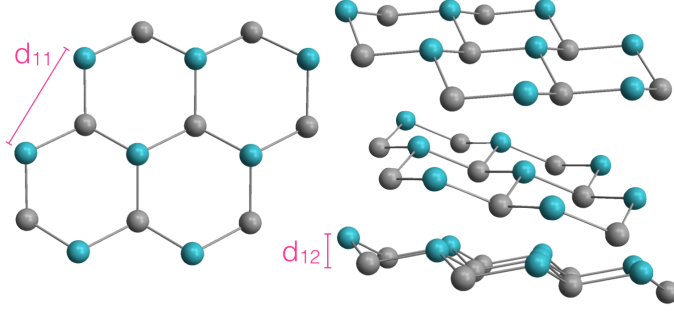
The starting point is the knowledge of the exact eigenstates and eigenenergies of the two zero-energy modes for the unbiased system:

$$\begin{aligned}
 n = 0 : \quad E_0^{\Delta_B=0} = 0, \quad \psi_{K_+,0}^{\Delta_B=0} &= \begin{pmatrix} |0\rangle \\ 0 \\ 0 \\ 0 \end{pmatrix}, \\
 n = 1 : \quad E_1^{\Delta_B=0} = 0, \quad \psi_{K_+,1}^{\Delta_B=0} &= \begin{pmatrix} c_1|1\rangle \\ 0 \\ -\frac{c_1}{g_1}|0\rangle \\ 0 \end{pmatrix}, \quad (\text{II.39})
 \end{aligned}$$

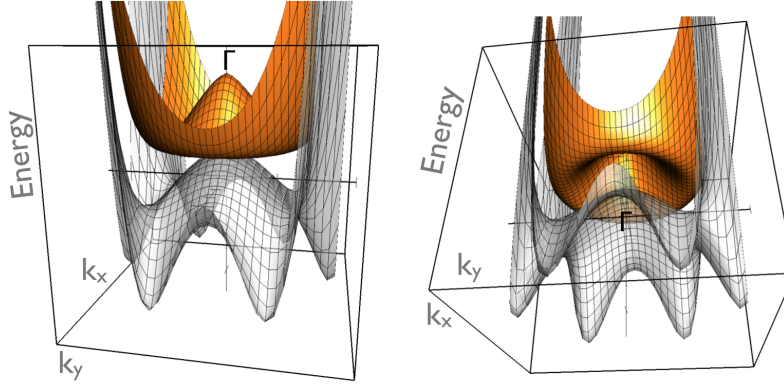
with coefficient  $c_1^2|_{\Delta_B=0} = \frac{g_1^2}{g_1^2+1}$ .

Computing the energy corrections due to the sub-leading terms from first order perturbation theory,  $E_{0,1} \approx E_{0,1}^{\Delta_B=0} + \lambda\epsilon_{0,1}^\lambda$ , where  $\epsilon_{0,1}^\lambda = \langle 1,0|M_\lambda|0,1\rangle$ , we obtain the following expressions:

$$\begin{aligned}
 \epsilon_0^{\delta_{AB}} = \langle 0|M_{\delta_{AB}}|0\rangle &= 1, \quad \epsilon_1^{\delta_{AB}} = \langle 1|M_{\delta_{AB}}|1\rangle = c_1^2. \\
 \epsilon_0^{\gamma_3} = \langle 0|M_{\gamma_3}|0\rangle &= 0, \quad \epsilon_1^{\gamma_3} = \langle 1|M_{\gamma_3}|1\rangle = 0, \\
 \epsilon_0^{\gamma_4} = \langle 0|M_{\gamma_4}|0\rangle &= 0, \quad \epsilon_1^{\gamma_4} = \langle 1|M_{\gamma_4}|1\rangle = -2\frac{c_1^2}{g_1}. \quad (\text{II.40})
 \end{aligned}$$


**Figure II.9**

Lattice structure of the Bi(111) surface seen from the top (left) and from the side under different tilt angles (right).


**Figure II.10**

Band structure of the Bi(111) surface state around the  $\Gamma$  point.

We thus obtain the corrected single particle energies

$$\begin{aligned} E_0^{\Delta_B=0} &= \delta_{AB}, \\ E_1^{\Delta_B=0} &= -2\hbar\omega_c \frac{\gamma_4}{\gamma_0} \frac{c_1^2}{g_1} + c_1^2 \delta_{AB}. \end{aligned} \quad (\text{II.41})$$

From this analysis we learn that including corrections due to non-vanishing values of  $\delta_{AB}$  and  $\gamma_4$  alters the single particle energies of the Landau levels  $n = 0$  and  $n = 1$  and the degeneracy between the  $n = 0$  and  $n = 1$  Landau level is lifted. The splitting  $\Delta_{01}^{\text{pert}}$  induced by these perturbative effects reads

$$\Delta_{01}^{\text{pert}} = -\delta_{AB}(1 - c_1^2) - 2\frac{\gamma_4}{\gamma_0\gamma_1} c_1^2 (\hbar\omega_c)^2. \quad (\text{II.42})$$

## II.1.2 Bismuth(111): Approximate Description of the Dispersion and Anisotropic Landau Level Quantisation

### Lattice of the Bi(111) Surface, Model to the Dispersion

Elemental bismuth crystallises in a lattice with rhombohedral symmetry [Ohtsubo and Kimura, 2016; Du et al., 2016]. The surface (111) is of particular interest due to

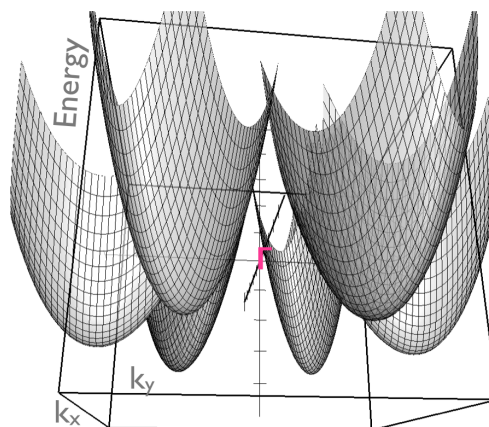


**Figure II.11**

The low-energy part of the Bi(111) surface state dispersion is modelled by six elliptical valleys arranged in a star-like configuration around the  $\Gamma$  point.

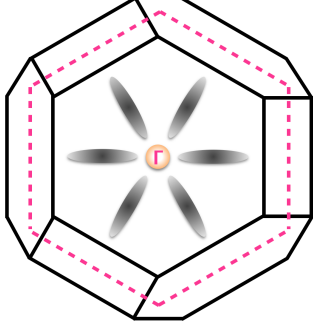
its peculiar electronic structure: the bismuth bulk crystal terminates in a buckled honeycomb lattice in which the Bi atoms arrange in two planes [Jezequel et al., 1986; Du et al., 2016]. In figure II.9 we show a top view and side views on this hexagonal surface lattice of the Bi(111) face. The surface electrons hence represent a two-dimensional electron system. The lattice parameters of the Bi(111) surface are  $d_{11} \approx 0.4453$  nm for the distance between two equivalent Bi atoms within one plane and  $d_{12} \approx 0.1590$  nm for the distance between the two planes of Bi atoms.

The dispersion of the surface states is of complex shape forming multiple electron-hole pockets. Within the energy region closest to the Fermi surface there are six anisotropic valleys centred around the  $\Gamma$ -point in the first Brillouin zone [Ast and Höchst, 2001; Du et al., 2016]. A symbolic sketch of the band structure of the Bi(111) surface state in the first Brillouin zone is shown in figure II.10.

We model the low-energy part of the electronic dispersion of Bi(111) as six identical valleys of elliptical shape, rotated with respect to each other by an angle of  $\frac{\pi}{3}$  and arranged in a star-like structure around the  $\Gamma$ -point as shown in figure II.11. This represents a minimal model taking into account the sixfold valley degeneracy and the anisotropic character of either of the valleys.

### Bi(111): Anisotropic Landau Level Quantisation

The presence of a sufficiently strong magnetic field will quantise the low-energy electronic dispersion of figure II.11 into a discrete Landau level structure. The specific features of this particular dispersion will translate into the Landau level scheme: due to the elliptical shape of the valleys in Bi(111), also the resulting Landau level orbitals exhibit anisotropic features such as anisotropic masses


**Figure II.12**

Projection of the three dimensional bulk Brillouin zone of bismuth (solid black lines) onto the two-dimensional (111)-surface Brillouin zone (magenta, dashed lines). Ellipses represent the projections of the six anisotropic valley pockets.

[Feldman et al., 2016].

We demonstrate anisotropic Landau level quantisation per single valley. Approximating the  $\tau$ th valley as an elliptical energy band with parabolic dispersion we write the corresponding low-energy Hamiltonian as

$$H = -\hbar\omega_{c,\tau} a_{\tau}^{\dagger} a_{\tau}, \quad (\text{II.43})$$

in terms of the anisotropic ladder operators  $a_{\tau}^{\dagger} = \frac{1}{\sqrt{2\hbar}}(\alpha_{\tau}\pi_x - i\beta_{\tau}\pi_y)$ ,  $a_{\tau} = \frac{1}{\sqrt{2\hbar}}(\alpha_{\tau}\pi_x + i\beta_{\tau}\pi_y)$ . These ladder operators define an algebra where the valleys are connected among themselves by discrete rotations [Feldman et al., 2016; Li et al., 2016; Sodemann et al., 2017]. The anisotropy is encoded in the anisotropy parameters  $\alpha_{\tau} = \frac{1}{\sqrt{\lambda}} \cos \theta_{\tau} + i\sqrt{\lambda} \sin \theta_{\tau}$ ,  $\beta_{\tau} = \sqrt{\lambda} \cos \theta_{\tau} + i\frac{1}{\sqrt{\lambda}} \sin \theta_{\tau}$ , where the dependence on the respective valleys labelled by  $\tau \in [1, \dots, 6]$  is contained in the angle  $\theta_{\tau} = (\tau - 1)\frac{\pi}{3}$  connecting the different valleys by rotation and the squeezing parameter  $\lambda = \sqrt{\frac{m_{\parallel}}{m_{\perp}}} \approx 5$  which realises the elliptical squeezing.

With these conventions, the anisotropic ladder operators  $a_{\tau}$ ,  $a_{\tau}^{\dagger}$  act on the state with  $n$  excitations in the  $\tau$ th valley as

$$a_{\tau}\psi_{n,\tau} = -i\frac{\alpha_{\tau}^*}{|\alpha_{\tau}|}\sqrt{n}\psi_{n-1,\tau}, \quad a_{\tau}^{\dagger}\psi_{n,\tau} = -i\frac{|\alpha_{\tau}|}{\alpha_{\tau}^*}\sqrt{n+1}\psi_{n+1,\tau}. \quad (\text{II.44})$$

Unlike the ladder operators  $a_{\tau}$  and  $a_{\tau}^{\dagger}$  for Landau level quantisation of the anisotropic valleys, the annihilation and creation operators of the quantum number  $m$ ,  $b$  and  $b^{\dagger}$  corresponding to the quantisation of the guiding centre coordinate, remain unchanged as compared to the free electron gas or to the graphene case. The full quantum state of the electron therefore again is given simply by  $\psi_{n,\tau,m} = \psi_{n,\tau} \otimes |m\rangle$ .

We adopt the Landau gauge  $\mathbf{A} = (0, -Bx)$  for the vector potential to write an explicit form of the wave functions in real space. As a consequence of the anisotropic action of the ladder operators  $a_\tau$ ,  $a_\tau^\dagger$  as defined in equation (II.44) the Landau gauge wave functions of the  $n$ th Landau level are of the form

$$\phi_{n,\tau,k_y}(\mathbf{r}) = \langle \mathbf{r} | \psi_{n,\tau,m} \rangle = \langle \mathbf{r} | n, \tau, k_y \rangle = \frac{1}{L_y} e^{ik_y y} \frac{1}{\sqrt{2^n n! \sqrt{\pi} |\alpha_\tau| \ell_B}} e^{\alpha_\tau^* \beta_\tau \frac{(\xi_\tau)^2}{2}} H_n(\xi_\tau), \quad (\text{II.45})$$

where  $k_y$  is the  $y$ -component of the Landau gauge momentum with  $k_y = \frac{2\pi}{L_y} |m|$  for a system of extension  $L_y$  in  $y$ -direction, and we write  $\xi_\tau = \frac{1}{|\alpha_\tau| \ell_B} (x - X_{k_y})$  with guiding centre coordinate  $X_{k_y} = k_y \ell_B^2$ . With  $H_n$  we denote the  $n$ th Hermite polynomial.

## II.2 Quantum Hall Ferromagnetism and Hartree Fock Theory

This chapter elucidates the concept of *quantum Hall ferromagnetism* [Sarma and Pinczuk, 1996; Barlas et al., 2012] and discusses how a quantum Hall ferromagnet can be described within *Hartree Fock theory*. We demonstrate how different physical systems can be described within this framework as multicomponent spin systems. The respective symmetries that play a role when describing a quantum Hall ferromagnet are discussed as well as how we understand and use the term *symmetry breaking* in this context. We then motivate why Hartree Fock theory is an appropriate tool to theoretically investigate a quantum Hall ferromagnet.

### II.2.1 The SU(N) Quantum Hall Ferromagnet

#### Describing a Multicomponent System

Given a quantum Hall system in which each single particle is characterised by a discrete internal degree of freedom  $\xi$  which exhibits SU(N) symmetry. By this we mean that for every single particle quantum state there are N different possible configurations which are energetically degenerate. Examples for such discrete degrees of freedom include the spin of the electron ( $\xi = \sigma \in \{\uparrow, \downarrow\}$ , hence N=2), the orbital index of bilayer graphene ( $\xi = \lambda \in \{0, 1\}$ ), or the valley index  $\xi = \tau \in \{+, -\}$  in mono- and bilayer graphene, and  $\xi = \tau \in \{1, \dots, 6\}$  in Bi(111), as introduced in the previous section II.1.2. Combining multiple degrees of freedom yields an even richer picture: for electrons in monolayer graphene for instance we have  $\xi \in \{(\uparrow, +), (\uparrow, -), (\downarrow, +), (\downarrow, -)\}$  and therefore N=4.

In an interacting quantum Hall system with such a multicomponent structure the ground state will be generally of fully homogeneous, ferromagnetic order, provided the interactions are  $SU(N)$  invariant giving rise to a fully  $SU(N)$  invariant Hamiltonian. The physical origin of this behaviour lies in the repulsive nature of the electron-electron Coulomb interaction: this interaction energy is minimised for a maximally antisymmetric orbital wave function. As in translationally invariant quantum Hall systems the Landau levels are essentially flat bands, there is no cost in kinetic energy to compete with the energetic gain for ferromagnetic ordering. As a consequence, the energetically preferred state of the system will be that of complete antisymmetry of the orbital part of the wave function. Meanwhile, the total fermionic wave function describing the electronic state must equally be of antisymmetric nature; it thus follows that the part of the wave function describing the multicomponent degrees of freedom must be completely symmetric, representing a generalised ferromagnetic state.

### Symmetries and Symmetry Breaking

In the fully  $SU(N)$  symmetric case the Hamiltonian is invariant under any  $SU(N)$  rotation and its ground state, given by the  $SU(N)$  quantum Hall ferromagnet, is an irreducible representation of  $SU(N)$ . The symmetry, however, is not always fully exact. There are several different ways in which the symmetry of the system may be reduced. We distinguish between the following mechanisms of symmetry breaking:

#### Spontaneous symmetry breaking

Choosing a direction of polarisation for the ferromagnetic, polarised ground state spontaneously breaks the  $SU(N)$  symmetry of the system. This direction, although somewhat arbitrary in the first place, once fixed reduces the system's symmetry from  $SU(N)$  to  $SU(k) \times SU(N-k)$ , where  $k$  denotes the number of occupied configurations.

#### Internal explicit symmetry breaking

If the interactions are not fully  $SU(N)$  symmetric, the Hamiltonian of the system does not possess  $SU(N)$  invariance. A type of interaction not respecting the symmetry of a certain degree of freedom  $\xi$  means that this interaction couples to  $\xi$  and is able to alter the configuration of the state. In the case of the Coulomb interactions between electrons, for instance, it always respects spin symmetry. This is, however, not necessarily true for other pseudospin degrees of freedom: in graphene, Coulomb interactions can be approximately described as valley symmetric as valley-breaking processes are negligible. In other materials, these processes cannot be neglected. See appendix D for details.

### External explicit symmetry breaking

The  $SU(N)$  symmetry of the system can be explicitly broken by any effect that lifts the degeneracy of the  $N$  different configurations. For the example of the spin of the electron, the most obvious mechanism would be to account for the presence of an external magnetic field which lifts the degeneracy between the  $\uparrow$  and  $\downarrow$  configuration via the Zeeman effect.

### Theoretical Description of a Quantum Hall Ferromagnet

In the present work, we will characterise monolayer graphene, bilayer graphene, and the Bi(111) surface in the quantum Hall regime by different sets of discrete, internal spin and isospin degrees of freedom, respectively, and describe them as quantum Hall ferromagnets. We recap the degrees of freedom captured within this description of these materials, respectively, and discuss the symmetries to be considered in either case.

#### *Describing the Materials as Quantum Hall Ferromagnets*

##### Monolayer Graphene

To the electrons in monolayer graphene we assign two different discrete degrees of freedom. The spin degree of freedom, as the electrons are spin one-half fermions:  $\sigma = +\frac{\hbar}{2} \equiv \uparrow$  and  $\sigma = -\frac{\hbar}{2} \equiv \downarrow$ . The valley isospin degree of freedom, encoding the degeneracy in momentum space due to the equivalence of the low-energy description in the vicinity of either of the two inequivalent Dirac points in the first Brillouin zone of graphene:  $\tau = + \equiv K_+$  and  $\tau = - \equiv K_-$ . Both, the spin and the valley isospin, come in two possible discrete configurations, respectively. Hence they both give rise to  $SU(2)$  symmetry. We summarise the spin and isospin index for the electrons in monolayer graphene as  $\xi \in \{\uparrow +, \uparrow -, \downarrow +, \downarrow -\}$ . The total spin and isospin space of monolayer graphene,  $\mathcal{H}_{MLG} = \mathcal{H}_{spin} \otimes \mathcal{H}_{valley}$ , is therefore of  $SU(4)$  symmetry.

##### Bilayer Graphene

For the electrons in bilayer graphene we identify the following three different discrete degrees of freedom. The spin and the valley isospin  $\sigma$  and  $\tau$  similarly to the case of monolayer graphene. Additionally, the orbital isospin degree of freedom, accounting for the degeneracy between the  $n = 0$  and the  $n = 1$  Landau level in the bilayer graphene Landau level spectrum:  $\lambda = 0$  and  $\lambda = 1$ . In bilayer graphene these spins and isospins can be summarised with the index  $\xi = (\lambda, \sigma, \tau)$ .

##### Bismuth(111)

For the surface state of Bi(111) we assume full spin polarisation of the elec-

tronic state due to the spin-orbit coupling known to be of sizeable strength in bismuth [Koroteev et al., 2004; Feldman et al., 2016]. Spin-orbit interaction leads to a splitting of the spin bands and hence occupation of one spin configuration will be energetically preferred over the other. Therefore, for the electrons of the Bi(111) surface we consider the valley isospin as the only discrete degree of freedom of the electrons. In the case of the Bi(111) surface, it can take six different configurations corresponding to the six degenerate valleys of the Bi(111) Fermi surface:  $\tau \in \{1, \dots, 6\}$ .

### *Investigating a Material as a Quantum Hall Ferromagnet*

Starting point for any realistic model of the above materials, including a variety of different effects that may break the respective corresponding symmetries, is a basic, unperturbed model within the single particle picture which respects the  $SU(N)$  symmetry of the respective system. Unbroken  $SU(N)$  symmetry implies that all the different spin and isospin configurations are energetically equivalent. Beyond this idealised picture, we are interested in the situation in which this symmetry is no longer exact but where it is broken by certain physical processes. Those symmetry breaking effects, which will be specified separately in detail for each of the materials under investigation in the respective chapter, can be of very different physical nature and origin. On the level of the single particle picture, there may be external effects such as fields or strain, as well as internal effects, such as lattice asymmetries. Furthermore, when accounting for many particles and their mutual interactions, one has to resolve whether or to what extent these interactions, such as electron-electron Coulomb interactions or electron-phonon interactions do or do not respect the underlying  $SU(N)$  spin and isospin symmetry.

Each of these symmetry breaking effects when considered separately might energetically favour a different specific spin and isospin configuration. When several effects are considered jointly, this will lead to energetic competition among them. The question arises, given certain symmetry breaking mechanisms as perturbations to a specific  $SU(N)$  symmetric model, which is the spin and isospin configuration singled out by this combination of symmetry breaking effects?

We start from the  $SU(N)$  invariant configuration. To the perfectly  $SU(N)$  invariant Hamiltonian of an  $SU(N)$  quantum Hall ferromagnet at integer filling factor  $\nu = k \in \mathbb{N}^0$  with  $k \leq N$ , the eigenstates are known exactly. They are given by  $SU(N)$  quantum Hall ferromagnet states

$$\psi_{SU(N)} = \prod_m c_{\xi_1}^\dagger(m) \cdots c_{\xi_k}^\dagger(m) |0\rangle, \quad (\text{II.46})$$

where  $m$  labels the Landau orbitals,  $\xi_i$  is the index of the discrete flavour degree of freedom, *i.e.*, the quantum numbers of the spin and isospins, and  $|0\rangle$  corresponds to the vacuum state. The quantum state of equation (II.46) simply is the Slater determinant state consisting of  $k$  filled subbranches chosen arbitrarily from the  $N$  flavour states.

The theory of quantum Hall ferromagnetism is based on the idea to use wave functions of the form of equation (II.46) as Ansätze for the ground state wave function of an  $N$ -multicomponent system. As for the perfectly SU(N) symmetric system these Slater determinant states of equation (II.46) are *exact* eigenstates to the SU(N) invariant Hamiltonian, they appear as good candidates for a trial wavefunction also for a system where the SU(N) symmetry is slightly broken. This will be the guiding idea at the very heart of this work: to use Slater determinant states akin to the ones written in equation (II.46) as trial wavefunctions in a variational analysis of broken symmetry systems.

The fact that within this framework we are using single Slater determinant states to approximate the true ground state of the system makes these kinds of problems eligible to be treated within *Hartree Fock theory*.

## II.2.2 Hartree Fock Decoupling of a Two-Particle Interaction

### The Hartree Fock Method - General Procedure

We briefly present the theory of the *Hartree Fock* method which is used to treat interacting many-particle systems [Heenen and Godefroid, 2012].

Consider a two-body operator of the form

$$H_V = \frac{1}{2} \sum_{\alpha\beta\gamma\delta} V_{\alpha\beta\gamma\delta} c_{\alpha}^{\dagger} c_{\beta}^{\dagger} c_{\delta} c_{\gamma}, \quad (\text{II.47})$$

where  $\alpha, \beta, \gamma, \delta$  label the single particle states in a chosen single particle basis  $\{|\psi_{\alpha}\rangle\}$  and  $V_{\alpha\beta\gamma\delta} = \langle\psi_{\alpha}\psi_{\beta}|V|\psi_{\gamma}\psi_{\delta}\rangle$  denotes the matrix elements of some two-body operator  $\hat{V}$  in that single particle basis.

To tackle a two-body operator as the operator  $H_V$  of equation (II.47), throughout this work we employ the Hartree Fock approach for fermionic systems. The major ingredient of the Hartree Fock method for fermions consists in approximating the ground state of an interacting Hamiltonian by one single Slater determinant. This correctly takes into account the exchange statistics of the fermionic particles, while yet in most cases remaining an approximation to the true ground state wave

function.<sup>¶</sup> Subsequently, the procedure of Hartree Fock consists in minimising the energy of the Slater determinant state with respect to the single particle states it is constructed from.

To characterise the system in the complete single particle basis chosen above in equation (II.47), we introduce the notion of the single particle states  $|\psi_\alpha\rangle = c_\alpha^\dagger|0\rangle$ , where the single particle creation operator acts on the vacuum state  $|0\rangle$  of the system, and the notion of the one-body density matrix  $\rho_{\alpha\beta} = \langle\Psi|c_\alpha^\dagger c_\beta|\Psi\rangle$  in terms of the many-particle state  $|\Psi\rangle$ .

For a total number of  $N$  particles, a single Slater determinant many-particle state written in this single particle basis reads

$$|\Psi^{Sl}\rangle = \prod_{\alpha=1}^N c_\alpha^\dagger|0\rangle. \quad (\text{II.48})$$

For this particular many-particle state the density operator takes the form of a simple sum

$$\rho^{Sl} = \sum_{\alpha=1}^N |\psi_\alpha\rangle\langle\psi_\alpha|. \quad (\text{II.49})$$

Computing the energy of the Slater determinant state as written in equation (II.49) yields the Hartree Fock energy functional

$$E_{HF}[\rho^{Sl}] = \frac{1}{2} \sum_{ijkl} \rho_{ki}^{Sl} (V_{ijkl} - V_{ijlk}) \rho_{lj}^{Sl}. \quad (\text{II.50})$$

The anti-symmetrised matrix element  $(V_{ijkl} - V_{ijlk})$  arises due to the fermionic statistics of the interacting particles. The two terms  $V_{ijkl}$  and  $V_{ijlk}$  are commonly referred to as the *Hartree* term, reflecting direct interaction, and the *Fock* term, encoding exchange interaction between particles.

Finding the Hartree Fock ground state energy consists in minimising  $E_{HF}[\rho^{Sl}]$  with respect to the single particle states that enter into  $\rho^{Sl}$ .

The energy functional of equation (II.50) can equivalently be cast into matrix form

$$\mathbf{H}_{HF} = \sum_{lk} h_{lk}^{HF} c_l^\dagger c_k, \quad (\text{II.51})$$

---

<sup>¶</sup> This step corresponds to a cut-off approximation: for any basis, the ground state can be written as an infinite linear combination of Slater determinants formed from the single particle states of the basis. Approximating the ground state by just one single Slater determinant corresponds to the simplest possible truncation.

where the Hartree Fock matrix elements are given by

$$h_{lk}^{HF} = \sum_{ij} (V_{likj} - V_{lijk}) \rho_{ji}^{Sl}. \quad (\text{II.52})$$

The Hartree Fock Hamiltonian as written in equation (II.51) is a *one-body operator* that describes the energetics of an effective *one-body problem* of a single particle dressed by a mean field generated by interaction with the other particles.

Diagonalising the Hartree Fock Hamiltonian of equation (II.51) yields a set of effective single particle energies and single particle states as the eigenvalues and eigenstates of  $H_{HF}$  according to

$$H_{HF}|i\rangle = \varepsilon_i|i\rangle, \quad (\text{II.53})$$

which, by constructing the density operator  $\rho^{Sl}$  from these single particle basis, allows to write the matrix elements of equation (II.52) in this basis where they are diagonal:  $h_{ij}^{HF} = \varepsilon_i \delta_{ij}$ .

As a consequence of equations (II.51) and (II.52), both the right and the left hand side of equation (II.53) depend on the set of single particle states and the corresponding density matrix  $\rho^{Sl}$ : the Hartree Fock Hamilton operator depends itself on the density matrix which is determined in turn by its solutions. In this sense, the problem imposed by equation (II.53) must be solved by virtue of a *self-consistent* minimisation routine.

The effective single particle energies are connected to the Hartree Fock energy of equation (II.50) as

$$E_{HF} = \sum_{i=1}^N \varepsilon_i - \sum_{i,j=1}^N (V_{ijij} - V_{ijji}). \quad (\text{II.54})$$

### Hartree Fock and Quantum Hall Ferromagnetism

The connection between quantum Hall ferromagnetism and Hartree Fock theory lies in the common approach to write the many-particle state of the system by a single Slater determinant of the single-particle states. As expounded in section II.2.1, for an SU(N) quantum Hall ferromagnet this idea stems from the fact that the single Slater determinant is indeed an exact eigenstate of the perfectly SU(N) symmetric Hamiltonian. Within Hartree Fock theory, see section II.2.2, the single Slater determinant approximation allows to deal with the many-particle problem while treating correctly the statistics of the particles. Therefore, Hartree Fock theory is *exact* in the case of a quantum Hall ferromagnet, provided Landau level mixing is

neglected.

Summoning the above, the idea behind the work in this thesis is the following: we treat monolayer graphene, bilayer graphene, and Bi(111) as quantum Hall ferromagnetic systems exhibiting  $SU(N)$  symmetry in the absence of all symmetry breaking effects. In the case when there are symmetry breaking perturbations, continuing to use the single Slater determinant states as Ansätze for the ground state wave functions enables us to employ Hartree Fock theory in order to investigate the respective systems in the presence of symmetry breaking effects and interactions.



### Edge State Structure of Graphene Monolayers in the $\nu = 0$ Quantum Hall State

---

#### III.1 Edge State Structure of Monolayer Graphene - Introduction

This chapter presents results on the edge state structure in monolayer graphene. Starting from what is known about the spin and isospin properties for an infinite, translational invariant sheet of monolayer graphene, our aim is to understand how these properties might be influenced by the presence on a terminating edge in a finite sample.

This question has been motivated by the following experimental observation (see also the discussion about experimental motivation in the introduction chapter I, section I.3): for a finite piece of graphene placed in an external magnetic field, a transition can be observed from conducting to insulating behaviour as the angle of the magnetic field is changed with respect to the graphene sample. This gives rise to two questions: on the one hand, how is the state of the system affected by the change of the magnetic field? For the translationally invariant system, *i.e.*, for the bulk material, theory has suggested [Kharitonov, 2012c] to characterise different phases of the system by different possible spin and isospin configurations that may be affected by an external magnetic field: this predicts that transitions between multiple different ground state phases can be driven by varying the magnitude or the orientation of the external magnetic field. On the other hand, as conductance and charge transport are inherently related to the properties of the edge states rather than the bulk material, one has to ask furthermore: to what extend the

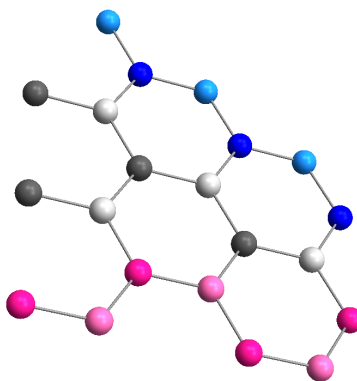


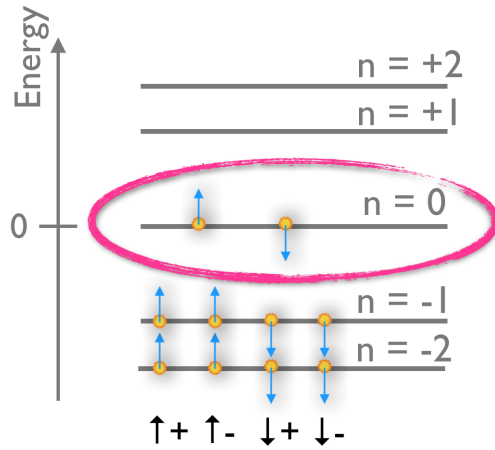
**Figure III.1**

A finite piece of monolayer graphene with different edge configurations: zigzag (blue atoms) and armchair boundaries (magenta atoms).

predictions for the bulk still remain valid in the vicinity of an edge? This question lies at the very heart of this project. In previous studies of this aspect, typically strongly simplified models for the terminating edge are employed. For instance, the influence of the edge on the ground state spin and isospin configuration is neglected or oversimplified functions are used for mimicking the edge potential. Therefore, it is to be suspected that these simple models, while in cases tractable analytically, are not providing realistic descriptions of the edge state structure of monolayer graphene.

The aim of the project presented in this chapter is to combine the following two aspects: on one side we consider the existing knowledge about the ground state spin and isospin properties of bulk monolayer graphene including electron-electron interactions and the influence of lattice vibrations, *i.e.*, electron-phonon interactions. The key feature here is the resulting dependence of the ground state phase on the external magnetic field; On the other hand we include a realistic model of the atomic edge terminating a finite monolayer graphene sample. We wish to understand how the bulk ground state structure may be altered in the vicinity of the edge.

To this end, we derive a realistic model for the effective potential induced by an edge of the monolayer graphene sample. We start from microscopic considerations of the terminating boundary of the monolayer graphene lattice on the atomic scale. We investigate how the Landau levels in a finite piece of monolayer graphene evolve when they approach an edge. The existing theory for the physics of ground state spin and isospin phases in a translational invariant system is complemented by including the influence of the effective edge potential. This way, we draw a complete picture of the ground state phases upon evolving from the bulk configuration towards a terminating edge.


**Figure III.2**

Electronic occupation of the Landau levels for the  $\nu = 0$  charge neutral state of monolayer graphene: the negative energy states  $n < 0$  are filled, the positive energy states  $n > 0$  are empty. Half filling implies two electrons per orbital in the  $n = 0$  zero energy state.

The main results of this project are the studies of several different properties of monolayer graphene, such as the ground state spin and isospin configuration, the evolution of the ground state wave function, as well as the behaviour of the excited states' energy levels and spin and isospin properties, as functions of a spatial coordinate that runs in real space from the bulk to the vicinity of the edge. Within a Hartree Fock mean field treatment we study the spin and isospin configurations of the ground state. Furthermore, we investigate the energies and properties of the Hartree Fock single particle excited states in order to understand the resulting edge state structure.

This chapter is based on the work published in reference [Knothe and Jolicœur, 2015].

### III.1.1 Theoretical Framework and Model Hamiltonian

We formulate the model for a finite piece of neutral monolayer graphene in the quantum Hall regime.

The charge-neutrality point corresponds to the particle-hole symmetric situation in which the Landau level ladder is exactly half filled with electrons: all the negative energy Landau levels with  $n < 0$  are completely filled and all the positive energy Landau levels with  $n > 0$  are empty, while the  $n = 0$  Landau level is half filled with two electrons per orbital. We show a sketch of this electronic configuration of the Landau levels in figure III.2. This state of monolayer graphene is referred to as the state with filling factor  $\nu = 0$ .

In the limit of sufficiently strong magnetic fields where the splitting between adjacent Landau levels is large, the lower-lying negative energy levels can be considered as inert and the higher lying positive levels are split far off: hence, we assume that under this condition of a strong magnetic field, mixing between Landau levels can be neglected and we focus on the properties of the partially filled  $n = 0$  Landau level.

### Description of the Electronic States

Quoting the results of the introductory chapter II, section II.1, and including the index  $\sigma = \uparrow, \downarrow$  for the spin degree of freedom, the single particle state in the  $n = 0$  Landau level reads

$$\psi_{n=0,\sigma,m} = \begin{pmatrix} \psi_{n=0,m}^{\tau=+} \\ \psi_{n=0,m}^{\tau=-} \end{pmatrix} = \begin{pmatrix} 0 \\ |0, m\rangle \\ 0 \\ -|0, m\rangle \end{pmatrix}_{H_{K_+,K_-} \otimes H_{A,B}}, \quad (\text{III.1})$$

where  $m$  denotes the intra Landau level index and the subindex  $H_{K_+,K_-} \otimes H_{A,B}$  indicates that the state  $\psi_\sigma$  lives in the Hilbert space formed as the direct product between Dirac valley space  $H_{K_+,K_-}$  and the  $A, B$  sub-lattice space  $H_{A,B}$  for which we used the basis  $\{\psi_{A,K_+}, \psi_{B,K_+}, \psi_{B,K_-}, \psi_{A,K_-}\}$ .

For later use, we note the real space representation of the electronic states quoting equation (II.28) from the introductory chapter II for the Landau level  $n = 0$ :

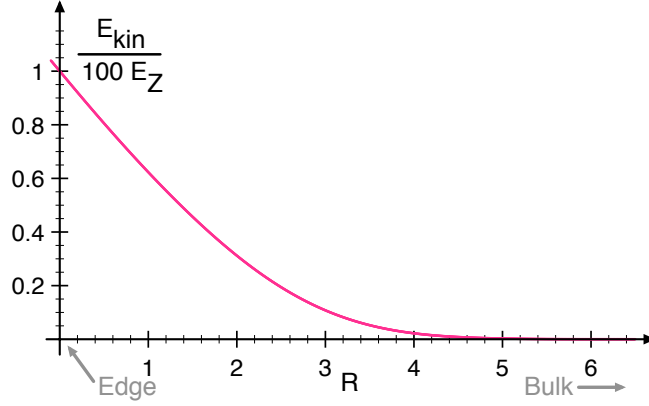
$$\phi_{0,k_y}(\mathbf{r}) = \langle \mathbf{r} | 0, m \rangle = \frac{1}{L_y} e^{ik_y y} \frac{1}{\sqrt[4]{\pi} \sqrt{\ell_B}} e^{-\frac{(x-X_{k_y})^2}{2\ell_B^2}}, \quad (\text{III.2})$$

where  $k_y$  denotes the  $y$ -component of the Landau gauge momentum with  $k_y = \frac{2\pi}{L_y} |m|$  for a system of extension  $L_y$  in  $y$ -direction and  $X_{k_y} = k_y \ell_B^2$  is the guiding centre coordinate.

We simplify the notation by collecting only the non-zero entries of the  $n = 0$  spinor in equation (III.1) as:

$$\psi_0 = \begin{pmatrix} |\uparrow +\rangle \\ |\uparrow -\rangle \\ |\downarrow +\rangle \\ |\downarrow -\rangle \end{pmatrix}_H, \quad (\text{III.3})$$

identifying the valley and the sub-lattice indices in a common valley isospin  $\tau$  as  $\tau = + \hat{=} K_+ \leftrightarrow A$  and  $\tau = - \hat{=} K_- \leftrightarrow B$ . In the four-dimensional Hilbert space


**Figure III.3**

Kinetic energy effective edge potential  $E_{kin}$  in a finite piece of monolayer graphene: the  $n = 0$  Landau level, being flat deep within the bulk, bends to non-zero energies in the vicinity of edge.

$H = H_{spin} \otimes H_{valley}$  we use the indices  $\mu, \nu$  to label the four possible configurations of spin and isospin in this space:  $\mu, \nu \in \{\uparrow +, \uparrow -, \downarrow +, \downarrow -\}$ .

Hence in monolayer graphene at neutrality we encounter an example of a quantum Hall ferromagnet with four discrete degrees of freedom given by the spin and the valley isospin. For any  $SU(4)$  symmetric interaction, the ground state is thus highly degenerate and forms an irreducible representation of  $SU(4)$ .

### Structure of the Model Hamiltonian

The model Hamiltonian we study consists of the four terms

$$H = H_{kin} + H_{Coul} + H_Z + H_{aniso}, \quad (\text{III.4})$$

where we include a kinetic energy part  $H_{kin}$  which includes the dependency of the single particle energy Landau levels on the presence of a boundary, a Coulomb interaction term  $H_{Coul}$  describing mutual Coulomb interactions between electrons, a Zeeman term  $H_Z$  as we are treating spinful electrons in a magnetic field, and an anisotropic contribution  $H_{aniso}$  which captures short range interaction effects on the lattice scale.

The last three terms are equivalent to those of a Hamiltonian describing infinite, translationally invariant monolayer graphene while the first term  $H_{kin}$  explicitly encodes the edge effects induced by a terminating boundary of the sample.

In detail, the respective terms stand for the following:

### Coulomb interaction $H_{Coul}$

The Coulomb interaction term we write as

$$H_{Coul} = \frac{1}{2} \sum_{i \neq j} \frac{e^2}{\varepsilon} \frac{1}{|\mathbf{r}_i - \mathbf{r}_j|}, \quad (\text{III.5})$$

where  $\varepsilon$  is an effective dielectric constant which depends upon the substrate [Santos and Kaxiras, 2013]. We consider the mutual Coulomb interaction between the electrons in the  $n = 0$  state. In graphene, considering Coulomb interaction between electrons as fully SU(4) symmetric is known to be an excellent approximation: while the SU(2) spin symmetry is always respected by the Coulomb interaction, any processes that might violate the SU(2) symmetry in valley space can be shown to be suppressed by several orders of magnitude due to the large separation of the two valleys  $K_+$  and  $K_-$  in momentum space (see [Nomura and MacDonald, 2006; Goerbig, 2011] and appendix D).

### Zeeman effect $H_Z$

The contribution of the Zeeman effect to the total energy can be written as

$$H_Z = -E_Z \sum_i \sigma_z^i, \quad (\text{III.6})$$

where  $\sigma_z = \sigma_z^{2 \times 2} \otimes \mathbb{1}^{2 \times 2}$  denotes the Pauli matrix  $\sigma_z^{2 \times 2}$  translated to the Hilbertspace  $\mathcal{H}_{spin} \otimes \mathcal{H}_{valley}$  which acts on the spin degree of freedom, only, and the index  $i$  is a spatial index labelling the positions of the electron orbits in real space. With  $E_Z = \mu_B B$  we denote the characteristic Zeeman energy in terms of the Bohr magneton  $\mu_B$  and the strength of the total magnetic field  $B$ .

The Zeeman effect explicitly breaks the SU(2) symmetry in spin space as it lifts the degeneracy between the up and down configuration  $\sigma = \uparrow$  and  $\sigma = \downarrow$  of the spin.

### Anisotropic symmetry breaking $H_{aniso}$

Assuming an SU(4) symmetric form of the many particle effects is only an approximation. In fact it is weakly broken by lattice-scale effects that include short-range Coulomb interactions and electron-phonon couplings. It is difficult to obtain precise estimates of these effects but their symmetry-breaking properties can be encoded in a spatially local interaction Hamiltonian:

$$H_{aniso} = \frac{1}{2} \sum_{i \neq j} [g_x \tau_x^i \tau_x^j + g_y \tau_y^i \tau_y^j + g_z \tau_z^i \tau_z^j] \delta^2(\mathbf{r}_i - \mathbf{r}_j), \quad (\text{III.7})$$

with  $\tau_\alpha = \mathbb{1}^{2 \times 2} \otimes \sigma_\alpha^{2 \times 2}$  the Pauli matrices acting only in valley space and  $V^{aniso}(\mathbf{r}_i, \mathbf{r}_j) = \delta^2(\mathbf{r}_i - \mathbf{r}_j)$  the local interaction potential in terms of the Dirac delta function in two dimensions. The parameters  $g_\alpha$  represent coupling constants for the three spatial directions.

Earlier theoretical works on symmetry breaking at the lattice scale in graphene include [Alicia and Fisher, 2007]. The Hamiltonian  $H_{aniso}$  of equation (III.7) has been proposed by Aleiner *et al.* [Aleiner *et al.*, 2007]. Its effects for an infinite piece of translationally invariant monolayer graphene have been analysed at the mean-field level by Kharitonov [Kharitonov, 2012c]. Its symmetry properties and phase diagram have been studied by exact diagonalisation [Wu *et al.*, 2014].

The exact values of the coupling constants  $g_{x,y,z}$  are not known with precision. It is likely that the ratio of the energy scales between Coulomb interaction and these anisotropies is of the order of  $10^2$ . It is thus best to explore the complete phase diagram taken these parameters as unknowns.

#### Kinetic energy effective edge potential $H_{kin}$

To describe the behaviour of a finite piece of monolayer graphene we include a space dependent kinetic energy induced by the presence of the boundary:

$$H_{kin} = - \sum_i E_{kin}(\mathbf{r}_i) \tau_x^i, \quad (\text{III.8})$$

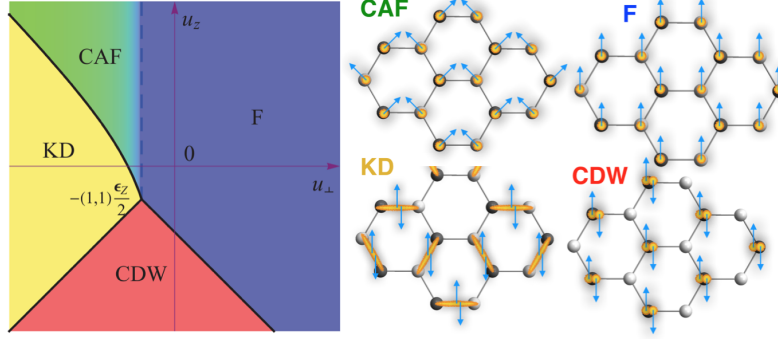
with  $i$  running over the different electron orbits in real space. The kinetic energy effective edge potential  $E_{kin}(\mathbf{r}_i)$  is induced by the boundary of the system: the hexagonal graphene lattice can be terminated in many different ways, yielding several possible edge structures. Every different atomic configuration leads to different boundary conditions for the wavefunction [Akhmerov and Beenakker, 2008]. Therefore, the spectrum of a finite piece of monolayer graphene depends on the nature of the edges. Two extreme cases are the so-called *zigzag* and *armchair* edges [Brey and Fertig, 2006a]. A finite piece of graphene terminated by a zigzag edge and an armchair edge is shown in figure III.1. The kinetic energy and the corresponding eigenstates of the electronic problem on the hexagonal lattice in the presence of hard-wall boundary conditions on the terminating lattice sites can be obtained analytically [Abanin *et al.*, 2006; Brey and Fertig, 2006a; Mei and Lee, 1983; Janssen *et al.*, 1994]. The corresponding eigenfunctions are given by the so-called *Weber functions* and yield the energy levels plotted in figure III.3 (see appendix A for more details). This approach is equivalent to turning the level index

into a space dependent quantity  $n(R)$  where  $R$  relates to the distance to the edge  $r$  as  $r = R \frac{\ell_B}{\sqrt{2}}$ . In figure III.3 we show the spatial shape of the kinetic energy  $E_{kin}$  obtained by this procedure for the  $n = 0$  Landau level as we will use it in the subsequent calculations.

We write the kinetic energy as a space-dependent potential proportional to  $\tau_x$  (a comparable treatment can be found in references [Kharitonov, 2012c; Murthy et al., 2014]). This corresponds to a perturbative treatment as it assumes an expansion of the perturbed edge states in terms of the unperturbed bulk basis states. It restricts our description to the case of "armchair-like" boundaries: we assume that one can always infer the number of branches in the single particle edge spectrum as being equal to the number of degenerate single particle levels in the bulk. This allows to apply a perturbative expansion as implied by equation (III.8). A derivation of such a Hamiltonian describing the kinetic potential of a graphene edge using arguments of perturbation theory can be found in reference [Kharitonov, 2012c]. We note, however, that edges with by a zigzag boundary, as they are terminated by a single line of atoms of the same sub-lattice type, support additional surface states [Nakada et al., 1996; Brey and Fertig, 2006a,b; Castro Neto et al., 2009]: unlike the case of armchair-like boundaries, zigzag edges support states which are localised on the edge in real space and decay into the bulk. These states therefore hence are dispersionless and exhibit flat bands. The existence of such additional surface states break the simple correspondence between the number of edge states and the number of bulk states. Therefore, they are beyond our simple treatment. The form of the kinetic energy in equation (III.8) is valid only in the regime  $E_{kin} \ll \hbar\omega_c$ , *i.e.*, spatially not too close to the edge. As can be seen from figure III.3 this condition is very well met if we restrict the subsequent discussion to the regime  $R > 3$ . Hence the restriction  $R > 3$  corresponds to a minimal distance  $r_{min} \approx 2.12\ell_B$ , which at realistic experimental values corresponds to  $r_{min} \approx 120a$ , where  $a$  denotes the lattice constant of graphene.

### State of the Art and General Idea

The idealised case of infinitely extended, translationally invariant monolayer graphene corresponds to situation in which the kinetic energy term is perfectly flat and can thus be discarded as a redundant constant; this setup has been studied by Kharitonov in reference [Kharitonov, 2012c]. As a function of the coupling constants  $g_\alpha$  Kharitonov found the phase diagram of the infinite sample as shown in figure III.4, where the anisotropy energies  $u_\alpha$  relate to the couplings as  $u_\alpha = \frac{g_\alpha}{2\pi\ell_B^2}$ .


**Figure III.4**

Left: Ground state phase diagram for infinite monolayer graphene from [Kharitonov, 2012c]; Right: Electronic configuration on the lattice.

The anisotropies  $u_{\perp}, u_z$ , and the Zeeman term  $E_Z$  select some subset of the manifold of  $SU(4)$  ferromagnetic ground states. Each phase is characterised by a different spin and isospin texture, *i.e.*, by a different configuration of the total spin  $\mathbf{S}$  and the total valley isospin  $\mathbf{T}$ .

We review the different spin and isospin phases which Kharitonov in reference [Kharitonov, 2012c] identified as the four possible ground states of bulk monolayer graphene:

★  $u_{\perp} > -\frac{E_Z}{2}, u_z > -E_Z - u_{\perp}$  : Ferromagnetic phase (F)

The ground state is given by

$$|\psi_F\rangle = \prod_p c_{\uparrow,+}^{\dagger}(p) c_{\uparrow,-}^{\dagger}(p) |0\rangle, \quad (\text{III.9})$$

where  $p$  denotes the Landau gauge momentum labelling the orbitals as  $p = \frac{2\pi}{L_y} \hbar |m|$  and the vacuum  $|0\rangle$  consists of the completely occupied set of states for all  $n < 0$  and completely empty states for all  $n > 0$ .

Both electrons occupying the same spin state but being in opposite valley isospin configurations entails the total spin to be fully polarised and the total valley isospin to vanish:

$$S_z = 1, T_x = T_z = 0. \quad (\text{III.10})$$

★  $u_{\perp} < -\frac{E_Z}{2}, u_z > \frac{E_Z^2}{2u_{\perp}} - u_{\perp}$  : Canted antiferromagnetic phase (CAF)

The ground state is given by

$$|\psi_{CAF}\rangle = \prod_p \left( \cos \frac{\theta}{2} c_{\uparrow,+}^\dagger(p) + \sin \frac{\theta}{2} c_{\uparrow,-}^\dagger(p) \right) \left( \cos \frac{\theta}{2} c_{\downarrow,+}^\dagger(p) - \sin \frac{\theta}{2} c_{\downarrow,-}^\dagger(p) \right) |0\rangle, \quad (\text{III.11})$$

where the optimal canting angle of the spin is determined by  $\cos \theta = \frac{E_Z}{2|u_\perp|}$ .

For this superposition of different weighted spin states the total spin follows to be in a canted configuration inclined by the angle  $\theta$ :

$$S_z = \cos \theta = \frac{E_Z}{2|u_\perp|}, \quad T_x = T_z = 0. \quad (\text{III.12})$$

★  $u_\perp < u_z, u_z < \frac{E_Z^2}{2u_\perp} - u_\perp$  : Kekulé phase (KD)

The ground state of this phase reads

$$|\psi_{KD}\rangle = \frac{1}{2} \prod_p \left( c_{\uparrow,+}^\dagger(p) + c_{\uparrow,-}^\dagger(p) \right) \left( c_{\downarrow,+}^\dagger(p) + c_{\downarrow,-}^\dagger(p) \right) |0\rangle. \quad (\text{III.13})$$

Hence, we find an antiferromagnet in spin space but an isospin vector which lies in the  $x$ - $y$ -plane:

$$S_z = 0, \quad T_x = 1, \quad T_z = 0 \quad (\text{III.14})$$

★  $u_\perp > u_z, u_z < -E_Z - u_\perp$  : Charge density wave phase (CDW)

The ground state of this phase is given by

$$|\psi_{CDW}\rangle = \prod_p c_{\uparrow,+}^\dagger(p) c_{\downarrow,+}^\dagger(p) |0\rangle. \quad (\text{III.15})$$

Here, the two electrons occupying two opposite spin states cause the total spin to vanish while the total valley isospin is fully polarised:

$$S_z = 0, \quad T_x = 0, \quad T_z = 1. \quad (\text{III.16})$$

Similar phases have also been discussed previously in references [Alicea and Fisher, 2006; Jung and MacDonald, 2009] We illustrate the electronic configuration on the monolayer graphene lattice on the right hand side of figure III.4.

This mean-field phase diagram is correct beyond mean-field as shown by exact diagonalisation techniques [Wu et al., 2014]. Notably none of these bulk phases

involve spin-valley entanglement.

Further earlier theoretical works on monolayer graphene edge properties include references [Kharitonov, 2012c] and [Murthy et al., 2014] where either the evolution of the bulk spin and isospin configuration upon approaching the edges has been neglected or an unrealistic model for the edge potential has been used.

Our aim is to develop further the idea of reference [Kharitonov, 2012c]: by including a realistic model of the kinetic energy effective edge potential as in equation (III.8) we retrace how the phases of figure III.4 evolve upon approaching the sample boundary. Subsequently, we analyse the possible consequences for the physical properties of the system.

### Hartree Fock Treatment

We perform a Hartree Fock study of the symmetry breaking terms of the total Hamiltonian of equation (III.4) including the edge potential. We note that in this approach we neglect all possible spatial dependence of the coupling constants, which is justified as long as we analyse a spatial domain not too close to the edge.

The neutral  $\nu = 0$  state corresponds to the half-filled case where two of the four available states per orbital are occupied. Following the general ideas about Hartree Fock treatment of quantum Hall ferromagnetic states expounded in the introductory sections II.2.1 and II.2.2, we look for the ground state within the family of Slater determinant states of the form:

$$|\psi_{GS}\rangle = \prod_p \left( \frac{1}{2} \sum_{\mu,\nu} g_{\mu\nu} c_{\mu}^{\dagger}(p) c_{\nu}^{\dagger}(p) \right) |0\rangle, \quad (\text{III.17})$$

where, as above,  $p$  denotes the Landau-gauge momentum component along the edge and  $|0\rangle$  is vacuum state with all  $n < 0$  completely occupied and  $n > 0$  completely empty. In equation (III.17)  $g$  is a 4 by 4 antisymmetric matrix, *i.e.*,  $g_{\mu\nu} = -g_{\nu\mu}$ , in order to describe a valid fermionic state, and  $\text{Tr}[gg^{\dagger}] = 2$  to ensure normalisation of the two-particle state. We minimise the energy of the Slater determinant by varying the entries of  $g$ .

To capture the effect of the edge potential we take the  $g$  matrix to be momentum dependent, *i.e.*,  $g \equiv g(p)$  in equation (III.17). Due to the duality between the longitudinal momentum  $p$  and the transverse coordinate  $r_p = \frac{p\ell_B^2}{\hbar}$  this is equivalent to a space dependent description of the problem.

In the spirit of chapter II.2, section II.2.2, we perform a Hartree Fock treatment of the interacting symmetry breaking terms of  $H_{aniso}$  of equation (III.7) using the Slater determinant Ansatz for the ground state of equation (III.17). The Hartree Fock decoupling is done with respect to the single particle basis labelled by the Landau momentum  $p$ .

For each term of the Hamiltonian  $H_{aniso}$  of equation (III.7), decoupling yields

$$\begin{aligned}
 & \langle \psi_{GS} | H_{aniso}^\alpha | \psi_{GS} \rangle \\
 &= \frac{1}{2} g_\alpha \sum_{\substack{p_1, p_2, \mu_1, \mu_2, \\ p_3, p_4, \mu_3, \mu_4}} V_{p_1, p_2, p_3, p_4}^{aniso} [\tau_\alpha]_{\mu_1 \mu_4} [\tau_\alpha]_{\mu_2 \mu_3} \langle \psi_{GS} | c_{\mu_1}^\dagger(p_1) c_{\mu_2}^\dagger(p_2) c_{\mu_3}(p_3) c_{\mu_4}^\dagger(p_4) | \psi_{GS} \rangle \\
 &\stackrel{\text{HF}}{\approx} \frac{1}{2} g_\alpha \sum_{p_1, p_2} \left[ V_{p_1, p_2, p_2, p_1}^{aniso} \underbrace{\sum_{\mu_1, \mu_4} [\tau_\alpha]_{\mu_1 \mu_4} P_{\mu_4 \mu_1}(p_1)}_{\sum_{\mu_1} [\tau_\alpha P(p_1)]_{\mu_1 \mu_1} = \text{Tr}[\tau_\alpha P(p_1)]} \underbrace{\sum_{\mu_2, \mu_3} [\tau_\alpha]_{\mu_2 \mu_3} P_{\mu_3 \mu_2}(p_2)}_{\sum_{\mu_2} [\tau_\alpha P(p_2)]_{\mu_2 \mu_2} = \text{Tr}[\tau_\alpha P(p_2)]} \right. \\
 &\quad \left. - V_{p_1, p_2, p_1, p_2}^{aniso} \underbrace{\sum_{\mu_1, \mu_2} \sum_{\mu_3} [\tau_\alpha]_{\mu_2 \mu_3} P_{\mu_3 \mu_1}(p_1)}_{[\tau_\alpha P(p_1)]_{\mu_2 \mu_1}} \underbrace{\sum_{\mu_4} [\tau_\alpha]_{\mu_1 \mu_4} P_{\mu_4 \mu_2}(p_2)}_{[\tau_\alpha P(p_2)]_{\mu_1 \mu_2}} \right] \\
 &\quad \underbrace{\hspace{10em}}_{\text{Tr}[\tau_\alpha P(p_1) \tau_\alpha P(p_2)]} \\
 &= \frac{1}{2} g_\alpha \sum_{p_1, p_2} \left[ V_{p_1, p_2, p_2, p_1}^{aniso} \text{Tr}[\tau_\alpha P(p_1)] \text{Tr}[\tau_\alpha P(p_2)] - V_{p_1, p_2, p_1, p_2}^{aniso} \text{Tr}[\tau_\alpha P(p_1) \tau_\alpha P(p_2)] \right] \quad (\text{III.18})
 \end{aligned}$$

where we introduced the notation of the density matrix

$$P_{\mu\nu} = gg^\dagger = \langle \psi_{GS} | c_\nu^\dagger c_\mu | \psi_{GS} \rangle, \quad (\text{III.19})$$

and used the property  $\langle \psi_{GS} | c_\nu^\dagger(p) c_\mu(p') | \psi_{GS} \rangle = \delta_{pp'} P_{\mu\nu}(p)$ . Furthermore, with  $V_{p_i}$  we denote the matrix elements of an interaction  $V$ :

$$V_{p_i} = \iint d\mathbf{r}_1 d\mathbf{r}_2 \phi_{0, p_1}^*(\mathbf{r}_1) \phi_{0, p_2}^*(\mathbf{r}_2) \phi_{0, p_3}(\mathbf{r}_2) \phi_{0, p_4}^*(\mathbf{r}_1) V(\mathbf{r}_1, \mathbf{r}_2), \quad (\text{III.20})$$

in terms of the explicit real-space representations of the  $n = 0$  Landau level single particle wavefunctions  $\phi_{0, p_i}$  as given in equation III.2. In the case of the anisotropic short-range interactions, due to the locality in real space of the interaction potential of equation III.7, we find equality of the direct and the exchange matrix element:

$$V_{p_1, p_2, p_2, p_1}^{aniso} = V_{p_1, p_2, p_1, p_2}^{aniso} = \frac{1}{L_y} \frac{1}{\sqrt{2\pi} \ell_B} e^{-\frac{(X_{p_1} - X_{p_2})^2}{2\ell_B^2}}. \quad (\text{III.21})$$

This is a particular property of the delta-like interaction. The sums over the orbitals can be evaluated by going to the continuum limit (allowing for a  $y$ -dependence

of the spatial integral)  $\sum_p \rightarrow \frac{N_\Phi}{L_x} \int dx \frac{1}{L_y} \int dy = \frac{1}{2\pi\ell_B^2} \int d\mathbf{r}$ . We work in a local approximation for the density matrix, assuming  $P$  to vary sufficiently slowly in space for spatial gradient terms of higher order than zero in a gradient expansion to be negligible:

$$P(\mathbf{r}_2) = P(\mathbf{r}_1) + (\mathbf{r}_2 - \mathbf{r}_1) \nabla_{\mathbf{r}_1} P(\mathbf{r}_1) + \frac{1}{2} (\mathbf{r}_2 - \mathbf{r}_1)^2 \nabla_{\mathbf{r}_1}^2 P(\mathbf{r}_1) + \dots \approx P(\mathbf{r}_1). \quad (\text{III.22})$$

Due to the locality of the anisotropic interaction in real space, the interaction matrix elements of the this interaction contribution ultimately reduce to a simple, constant coupling energy:

$$g_\alpha \frac{1}{2\pi\ell_B^2} \iint dx_2 dy_2 V^{aniso}(x_1, x_2) = \frac{g_\alpha}{2\pi\ell_B^2} =: u_\alpha. \quad (\text{III.23})$$

This allows to combine the terms in equation III.18, such the energy contribution per orbital from the symmetry breaking interaction Hamiltonian of equation (III.7) is given by (suppressing the orbital index in the following):

$$\langle \psi_{GS} | H_{aniso} | \psi_{GS} \rangle = \frac{1}{2} \sum_\alpha u_\alpha \left( \text{Tr}[\tau_\alpha P]^2 - \text{Tr}[\tau_\alpha P \tau_\alpha P] \right). \quad (\text{III.24})$$

It is convenient to rewrite the problem in terms of the following simple expectation values:

$$S_\alpha = \frac{1}{2} \langle \psi_{GS} | c^\dagger(p) \sigma_\alpha c(p) | \psi_{GS} \rangle = \frac{1}{2} \text{Tr}[\sigma_\alpha g g^\dagger] = \frac{1}{2} \text{Tr}[\sigma_\alpha P], \quad (\text{III.25a})$$

$$T_\alpha = \frac{1}{2} \langle \psi_{GS} | c^\dagger(p) \tau_\alpha c(p) | \psi_{GS} \rangle = \frac{1}{2} \text{Tr}[\tau_\alpha g g^\dagger] = \frac{1}{2} \text{Tr}[\tau_\alpha P], \quad (\text{III.25b})$$

$$R_{\alpha\beta} = \frac{1}{2} \langle \psi_{GS} | c^\dagger(p) \sigma_\alpha \tau_\beta c(p) | \psi_{GS} \rangle = \frac{1}{2} \text{Tr}[\sigma_\alpha \tau_\beta g g^\dagger] = \frac{1}{2} \text{Tr}[\sigma_\alpha \tau_\beta P]. \quad (\text{III.25c})$$

The expressions of equations (III.25a) and (III.25b) yield the components of the total spin  $S_\alpha$  and isospin  $T_\alpha$  per orbital  $p$ .

Using equation (III.25) and equation (III.24), we obtain the following expression for the Hartree Fock functional of the total energy  $E_{tot} = \langle \psi_{GS} | H | \psi_{GS} \rangle$ :

$$E_{tot} = -2E_{kin} T_x - 2E_Z S_z + \sum_\alpha u_\alpha \left( T_\alpha^2 - \sum_i R_{i\alpha}^2 - \mathbf{S}^2 \right). \quad (\text{III.26})$$

### Parametrisation of the Energy Functional and Minimisation Routine

The goal is to determine the Hartree Fock ground state by minimising the ground state energy with respect to the single particle basis, *i.e.*, with respect to the entries

of  $g$  or the density matrix  $P = gg^\dagger$ . The most general antisymmetric matrix  $g$  has 12 real parameters. By exploiting the symmetry properties of the state  $|\psi_{GS}\rangle$  and the Hamiltonian, one can reduce the number of free parameters. We use the same strategy as in reference [Ezawa et al., 2005] where an equivalent problem was studied in the context of electronic bilayer systems.

In  $E_{tot}$  as written in equation (III.26) the  $12 - 2 = 10$  free parameters of the problem (dropping the overall phase and normalisation constant) are encoded in the 6 components of the total spin  $\mathbf{S}$  and the total isospin  $\mathbf{T}$ , together with 4 out of 9 components of  $R_{\alpha\beta}$  which can be chosen independently. The invariance of  $E_{tot}$  in equation (III.26) under rotations of  $\mathbf{S}$  in spin space and rotations of  $\mathbf{T}$  around the  $z$ -axis in isospin space allows to choose  $S_y = S_x = T_y = 0$  with no loss of generality, yielding seven variables to be determined. The dimension of parameter space can be further reduced by careful consideration of all the symmetries of the problem. As demonstrated by Ezawa *et al.* [Ezawa et al., 2005] in a situation of an equivalent symmetry class, reduction is possible to a total number of three free parameters. For the present system, this leads us to a minimisation problem for the total energy  $E_{tot}$  with respect to a set of variational parameters  $-1 \leq \alpha \leq 1$ ,  $-1 \leq \beta \leq 1$ , and  $\chi \in \mathbb{R}$ , which are related to observables of equation (III.25) by:

$$S_z = \frac{1}{\sqrt{1+\chi^2}} \sqrt{1-\alpha^2}, \quad T_x = \frac{\chi}{\sqrt{1+\chi^2}} \alpha \sqrt{1-\beta^2}, \quad T_z = \frac{\chi}{\sqrt{1+\chi^2}} \alpha \beta, \quad (\text{III.27})$$

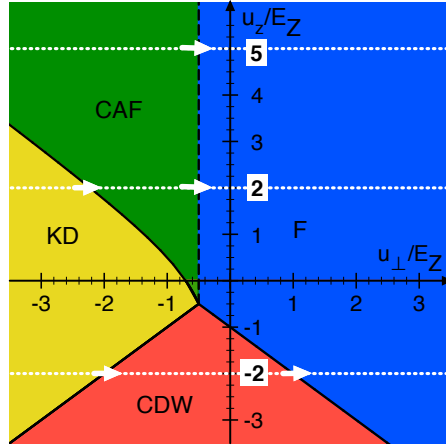
and

$$\sum_i R_{ix}^2 = \frac{T_z^2}{\chi^2}, \quad \sum_i R_{iy}^2 = \chi^2 \mathbf{S}^2, \quad \sum_i R_{iz}^2 = \frac{T_x^2}{\chi^2}, \quad (\text{III.28})$$

where the index  $i$  runs over the spatial components  $\{x, y, z\}$ . We demonstrate the details of the calculation leading to above parametrisation of the observables in appendix B. The density matrix  $P = gg^\dagger$  is connected to these quantities as (summation convention implied):

$$P = \frac{1}{2} \mathbb{1} + \frac{1}{2} \left( \sigma_i S_i + \tau_i T_i + \sigma_i \tau_j R_{ij} \right). \quad (\text{III.29})$$

For the minimisation routine, we proceed as follows: for a discretised set of values for  $R$ , parametrising the distance to the boundary, we numerically minimise the ground state energy  $E_{tot}(\alpha, \beta, \chi)$  of equation (III.26), including the space dependent edge potential of the shape shown in figure III.3 by varying the parameters  $\alpha, \beta, \chi$ . Then from the knowledge of the parameters  $\alpha(R), \beta(R), \chi(R)$ , we compute the values of the observables  $S_z(R), T_x(R), T_z(R)$  of the ground state  $|\psi_{GS}\rangle$  via equation (III.27). Furthermore, it is possible to construct the entire density matrix  $P$  characterising the ground state via equation (III.29).


**Figure III.5**

Choice of parameters for our investigation: for fixed  $E_Z$  and three values of  $u_z$  we vary  $u_\perp$  in the range  $-3E_Z \leq u_\perp \leq 3E_Z$ , corresponding to horizontal cuts through the bulk phase diagram (white dotted lines). Figure from reference [Knothe and Jolicoeur, 2015].

This procedure can be summarised in the following simple scheme:

Summary: Minimisation routine

$\forall R :$

minimise  $E_{tot}(\alpha, \beta, \chi)$  [eqn. III.26]

→ obtain parameters  $\{\alpha(R), \beta(R), \chi(R)\}$

→ construct  $\mathbf{S}, \mathbf{T}, \mathbf{R}$  [eqn. III.27],

density matrix  $\mathbf{P}$  [eqn. III.29]

→ ...

The final magenta arrow indicates that as soon as we have the density matrix for the Hartree Fock ground state at hand, we have full knowledge about that corresponding quantum state and can extract any information for use in a follow-up investigation.

## III.2 Edge State Structure of Monolayer Graphene - Results and Discussion

### III.2.1 Choice of Parameters

The full phase diagram of monolayer graphene in the plane spanned by the anisotropy energies  $u_z$  and  $u_\perp$  offers a big set of parameters that can be varied

in our theoretical model. In order to achieve a broad overview over the system's general behaviour, as well as a concise exposure of the most vital features, the results are presented in the following way: we first present the general behaviour of the respective quantity under study for a wide range of parameters. The detailed properties then are discussed for a small exemplary subset of system parameters which allows to demonstrate the characteristic main features of the system's behaviour. In order to obtain a full picture capturing the edge behaviour of all possible bulk phases shown in figure III.4, our choice of system parameters is guided by the following idea: for fixed Zeeman energy  $E_Z$ , we vary the coupling energies  $u_\perp$  and  $u_z$  because this can be realised experimentally by tilting the magnetic field: while the anisotropy energies  $u_z(B_\perp)$  and  $u_\perp(B_\perp)$  depend only on the component of the magnetic field perpendicular to the monolayer graphene sheet  $B_\perp$ , the Zeeman energy depends on the total absolute value  $B = \sqrt{B_\parallel^2 + B_\perp^2}$  via  $E_Z = \mu B$ . Therefore, tilting the magnetic field with respect to the sample while keeping its strength fixed alters  $u_z$  and  $u_\perp$  without affecting  $E_Z$ .

We choose three values of the perpendicular coupling energy  $u_z$ :  $u_z = 5E_Z$ ,  $u_z = 2E_Z$  and  $u_z = -2E_Z$ , and we vary the perpendicular coupling in the range  $-3E_Z \leq u_\perp \leq 3E_Z$ . This leads to horizontal cuts through the  $\nu = 0$  ground state phase diagram in the  $\{u_\perp - u_z\}$ -plane, marked by white, dotted lines in the phase diagram of figure III.5. A phase regime characterised by a certain set of system parameters we refer to by the corresponding bulk phase favoured at these values according to the respective point in the ground state phase diagram for the infinite graphene sheet in figure III.4. This procedure allows us to cross all the different bulk phases in a systematic fashion.

For  $u_z = 5E_Z$  and  $u_z = 2E_Z$  by varying  $u_\perp$  we meet the Kekulé, canted antiferromagnetic, and ferromagnetic phases:



For  $u_z = -2E_Z$  and varying again  $u_\perp$  we find the Kekulé, charge density wave, and ferromagnetic phases:



The corresponding bulk phase transitions are indicated by white arrows in the phase diagram in figure III.5.

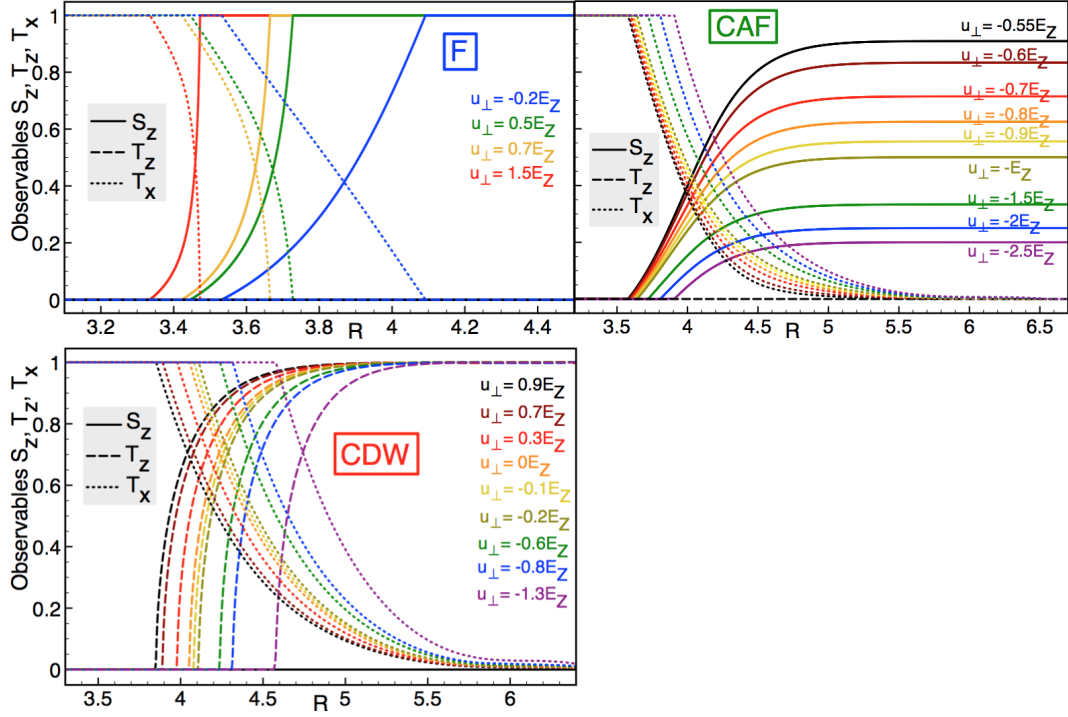


**Figure III.6**

Evolution of the spin and isospin components  $S_z$  (solid),  $T_z$  (dashed), and  $T_x$  (dotted) as functions of  $R = \sqrt{2}r/\ell_B$ , with  $r$  the distance from the edge for different system parameters. The three panels correspond to the different bulk phases **F** ( $u_z = 5E_Z$ ), **CAF** ( $u_z = 5E_Z$ ), and **CDW** ( $u_z = -2E_Z$ ), respectively.

### III.2.2 Ground State Properties

We study the evolution of the bulk phases of monolayer graphene upon approaching a spatial boundary, using the model and the Hartree Fock framework formulated in the previous section III.1.

#### Evolution of the Spin and Isospin Texture close to the Edge

We investigate the influence of the edge potential on the spin and isospin observables  $\mathbf{S}$  and  $\mathbf{T}$ . More precisely, we discuss the spatial evolution of the components  $S_z(R), T_x(R), T_z(R)$  for different choices of the anisotropy energies  $u_\perp$  and  $u_z$  compared to the Zeeman energy  $E_Z$ . As the ground state energy of equation (III.26) only depends on the  $z$ -component of  $\mathbf{S}$  and  $\mathbf{T}$  as well as the projection of  $\mathbf{T}$  onto the  $\{x-y\}$ -plane, this fully characterises the ground state spin and isospin texture

up to those parameters which leave the ground state energy invariant.

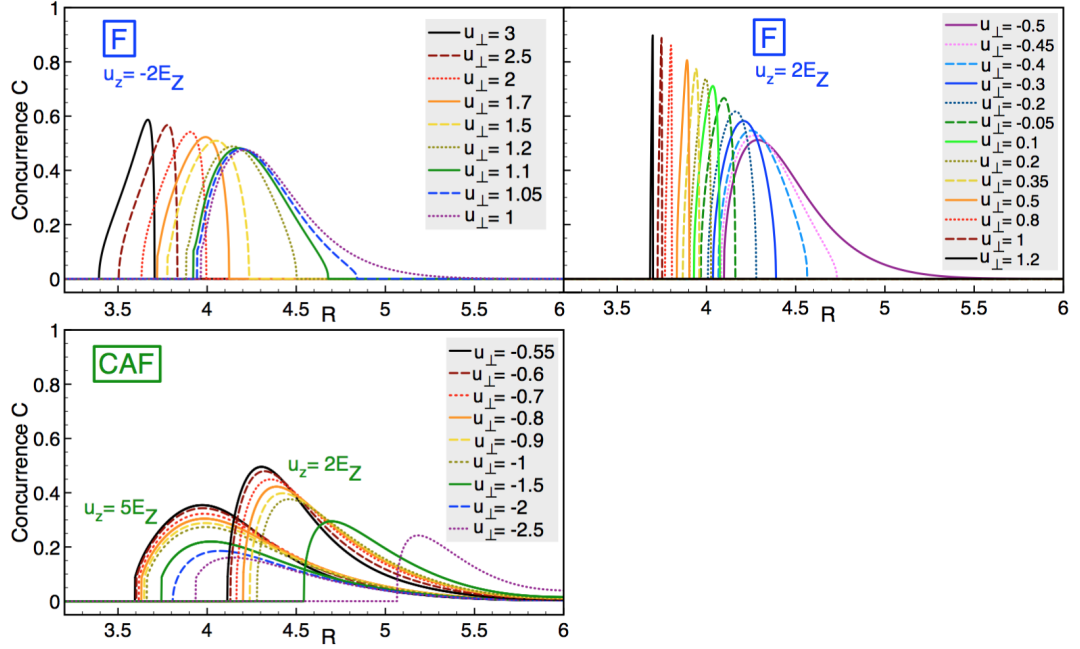
In figure III.6 we show the overall behaviour of the spin and isospin components as functions of  $R = \sqrt{2} \frac{r}{\ell_B}$ , with  $r$  the distance from the edge. System parameters are chosen such that in the upper left panel the bulk of the system is in a ferromagnetic phase, in the upper right panel the bulk establishes a canted antiferromagnetic configuration, whereas in the lower plot the bulk's ground state phase is of charge density wave order\*.

In all the three panels of figure III.6 we observe a non-trivial evolution of the spin and isospin configuration as function of space. We discuss the different regimes for the overall behaviour of the observables as a function of the distance  $r = \frac{\ell_B}{\sqrt{2}} R$  to the edge. There are three regimes to be distinguished:

- For sufficiently large values of  $R$ , *i.e.*, deep enough in the bulk, we recover the results of mean field theory for the infinite, translationally invariant monolayer graphene sheet [Kharitonov, 2012c].
- Close enough to the edge, the system is driven into a Kekulé phase with  $T_x = 1$  and  $S_z = T_z = 0$ , independently of the bulk phase it adopts. This behaviour is due to the edge potential in the kinetic energy Hamiltonian  $H_{kin}$  in equation (III.8): this term is proportional to  $\tau_x$ , hence it acts as a Zeeman effect in isospin space, polarising the isospin along the  $x$ -direction as soon as  $E_{kin}(R)$  is sufficiently large to dominate the ground state energy functional. This behaviour is consistent with previous works [Fertig and Brey, 2006; Murthy et al., 2014].
- In the cases where the bulk adopts a ferromagnetic, a canted antiferromagnetic, or in a Kekulé phase, there an intermediate regime in which we find a finite interval in space in which  $S_z \neq 1$ ,  $T_x \neq 1$  and  $T_z \neq 0$ ,  $N_x \neq 0$ , *i.e.*, the spin and the isospin are canted simultaneously with respect to their bulk values. In these cases, there is thus a domain wall at a small finite distance from the edge. For the canted antiferromagnetic configuration, this domain wall connects smoothly to the bulk configuration. For a system in a ferromagnetic phase in the bulk, however, the change in spin and isospin is abrupt and the domain wall is narrower with increasing  $u_\perp$ . Hence, for larger values of  $u_\perp$ , the ferromagnetic phase of the bulk proves to be more resistant against the increasing influence of the edge.

---

\* Curves for values of the anisotropy energies favouring a Kekulé phase in the bulk are not shown since in this case the system's spatial evolution is trivial in the sense that it does not undergo any transition whatsoever but remains in the bulk Kekulé phase all the way to the edge.


**Figure III.7**

Concurrence  $C(R)$  within the domain wall near the edge for different system parameters, favouring a **ferromagnetic** phase in the bulk (upper panels), or a **canted antiferromagnetic** bulk phase (lower plot). Curves for values of the anisotropy energies favouring a Kekulé phase or a charge density wave phase in the bulk are not shown since in these cases the concurrence remains strictly zero all the way from the bulk to the edge (*cf.* also figures III.8, III.9).

From the behaviour of the observables **S** and **T** shown in figure III.6 we draw the following conclusions: the ferromagnetic, canted antiferromagnetic, and charge density wave phase in the bulk of a finite sample of graphene do not remain unaffected close enough to the edge. Indeed the effective edge potential causes the bulk state to undergo a transition in which the polarisation of spin and isospin evolve simultaneously upon approaching the sample boundary. Sufficiently close to the edge the ground state is always driven into a Kekulé phase independently of the nature of the bulk phase.

### Spin-Valley Entanglement of the Edge States

After minimisation of the Hartree Fock ground state energy of equation (III.26) we can reconstruct the full density matrix  $P$  via equation (III.29) which gives access to the full information about the minimising Hartree Fock ground state and

its properties. A quantity of interest to investigate is the *spin-valley entanglement*, *i.e.*, the entanglement between spin and isospin degrees of freedom in the system. For the infinite bulk case, product states of the form  $|s\rangle \otimes |n\rangle$ , where  $|s\rangle$  denotes the single particle spin state and  $|n\rangle$  the single particle isospin state, have been used as an Ansatz to minimise the ground state energy [Kharitonov, 2012a,b,c]. Existing studies of edge states using a variational trial wave function approach have suggested [Murthy et al., 2014], however, that for a non-zero edge potential, spin and isospin might not remain independent, separable observables, but become *entangled*. In order to quantify the amount of entanglement in the bipartite two-level system  $H = H_{spin} \otimes H_{valley}$ , we calculate the *concurrence*  $C$  according to the definition [Mintert et al., 2005]:

$$C = \max(\lambda_1 - \lambda_2 - \lambda_3 - \lambda_4, 0), \quad (\text{III.30})$$

where the  $\lambda_i$  are the eigenvalues of the matrix

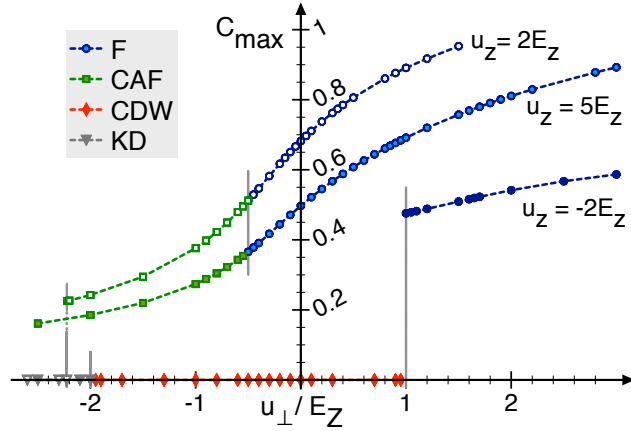
$$\mathfrak{R} = \sqrt{\rho_g}(\sigma_y \otimes \sigma_y)\rho_g^*(\sigma_y \otimes \sigma_y)\sqrt{\rho_g}, \quad (\text{III.31})$$

in decreasing order  $\lambda_i^2 \geq \lambda_{i+1}^2 \forall i$ . In equation (III.31),  $\sigma_y$  denotes the  $2 \times 2$  Pauli matrix. The quantity  $C$  ranges from 0 to 1 with  $C = 0$  meaning no entanglement and  $C = 1$  for maximally entangled states.

We plot the behaviour for the concurrence  $C$  as a function of the spatial coordinate  $R$  upon approaching the edge in figure III.7 for a variety of different system parameters. In the upper panels values are chosen such that the bulk is in a ferromagnetic configuration whereas the lower panel depicts the situation for a canted antiferromagnetic bulk phase.

The curves reveal several characteristics of the behaviour of the concurrence:

- The concurrence goes to zero deep enough in the bulk for all values of the anisotropies  $\lim_{R \rightarrow \infty} C(R) = 0 \forall u_z, u_\perp$ .
- Close enough to the edge, the concurrence is also equal to zero for all possible bulk phases, as can be seen in figure III.7 for  $C(R \approx 3) \equiv 0 \forall u_z, u_\perp$ .
- In an intermediate regime for which the system is in a ferromagnetic or canted antiferromagnetic phase in the bulk, we find that the concurrence develops a sharp peak in the vicinity of the boundary. This peak appears precisely within the domain wall separating the bulk phase from the Kekulé phase near the edge. The peak is sharper and higher with rising  $u_\perp$ , as the domain wall becomes more and more narrow in space.


**Figure III.8**

Maximum value of the concurrence  $C$  within the domain wall close to the edge,  $C_{max}$ , for different system parameters. This characterises the behaviour of spin-valley entanglement in the different phases. Figure from reference [Knothe and Jolicoeur, 2015].

- The situation is different when the bulk is in a charge density wave phase. Here, the concurrence remains zero independently of the distance from the edge:  $C(R) \equiv 0 \forall R$ .

The overall behaviour of non-zero concurrence in our model of monolayer graphene edges is summarised in figure III.8. We plot the maximum concurrence  $C_{max}$  as a function of  $u_{\perp}$ . The value of  $C_{max}$  has been extracted as the maximum peaks heights of curves akin to those shown in figure III.7.

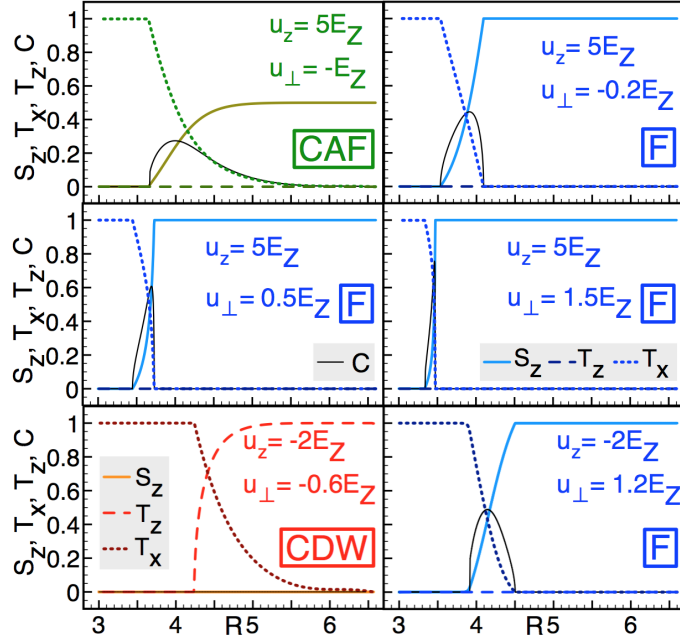
The resulting curves  $C_{max}(u_{\perp})$  characterise the behaviour of the spin-valley entanglement of the edge states:

- Non-zero values of the concurrence are found only for anisotropies favouring a canted antiferromagnetic phase (green squares) or a ferromagnetic phase (blue circles) in the bulk.
- The concurrence is strictly zero whenever the bulk is in a charge density wave (red diamonds) or Kekulé phase (grey triangles).
- In the nontrivial regimes, the maximum concurrence  $C_{max}$  is a monotonously rising function of the perpendicular coupling  $u_{\perp}$ . There is no discontinuity at the value  $u_{\perp} = -\frac{E_Z}{2}$  which would correspond to the critical coupling energy, at which the bulk phase undergoes a transition from the canted antiferromagnetic to the ferromagnetic phase. Discontinuous jumps do appear at values of  $u_{\perp}$  corresponding to the transitions from the Kekulé phase to the canted antiferromagnetic phase or to the transition from a charge density wave configuration to a ferromagnetic configuration in the bulk.

Combining the information from figures III.7 and III.8, we draw the following conclusions about the nature of the ground state of monolayer graphene close to an

**Figure III.9**

Ground state properties of a finite sample of monolayer graphene in the vicinity of a boundary: we summarise the behaviour of spin and isospin texture and spin-valley entanglement as a function of  $R$  upon approaching the edge. From reference [Knothe and Jolicœur, 2015] (edited).



edge: unlike the states in an infinite system, the ground state in the presence of a boundary may exhibit nonzero spin-valley entanglement. The concurrence is exactly zero in all configurations where either the spin or the isospin is strictly zero. Non-zero values of the concurrence appear only for configurations in which both spin and isospin are canted *simultaneously*.

### Ground State Properties - Summary

The insights we gained in this section about the ground state properties of a finite sample of monolayer graphene in the vicinity of a boundary are summarised in figure III.9: here, we plot at a glance the spatial evolution as a function of the rescaled distance to the edge,  $R = \sqrt{2} \frac{r}{\ell_B}$ , of the spin and isospin texture, characterised by the spin and isospin components  $S_z(R)$ ,  $T_x(R)$ ,  $T_z(R)$ , and the concurrence  $C(R)$ , characterising the spin-valley entanglement of the state.

We summarise our findings about the ground state phase of a finite piece of monolayer graphene as follows:

Summary: Ground State Properties

- Compared to the bulk case, the boundary of the monolayer graphene lattice gives rise to **novel ground state phases** close to the edge.
- These novel phases emerge in a **domain wall** forming between the bulk and the edge that interpolates between the respective bulk phase and a Kekulé phase at the edge for all values of the system parameters.
- The phases exhibit **simultaneous canting of spin and isospin**,  $0 < \mathbf{S} < 1$ ,  $0 < \mathbf{T} < 1$ , and **non-zero spin-valley entanglement**. They cannot be described using trial wave functions in the form of separable product states.

### III.2.3 Mean Field Spectrum and Excited States

In the previous section III.2.2 we investigated the ground state properties within a mean field Hartree Fock picture. In a subsequent step, we now consider the entire Hartree Fock level spectrum which consists of the effective single particle ground and excited states. The spectrum of the excited states is of particular interest, since the conduction properties of real graphene samples are governed by the edge modes in the quantum Hall regime. As expounded in the introduction chapter I, recent conductance experiments have shown [Young et al., 2014] that upon tilting the applied magnetic field there is a transition from an insulating regime to a conducting phase in which presumably the edge states carry a non-zero current. Tilting the magnetic field in our model corresponds to varying the parameter  $\frac{u_{\perp}}{E_Z}$  in the system. These experimental observations therefore suggest that the gap to excited states in the edge spectrum varies as a function of  $\frac{u_{\perp}}{E_Z}$  and closes, eventually, giving rise to a metal-insulator transition.

#### Mean Field Hartree Fock Hamiltonian

In order to access the full spectrum of effective Hartree Fock energy levels we proceed by diagonalising the single particle Hartree Fock Hamiltonian following the general Hartree Fock procedure of section II.2.2. We denote the one-body Hartree Fock Hamiltonian corresponding to the full Hamiltonian  $H$  of equation (III.4) by

$\mathfrak{h}^{HF}$ .

Via Hartree Fock decoupling we obtain a Hartree Fock mean field Hamiltonian which consists of four parts:

$$\mathfrak{h}_{\mu\nu}^{HF}(p) = -E_{kin}(p)[\tau_x]_{\mu\nu} - E_Z[\sigma_z]_{\mu\nu} + {}^C\Delta_{\mu\nu} + {}^a\Delta_{\mu\nu}, \quad (\text{III.32})$$

which, as in the previous discussion, encode symmetry breaking terms due to the effective edge potential  $E_{kin}(p)$ , due to the Zeeman effect  $E_Z$ , as well as the contribution from the  $SU(4)$  symmetric Coulomb interaction  ${}^C\Delta$ , and short-range symmetry breaking interactions  ${}^a\Delta$ .

For the mean field potential from the Coulomb interaction Hamiltonian of equation (III.5) we find

$${}^C\Delta_{\mu\nu} = -u_0[gg^\dagger]_{\mu\nu} = -u_0 P_{\mu\nu}, \quad (\text{III.33})$$

where  $u_0$  describes the exchange term of the Coulomb interaction Hamiltonian of equation (III.5). This formula is valid provided we neglect the spatial dependence of  $g$ . It means that we do not capture the spin texture effects of the Coulomb exchange interaction. For completeness, in the following analytical calculations and expressions the Coulomb contribution of equation (III.33) will be written explicitly.

The mean field potential due to the interactions breaking  $SU(4)$ -symmetry is given by:

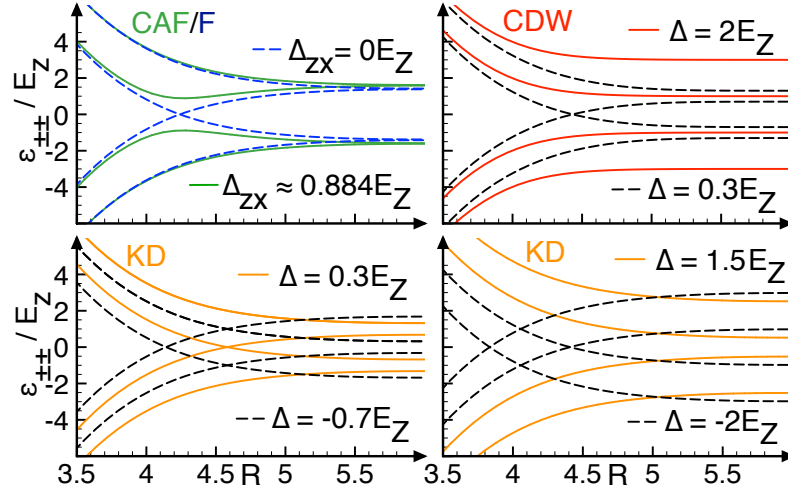
$$\begin{aligned} {}^a\Delta_{\mu\nu} &= \sum_{\alpha} u_{\alpha} \left( [\tau_{\alpha}]_{\mu\nu} \text{Tr}[gg^\dagger \tau_{\alpha}] - [\tau_{\alpha} gg^\dagger \tau_{\alpha}]_{\mu\nu} \right) \\ &= \sum_{\alpha} u_{\alpha} \left( [\tau_{\alpha}]_{\mu\nu} \text{Tr}[P \tau_{\alpha}] - [\tau_{\alpha} P \tau_{\alpha}]_{\mu\nu} \right) \end{aligned} \quad (\text{III.34})$$

For the single particle eigenenergies  $\varepsilon_i$ , which we obtain from the diagonalising the Hamiltonian as  $\mathfrak{h}^{HF}|i\rangle = \varepsilon_i|i\rangle$ , with  $|i\rangle$  the  $i$ th single particle Hartree Fock eigenstate, in the following we assume the ordering  $\varepsilon_1 \leq \varepsilon_2 \leq \varepsilon_3 \leq \varepsilon_4$ .

### Simplified Treatment: Analytical Results

#### *Mean Field Single Particle Hamiltonians and Spectra in Constant Phases*

In earlier work by Kharitonov [Kharitonov, 2012a], the Hartree Fock Hamiltonian of equation (III.32) has been studied under the assumptions for the order parameter to be constant up to the edge and for the ground state wave functions to be of simple tensor product form. However, the explicit effective valley field due to


**Figure III.10**

Single particle energy levels  $\varepsilon_{\pm\pm}$  obtained within the simplified analytical treatment of section III.2.3. Different signs and the magnitudes of the mean field potential  $\Delta$  may induce different behaviour and different numbers of crossings, even for the same phase. Very left: CAF (green, solid), F (blue, dashed). Middle left: CDW for  $|\Delta| > E_Z$  (red, solid) and  $|\Delta| < E_Z$  (black, solid). Middle right: KD for  $|\Delta| < E_Z$  with  $\Delta > 0$  (orange, solid) or  $\Delta < 0$  (black, dashed). Very right: KD for  $|\Delta| > E_Z$  with  $\Delta > 0$  (orange, solid) or  $\Delta < 0$  (black, dashed). Figure from [Knothe and Jolicœur, 2015].

the edge certainly invalidates this simple assumption. As we have seen in the previous section III.2.2, in the intermediate regime between the bulk state and the edge the Hartree Fock ground state phase does not remain constant. Nor is the ground state given by a simple tensor product state even within the Hartree Fock approximation which leads to the appearance of non-trivial spin-valley entanglement.

Nevertheless, this simplified analysis under the above assumptions is not devoid of a certain interest as it allows a fully analytical treatment of the Hartree Fock Hamiltonian of equation (III.32). In the following discussion we compare our more general, numerical results to these analytical considerations, and employ some of the analytical, approximate arguments in order to understand the behaviour. Therefore, we briefly review the results of Kharitonov: in reference [Kharitonov, 2012a] the analytical expressions for the mean field levels were presented for the ferromagnetic and canted antiferromagnetic case. A calculation of the same type allows direct extension to the Kekulé and the charge density

wave configuration.

The single particle ground states  $|\psi_{GS}\rangle$  considered in reference [Kharitonov, 2012a] are formed as Slater determinants over two-particle states of the form:

$$|\psi_{GS}\rangle = |\mathbf{s}_a\rangle \otimes |\mathbf{t}_a\rangle + |\mathbf{s}_b\rangle \otimes |\mathbf{t}_b\rangle, \quad (\text{III.35})$$

where  $\mathbf{s}_{a/b}$ ,  $\mathbf{t}_{a/b}$  describe the spin and isospin polarisation of the two electrons per orbital, labeled by  $a$  and  $b$ , respectively. For one such state taken to be fixed,  $\mathbf{h}^{HF}$  can be computed and diagonalised straightforwardly by analytical means.

In the following section we discuss what insights can be gained from this simplified, analytical treatment of the ground state structure of monolayer graphene. The results are structured as follows:

For each phase, from the single particle ground state Ansatz as given in equation (III.35) and the corresponding density matrix  $P$ , we compute the mean field potential  ${}^a\Delta$  from equation (III.34), which we then insert into the Hartree Fock Hamiltonian  $\mathbf{h}_{HF}$  of equation (III.32). We write the Hartree Fock Hamiltonian  $\mathbf{h}_{HF}$  as a decomposition into four  $2 \times 2$  matrices as:

$$\mathbf{h}^{HF}(p) = \begin{bmatrix} \gamma_1 & \gamma_2 \\ \gamma_3 & \gamma_4 \end{bmatrix}, \quad (\text{III.36})$$

where the respective entries  $\gamma_i$  involve the mean field potentials of the respective phases. We diagonalise the  $4 \times 4$  matrices analytically to obtain as their eigenvalues the four branches of the effective single particle energy spectrum. In a first step, we discuss the resulting spectra and their most important features. Subsequently, we explain and understand these features, and the differences and similarities among the phases, by relating to the symmetries of the underlying Hartree Fock Hamiltonian of the respective phase. Special attention we pay to either the gaps between the single particle energy levels or to the nature and number of crossings between the levels.

### Canted antiferromagnetic/ Ferromagnetic

$$|\psi_{GS}\rangle = |\mathbf{s}_a\rangle \otimes |+\mathbf{t}_z\rangle + |\mathbf{s}_b\rangle \otimes |-\mathbf{t}_z\rangle,$$

with  $\mathbf{t}_z = (0, 0, 1)$  and  $\mathbf{s}_{a/b} = (\pm \sin \theta_s, 0, \cos \theta_s)$ , where  $\theta_s$  describes the canting angle between the two spins:  $\mathbf{s}_a \cdot \mathbf{s}_b = \cos 2\theta_s$ .

For this ground state configuration, the mean field Hartree Fock Hamiltonian exhibits the following features:

- Mean field potential of the symmetry breaking terms, dropping the constant term  $-\frac{1}{2}(u_0 + 2u_\perp + u_z)\mathbb{1} \otimes \mathbb{1}$ :

$${}^a\Delta^{CAF/F} = {}^a\Delta_{0z}^{CAF/F}\mathbb{1} \otimes \sigma_z + {}^a\Delta_{zx}^{CAF/F}\sigma_z \otimes \sigma_x, \quad (\text{III.37})$$

with:

$${}^a\Delta_{0z}^{CAF/F} = -\frac{1}{2}(u_0 + u_z + 2u_\perp) \cos \theta_s, \quad (\text{III.38a})$$

$${}^a\Delta_{zx}^{CAF/F} = -\frac{1}{2}(u_0 + u_z - 2u_\perp) \sin \theta_s. \quad (\text{III.38b})$$

- Full mean field Hamiltonian:

$$\begin{aligned} \gamma_1 &= {}^a\Delta_{zx}\sigma_x - (E_Z - {}^a\Delta_{0z})\sigma_z, \\ \gamma_2 &= \gamma_3 = -E_{kin}(p)\mathbb{1}, \\ \gamma_4 &= -{}^a\Delta_{zx}\sigma_x - (E_Z - {}^a\Delta_{0z})\sigma_z, \end{aligned} \quad (\text{III.39})$$

- Eigenvalues<sup>†</sup>:

$$\varepsilon_{\pm\pm}^{CAF/F} = \pm\sqrt{[E_{kin}(p) \pm (E_Z - {}^a\Delta_{0z}^{CAF/F})]^2 + ({}^a\Delta_{zx}^{CAF/F})^2}. \quad (\text{III.40})$$

From the analytic expressions for the branches given in equation (III.40) we can compute the minimal gaps as  $\Delta_\varepsilon^{CAF/F} = 2\varepsilon_{+-}^{CAF/F}$  for  $\frac{\partial\varepsilon_{+-}^{CAF/F}}{\partial p}|_{p_0} = 0$  at the edge or  $E_{kin} \equiv 0$  in the bulk.

- Minimum gaps in the bulk and at the edge:

$$\Delta\varepsilon_{edge}^{CAF/F} = 2|{}^a\Delta_{zx}^{CAF/F}|, \quad (\text{III.41a})$$

$$\Delta\varepsilon_{bulk}^{CAF} = u_0 + u_z - 2u_\perp, \quad (\text{III.41b})$$

$$\Delta\varepsilon_{bulk}^F = 2|E_Z - {}^a\Delta_{0z}^{CAF/F}|. \quad (\text{III.41c})$$

<sup>†</sup> We note for this equations as well as for all the following: the notation of equation III.40 understands that there are two indices for the energy eigenvalues  $\varepsilon$  for which the two different signs, + or -, can be chosen, respectively, what makes a total of four different possible combinations yielding the four different eigenenergies.

**Charge Density Wave / Kekulé Phase**

$$|\psi_{GS}\rangle = |+\mathbf{s}\rangle \otimes |\mathbf{t}\rangle + |-\mathbf{s}\rangle \otimes |\mathbf{t}\rangle,$$

with  $\mathbf{t} = \mathbf{t}_z = (0, 0, 1)$  in the charge density wave phase and  $\mathbf{t} = \mathbf{t}_\perp = (1, 0, 0)$  in the Kekulé phase.

- Mean field potential of the symmetry breaking terms (again, dropping the same constant term as in the CAF/F case):

$$\begin{aligned} & {}^a\Delta^{CDW/KD} \\ &= {}^a\Delta_{x0}^{CDW/KD} \sigma_x \otimes \mathbb{1} + {}^a\Delta_{y0}^{CDW/KD} \sigma_y \otimes \mathbb{1} + {}^a\Delta_{z0}^{CDW/KD} \sigma_z \otimes \mathbb{1}, \end{aligned} \quad (\text{III.42})$$

with:

$${}^a\Delta_{x0}^{KD/CDW} = -\frac{1}{2}(u_0 t_x - u_z t_x - 4u_\perp t_x), \quad (\text{III.43a})$$

$${}^a\Delta_{y0}^{KD/CDW} = -\frac{1}{2}(u_0 t_y - u_z t_y - 4u_\perp t_y), \quad (\text{III.43b})$$

$${}^a\Delta_{z0}^{KD/CDW} = -\frac{1}{2}(u_0 t_z - 3u_z t_z - 2u_\perp t_z). \quad (\text{III.43c})$$

When inserting  $\mathbf{t}_z$  or  $\mathbf{t}_\perp$  for the charge density wave or the Kekulé phase in equation (III.43), we find for both phases, respectively, only one of above terms of to be non-zero for each phase:

$${}^a\Delta_{z0}^{CDW} = -\frac{1}{2}(u_0 - 3u_z - 2u_\perp), \quad (\text{III.44a})$$

$${}^a\Delta_{x0}^{KD} = -\frac{1}{2}(u_0 - u_z - 4u_\perp). \quad (\text{III.44b})$$

- In these cases we compute the respective entries of the full mean field Hamiltonian for the charge density wave as

$$\begin{aligned} \gamma_1 &= -E_Z \sigma_z + {}^A\Delta_{z0} \mathbb{1}, \\ \gamma_2 &= \gamma_3 = -E_{kin}(p) \mathbb{1}, \\ \gamma_4 &= -E_Z \sigma_z - {}^a\Delta_{z0} \mathbb{1}, \end{aligned} \quad (\text{III.45})$$

while for the Kekulé phase we find:

$$\begin{aligned} \gamma_1 &= \gamma_4 = E_Z \sigma_z, \\ \gamma_2 &= \gamma_3 = \left( {}^a\Delta_{x0}^{KD} - E_{kin}(p) \right) \mathbb{1}. \end{aligned} \quad (\text{III.46})$$

- Eigenvalues:

$$\varepsilon_{\pm\pm}^{CDW} = \pm E_Z \pm \sqrt{E_{kin}(p)^2 + ({}^a\Delta_{z0}^{CDW})^2}, \quad (\text{III.47a})$$

$$\varepsilon_{\pm\pm}^{KD} = \pm E_Z \pm [E_{kin}(p) - {}^a\Delta_{x0}^{KD}]. \quad (\text{III.47b})$$

- Minimum bulk gap for  $E_{kin} \equiv 0$ :

$$\Delta\varepsilon_{bulk}^{CDW/KD} = 2|E_Z - |{}^a\Delta_{z0/x0}^{CDW/KD}||. \quad (\text{III.48})$$

We show examples for the Hartree Fock single particle spectra  $\varepsilon_{\pm\pm}(R)$  in the different phases obtained within this simplified, analytical treatment in figure III.10. Depending on the choice of sign and magnitude of the mean field potential  $\Delta$  for the respective phase we obtain curves with different functional dependence on the spatial coordinate  $R$ . We discuss their behaviour with special attention to the number of crossings we observe in the different cases, respectively, as this will be a point of major importance in the subsequent line of argumentation.

- In the case of a ferromagnetic phase, the inner pair of single particle energy levels crosses at exactly one point while the outer pair disperses; this leads to one gapless edge state. For a canted antiferromagnetic configuration, however, the inner pair of levels, after bending slightly towards each other, disperses just as the outer pair. Therefore, the Hartree Fock single particle spectrum of the canted antiferromagnetic phase always remains gapped (upper left panel of figure III.10). This observation led to the conclusion that monolayer graphene in a ferromagnetic phase should be conducting, while exhibiting insulating behaviour when it is in a canted antiferromagnetic configuration [Kharitonov, 2012a; Young et al., 2014].
- The situation is more complex for a charge density wave or a Kekulé phase (upper right and lower panels of figure III.10): here, the question whether the levels cross each other when approaching the edge or whether they remain gapped depends crucially on the choice of  ${}^a\Delta_{z0/x0}^{CDW/KD}$ : in the charge density wave phase,  $\varepsilon_{+-}$  and  $\varepsilon_{-+}$  cross if  $|{}^a\Delta_{z0}^{CDW}| < E_Z$ , but they disperse for  $|{}^a\Delta_{z0}^{CDW}| > E_Z$ . In the case of a Kekulé phase, the single particle levels exhibit multiple crossings whenever  ${}^a\Delta_{x0}^{KD} > 0$ . The scenario of one single crossing of  $\varepsilon_{+-}$  and  $\varepsilon_{-+}$  is established if  ${}^a\Delta_{x0}^{KD} < 0$  with  $|{}^a\Delta_{x0}^{KD}| < E_Z$ . The case of gapless dispersing energy levels then corresponds to the case  ${}^a\Delta_{x0}^{KD} <$

$$0, |{}^a\Delta_{x0}^{KD}| > E_Z.$$

It has to be noted, however, that the conditions on the coupling energies  $u_\perp$  and  $u_z$  imposed by the relations detailed in section III.1.1 which define the different phases prevent any crossings of the single particle levels both in the charge density wave and in the Kekulé regime: the conditions  $u_z < u_\perp$  in the case  $u_z, u_\perp < 0$  or  $u_z < -E_Z - u_\perp$  for  $u_z < 0, u_\perp > 0$ , necessary for the bulk ground state to be a charge density wave phase, force  $|{}^a\Delta_{z0}^{CDW}| > E_Z$ ; Equivalently, the relations to be fulfilled in order to find a Kekulé phase in the bulk, *i.e.*,  $u_\perp > u_z$  and  $u_z < \frac{E_Z^2}{2u_\perp}$ , entail  ${}^A\Delta_{x0}^{KD}$  to be positive and, even stronger,  ${}^a\Delta_{x0}^{KD} > E_Z$ . Hence, within a framework where the phase of the bulk is assumed to be constant up to the boundary, no gapless edge states can be observed for the charge density wave or Kekulé phase. Nevertheless, the remaining cases of  ${}^a\Delta_{z0}^{CDW}$  and  ${}^a\Delta_{x0}^{KD}$  (all to be seen in figure III.10), which *a priori* are forbidden by the properties of the phases themselves, will be of importance in the following, as they make level crossings and gapless edge modes in these phases possible *in principle*. We will come back to this point in section III.2.3, where we discuss the properties of the level crossings in the respective phases in our numerical data in detail.

### Single Particle Level Crossings in a Constant Phase - Analytical Treatment

The number of crossings is governed by the symmetries of the Hartree Fock Hamiltonian and the magnitude of the Hartree Fock self-consistent potentials. This can be seen from the decomposition of the Hartree Fock Hamiltonians presented above and the corresponding gaps they yield. We discuss the relation between the behaviour of gaps and crossings within one, constant phase to the properties of the underlying corresponding Hartree Fock Hamiltonian.

#### Canted antiferromagnetic / Ferromagnetic transition

The size of the gap in the canted antiferromagnetic or ferromagnetic phase, equation (III.41), is governed by the first off-diagonal coupling matrix elements  ${}^a\Delta_{zx}^{CAF/F}$ . If  ${}^a\Delta_{zx}^{CAF/F} \neq 0$ , as is the case for any non-zero canting angle  $\theta \neq 0$ , the eigenvalues of the Hamiltonian  $h_{CAF/F}^{HF}$  exhibit the characteristic behaviour of avoided crossings. The single particle levels are allowed to cross only for  ${}^a\Delta_{zx}^{CAF/F} = 0$  at  $\theta = 0$ , *i.e.*, in the ferromagnetic phase. In the bulk, *i.e.*, at  $E_{kin} \equiv 0$ , all values of the coupling energies  $u_z$  and  $u_\perp$  allowed for the ferromagnetic phase yield the same ordering of the single particle energy levels  $\varepsilon_{\pm\pm}^{F,0} = \varepsilon_{\pm\pm}^{F,0}(E_{kin} \equiv 0)$ , independently of the sign or the

modulus of  $\Delta_{0z}^{CAF/F}$ :  $\varepsilon_{+-}^{F,0} = \varepsilon_{-+}^{F,0} < 0 < \varepsilon_{--}^{F,0} = \varepsilon_{++}^{F,0}$ . Hence, there is only one possible scenario of level crossings when approaching the boundary as the increasing edge potential is driving the single particle levels away from their bulk values. This leads to exactly one crossing of the levels  $\varepsilon_{+-}^F$  and  $\varepsilon_{--}^F$ , shown by the blue, dashed lines in the upper left panel of figure III.10.

### Charge density wave or Kekulé phase

We see from equation (III.45) and equation (III.46) that the Hamiltonians for the charge density wave phase and the Kekulé phase turn out to have higher symmetry than in the canted antiferromagnetic phase: in  $h_{CDW}^{HF}$  and  $h_{KD}^{HF}$ , all entries of the two first off-diagonals as well as of the anti-diagonal are zero. Pairwise degeneracy of the corresponding eigenvalues, *i.e.*, crossings between the single particle energy levels are now allowed. We note that, unlike the transition from a canted antiferromagnetic to a ferromagnetic phase, all other transitions do not correspond to smooth transitions. In these cases a phase transitions go along with an abrupt change of the symmetry properties of the spin and isospin configuration of the ground state and the corresponding Hamiltonian.

There are different possible scenarios of single particle level crossings in the charge density wave and Kekulé phases:

The single particle energy levels of the charge density wave phase,  $\varepsilon_{\pm\pm}^{CDW}$  in section III.2.3, are independent of the sign of  ${}^a\Delta_{z0}^{CDW}$ . Different orderings of the bulk levels  $\varepsilon_{\pm\pm}^{CDW,0}$  at  $E_{kin} \equiv 0$  may, however, appear depending on the modulus of  ${}^a\Delta_{z0}^{CDW}$ : for  $|{}^a\Delta_{z0}^{CDW}| > E_Z$ , the bulk states are ordered as  $\varepsilon_{--}^{CDW,0} < \varepsilon_{+-}^{CDW,0} < \varepsilon_{-+}^{CDW,0} < \varepsilon_{++}^{CDW,0}$ . In this case, when approaching the boundary, the kinetic energy potential drives the positive and the negative energy states further apart from each other such that they do not cross. In the case where  $|{}^a\Delta_{z0}^{CDW}| < E_Z$ , however, the bulk states rather follow the hierarchy  $\varepsilon_{--}^{CDW,0} < \varepsilon_{-+}^{CDW,0} < 0 < \varepsilon_{+-}^{CDW,0} < \varepsilon_{++}^{CDW,0}$ . In this case, turning on the effective edge potential drives the levels  $\varepsilon_{-+}^{CDW,0}$  and  $\varepsilon_{+-}^{CDW,0}$  towards each other and they cross at zero energy. These two different scenarios are depicted in the upper right panel of figure III.10, where the red, solid lines show the levels  $\varepsilon_{\pm\pm}^{CDW}$  in section III.2.3 at  ${}^a\Delta_{z0}^{CDW} = 2E_Z > E_Z$  and the black, dashed lines show the spectrum for  ${}^a\Delta_{z0}^{CDW} = 0.3E_Z < E_Z$ . The latter case,  $|{}^a\Delta_{z0}^{CDW}| < E_Z$ , however, is prohibited by the conditions imposed on the couplings  $u_z$  and  $u_\perp$  in order for the system to establish a charge density wave phase in the bulk. Requiring  $u_z < u_\perp$  and  $u_z < -E_Z - u_\perp$  will always force  $|{}^a\Delta_{z0}^{CDW}| > E_Z$ . Therefore, treating the system as having a stable

charge density wave phase in the bulk and all the way to the edge will never lead to any crossings of the single particle edge levels.

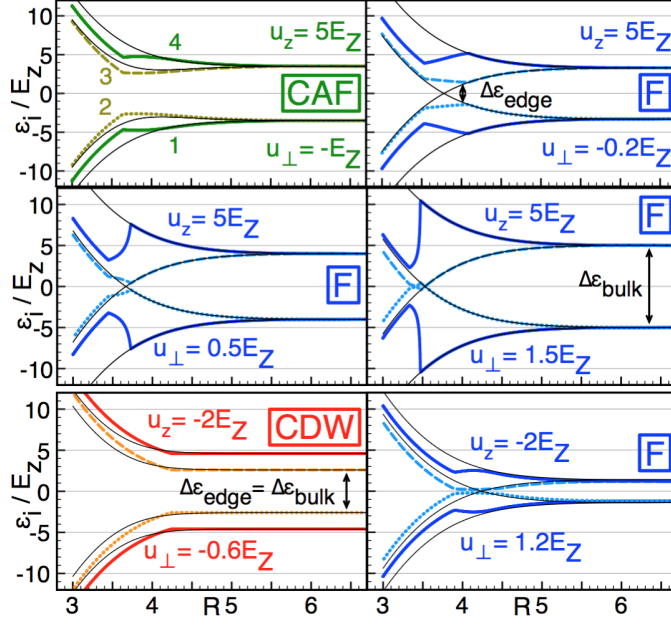
For the more important case of the Kekulé phase, the situation becomes even richer. Here, depending on the sign and the modulus of  ${}^a\Delta_{x0}^{KD}$ , four different single particle level orderings in the bulk and four resulting crossing scenarios may appear. For  $|{}^a\Delta_{x0}^{KD}| < E_Z$ , if  ${}^a\Delta_{x0}^{KD} > 0$ , there is one level crossing at zero energy and two additional crossings above and below the zero energy line, respectively, whereas for negative  ${}^a\Delta_{x0}^{KD}$ , only one crossing at zero energy is present. The case  $|{}^a\Delta_{x0}^{KD}| > E_Z$  can lead to four crossings, two at zero energy plus one above and one below, respectively, if  ${}^a\Delta_{x0}^{KD} > 0$ , whereas for  ${}^a\Delta_{x0}^{KD} < 0$ , the four levels do not cross.

We summarise for the constant Kekulé phase:

$$\begin{aligned}
 & {}^a\Delta_{x0}^{KD} > 0, |{}^a\Delta_{x0}^{KD}| < E_Z : \\
 & \text{for } E_{kin} \equiv 0 : \varepsilon_{-+}^{KD,0} < \varepsilon_{--}^{KD,0} < 0 < \varepsilon_{++}^{KD,0} < \varepsilon_{+-}^{KD,0} \\
 & \text{for } E_{kin} \neq 0 : 3 \text{ crossings...} \\
 & \dots \text{between } \varepsilon_{+-}^{KD} \text{ and } \varepsilon_{++}^{KD} \text{ at energy } > 0 \\
 & \dots \text{between } \varepsilon_{+-}^{KD} \text{ and } \varepsilon_{-+}^{KD} \text{ at energy } = 0 \\
 & \dots \text{between } \varepsilon_{--}^{KD} \text{ and } \varepsilon_{-+}^{KD} \text{ at energy } < 0
 \end{aligned} \tag{III.49}$$

$$\begin{aligned}
 & {}^a\Delta_{x0}^{KD} > 0, |{}^a\Delta_{x0}^{KD}| > E_Z : \\
 & \text{for } E_{kin} \equiv 0 : \varepsilon_{-+}^{KD,0} < \varepsilon_{++}^{KD,0} < 0 < \varepsilon_{--}^{KD,0} < \varepsilon_{+-}^{KD,0} \\
 & \text{for } E_{kin} \neq 0 : 4 \text{ crossings...} \\
 & \dots \text{between } \varepsilon_{+-}^{KD} \text{ and } \varepsilon_{++}^{KD} \text{ at energy } > 0 \\
 & \dots \text{between } \varepsilon_{--}^{KD} \text{ and } \varepsilon_{++}^{KD} \text{ at energy } = 0 \\
 & \dots \text{between } \varepsilon_{+-}^{KD} \text{ and } \varepsilon_{-+}^{KD} \text{ at energy } = 0 \\
 & \dots \text{between } \varepsilon_{--}^{KD} \text{ and } \varepsilon_{-+}^{KD} \text{ at energy } < 0
 \end{aligned} \tag{III.50}$$

$$\begin{aligned}
 & {}^a\Delta_{x0}^{KD} < 0, |{}^a\Delta_{x0}^{KD}| < E_Z : \\
 & \text{for } E_{kin} \equiv 0 : \varepsilon_{--}^{KD,0} < \varepsilon_{-+}^{KD,0} < 0 < \varepsilon_{+-}^{KD,0} < \varepsilon_{++}^{KD,0} \\
 & \text{for } E_{kin} \neq 0 : 1 \text{ crossings...} \\
 & \dots \text{between } \varepsilon_{+-}^{KD} \text{ and } \varepsilon_{-+}^{KD} \text{ at energy } = 0
 \end{aligned}$$


**Figure III.11**

Spatial behaviour of the single particle Hartree Fock spectra for different bulk phases. Thick, colourful lines show our numerical results. Different line shapes distinguish between different single particle energy levels  $\varepsilon_1 \leq \varepsilon_2 \leq \varepsilon_3 \leq \varepsilon_4$ . Thin, black lines compare to the analytical formulas for  $\varepsilon_{\pm\pm}(R)$ , in which no modulation of the underlying spin/isospin texture is taken into account. From [Knothe and Jolicoeur, 2015].

$$\begin{aligned}
 & {}^a \Delta_{x0}^{KD} < 0, \quad |{}^a \Delta_{x0}^{KD}| > E_Z : \\
 & \text{for } E_{kin} \equiv 0 : \quad \varepsilon_{--}^{KD,0} < \varepsilon_{+-}^{KD,0} < 0 < \varepsilon_{-+}^{KD,0} < \varepsilon_{++}^{KD,0} \\
 & \text{for } E_{kin} \neq 0 : \quad \text{no crossings, dispersing levels.} \quad (III.51)
 \end{aligned}$$

In above relations  $\varepsilon_{\pm\pm}^{KD}$  denote the energy levels obtained from equation (III.47b) and  $\varepsilon_{\pm\pm}^{KD,0}$  the corresponding bulk levels at  $E_{kin} \equiv 0$ .

### Space Dependent Hartree Fock Spectra: Numerical Approach

As we saw in the foregoing section III.2.2, the Ansatz we introduced in section III.1.1 is able to describe spatial dependence of the spin and isospin order and also to capture spin-valley entanglement.

The numerical routine we use to study the Hartree Fock mean field spectra extends the minimisation routine introduced in section III.1.1: for every point in space  $R$ , by minimising the total energy  $E_{tot}$  of equation (III.26), we obtain a set of parameters  $\{\alpha(R), \beta(R), \chi(R)\}$  characterising the matrix  $g$  that makes the ground state  $|\psi_{GS}\rangle$ . From these space dependent parameters

we construct the corresponding density matrix  $P = gg^\dagger$  via equation (III.29), which in turn allows to reconstruct and diagonalise  $h^{HF}$  of equation (III.32). This analysis is repeated for every  $R$ , thereby yielding the spatial behaviour of  $h^{HF}$  and its eigenvalues and eigenvectors as a function of the distance from the edge.

We choose the system parameters for our analysis to be the same as introduced in section III.2.1.

In figure III.11 we illustrate the behaviour of the single particle Hartree Fock energy spectra for different bulk phases. Here, thick, colourful lines represent the results of our numerical investigation while the thin, black lines compare to the simplified, analytical spectra  $\varepsilon_{\pm\pm}(R)$  of the previous section.

We first discuss the behaviour of the numerical data:

- In the cases of canted antiferromagnetic or ferromagnetic ordering in the bulk, the single particle spectra show the following behaviour: two flat energy levels, separated by the gap  $\Delta\varepsilon_{bulk}$ , are present in the bulk, both two-fold degenerate and they split into four branches when approaching the edge. The two intermediate levels, being labeled  $\varepsilon_2$  and  $\varepsilon_3$ , first bend towards each other, establishing the minimum energy gap  $\Delta\varepsilon_{edge} < \Delta\varepsilon_{bulk}$ , before, even closer to the edge, the two lowest and the two highest levels  $\varepsilon_1, \varepsilon_2$  and  $\varepsilon_3, \varepsilon_4$  are driven apart in two parallel pairs, respectively.
- For the charge density wave bulk phase the behaviour is qualitatively different: there are four non-degenerate levels in the bulk. In contrast to the levels of the canted antiferromagnetic or ferromagnetic case, they do not bend towards each other and there is no minimum energy induced by the edge behaviour. Hence, we find that the minimum edge gap is equal to the bulk gap:  $\Delta\varepsilon_{edge} = \Delta\varepsilon_{bulk}$ . Sufficiently close to the edge, the levels again form two parallel pairs.
- The spectra for the Kekulé phase in the bulk are not shown because, as mentioned in section III.2.2, this state does not undergo any significant evolution when approaching the edge. The spectra do not differ from the analytical prediction for  $\varepsilon_{\pm\pm}$  shown for  ${}^a\Delta_{x0}^{KD}$  in figure III.10.

Next we compare the results of our our numerical study to the predictions from the simplified, analytical treatment:

- Deep in the bulk we find that all curves coincide as they should. Furthermore, from the discussion in section III.2.2, we know that there is no spin-valley entanglement in the bulk, *i.e.*, the bulk states indeed are of separable product form compatible with the Ansätze assumed for the ground state wave function in the analytical calculations.
- Significant deviations between the numerical results capturing the full ground state properties and the analytical curves from the simplified treatment are observed when moving closer to the edge, where the ground state spin and isospin configuration starts to deviate from the bulk phase (see figure III.6). The single particle energies  $\varepsilon_i$  have kinks whenever the underlying spin and isospin texture changes and exhibit qualitatively different behaviour in the different texture regimes. Thus, the emergence of different spin and isospin configurations due to the edge potential when approaching the edges directly translates into the single particle spectra leading to a complex energy structure as a function of space.
- Furthermore, in reference [Kharitonov, 2012a] it is claimed that for a system being in a canted antiferromagnetic phase, the edge spectra always exhibit a gap, which closes when approaching a ferromagnetic phase, such that a system in the ferromagnetic phase always supports gapless edge states. Due to the fact, however, that the system does not remain in its bulk phase when approaching the edge, we see from figure III.11 that configurations can be found in which the bulk indeed is in a ferromagnetic phase, but the edge states still exhibit a finite gap  $\Delta\varepsilon_{edge} \neq 0$ . In figure III.11, this is the case for the anisotropy energies  $u_{\perp} = -0.2 E_Z$  and  $u_{\perp} = 0.5 E_Z$  at  $u_z = 5 E_Z$  (blue lines in the upper right and middle left panel, respectively). As the value of  $u_{\perp}$  rises, the gap  $\Delta\varepsilon_{edge}$  becomes smaller, until it finally does close, as to be seen in the middle right panel of figure III.11 for  $u_{\perp} = 1.5 E_Z$ .

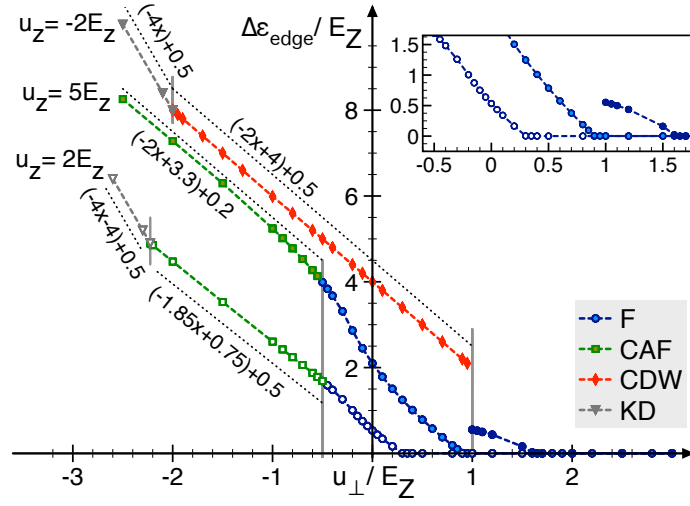
### Single Particle Level Crossings in Different Texture Regimes - Numerical Results

#### *Behaviour of the Gap in Different Texture Regimes:*

As we have seen in the previous section III.2.3, the single particle Hartree Fock spectra show a complex structure as a function of space resulting from the spatial changes of the spin and isospin texture when approaching the monolayer graphene edge. In particular, in some configurations, the single particle spectra exhibit a finite gap, whereas for other system parameters the

**Figure III.12**

Edge gap  $\Delta\varepsilon_{edge}$  in the single particle spectra when the bulk is in different phases. Dotted, black lines trace linear behaviour of the data (shifted by a constant offset). Grey vertical lines indicate the critical values for bulk phase transitions. Figure from [Knothe and Jolicoeur, 2015].



single particle levels cross, yielding gapless edge states.

We aim to understand how the gap of the edge states depends on the system parameters in the full, space dependent treatment, in order to predict for which phases gapped or gapless edge states are to be expected. To this end we discuss the properties of the edge gap and its behaviour when approaching the critical values where it closes.

The spatial variation of the order parameters has a direct impact on the overall shape of the dispersion of edge modes as to be seen from figure III.11, where we plot the dispersions from our numerical calculation including edge effects and the direct comparison with analytical results using only bulk values without spatial variation. In order to investigate the closure of the edge gap  $\Delta\varepsilon_{edge}$  as a function of the ratio  $\frac{u_{\perp}}{E_Z}$ , we evaluate the size of the minimum gap in the single particle spectra for various system parameters. The resulting curves  $\Delta\varepsilon_{edge}(\frac{u_{\perp}}{E_Z})$  are shown in figure III.12. For all values of  $u_z$  and for all bulk phases we find that the size of the edge gap  $\Delta\varepsilon_{edge}$  is a strictly monotonous decreasing function of  $\frac{u_{\perp}}{E_Z}$ .

In particular, depending on the bulk phase configuration, the curves for  $\Delta\varepsilon_{edge}(u_{\perp}/E_Z)$  exhibit the following behaviour:

- When the bulk is in a Kekulé or charge density wave phase, the flat bulk single particle levels split further apart when approaching the edge so that the minimum gap in the spectrum is equal to the bulk gap

$\Delta\varepsilon_{edge} = \Delta\varepsilon_{bulk}$ . In these two cases we find that the bulk gap is a linear function of the perpendicular coupling energy:  $\Delta\varepsilon_{bulk}^{KD/CDW} \propto \frac{u_{\perp}}{E_Z}$ . The numerical results in figure III.12 follow exactly the analytical prediction given in section III.2.3: at  $u_z = -2E_Z$ , we find  $\Delta\varepsilon_{bulk}^{KD} = -4u_{\perp}$  and  $\Delta\varepsilon_{bulk}^{CDW} = -2u_{\perp} + 4E_Z$ , whereas the Kekulé edge gap at  $u_z = 2E_Z$  behaves as  $\Delta\varepsilon_{bulk}^{KD} = -4u_{\perp} - 4E_Z$ . These analytical curves are plotted in figure III.12 as dotted lines for comparison (they are shifted by a constant offset with respect to the numerical results for better visibility).

As a consequence of this linear behaviour as a function of  $u_{\perp}$ , for couplings favouring Kekulé or charge density wave order in the bulk, at the system parameters chosen in figure III.12, there is always a non-zero gap in the single particle spectrum.

- When the ground state in the bulk is in a canted antiferromagnetic or in a ferromagnetic phase, the single particle spectra bend towards each other when approaching the edge and therefore exhibit a minimum energy gap  $\Delta\varepsilon_{edge}$  near the edge, which is smaller than the bulk gap.
  - ★ For  $u_{\perp} \leq -\frac{E_Z}{2}$  where the bulk is in a canted antiferromagnetic phase (green squares in figure III.12), the spectrum always exhibits a non-zero edge gap which is almost linear as a function of the perpendicular coupling.
  - ★ At values  $u_{\perp} \geq -\frac{E_Z}{2}$ , hence for a ferromagnetic bulk phase (blue circles in figure III.12), the shape of the spectrum changes qualitatively and the bulk gap closes in a non-linear way, asymptotically approaching zero at sufficiently large values of  $u_{\perp}$ .

For the transverse couplings chosen in figure III.12,  $u_z = 5E_Z$ ,  $u_z = 2E_Z$ , and  $u_z = -2E_Z$ , the edge gap  $\Delta\varepsilon_{edge}$  closes at  $u_{\perp} \approx E_Z$ ,  $u_{\perp} \approx 0.3E_Z$ , and  $u_{\perp} \approx 1.6E_Z$ , respectively.

Hence, at all these values, the bulk phase order is ferromagnetic, but the gap closure point clearly differs from the value  $u_{\perp} = -\frac{E_Z}{2}$ , which has been predicted as the critical value for closing the gap [Kharitonov, 2012a], as it corresponds to the transition between canted antiferromagnetic and ferromagnetic order in the bulk (see the bulk phase diagram in figure III.4).

The reason for this discrepancy with earlier predictions for the behaviour of the edge gap lies in the changes of the spin and isospin configuration of the ground state induced by the effective edge poten-

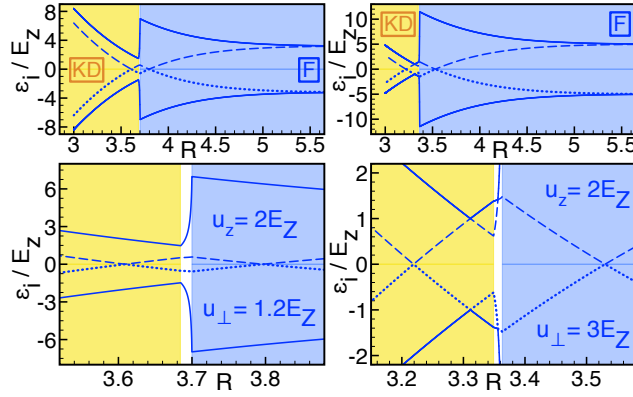
tial as we approach the boundary. Indeed, even for values of the couplings favouring ferromagnetic order in the bulk, the system does not remain in a ferromagnetic phase configuration all the way from the bulk to the edge. During its transition into a Kekulé phase close to the boundary, there is an intermediate regime with non-trivial ground state configurations, involving non-zero spin-valley entanglement and simultaneous canting of both spin and isospin. Hence, in this transition regime there is no reason for  $\Delta_{edge}^{CAF/F}$  as predicted by the analytical treatment of section III.2.3 to yield a correct description of the edge gap. Nevertheless, if we assume continuous changes of the systems properties, some intuition at least about the behaviour of the onset of the transition regime can be gained from extrapolating the analytical predictions: The gap derived from the properties of the bulk ground state,  $\Delta\varepsilon_{edge}^{CAF/F}$ , as given in section III.2.3, does indeed yield non-zero values for all canting angles  $\theta_s \neq 0$ , *i.e.*, as soon as the spin starts tilting away from the perfect alignment of the ferromagnetic phase, hence describing a situation without level crossing.

For the gap between the two degenerate single electron levels in the bulk,  $\Delta\varepsilon_{bulk}^{CAF/F}$ , we recover the analytical results of section III.2.3 for all values of the system parameters.

From this analysis of the gaps of the single particle spectra we can draw the following conclusion:

Compared to a treatment in which any spatial variation of the underlying spin and isospin texture when approaching the boundary of the graphene lattice is neglected [Kharitonov, 2012a], the modification of the single particle spectra induced by this modulation in space of the underlying phase is found to influence the way the single particle edge gap closes: instead of going along with the sharp transition from canted antiferromagnetic to ferromagnetic phase in the bulk at  $u_{\perp} = -\frac{E_Z}{2}$ , the gap closing is "smeared out", becoming a smooth and gradual process, where the convergence asymptotically extends into the parameter range of the ferromagnetic phase.

When the bulk is charge density wave, Kekulé, or canted antiferromagnetic phase, the single particle energy levels always have non-zero gaps. *However, for a bulk ferromagnetic phase, both gapped and gapless spectra are possible, depending on the values of the coupling energies.* Hence, taking into account the spatial variation of the trial Hartree Fock state leads to qualitatively different results than obtained from a treatment in which all spatial dependence


**Figure III.13**

Close-up on spectra with multiple crossings. Blue lines show the single particle energy levels  $\varepsilon_i$ . Different backgrounds mark regions with different ground state textures: F (blue), transition region (white), KD (yellow). The crossings occur in regions of different phases. Figure from [Knothe and Jolicœur, 2015].

of the spin and isospin order is ignored.

#### *Number of Level Crossings in the Different Texture Regimes*

As we can see from the single particle Hartree Fock spectra in figure III.11 as well as figure III.13, the single particle energy levels we obtain from our numerical, space dependent analysis can exhibit different numbers of crossings points. There may be either gapped states, *i.e.*, zero crossings, or gapless edge modes with either one or two crossings. We wish to understand the nature of the crossings as well the reasons and predictions for their multitude. The number of crossing points and the resulting number of gapless edge channels is vital in order to make connection to experimental conduction measurements.

Previously, we discussed within the simplified analytical description in which the change of the order parameter as a function of space is neglected. We saw that the occurrence of level crossings depends on the symmetry of the corresponding Hartree Fock Hamiltonian of this particular spin and isospin configuration.

This simple picture drawn for constant order parameters changes when considering the electronic ground state structure described in section III.2.2. Here, we discuss the occurrence of multiple crossings and the relation with the underlying spin and valley texture in the fully space dependent scenario.

Indeed the ground state spin and isospin texture deviates from the bulk phase when moving towards the edge as a consequence of the growing edge potential. The following observation is of major importance for this discussion: sufficiently close to the edge the system is always driven into a Kekulé phase. Hence when moving sufficiently close to the edge the ground state will be of Kekulé order even though the system parameters  $u_z$  and  $u_\perp$  do not allow a Kekulé phase in the bulk.

Two examples are shown in the close-ups in figure III.13. Parameters in both panels are chosen such that the bulk system at  $E_{kin} \equiv 0$  is in a ferromagnetic phase. When moving towards the edge the energy levels evolve according to  $\varepsilon_{\pm\pm}^F$  of section III.2.3. In figure III.13, this corresponds to the evolution within the blue region. A first crossing between the intermediate levels occurs as predicted by the analysis of the ferromagnetic phase energy levels. After the transition region (left white in figure III.13), the ground state is of Kekulé order, marked by the yellow shading in figure III.13. However, the system parameters do not force  ${}^a\Delta_{x0}^{KD} > E_Z$  as it would be the case for a bulk Kekulé phase: in the left panel of figure III.13, we find  ${}^a\Delta_{x0}^{KD} = -3.4E_Z$  and in the right panel we have  ${}^a\Delta_{x0}^{KD} = -7E_Z$ . Therefore the energy levels now evolve according to  $\varepsilon_{\pm\pm}^{KD}$  as given in section III.2.3, but for the case  ${}^a\Delta_{x0}^{KD} < 0$ ,  $|{}^a\Delta_{x0}^{KD}| < E_Z$ . Most importantly, this case is only allowed for values of  $u_z$  and  $u_\perp$  favouring a bulk ferromagnetic phase, not for a bulk Kekulé phase. As a consequence, in this regime of Kekulé type evolution of the edge energy levels under bulk ferromagnetic conditions, one more level crossing may occur. Hence, the appearance of several crossings of the single particle energy levels in the numerical spectra as in figure III.11 and figure III.13 can be explained combining the insight of section III.2.2 that any bulk phase by the edge potential always is driven into a Kekulé phase close to the boundary, with the understanding of the possible behaviour of  $\varepsilon_{\pm\pm}^{KD}$  depending on the value of  ${}^a\Delta_{x0}^{KD}$  as a function of the coupling energies  $u_z$  and  $u_\perp$  for all possible values of the couplings and not only those actually favouring Kekulé order in the bulk.

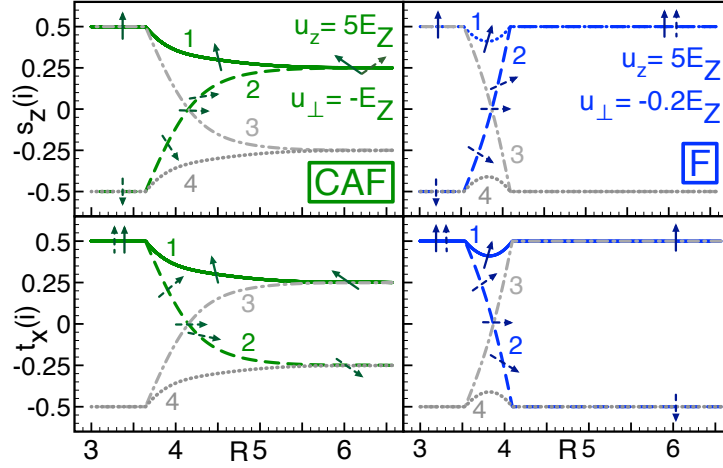
The single particle energy levels describing the numerical results of figure III.11 and figure III.13 can be summarised in the following scheme:

$$\varepsilon_{\pm\pm}(R) = \begin{cases} \varepsilon_{\pm\pm}^{bulk}(R) & \text{for } R > R_2, \\ \text{unknown} & \text{for } R_1 < R < R_2, \\ \varepsilon_{\pm\pm}^{KD}(R) & \text{for } R < R_1, \end{cases} \quad (\text{III.52})$$

where  $\varepsilon_{\pm\pm}^{bulk}(R)$  denotes the level spectra for the bulk phase established at a given choice of system parameters and  $R_2$  and  $R_1$  label the inner and outer limits in space of the domain wall, for which there is no simple analytic expression. The evolution of  $\varepsilon_{\pm\pm}^{KD}(R)$  is no longer limited to the non-crossing behaviour imposed for a bulk Kekulé phase, but it can exhibit any of the shapes drawn in the corresponding panels of figure III.10. Which of these curves describes the Kekulé-like evolution of the edge states correctly is determined by the system parameters  $u_{\perp}$  and  $u_z$  that govern the *bulk* texture phase.

From the analysis of the number of single particle level crossings we hence learn that, in principle, by choosing appropriate values of  $u_z$  and  $u_{\perp}$ , single particle energy levels can have zero, one, two, or even three crossings at zero energy. Among these crossings, only one is due to the symmetry properties of the bulk ferromagnetic phase. The remaining crossings appear in the Kekulé phase close to the boundary, which in this regime shows novel properties not present for a spatially invariant Kekulé phase in the bulk.

Furthermore, these crossings occur at different distances from the edge - at the distance where the corresponding Kekulé phase single particle levels for a certain  ${}^a\Delta_{x0}^{KD}$  cross, it is necessary for the system already to have evolved from the bulk phase into the Kekulé edge phase in order for the additional single particle level crossings to occur. This is the reason why we do not see any crossings in the single particle spectrum shown in the panel of figure III.11 where the bulk is in a charge density wave phase: at the distance  $R_{cross}$ , where the Kekulé-like levels near the edge would cross, the system still behaves according to its bulk charge density wave configuration. In this case, the crossing is thus prevented by the fact that the crossing point lies outside the Kekulé region:  $R_{cross} > R_2$ . Nevertheless, a situation in which the bulk is a charge density wave but the single particle edge states are gapless due to crossings of the Kekulé-like levels close to the boundary is not forbidden by the underlying symmetry principles. This can be seen from the fact that the restrictions for the coupling energies of the charge density wave bulk phase allow negative values of  ${}^a\Delta_{x0}^{KD}$ . The exact distances from the edge  $R_1$ ,  $R_2$ , or  $R_{cross}$ , which define the points of crossing, involve the explicit form of the kinetic energy  $E_{kin}(R)$  as they are determined by the eventual dominance of the kinetic energy. Numerical values for  $R_1$ ,  $R_2$ , or  $R_{cross}$  therefore strongly depend on the model potential chosen for  $E_{kin}(R)$ . This is not true, however, for the answer to the question whether crossings are allowed or not, since the values of  ${}^a\Delta$  are determined generically by the system parameters  $u_{\perp}$  and  $u_z$ .


**Figure III.14**

Evolution of the single electron spin and isospin components  $s_z(i)$  and  $t_x(i)$  of the single particle eigenstates  $|i\rangle$  from the bulk to the edge for a canted antiferromagnetic bulk phase (green) and a ferromagnetic bulk phase (blue). Different line shapes distinguish between the four single particle energy levels  $\varepsilon_1 \leq \varepsilon_2 \leq \varepsilon_3 \leq \varepsilon_4$ . Green/blue lines: the two lowest-lying states which are occupied in the Hartree Fock ground state. Gray lines: higher-lying single particle states. Arrows show the behaviour of the spin and isospin polarisation. The second and third levels  $|2\rangle$  and  $|3\rangle$  are oppositely polarised in spin and isospin at the edge. Figure from [Knothe and Jolicœur, 2015].

#### *Nature of the Single Particle States in the Different Texture Regimes*

As we saw in the previous section, a finite piece of monolayer graphene exhibits a complex edge state structure of the single particle level spectra depending on the underlying ground state spin and isospin configuration. There may be gapless edge states with single or multiple crossings or configurations which exhibit finite gaps to single particle excitations. We wish to understand the nature of the corresponding single particle excited states. To this end, we analyse the properties of the effective single electron Hartree Fock states. More precisely, we compute the single particle spin and isospin components  $s_z(i) = \frac{1}{2}\langle i|\sigma_z|i\rangle$  and  $t_x(i) = \frac{1}{2}\langle i|\tau_x|i\rangle$  as a function of space from the bulk towards the edge. The results for a canted antiferromagnetic bulk phase and a ferromagnetic bulk phase are shown in figure III.14.

The evolution of the single particle observables  $s_z(i)$  and  $t_x(i)$  can be summarised by the following scheme:

$s_z(i)$	edge	intermediate	bulk	$t_x(i)$	edge	intermediate	bulk
$s_z(1) :$	↑	↗	↑	$t_x(1) :$	↑	↗	↑
$s_z(2) :$	↓	↘ → ↗	↑	$t_x(2) :$	↑	↗ → ↘	↓
$s_z(3) :$	↑	↗ → ↘	↓	$t_x(3) :$	↓	↘ → ↗	↑
$s_z(4) :$	↓	↙	↓	$t_x(4) :$	↓	↙	↓

(III.53)

where arrows schematically represent the spin and isospin vectors.

The Hartree Fock ground state  $|\psi_{GS}\rangle$  is built from Slater determinants of the two states corresponding to the two energetically lowest lying branches  $\varepsilon_1$  and  $\varepsilon_2$ , *i.e.*, of  $|1\rangle$  and  $|2\rangle$  in figure III.11. The lowest energy single particle excitations hence correspond to exciting one electron from the second to the third level:  $\varepsilon_2 \rightarrow \varepsilon_3$ . As we see from figure III.14, these two states  $\varepsilon_2$  and  $\varepsilon_3$  have oppositely polarised spin and isospin components. The closing of the gap  $\Delta\varepsilon_{edge}$  between the second and the third single particle level which we observed in figure III.11 hence is a transition from insulating to conducting behaviour in which a pair of counter propagating edge states exhibiting opposite spin and isospin polarisation will carry the current. We thus find a pair of gapless helical edge states which is the signature of a *quantum Hall spin* state [Hasan and Kane, 2010]. In these states, spinful particles form edge currents, which may not only carry charge, but also as spin degree of freedom.

### Mean Field Spectrum and Excited States - Summary

In this section we studied the influence of a boundary of a finite piece of monolayer graphene on the mean field Hartree Fock effective single particle energy spectra. Our findings about the resulting edge state structure we summarise as follows:

## Summary: Spectrum and Excited States

- The variation of the ground state spin and isospin structure close to the edge found in section III.2.2 directly translates into the single particle spectra: the energy levels show different behaviour in different texture regimes giving rise to a **complex overall pattern**.
- The single particle edge states can exhibit either zero, single, or multiple crossings of the levels. When taking the spatial variation of the order parameter into account, there is **no one-to-one correspondence between whether the edge states are gapped or gapless and the bulk ground state phase**. Rather, the crossings must be understood from the symmetries of the respective Hartree Fock Hamiltonian corresponding underlying phase *as a function of space*. This contradicts previous predictions from analytical studies using the assumption of constant spin and isospin, which directly relate the conductance properties of the edge channels to the ground state phase of the bulk.
- When analysing the single particle properties of the effective Hartree Fock single particle ground and excited states, we find that the lowest single particle excitations correspond to flipping both, the spin and the isospin degree of freedom. Gapless, conducting edge channels hence form the **helical edge states of quantum Hall spin states**.

### III.2.4 Edge State Structure of Monolayer Graphene - Conclusions and Remarks

Within this chapter we analysed the edge state structure of monolayer graphene in the quantum Hall regime. Within a numerical Hartree Fock treatment we took into account the influence of a terminating boundary in a simple model as a field in the valley isospin space. This approach is able to trace the spatial evolution of the system from the bulk to the edge in order to analyse the spin and valley isospin properties of the system as a function of the distance to the edge.

## Summary: Edge State Structure of Monolayer Graphene

- In a first part, section III.2.2, we studied the **ground state properties**. We saw that the ground state spin and isospin configuration deviates from its bulk phase in the vicinity of an edge. It rotates smoothly from its bulk configuration to a Kekulé phase near the boundary. Within the transition region that interpolates between the bulk phase and the Kekulé edge phase we found evidence for novel ground states, exhibiting simultaneous canting of the spin and the valley isospin, and non-trivial spin-valley entanglement. This represents a novel type of phase which is not present in the bulk.
- Subsequently, in section III.2.3, the properties of the **Hartree Fock effective single particle energy spectrum** was analysed. We saw that the evolution of the underlying spin and isospin phase when approaching the edge directly translates into the behaviour of the energy spectrum, leading to a complex spatial behaviour of the levels. In particular, the levels may be either gapped or cross single or multiple times. The origin of the crossings were traced back to the symmetries of the underlying spin and isospin phases as that the picture we obtain in a space dependent treatment is more complex than that obtained by assuming the order not to change up to the edge. Most importantly, the direct correspondence between the conductance properties of the edge states and the bulk phase is lost. The analysis of the single particle eigenstates shows that the lowest single particle excitation describes counter propagating helical edge states carrying opposite spin and isospin polarisations.

We comment on the possible implications of above findings for experiments: In our model, we found the transport properties to be governed by either zero, one, or multiple single particle level crossings. We saw that the number of levels crossing the Fermi energy can be varied by changing the parameter  $\frac{u_{\perp}}{E_Z}$ . This implies that there are metal-insulator transitions when tilting the magnetic field. This is consistent with the experimental findings in monolayer graphene we presented in the introductory chapter I of Young *et al.* [Young *et al.*, 2014]. If we adopt the estimates for the approximate magnetic field dependencies of  $E_Z$  and  $u_{\perp}$  stated in reference [Kharitonov, 2012c] and reference [Kharitonov, 2012a] as  $E_Z(B) \approx 0.7B$  [T]K and  $u_{\perp}(B_{\perp}) \approx 1 - 10B_{\perp}$  [T]K, where  $B$  denotes the total magnetic field and  $B_{\perp}$  its component perpendicular to the device plane, the values for the parameters stated in reference [Young *et al.*, 2014] suggest that the authors were able to exper-

imentally tune the ratio  $\frac{u_{\perp}}{E_Z}$  roughly in a range from -13 to -0.5. The findings of our numerical, space dependent study taking into account the spatial evolution of the order parameter upon approaching the edge suggest that the occurrence of the metal-insulator transition, while it sets constraints on the microscopic parameters, does not imply that the bulk is canted antiferromagnetic ordered. The observation of a conductance  $G \approx 2\frac{e^2}{h}$ , which corresponds to two conducting channels, *i.e.*, to one single level crossing, has *two* possible explanations: *either the bulk is in a ferromagnetic phase leading to one crossing unaffected by the Kekulé edge regime. Or the bulk has non-crossing single particle levels, but the crossing occurs in the Kekulé regime close to the edge.* Furthermore, the fact that in our model multiple level crossings may occur gives a hint that the observation of exactly one crossing only corresponds to a limited parameter range. Varying the anisotropies parameters may lead to the observation of conductance values of higher multiples of two, corresponding to several crossings in the single particle edge spectrum.

Due to the breakdown of the one-to-one correspondence between the appearance of gapped or gapless edge states and the bulk phase in our numerical results, our findings suggest that the mere conductance properties of the edge channels in monolayer graphene may not be a sufficient and unambiguous criterion to make statements about the bulk spin and isospin configuration in a certain setup. Other tools must be found which allow to learn about the ground state configuration and to distinguish in a clear and unequivocal manner between the different phases. Possible recent suggestions include spin-superfluidity, which is suspected to appear for the canted antiferromagnetic phase due to the invariance of the spin under rotations around the  $z$ -axis in spin-space [Takei et al., 2016] or the collective spin and isospin modes in the different phases [de Nova and Zapata, 2017].

Of course there are obvious limitations of our theoretical approach: most importantly, we apply a perturbative treatment of the edge, whose validity is limited to a certain range. We discuss this point after equation (III.8). Besides, the appearance of a Kekulé phase in the vicinity of the edge is a direct consequence of treating the effective edge potential perturbatively. Furthermore, in our calculations we assume the anisotropy energies  $u_{\perp}$  and  $u_z$  to remain constant at their bulk values as explained after equation (III.7). This approximation certainly becomes less justified as we approach the boundary. Also we have neglected the exchange energy effects that will create textures in the charge carrying states.

### Phase Diagram of a Graphene Bilayer in the Zero-Energy Landau Level

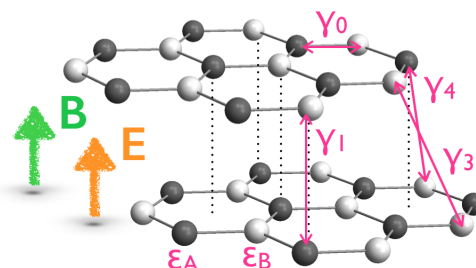
---

#### IV.1 Bilayer Graphene in the Zero-Energy Landau Level - Introduction

This chapter reports on a study of the ground state structure of bilayer graphene in the quantum Hall regime in the presence of external electric and magnetic fields. This project has been motivated by experimental results: as described in the introduction, chapter I, section I.3, there is experimental evidence for the occurrence of multiple different phase transitions for different numbers of electrons in the zero energy Landau level of bilayer graphene upon variation of the strength of the applied fields. Despite theoretical treatments of the problem in several different models and frameworks, a satisfactory explanation of the phenomena observed in experiment has not yet been provided. One possible reason lies in the complexity of the problem: in reference [Lambert and Côté, 2013], Lambert and Côté have carried out a study of the spin and isospin ground state phases of bilayer graphene using a single particle model Hamiltonian of bilayer graphene which takes into account a great variety of lattice details. However, the authors work with the effective two-band model of bilayer graphene. Furthermore, when considering the effect of electron-electron Coulomb interactions, they take into account exclusively the interactions among the electrons occupying the zero-energy mode. On the other hand, Shizuya showed in his seminal work [Shizuya, 2012] that the electronic interactions of the zero-energy electrons with the lower-lying electrons of the filled Dirac sea leads to noticeable effects when treated in the frame of the full four-band model already on the level of Hartree

**Figure IV.1**

Bilayer graphene lattice under external electric and magnetic fields,  $\mathbf{E}$  and  $\mathbf{B}$ , applied perpendicularly to the sample. Magenta symbols indicate the relevant tight-binding parameters in our model.

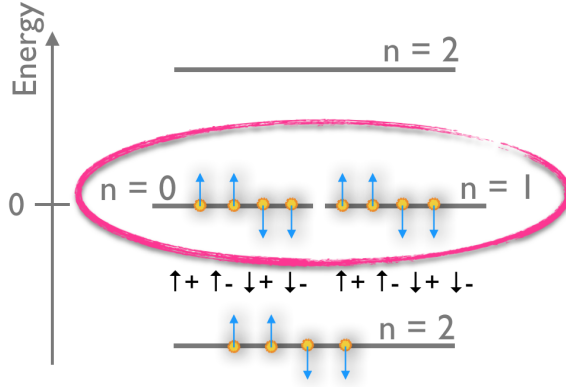


Fock mean field calculations. Most importantly, the Coulomb interaction with the Dirac sea lifts the degeneracy between the  $n = 0$  and  $n = 1$  Landau level mode and hence introduces a splitting between the states of the zero-energy octet.

Our aim in this project is to make an attempt to partially make up for this shortcoming by providing a more realistic, yet more detailed model of bilayer graphene in the quantum Hall regime which unifies several of the effects and features included in previous models. The setup we are studying is shown in figure IV.1. We consider the full band structure of bilayer graphene to be quantised by a strong magnetic field in the quantum Hall regime. The resulting wave functions are used to compute the electron-electron Coulomb interactions on the mean field level. Therefore, the modifications of the energetic structure pointed out by Shizuya, including, most importantly, the splitting between the  $n = 0$  and  $n = 1$  orbital, are present in our treatment. Meanwhile, we retain all significant lattice details and microscopic parameters from the tight binding treatment of bilayer graphene in our model. On this our model Hamiltonian we conduct a mean field Hartree Fock analysis of the ground state properties. The parameters that can be varied are the numbers of electrons present in the system as well as the strength of external electric and magnetic fields. In this setup, we study the different configurations of the spin and isospin degrees of freedom which emerge and classify them into different ground state phases.

The main results of this project consist in the ground state phase diagrams for the seven non-trivial filling factors as functions of the electric and magnetic field strength: for between one and seven electrons occupying states of zero energy we identify the different possible ground state phases characterised by different configurations of the spin, the valley isospin, and the orbital isospin within a parameter range that allows for comparison to experimental results.

This chapter quotes the results of the work published in reference [Knothe and Jolicœur, 2016].


**Figure IV.2**

Electronic occupation of the Landau levels for bilayer graphene: negative energy states are filled, positive energy states are empty. The state of zero energy is partially filled, *i.e.*, there are different numbers of electrons in the **zero-energy octet**

### IV.1.1 Theoretical Framework and Model Hamiltonian

We provide the theoretical background and assemble the model Hamiltonian which we use to describe the zero-energy state of bilayer graphene in the quantum Hall regime. We focus on the situation laid out in the introductory chapter II.1: the energy structure of bilayer graphene in a strong magnetic field forms discrete Landau levels, where the zero energy state is of particular interest: electrons in both, the  $n = 0$  and the  $n = 1$  Landau level turn out to have zero energy. Being degenerate in the spin and the valley isospin degree of freedom, this gives rise to a total of eight states of vanishing energy in bilayer graphene. We refer to these states as the *zero-energy octet*, see figure IV.2. We assume the higher energy states with non-zero positive energy to be completely empty and the states of energy below the octet states  $\epsilon_{-n} < \epsilon_{0,1} \approx 0$  to be completely filled. Those lower-lying electrons we describe them as a manifold of inert levels  $-n \leq -2$  labeled with negative indices and refer to them as the *Dirac sea*.

In the following, we focus on the physics of the *octet electrons*. This is sensible for strong magnetic fields and as long as a bias potential due to an electric field is sufficiently small compared to the Landau level gap. We consider different *partial fillings* of the zero-energy state, *i.e.*, different integer numbers  $0 \leq n_e \leq 8$  of electrons occupying the eight states of the octet giving rise to partial fillings  $\nu \in [-4, 4]$ . While in this regime we neglect Landau level mixing effects, thus assuming the spacing between Landau levels to be sufficiently large so that transitions between Landau levels do not play a role, we nevertheless do not fully forget about the presence of the electrons in the lower-lying Landau levels: we consider them to be inert due to suppressed inter-Landau level hopping, but we do take into account their Coulomb interaction with the electrons in the octet.

### Non-Interacting Picture: The Single Particle Hamiltonian

Quoting the introductory section II.1.1, where we detailed the description of non-interacting electronic states on the bilayer graphene lattice in the quantum Hall regime, we condense the single particle effects into an effective single particle Hamiltonian describing the  $n = 0, 1$  orbitals of the non-interacting system by writing three terms:

$$\begin{aligned} H_0 &= H_{bias} + H_Z + H_{01,pert} \\ &= \sum_p \sum_{n,\sigma,\xi} \left[ -\frac{\Delta_B}{2} \tau_z + z \frac{\Delta_B}{4} (\tau_z + \lambda_z \tau_z) - \frac{\Delta_{01}^{pert}}{2} \lambda_z - \frac{\Delta_Z}{2} \sigma_z \right] c_{n,\sigma,\xi}^\dagger(p) c_{n,\sigma,\xi}(p), \end{aligned} \quad (IV.1)$$

where we work in the tensor space  $\mathcal{H} = \mathcal{H}_{orb} \otimes \mathcal{H}_{spin} \otimes \mathcal{H}_{valley}$  and use the notation  $\sigma_\alpha = \mathbb{1}^{mode} \otimes \sigma_\alpha^{spin} \otimes \mathbb{1}^{valley}$ ,  $\tau_\alpha = \mathbb{1}^{mode} \otimes \mathbb{1}^{spin} \otimes \sigma_\alpha^{valley}$ , and  $\lambda_\alpha = \sigma_\alpha^{mode} \otimes \mathbb{1}^{spin} \otimes \mathbb{1}^{valley}$  for the Pauli operators acting in spin, in valley, and in orbital space and  $\lambda_\alpha \tau_\beta = \sigma_\alpha^{mode} \otimes \mathbb{1}^{spin} \otimes \sigma_\beta^{valley}$ .

The respective terms in equation (IV.1) describe the following:

#### Effect of a bias $\Delta_B$

As to be seen from equation (II.37), a perpendicular electric field of strength  $E$  lifts both, the degeneracy between the  $n = 0$  and the  $n = 1$  Landau level, as well as the valley degeneracy by introducing a splitting proportional to the bias  $\Delta_B = edE$ .

#### Zeeman splitting $\Delta_Z$

The Zeeman effects lifts the degeneracy in spin space by opening the Zeeman gap  $\Delta_Z = g\mu_B B$  with  $g = 2$  between the up and the down configuration of the spin of the electrons.

#### Orbital splitting $\Delta_{01}^{pert}$

We showed in section II.1.1 that in biased bilayer graphene microscopic asymmetries of the lattice break the degeneracy in orbital space and introduce the orbital splitting  $\Delta_{01}^{pert} = \delta_{AB}(1 - c_1^2) + 2\frac{\gamma_4}{\gamma_0\gamma_1} c_1^2 (\hbar\omega_c)^2$  in terms of the lattice parameters  $\delta_{AB}$  and  $\gamma_i$  indicated in figure IV.1.

### Interacting Picture: Hartree Fock Treatment

To study the system for interacting electrons, we include Coulomb interactions between the electrons written as

$$\begin{aligned}
 H_C &= \frac{1}{2} \sum_{n,n'} \sum_{\sigma,\sigma'} \sum_{\xi,\xi'} \iint d\mathbf{r}d\mathbf{r}' \psi_{n_1,\sigma,\xi}^\dagger(\mathbf{r}) \psi_{n_2,\sigma',\xi'}^\dagger(\mathbf{r}') V^C(\mathbf{r}-\mathbf{r}') \psi_{n_3,\sigma',\xi'}(\mathbf{r}') \psi_{n_4,\sigma,\xi}(\mathbf{r}),
 \end{aligned} \tag{IV.2}$$

where  $\psi_{n,\sigma,\xi}(\mathbf{r}) = \sum_p \langle \mathbf{r} | n, \sigma, \xi; p \rangle c_{n,\sigma,\xi}(p)$  denotes the field operator of the electrons. For the interaction potential  $V^C = \frac{e^2}{\epsilon|\mathbf{r}-\mathbf{r}'|}$  we make the following choices:

As a first approximation to the electron-electron interaction, the fully symmetric potential is  $V^C = \frac{e^2}{\epsilon|\mathbf{r}-\mathbf{r}'|}$  with  $\epsilon$  the effective dielectric constant can be chosen. A more realistic approach to the specific geometry of the bilayer system is given by a corrected potential which accounts for the finite distance  $d$  between the upper and the lower graphene layer:  $V_{\xi,\xi'}^C = \frac{e^2}{\epsilon|\mathbf{r}-\mathbf{r}' + (1-\delta_{\xi,\xi'})d\mathbf{e}_z|}$ , where  $\xi, \xi'$  is the valley index. Note that within the four-band model of bilayer graphene, it is not exact to identify the valley index with the sub-layer index. We discuss the validity of this approximation below. To keep calculations as simple as possible, we use the corrected Coulomb potential only when it has notable effects.

We treat the electron interactions in self-consistent Hartree Fock theory as laid out in section II.2.2. We decouple the interaction operator in the single particle basis labelled by the orbital momentum  $p$  into a direct Hartree part  $H_{C,D}$  and an exchange Fock part  $H_{C,X}$ :

$$\begin{aligned}
 H_C &\longrightarrow H_{C,D} - H_{C,X}, \\
 \text{via} & \\
 &\langle c_{n_1,\sigma,K}^\dagger(p_1) c_{n_2,\sigma',K'}^\dagger(p_2) c_{n_3,\sigma,K}(p_3) c_{n_4,\sigma',K'}(p_4) \rangle \\
 &\longrightarrow \langle c_{n_1,\sigma,K}^\dagger(p_1) c_{n_4,\sigma',K'}(p_4) \rangle \langle c_{n_2,\sigma,K}^\dagger(p_2) c_{n_3,\sigma',K'}(p_3) \rangle \\
 &\quad - \langle c_{n_1,\sigma,K}^\dagger(p_1) c_{n_3,\sigma',K'}(p_3) \rangle \langle c_{n_2,\sigma,K}^\dagger(p_2) c_{n_4,\sigma',K'}(p_4) \rangle.
 \end{aligned} \tag{IV.3}$$

Summarising the different spin and isospin degrees of freedom as  $\xi = (n, \sigma, \tau)$ , Hartree Fock decoupling of the general two-body interaction operator written in equation (IV.2) yields the direct and the exchange interaction terms according to

$H_{HF} = H_D - H_X$  which we compute separately as

$$H_D = \frac{1}{S} \sum_{\xi_i} \sum_{\mathbf{q}} V(\mathbf{q}) \iint d\mathbf{r} d\mathbf{r}' \langle \psi_{\xi_1}^\dagger(\mathbf{r}) \psi_{\xi_4}(\mathbf{r}) \rangle e^{i\mathbf{q}(\mathbf{r}-\mathbf{r}')} \psi_{\xi_2}^\dagger(\mathbf{r}') \psi_{\xi_3}(\mathbf{r}')$$
(IV.4)

and

$$H_X = \frac{1}{S} \sum_{\xi_i} \sum_{\mathbf{q}} V(\mathbf{q}) \iint d\mathbf{r} d\mathbf{r}' \langle \psi_{\xi_1}^\dagger(\mathbf{r}) \psi_{\xi_3}(\mathbf{r}') \rangle e^{i\mathbf{q}(\mathbf{r}-\mathbf{r}')} \psi_{\xi_2}^\dagger(\mathbf{r}') \psi_{\xi_4}(\mathbf{r}).$$
(IV.5)

To evaluate the expressions above explicitly in the frame of the four-band model of bilayer graphene, we exploit the real space representations of the state for instance in valley  $K_+$  as introduced in section II.1.1 as

$$\langle \mathbf{r} | n, \sigma, K_+ \rangle = \frac{1}{\sqrt{L_y}} \begin{pmatrix} b_{(n),1} \phi_n(\mathbf{x} - \mathbf{x}_p) \\ b_{(n),2} \phi_{n-2}(\mathbf{x} - \mathbf{x}_p) \\ b_{(n),3} \phi_{n-1}(\mathbf{x} - \mathbf{x}_p) \\ b_{(n),4} \phi_{n-1}(\mathbf{x} - \mathbf{x}_p) \end{pmatrix} e^{iK_+x},$$
(IV.6)

where we used the notations of the coefficients  $b_{(n),i}$  as in section II.1.1. In equation (IV.6) we wrote both, the slowly varying envelope function  $\phi_n$  in the valley labelled by  $K_+$ , as well as the rapidly oscillating part  $e^{iK_+x}$  of the terms contributing in the vicinity of the  $K_+$  valley.

Furthermore, we will use the following relation:

$$\begin{aligned} & \frac{1}{L_y} \int d\mathbf{r} e^{i\mathbf{q}\mathbf{r}} e^{i(K_\tau - K_{\tau'})x} \phi_{n'}^*(\mathbf{x} - \mathbf{x}_{p'}) \phi_n(\mathbf{x} - \mathbf{x}_p) \\ & = \Theta_{n,p,K; n',p',K} \approx \delta_{p-p', -q_y} e^{i\frac{q_x(p+p')\ell_B^2}{2}} K_{n,n'}(\mathbf{q}) \delta_{\tau,\tau'}, \end{aligned}$$
(IV.7)

with

$$K_{n,n'}(\mathbf{q}) = \begin{cases} F_{n,n'}(\mathbf{q}), & \text{for } n' \leq n \\ F_{n,n'}^*(-\mathbf{q}), & \text{for } n' > n, \end{cases}$$
(IV.8)

where, in terms of the associated Laguerre polynomials  $L_{n'}^{n-n'}$ ,

$$F_{n,n'}(\mathbf{q}) = \sqrt{\frac{n!}{n'}} \left( \frac{\ell_B}{\sqrt{2}} \right)^{n-n'} (iq_x + q_y)^{n-n'} e^{-\frac{\ell_B^2 q^2}{4}} L_{n'}^{n-n'} \left[ \frac{\ell_B^2 q^2}{2} \right].$$
(IV.9)

Note that equation (IV.7) represents an approximation suggesting *conservation of the total valley isospin*: we assume for the electron-electron Coulomb interaction in bilayer graphene to conserve the valley isospin  $\tau$  just as it leaves the real spin  $\sigma$  invariant. More precisely, we require in equation (IV.2) the spin and the valley index not to change upon scattering on  $V^C$ :  $\tau_4 = \tau_1 = \tau$ ,  $\sigma_4 = \sigma_1 = \sigma$ , and  $\tau_3 = \tau_2 = \tau'$ ,  $\sigma_3 = \sigma_2 = \sigma'$ . While for the spin this represents an exact symmetry of the Coulomb interaction, for the valley isospin it amounts to the following approximation: we neglect all scattering processes altering the valley isospin. As we show in appendix D, in the case of graphene, these processes can be shown to be suppressed due to the large separation of the two valleys  $K_+$  and  $K_-$  in momentum space [Goerbig, 2011]. The same approximation was also applied for monolayer graphene in chapter III, equation (III.5), leading to approximate SU(4) in the case of monolayer graphene.

This allows us to restrict to one single valley and to formulate an electron density operator in valley  $K_+$  as

$$\begin{aligned}
 \rho_{K_+} &= \sum_{n,n'} \sum_{\sigma,\sigma'} \sum_{p,p'} \int d\mathbf{r} e^{i\mathbf{q}\mathbf{r}} \langle \mathbf{r} | n', \sigma', K_+; p' \rangle^\dagger \langle \mathbf{r} | n, \sigma, K_+; p \rangle c_{n',\sigma',K_+}^\dagger(p') c_{n,\sigma,K_+}(p) \\
 &= \sum_{n,n'} \sum_{\sigma,\sigma'} \sum_{p,p'} \left[ b_{(n'),1}^* b_{(n),1} \Theta_{n,p,K_+; n',p',K_+} + b_{(n'),2}^* b_{(n),2} \Theta_{n-2,p,K_+; n'-2,p',K_+} \right. \\
 &\quad \left. + (b_{(n'),3}^* b_{(n),3} + b_{(n'),4}^* b_{(n),4}) \Theta_{n-1,p,K_+; n'-1,p',K_+} \right] c_{n',\sigma',K_+}^\dagger(p') c_{n,\sigma,K_+}(p) \\
 &= N_{LL} \sum_{n,n'} \sum_{\sigma,\sigma'} \left[ b_{(n'),1}^* b_{(n),1} K_{n,n'}(\mathbf{q}) + b_{(n'),2}^* b_{(n),2} K_{n-2,n'-2}(\mathbf{q}) \right. \\
 &\quad \left. + (b_{(n'),3}^* b_{(n),3} + b_{(n'),4}^* b_{(n),4}) K_{n-1,n'-1}(\mathbf{q}) \right] \rho_{n',\sigma',K_+; n,\sigma,K_+}(\mathbf{q}) \\
 &=: N_{LL} \sum_{n,n'} \sum_{\sigma,\sigma'} \mathfrak{K}_{n,n'}(\mathbf{q}) \rho_{n',\sigma',K_+; n,\sigma,K_+}(-\mathbf{q}), \tag{IV.10}
 \end{aligned}$$

where we introduced notion of the *bare guiding centre density*

$$\rho_{\xi_i; \xi_j}(\mathbf{q}) = \frac{1}{N_{LL}} \sum_{p_i, p_j} \delta_{p_i - p_j, q_y} e^{-\frac{i}{2} q_x (p_i + p_j) \ell_B^2} c_{\xi_i}^\dagger(p_i) c_{\xi_j}(p_j), \tag{IV.11}$$

for  $\xi_i = \{n_i, \sigma_i, K_i\}$  and  $N_{LL}$  the Landau level degeneracy, as well as the *effective form factor*

$$\begin{aligned}
 \mathfrak{K}_{n,n'}(\mathbf{q}) &= b_{(n'),1}^* b_{(n),1} K_{n,n'}(\mathbf{q}) + b_{(n'),2}^* b_{(n),2} K_{n-2,n'-2}(\mathbf{q}) \\
 &\quad + (b_{(n'),3}^* b_{(n),3} + b_{(n'),4}^* b_{(n),4}) K_{n-1,n'-1}(\mathbf{q}), \tag{IV.12}
 \end{aligned}$$

taking into account the shape of the wave functions in the four-band model of bilayer graphene.

In the following investigation, we simplify the above expressions under the assumption of homogeneity in real space and translational invariance: we restrict ourselves to searching only for Hartree Fock solutions uniform in real space. Physically, this amounts to not considering any possible solutions exhibiting any non-trivial spatial modulation of either the spin and isospin texture or the electronic density. We do not take into account any terms that involve possible correlations in real space. More precisely, neglecting any sort of real space correlations amounts to taking into account only the solutions at vanishing  $\mathbf{q}$  in momentum space. In the following, we write  $\rho_{\xi_i;\xi_j}(\mathbf{q} = 0) = \rho_{\xi_i;\xi_j}$  and

$$\langle \rho_{\xi_i;\xi_j}(\mathbf{q} = 0) \rangle = \frac{1}{N_{LL}} \sum_p \langle c_{\xi_i}^\dagger(p) c_{\xi_j}(p) \rangle =: \frac{1}{N_{LL}} \sum_p P_{\xi_j\xi_i}(p), \quad (\text{IV.13})$$

where we introduced the density matrix

$$P_{\substack{n',n \\ \sigma',\sigma;\xi',\xi}}(p) := \langle c_{n,\sigma,\xi}^\dagger(p) c_{n',\sigma',\xi'}(p) \rangle, \quad (\text{IV.14})$$

which will serve as a multicomponent order parameter.

We dissect the electronic Coulomb interactions into different contributions, which we treat separately before assembling them to the full effective Hartree Fock Hamiltonian for bilayer graphene of our model.

*Interactions of the Electrons within the Octet ( $n = 0, 1$ )*

Within in 01-octet we consider interaction between the electrons via the corrected potential

$$V_{\xi,\xi'}^C = \frac{e^2}{\epsilon|\mathbf{r} - \mathbf{r}' + (1 - \delta_{\xi,\xi'})d\mathbf{e}_z|}. \quad (\text{IV.15})$$

When working with the effective two-band model for the electronic states of bilayer graphene discussed in the introductory section II.1.1 [McCann and Fal'ko, 2006], within the zero-mode sector there is a direct one-to-one correspondence between the valley degree of freedom and the electrons occupation in the upper or the lower layer, respectively [Lambert and Côté, 2013]. This can be seen from the electronic states written within the two-band model in equation (II.31). Within the four-band model applied throughout this work, however, this correspondence valley  $\leftrightarrow$  layer within the pseudo-zero mode sector is no longer exact. Close investigation of the coefficients of equation (II.35) governing the electronic occupation

of the different atomic sites reveals the following: the occupation of the different sublayers which would stay fully unoccupied within the two-band model is governed by the coefficient  $b_{(1),3}$  in  $\psi_{K_+}^{(1)}$ . Hence, as addressed also in section II.1.1, the four-band model and the two-band model of bilayer graphene do predict different behaviour of the layer occupation of bilayer graphene. This will be of importance in the subsequent discussion. It is thus crucial to take into account the different behaviour of the  $n = 0$  and the  $n = 1$  modes within the two models. We estimate the error due to the correspondence valley  $\leftrightarrow$  layer for each valley index: as can be seen from figure II.8 in section II.1.1, the coefficient  $b_{(1),3}$  is largest in magnitude for zero bias - in this case, the relation  $b_{(1),3}^2 = \frac{b_{(1),1}^2}{\gamma^2}$  holds. Hence,  $b_{(1),3} \ll b_{(1),1}$  since  $\gamma \gg 1$  for the parameters listed in Table IV.1. We therefore use the form of the corrected Coulomb potential  $V_{\xi,\xi'}^C$  given in equation (IV.15) in order to include the effect of the anisotropic Coulomb interaction due to the finite separation between the layers.

We perform the Hartree Fock decoupling of the Coulomb-interaction term in the four-band model for the electrons in the octet similar to calculations within an effective two-band model of bilayer graphene presented in [Côté et al., 2010] and [Lambert and Côté, 2013].

### Direct interaction

The contribution from the direct interaction term competes with a positive, neutralising background. Using the explicit representation of the wave functions of the electronic states as in equation (IV.6), one can see that the estimation of this competition presented in reference [Lambert, 2013] is not altered when carried out in the four-band model compared to the two-band model considerations. It yields that the effective, resulting contribution is given by a capacitive energy of the form [Lambert and Côté, 2013; Lambert, 2013]

$$H_{D, \text{Octet}} = \sum_p \sum_{n,\sigma,\xi} \alpha \frac{d}{\ell_B} \left( \tilde{v}_\xi - \frac{\tilde{v}}{2} \right) c_{n,\sigma,\xi}^\dagger(p) c_{n,\sigma,\xi}(p), \quad (\text{IV.16})$$

where we denote with  $\tilde{v}_\xi = \sum_p \sum_{n\sigma} \langle c_{n,\sigma,\xi}^\dagger(p) c_{n,\sigma,\xi}(p) \rangle$  the total filling in valley  $\xi$ ,  $\tilde{v} = \nu + 4$  counts the total number of filled levels in the octet, and  $\alpha = \frac{e^2}{\epsilon \ell_B}$ .

### Exchange interaction

From the exchange part of the interaction we obtain the contribution

$$\begin{aligned}
 & H_{X, \text{Octet}} \\
 &= - \sum_{\substack{p_1, p_2 \\ p_3, p_4}} \sum_{\substack{n_1, n_3 \\ n_2, n_4}} \sum_{\substack{\sigma, \xi \\ \sigma', \xi'}} \mathfrak{X}_{n_1, n_3}^{\xi, \xi'}(0) \langle c_{n_1, \sigma, \xi}^\dagger(p_1) c_{n_3, \sigma', \xi'}(p_3) \rangle c_{n_2, \sigma', \xi'}^\dagger(p_2) c_{n_4, \sigma, \xi}(p_4),
 \end{aligned} \tag{IV.17}$$

where, following previous definitions, we find the exchange matrix elements

$$\mathfrak{X}_{n_1, n_2}^{\xi, \xi'}(\mathbf{q}) = \alpha \int \frac{d\mathbf{p} \ell_B^2}{2\pi} \frac{1}{p \ell_B} e^{-pd(1-\delta_{\xi, \xi'})} \mathfrak{R}_{n_1, n_4}(p) \mathfrak{R}_{n_3, n_2}(-p) e^{i\mathbf{p} \times \mathbf{q} \ell_B^2}, \tag{IV.18}$$

with

$$\begin{aligned}
 \mathfrak{R}_{0,0}(\mathbf{p}) &= e^{-\frac{\ell_B^2 p^2}{4}} \\
 \mathfrak{R}_{0,1}(\mathbf{p}) &= e^{-\frac{\ell_B^2 p^2}{4}} \frac{c_1 \ell_B}{\sqrt{2}} (ip_x + p_y) \\
 \mathfrak{R}_{1,0}(\mathbf{p}) &= e^{-\frac{\ell_B^2 p^2}{4}} \frac{c_1 \ell_B}{\sqrt{2}} (ip_x - p_y) \\
 \mathfrak{R}_{1,1}(\mathbf{p}) &= e^{-\frac{\ell_B^2 p^2}{4}} \left(1 - c_1 \frac{\ell_B^2 p^2}{2}\right).
 \end{aligned} \tag{IV.19}$$

For future use we introduce the notation  $\Delta_{n_1 n_2 n_3 n_4} := \mathfrak{X}_{n_1, n_2}^{\xi, \xi'}_{n_3, n_4}$  for the terms conserving the valley index and  $X_{n_1 n_2 n_3 n_4} := \mathfrak{X}_{n_1, n_2}^{\xi, \xi'}_{n_3, n_4}$  in the case  $\xi \neq \xi'$  for the valley index non-conserving terms. The corresponding matrix elements are listed explicitly in appendix C.

#### *Coupling with the Electrons filling the Dirac Sea ( $n \leq -2$ )*

In reference [Shizuya, 2012], Shizuya has shown that, while the direct interaction contributions are fully cancelled by a uniform positive background charge, exchange interactions with the electrons in the Dirac sea when treated within the four-band model of bilayer graphene lead to a splitting  $\Delta_{01}^{\text{int}}$  between the  $n = 0$  and  $n = 1$  orbitals. From the Coulomb exchange interaction between all the electrons in the system Shizuya extracts the contribution that stems from interaction between the Dirac sea electrons and the electrons in the octet. Further careful dissection of this interaction term into its different constituents reveals that the Dirac electrons couple differently to the octet electrons in the  $n = 0$  mode than to those occupying the  $n = 1$  mode. This effectively lifts the  $n = 0$  state above the  $n = 1$  state in energy entailing an interaction induced splitting  $\Delta_{01}^{\text{int}}$  between the two modes. Using the

fully symmetric Coulomb potential, this exchange phenomenon analogous to the Lamb shift of atomic energy levels\* leads to a term of the form

$$H_{X, \text{Dirac}} = - \sum_p \sum_{n, \sigma, \xi} \frac{\Delta_{01}^{\text{int}}}{2} \lambda_z c_{n, \sigma, \xi}^\dagger(p) c_{n, \sigma, \xi}(p), \quad (\text{IV.20})$$

where the Landau level index only runs over  $n = 0, 1$ . In above equation  $\lambda_\alpha = \sigma_\alpha^{\text{mode}} \otimes \mathbb{1}^{\text{spin}} \otimes \mathbb{1}^{\text{valley}}$  denotes the Pauli operators acting in 01-orbital space and  $\Delta_{01}^{\text{int}} = \frac{1}{8} \Delta_C c_1^2 (4 - 3c_1^2)$  is the splitting induced by the presence of the Dirac sea, where we defined  $\Delta_C = \sqrt{\frac{\pi}{2}} \alpha = \sqrt{\frac{\pi}{2}} \frac{e^2}{\epsilon \ell_B}$ .

Furthermore, in the very same reference [Shizuya, 2012], Shizuya demonstrates in a perturbative treatment up to the first order in  $\frac{d}{\ell_B}$  that the anisotropic inter-layer Coulomb interaction merely entails a simple rescaling as  $\Delta_B \rightarrow \Delta_{B, \text{eff}} = (1 - 16 \frac{W}{\hbar \omega_c}) \Delta_B$ , where  $W = \frac{d}{\ell_B} \alpha$ .

#### Full Hartree Fock Hamiltonian and Numerical Hartree Fock Routine

Assembling all terms from the discussion above, we arrive at the Hartree Fock Hamiltonian

$$H_{HF} = H_0 + H_{X, \text{Octet}} + H_{D, \text{Octet}} + H_{X, \text{Dirac}}. \quad (\text{IV.21})$$

Hence, in terms of the density matrix  $P$ , and assuming  $P(p) \approx P(p')$  as a local approximation justified as we are treating states uniform or varying sufficiently slowly in space (see also the comparable calculation of equation (III.18) for monolayer graphene leading to equation (III.24) in chapter III), we obtain for the Hartree Fock energy functional:

$$\begin{aligned} E_{HF} = & -\frac{1}{2} \sum_{\substack{n_1, n_3 \\ n_2, n_4}} \sum_{\substack{\sigma, \xi \\ \sigma', \xi'}} \mathfrak{X}_{n_1, n_3}^{\xi, \xi'}(\mathbf{0}) P_{n_3, n_1} P_{n_4, n_2} + \frac{\alpha}{4} \frac{d}{\ell_B} (\tilde{\nu}_K - \tilde{\nu}_{K'})^2 \\ & - \frac{\Delta_{01}}{2} \text{Tr}[\lambda_z P] + \frac{\Delta_Z}{2} \text{Tr}[\sigma_z P] - \frac{\Delta_{B, \text{eff}}}{2} \text{Tr}[\tau_z P] + z \frac{\Delta_{B, \text{eff}}}{4} \text{Tr}[(\tau_z + \lambda_z \tau_z) P], \end{aligned} \quad (\text{IV.22})$$

---

\* The Lamb shift in atomic systems, demonstrated in 1947 by Lamb and Retherford [Lamb and Retherford, 1947] for atomic hydrogen, denotes the lifting of the degeneracy between atomic energy levels which have equal main quantum number and equal total angular momentum quantum number, but differ in the orbital angular momentum quantum number, such as the levels  $2s_{1/2}$  and  $2p_{1/2}$  of the hydrogen atom. The origin of this shift in energy leading to a splitting between the levels can be understood when considering even in the absence of external fields or radiation, the presence of a quantum vacuum as the ground state of the electromagnetic quantum field. This vacuum will fluctuate, *i.e.*, it contains virtual particle-antiparticle pairs. These fluctuations effect the Coulomb interaction between the electron and the nucleus which leads to the shift in energy mentioned before.

where summation over  $p$  has been suppressed and we summarised  $\Delta_{01} = \Delta_{01}^{\text{pert}} + \Delta_{01}^{\text{int}}$  as the total splitting in orbital space induced by the different effects discussed above.

In this project, we study the model Hamiltonian  $H_{HF}$  given in equation (IV.21) within Hartree Fock theory. This Hamiltonian  $H_{HF}$  depends on  $P$  which in turn itself is determined by the lowest-energy solution to the corresponding eigenvalue problem. The numerical procedure leading to its solution must thus be carried out self-consistently. We briefly sketch the algorithm used in our analysis.

We fix different total numbers of electrons in the octet. The *filling factor*  $\nu$  of the octet is defined with respect to the half-filled, charge neutral case: we write  $\nu = -3$   $(-2, -1, 0, 1, 2, 3)$  for 1  $(2, 3, 4, 5, 6, 7)$  out of the eight available zero-energy levels being occupied. In sections IV.2 and IV.3, we present investigations and discussions of all the different non-trivial fillings factors  $\nu \in [-3, 3]$ . The density matrix is assumed to be independent of the guiding centre coordinate as we are looking only for spatially uniform solutions.

For a given filling factor  $\nu$  implying  $n$  occupied levels, we start by initialising  $n$  single particle vectors  $|i\rangle$ : the eight entries each are taken from a random uniform distribution, thereby respecting normalisation. The density matrix  $P^{\text{int}} = \sum_i^n |i\rangle\langle i|$  built from these vectors serves as a starting point for the self-consistent Hartree Fock minimisation procedure. The subsequent protocol proceeds as follows: using  $P^{\text{int}}$  we construct a first Hartree Fock Hamiltonian  $H_{HF}^{\text{int}}(P^{\text{int}})$  according to equation (IV.21). Diagonalising  $H_{HF}^{\text{int}}(P^{\text{int}})$  yields the corresponding eight eigenvectors and eigenenergies. The  $n$  lowest-lying eigenstates are used to construct a new density matrix  $P$ ; This new, improved  $P$  is then again inserted in equation (IV.21) to obtain a new, improved  $H_{HF}$  and reiterate the procedure. This algorithm is repeated until convergence of the density matrix is achieved, *i.e.*, until the difference between two successive density matrices becomes negligible:  $\|P^{j+1} - P^j\| < \epsilon$ , where  $\epsilon$  is a small positive number,  $j$  labels the number of iteration and  $\|\cdot\|$  denotes the Hilbert-Schmidt norm for a matrix  $\mathbf{A}$  defined as  $\|\mathbf{A}\| = \sqrt{\mathbf{A}\mathbf{A}^\dagger}$ . We require convergence of the algorithm until  $\epsilon < 10^{-25}$ . Iteration schemes similar to the one used here and equally based on the so-called *Roothaan algorithm* for self-consistent Hartree Fock iteration [Roothaan, 1951] have been applied earlier in Hartree Fock studies of quantum Hall systems [Sohrmann and Römer, 2007; Römer and Sohrmann, 2008].

A check for proper convergence to a true solution of the Hartree Fock equations is performed by always requiring the single particle energy eigenvalues to reproduce the energy yielded by the Hartree Fock energy functional of equation (IV.22) up to a precision better than  $10^{-5}$ .

We summarise the numerical self-consistent iteration routine used for Hartree

Fock of bilayer graphene as follows:

Summary: Hartree Fock Iteration Routine

1. Fix  $\nu$ , *i.e.*, fix the number  $n$  of electrons in the octet
2. Generate  $n$  single particle vectors  
 $|i\rangle = (a_1^i, a_2^i, a_3^i, a_4^i, a_5^i, a_6^i, a_7^i, a_8^i)$ ,  $1 \leq i \leq n$ , with  $a_\alpha^i \in [0, 1]$  chosen randomly and  $\sum_\alpha a_\alpha^i = 1$ .
3. Initialise the density matrix of the  $n$  particle state as  $P^{\text{int}} = \sum_i^n |i\rangle\langle i|$
4. Construct initial Hartree Fock Hamiltonian  $H_{HF}^{\text{int}}(P^{\text{int}})$  [equation (IV.21)]
5. Diagonalise  $H_{HF}^{\text{int}}(P^{\text{int}}) \Rightarrow$  Eigenvectors  $|v_i\rangle$
6. From the  $n$  lowest lying eigenvectors: build  $P^i = \sum_i^n |v_i\rangle\langle v_i|$
7. Compute  $H_{HF}^{\text{it}}(P^i) \Rightarrow$  Diagonalise
8. Repeat steps 6 and 7 until  $\|P^{j+1} - P^j\| < 10^{-25}$
9. The final density matrix  $P^{\text{final}}$  corresponds to the converged Hartree Fock ground state solution.

From the final converged density matrix  $P^{\text{final}}$  we calculate the components of the total spin  $\mathbf{S}$ , the total valley isospin  $\mathbf{T}$ , and the total orbital isospin degree of freedom  $\mathbf{L}$  according to

$$S_\alpha = \frac{1}{2}\text{Tr}[\sigma_\alpha P], \quad T_\alpha = \frac{1}{2}\text{Tr}[\tau_\alpha P], \quad L_\alpha = \frac{1}{2}\text{Tr}[\lambda_\alpha P], \quad (\text{IV.23})$$

for  $\alpha \in \{x, y, z\}$ . We identify different phases by different configurations of the spin and isospin degrees of freedom. By tracing their evolution as functions of the external parameters, *i.e.*, the bias potential  $\Delta_B$  and the magnetic field  $B$ , we determine the phase diagrams in the  $\{\Delta_B-B\}$ -plane. From this numerical Hartree Fock procedure we furthermore gain information about the Hartree Fock single particle eigenstates and eigenvalues for each value of  $\Delta_B$  and  $B$ . Hence we can infer the structure of the occupied and unoccupied single particle states for each phase within this Hartree Fock mean field picture. This knowledge about the ground state structure allows us to proceed further by analytical means: using a particular structure of the ground state eigenvectors to construct the corresponding density matrix  $P$  and minimising the Hartree Fock energy functional given in

equation (IV.22) for this P allows us to compute analytically properties of the various phases such as canting angles of the energetically favourable spin and isospin orientation or phase boundaries between different ground state phases.

We have not tried to search for spatially non-uniform Hartree Fock solutions. There is no clear experimental evidence for such states so far. The Hartree Fock investigations of Lambert and Côté have found such solutions only at very large bias.

System Parameters			
$\gamma_0$	3.1 eV	$\gamma_1$	0.39 eV
$\gamma_3$	0.1 eV	$\gamma_4$	0.13 eV
$v_0 = \frac{\sqrt{3}}{2} \frac{a_L \gamma_0}{\hbar}$	$1.1 \times 10^6$ m/s	$a_L$	0.246 nm
$\hbar\omega_c = \sqrt{2} \frac{\hbar v_F}{\ell_B}$	$36.3 v_0 [10^6 \frac{m}{s}] \sqrt{B[T]}$ meV	$d$	0.34 nm
$\ell_B = \sqrt{\frac{\hbar c}{eB}}$	$26 \text{nm} \frac{1}{\sqrt{B[T]}}$	$\epsilon$	5
$\delta_{A,B}$	0.016 eV		
Characteristic energies			
$\Delta_C = \sqrt{\frac{\pi}{2}} \alpha = \sqrt{\frac{\pi}{2}} \frac{e^2}{\epsilon \ell_B}$	$14.1 \sqrt{B[T]}$ meV	$\Delta_{01}$	$\frac{1}{8} \Delta_C c_1^2 (4 - 3c_1^2)$
$\Delta_Z = g\mu_B B$	$0.11 B[T]$ meV	$\Delta_B$	$edE_{\perp} [\frac{\text{mV}}{\text{nm}}]$

**Table IV.1**

Numerical values of the system parameters and the energy splittings used throughout the analysis.

## IV.2 Bilayer Graphene in the Zero-Energy Landau Level - Results (I): Hartree Fock Phase Diagrams

The main result of this project are the seven phase diagrams of bilayer graphene obtained for different filling factors  $\nu \in [-3, 3]$  using the Hartree Fock procedure described in the previous section IV.1. For the seven different filling factors as well as for varying the external magnetic and electric fields, this yields a vast amount of information. Presentation of the results is structured as follows: in order to provide an overview, we first present the full collection of phase diagrams and summarise all the corresponding ground state configurations and their properties. Subsequently, the seven different cases are discussed separately in detail, where most attention is paid to the easiest case  $\nu = -3$  for exemplary demonstration. The remaining cases are presented in analogy.

### IV.2.1 Overview over the Phases

In figure IV.3, we plot the phase diagrams for the different  $\nu$  in the plane spanned by the bias  $\Delta_B$  and the magnetic field  $B$ . From these phase diagrams, we identify a total of 32 different phases of the bilayer graphene system at different filling factors.

#### Phase Diagrams in the $\{\Delta_B-B\}$ -Plane

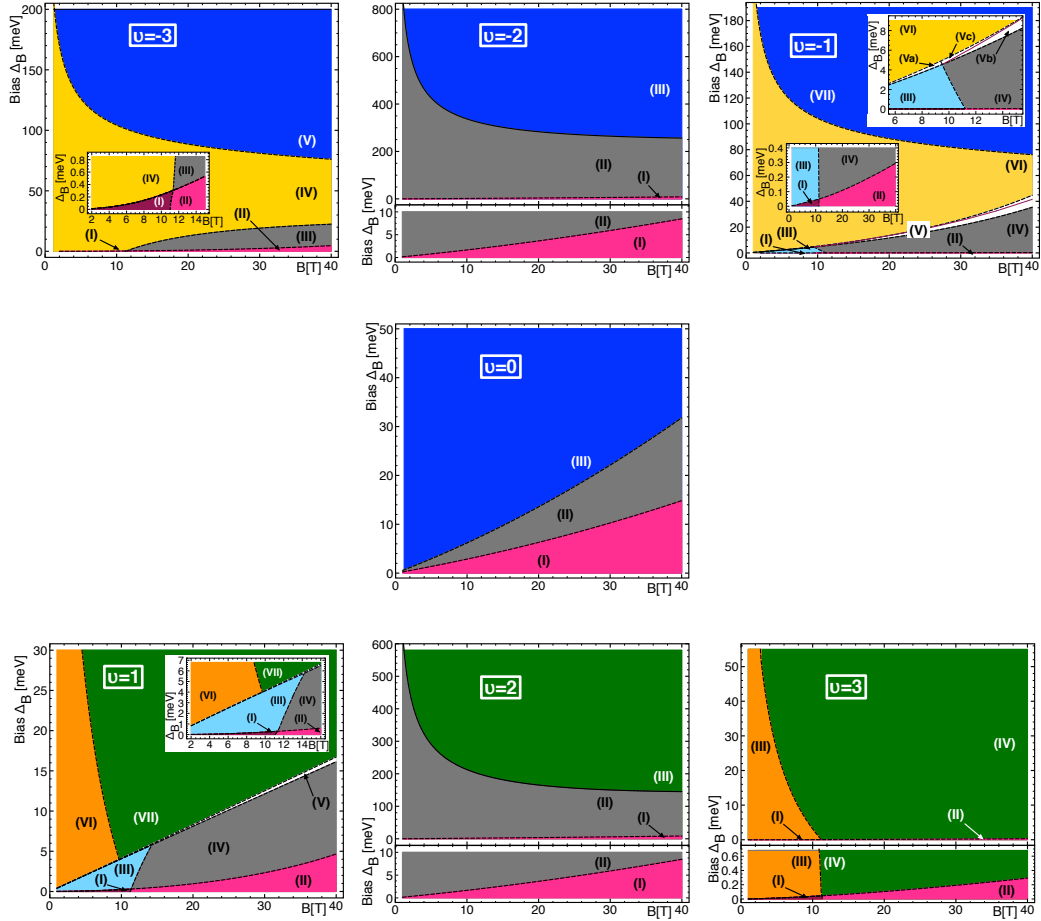


**Figure IV.3**

Ground state phase diagrams of bilayer graphene at the different filling factors  $\nu \in [-3, 3]$  obtained from Hamiltonian  $H_{HF}$  of equation (IV.21) in a Hartree Fock picture. Colour code for the phases: **bordeaux/magenta**:  $\mathbf{S} \propto \mathbf{e}_z$  and  $\mathbf{T}$  in a canted state  $\rightarrow$  valley coherence; **yellow/orange**:  $\mathbf{S} \propto \mathbf{e}_z$  and  $\mathbf{L}$  in a canted state  $\rightarrow$  orbital coherence; **grey/blue/green**:  $\mathbf{S}, \mathbf{T} \propto \mathbf{e}_z$  for  $\mathbf{L} \equiv 0$  or  $\mathbf{L} \propto \pm \mathbf{e}_z \rightarrow$  partial polarisation. Figures from reference [Knothe and Jolicœur, 2016] (edited).

The explicit form of the respective phases is listed in tables IV.2-IV.8. Their spin and isospin polarisation properties are given in tables IV.9 and IV.10 for negative and positive filling factors, respectively. In the first section of the text, we successively discuss the respective cases for each different filling factor. We next summarise these results and compare our findings for different  $\nu$  among each other.

Figure IV.3 shows the collection of phase diagrams obtained for the different filling factors  $\nu \in [-3, 3]$ .

## IV.2.2 Individual Presentation of the Phases

### ★ Phases of Different Spin and Isospin Properties: Exemplary Demonstration for one Electron, $\nu = -3$

For the easiest example, at  $\nu = -3$ , when there is only one electron present in the octet, we demonstrate the reasoning that leads to the ground state phase of figure IV.3.

In figure IV.4 we demonstrate how an individual phase diagram from the collection of figure IV.3 is to be read and what information is contained in it. We plot the phase diagram of the  $\nu = -3$  state in the  $\{\Delta_B-B\}$ -plane together with the evolution of the components of spin, valley isospin, and orbital isospin,  $S_i, V_i$ , and  $L_i$ , for a cut at fixed magnetic field  $B = 35$  T and increasing bias  $\Delta_B$ . This cut is marked in the adjoining phase diagram by a black line that traverses all the different ground state phases of the  $\nu = -3$  phase diagram. We see how different phases are related to regimes of different properties and different behaviour of the spin and the isospins. The different values of the total spins and isospins of the respective ground state phases are yielded from the Hartree Fock algorithm as well as the explicit form of the corresponding ground states. In many of the cases, when the ground state wave functions are sufficiently simple, from these the phase boundaries can be computed analytically.

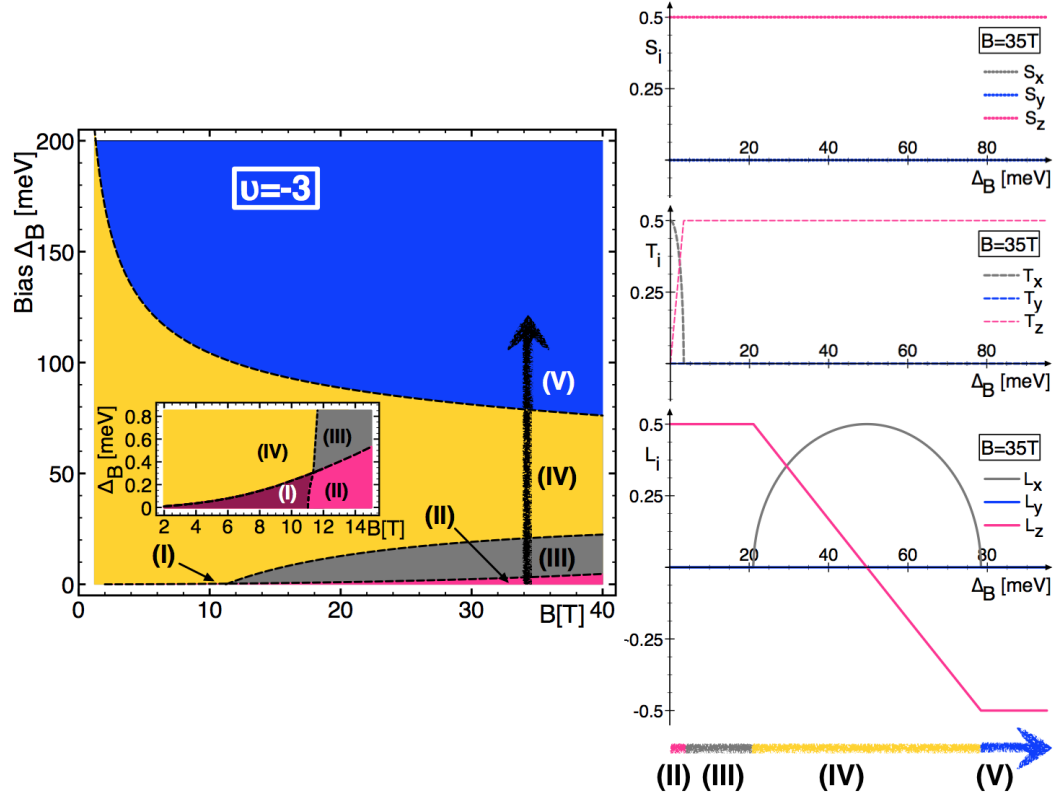
We describe and analyse the different phases in detail below.

#### Bias $\Delta_B \equiv 0$ ; Evolution as a Function of $B$

At zero bias, the ground state is of the form

$$|GS\rangle = \frac{1}{\sqrt{2}} \sin \theta \left[ |1, \uparrow, +\rangle + |1, \uparrow, -\rangle \right] + \frac{1}{\sqrt{2}} \cos \theta \left[ |0, \uparrow, +\rangle + |0, \uparrow, -\rangle \right], \quad (\text{IV.24})$$

where the optimal angle  $\theta_0$ , plotted in figure IV.15, varies as a function of  $B$  between  $\theta_0 \rightarrow 0$  at vanishing magnetic field  $B \rightarrow 0$  and  $\theta_0 = \frac{\pi}{2}$  at sufficiently high


**Figure IV.4**

Left: phase diagram of the  $\nu = -3$  ground state as yielded by Hartree Fock analysis. There are five different phases emerging, labelled (I)-(IV). The black line represents a cut through the different phases at fixed  $B = 35$  T and for increasing  $\Delta_B$ . On the right, we plot the evolution of the components of spin, valley isospin, and orbital isospin,  $S_i$ ,  $V_i$ , and  $L_i$ , that correspond to this cut. We characterise different ground state phases by regimes of different spin and isospin properties, marked in different colours.

magnetic field strengths above a certain critical value  $B_{crit}$ . It fulfils the relation

$$\cos \theta_0 = \frac{\sqrt{-\Delta_{0011} - 2\Delta_{01} - \Delta_{1001} + \Delta_{1111} - X_{0011} - X_{1001} + X_{1111}}}{\sqrt{\Delta_{0000} - 2\Delta_{0011} - 2\Delta_{1001} + \Delta_{1111} + X_{0000} - 2X_{0011} - 2X_{1001} + X_{1111}}}. \quad (\text{IV.25})$$

The state exhibits the properties

$$\begin{aligned} S_z &\equiv \frac{1}{2}, \quad S_x \equiv S_y \equiv 0, \\ T_z &= 0, \quad T_x \equiv \frac{1}{2}, \quad T_y \equiv 0, \\ L_z &= -\cos 2\theta, \quad L_x = \sin 2\theta, \quad L_y \equiv 0. \end{aligned} \quad (\text{IV.26})$$

Hence, the ground state in this phase is polarised along the  $z$ -axis in the spin degree of freedom, but not in the valley degree of freedom, where the corresponding isospin vector lies in the  $\{x-y\}$ -plane. The isospin corresponding to the orbital mode is in a canted configuration, thus we find a phase with orbital coherence.

Along the line of zero bias, the ground state hence undergoes a transition from a canted to a fully polarised state in the orbital isospin as a function of the magnetic field strength  $B$ .

### Phase (I): Canting in Valley Isospin and Orbital Isospin

At small but nonzero bias  $\Delta_B > 0$  and below a critical magnetic field strength  $B < B_{crit}$ , the ground state phase is characterised by the non-trivial composition

$$|GS\rangle = a_1|1, \uparrow, +\rangle + a_2|1, \uparrow, -\rangle + a_5|0, \uparrow, +\rangle + a_6|0, \uparrow, -\rangle, \quad (\text{IV.27})$$

with coefficients  $a_i$  varying as functions of  $\Delta_B$  and  $B$ . This entails the following spin and isospin structure:

$$\begin{aligned} S_z &= \frac{1}{2} \left( |a_1|^2 + |a_2|^2 + |a_5|^2 + |a_6|^2 \right) \equiv \frac{1}{2}, \\ S_x &\equiv S_y \equiv 0, \\ T_z &= |a_1|^2 - |a_2|^2 + |a_5|^2 - |a_6|^2, \\ T_x &= a_2 a_1^* + a_1 a_2^* + a_6 a_5^* + a_5 a_6^*, \\ T_y &\equiv 0, \\ L_z &= |a_1|^2 + |a_2|^2 - |a_5|^2 - |a_6|^2, \\ L_x &= a_5 a_1^* + a_1 a_5^* + a_6 a_2^* + a_2 a_6^* \\ L_y &\equiv 0. \end{aligned} \quad (\text{IV.28})$$

The ground state is spin polarised, but canted both in valley and orbital degrees of freedom.

Therefore, in phase (I), cuts along lines of increasing bias  $\Delta_B$ , for any strength of the magnetic field  $B$ , correspond to a rotation of the valley isospin vector from a configuration in the  $\{x-y\}$ -plane to a state fully aligned along the  $z$ -axis. At the same time, the orbital isospin components take non-trivial values  $0 < L_x, L_z < 1$ .

### Phase (II): Canting in Valley Isospin, Orbital Ferromagnet

The ground state of the phase is described by a state vector of the form

$$|GS\rangle = \sin\theta|1, \uparrow, +\rangle + \cos\theta|1, \uparrow, -\rangle, \quad (\text{IV.29})$$

where the optimal angle is determined by

$$\cos 2\theta_{II} = \frac{\Delta_{B,eff} \ell_B(z-1)}{\alpha d + \ell_B(\Delta_{1111} - X_{1111})}. \quad (\text{IV.30})$$

This phase is characterised by the spin and isospin properties

$$\begin{aligned} S_z &\equiv \frac{1}{2}, \quad S_x \equiv S_y \equiv 0, \\ T_z &= -\cos 2\theta, \quad T_x = \sin 2\theta, \quad T_y \equiv 0, \\ L_z &\equiv \frac{1}{2}, \quad L_x \equiv L_y \equiv 0. \end{aligned} \quad (\text{IV.31})$$

Hence, in phase (II), along any cut at a fixed  $B > B_{crit}$ , the state undergoes a rotation of the valley isospin as a function of the bias  $\Delta_B$ , from  $\mathbf{T}$  lying in the  $\{x-y\}$ -plane at  $\Delta_B = 0$  to a fully valley polarised state at sufficiently large  $\Delta_B$ .

### Phase (III): Fully Polarised in all Spins and Isospins

Over a certain range of bias and magnetic field strength, in an intermediate phase at sufficiently large values of the magnetic field  $B > B_{crit} \approx 11$  T and when the bias potential is raised beyond the regime of phase (II), the ground state stabilises a perfect ferromagnet in all spins and isospins. In this phase, all spin and isospin degrees of freedom are aligned (this is the case of phase II for the limiting value  $\theta_{II} \equiv \frac{\pi}{2}$ ):

$$|GS\rangle = |1, \uparrow, +\rangle, \quad (\text{IV.32})$$

$$\begin{aligned}
 S_z &\equiv \frac{1}{2}, \quad S_x \equiv S_y \equiv 0, \\
 T_z &\equiv \frac{1}{2}, \quad T_x \equiv T_y \equiv 0, \\
 L_z &\equiv \frac{1}{2}, \quad L_x \equiv L_y \equiv 0.
 \end{aligned}
 \tag{IV.33}$$

#### Phase (IV): Canting of the Orbital Isospin

Phase (IV) dominates the intermediate part of the  $\nu = -3$  phase diagram over the whole parameter range of bias  $\Delta_B$  and magnetic field strength  $B$ . It is characterised by full ferromagnetic polarisation of the spin and valley isospin, but canting of the orbital isospin resulting in an orbital coherent phase.

The ground state of this phase is given by the orbital coherent state

$$|GS\rangle = \sin\theta|1, \uparrow, +\rangle + \cos\theta|0, \uparrow, +\rangle, \tag{IV.34}$$

where for the optimal angle holds the expression

$$\cos 2\theta_{IV} = \frac{-\Delta_{0000} - 2\Delta_{01} + \Delta_{1111} + z\Delta_{B,eff}}{\Delta_{0000} - 2\Delta_{0011} - 2\Delta_{1001} + \Delta_{1111}}. \tag{IV.35}$$

Its spin and isospin configuration is given by

$$\begin{aligned}
 S_z &\equiv \frac{1}{2}, \quad S_x \equiv S_y \equiv 0, \\
 T_z &\equiv \frac{1}{2}, \quad T_x \equiv T_y \equiv 0, \\
 L_z &= -\cos 2\theta, \quad L_x = \sin 2\theta, \quad L_y \equiv 0.
 \end{aligned}
 \tag{IV.36}$$

In phase (IV), cuts as a function of the bias  $\Delta_B$  at any value of the magnetic field hence trace the rotation of the orbital isospin vector to the fully antiferromagnetically polarised state in orbital space.

#### Phase (V): Polarised in Spin and Valley, Anti-Polarised Orbital Spin

For sufficiently large values of the bias, we find the limiting case for the ground state to be fully polarised in spin and valley isospin, but antiferromagnetically polarised in the orbital degree of freedom. The ground state phase turns into

$$|GS\rangle = |0, \uparrow, +\rangle, \tag{IV.37}$$

with the properties

$$\begin{aligned}
 S_z &\equiv \frac{1}{2}, \quad S_x \equiv S_y \equiv 0, \\
 T_z &\equiv \frac{1}{2}, \quad T_x \equiv T_y \equiv 0, \\
 L_z &\equiv -\frac{1}{2}, \quad L_x \equiv L_y \equiv 0.
 \end{aligned} \tag{IV.38}$$

Phase (V) hence stabilised at fully polarised spin and valley isospin, while the orbital spin is fully anti-polarised.

### Analytic Description of the Phase Boundaries

At  $\nu = -3$ , all phases transform into one another via smooth rotations of the respective isospin degrees of freedom. All phase transitions in the  $\nu = -3$  phase diagram are of second order.

Analytic expressions for the biases where phase transitions occur can be obtained by considering the respective limits of the optimal canting angles  $\theta$  that define the boundaries of the phases. We give the critical biases at which transitions between the different phases occur:

(II)  $\longrightarrow$  (III):

$$\Delta_{B,eff}^{crit} = \frac{-\alpha d - \Delta_{1111} \ell_B + \ell_B X_{1111}}{\ell_B (z - 1)} \tag{IV.39}$$

(III)  $\longrightarrow$  (IV):

$$\Delta_{B,eff}^{crit} = \frac{2}{z} (\Delta_{0011} + \Delta_{01} + \Delta_{1001} - \Delta_{1111}) \tag{IV.40}$$

(IV)  $\longrightarrow$  (V):

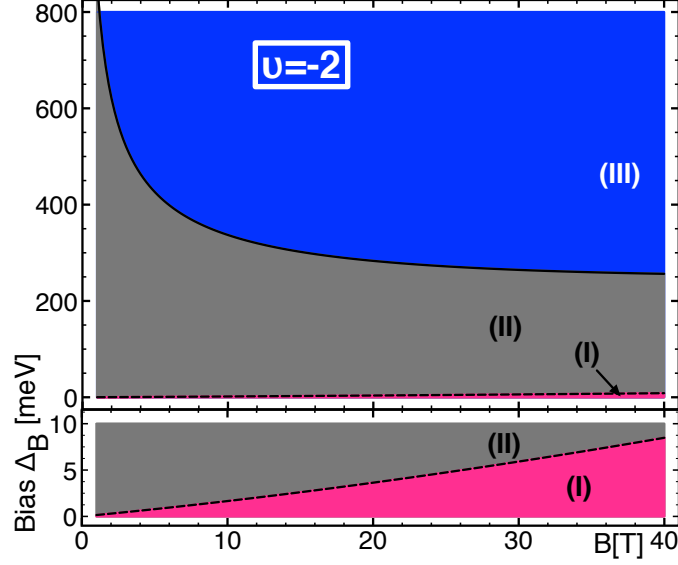
$$\Delta_{B,eff}^{crit} = \frac{2}{z} (\Delta_{0000} - \Delta_{0011} + \Delta_{01} - \Delta_{1001}) \tag{IV.41}$$

### ★ Two Electrons: $\nu = -2$

When there are two electrons per state within the octet, the ground state structure of the system is the following:

#### Phase (I): Rotation of the Valley Isospin

For small values of the bias,  $\Delta_B < \Delta_B^{crit}$ , the ground state is partially polarised in the spin, whereas the valley isospin is canted and the orbital isospin is ordered in


**Figure IV.5**

Phase diagram of the  $\nu = -2$  ground state as yielded by the Hartree Fock analysis. There are three different phases emerging, labelled (I), (II), and (III). Figure from reference [Knothe and Jolicœur, 2016].

an antiferromagnetic fashion.

This phase is characterised by the two vectors

$$\begin{aligned} |v_1\rangle &= \cos \theta |1, \uparrow, +\rangle + \sin \theta |1, \uparrow, -\rangle, \\ |v_2\rangle &= \cos \theta |0, \uparrow, +\rangle + \sin \theta |0, \uparrow, -\rangle, \end{aligned} \quad (\text{IV.42})$$

where optimal angle is determined by

$$\cos 2\theta_I = \frac{\Delta_{B,eff} \ell_B (z-2)}{-4\alpha d - \Delta_{0000} \ell_B - 2\Delta_{0011} \ell_B - \Delta_{1111} \ell_B + \ell_B X_{0000} + 2\ell_B X_{0011} + \ell_B X_{1111}}. \quad (\text{IV.43})$$

Therefore, we find for the spin and isospin components:

$$\begin{aligned} S_z &\equiv 1, \quad S_x \equiv S_y \equiv 0, \\ T_z &= -\cos 2\theta, \quad T_x = \sin 2\theta, \quad T_y \equiv 0, \\ L_z &\equiv \frac{1}{2}, \quad L_x \equiv L_y \equiv 0. \end{aligned} \quad (\text{IV.44})$$

Hence, in this phase, cuts along lines of increasing bias  $\Delta_B$ , for any strength of the magnetic field  $B$ , correspond to a rotation of the valley isospin vector from a configuration in the  $\{x-y\}$ -plane to fully aligned along the  $z$ -axis.

### Phase (II): Polarised in Spin and Valley Isospin

Within an intermediate range of the bias  $\Delta_B$ , the ground state is a fully polarised ferromagnet in spin and valley isospin. The orbital isospin degree of freedom,

however, is in an antiferromagnetic configuration, yielding zero overall orbital polarisation.

The ground state of the phase is described by state vectors of the form

$$\begin{aligned} |v_1\rangle &= |1, \uparrow, +\rangle \\ |v_2\rangle &= |0, \uparrow, +\rangle. \end{aligned} \quad (\text{IV.45})$$

We hence find for the the spin and isospin properties

$$\begin{aligned} S_z &\equiv 1, \quad S_x \equiv S_y \equiv 0, \\ T_z &\equiv 1, \quad T_x \equiv T_y \equiv 0, \\ L_z &\equiv L_x \equiv L_y \equiv 0, \end{aligned} \quad (\text{IV.46})$$

which implies, we observe a stable phase in which both, the spin and the valley isospin are fully aligned along the  $z$ -axis.

### Phase (III): Polarised Valley, Anti-Polarised Orbital Isospin

In the limit of a sufficiently large bias  $\Delta_B$ , we find the ground state to be an antiferromagnet in spin. The valley isospin is fully polarised, whereas the orbital isospin turns out to be fully antiferromagnetically polarised.

The ground state is given by

$$\begin{aligned} |v_1\rangle &= |0, \uparrow, +\rangle \\ |v_2\rangle &= |0, \downarrow, +\rangle, \end{aligned} \quad (\text{IV.47})$$

and exhibits the spin and isospin properties

$$\begin{aligned} S_z &\equiv S_x \equiv S_y \equiv 0, \\ T_z &\equiv 1, \quad T_x \equiv T_y \equiv 0, \\ L_z &\equiv -1, \quad L_x \equiv L_y \equiv 0, \end{aligned} \quad (\text{IV.48})$$

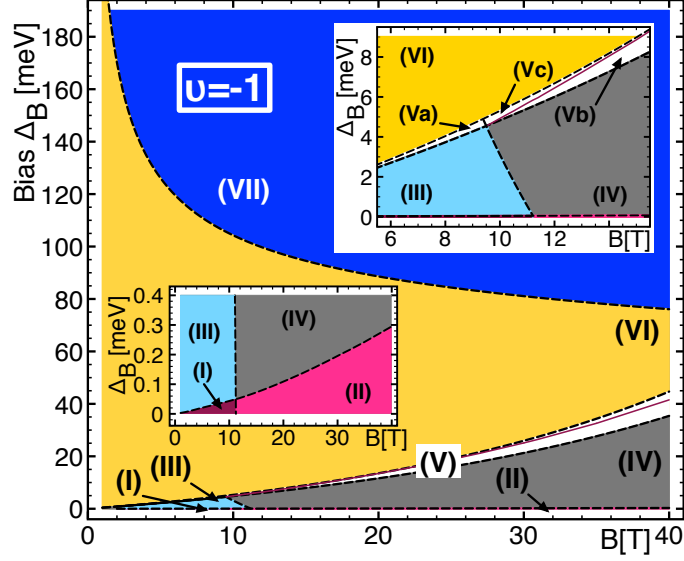
hence describing a state with zero total spin, which is fully polarised in the valley isospin and fully anti-polarised in the orbital isospin degree of freedom.

### Analytic Description of the Phase Boundaries

At filling factor  $\nu = -2$ , we observe two different types of phase transitions: going from phase (I) to phase (II) is achieved by a smooth rotation of the valley isospin. This is a second order transition. From phase (II) to phase (III), however, the system undergoes jumps in the spin and the orbital isospin degree of freedom, which

**Figure IV.6**

Phase diagram of the  $\nu = -1$  ground state as yielded by Hartree Fock analysis. There are nine different phases emerging, labelled (I)-(IV), (Va,b,c), (VI), and (VII). Figure from reference [Knothe and Jolicœur, 2016].



characterises a discontinuous first order phase transition.

We give the critical biases at which transitions between the different phases occur.

(I)  $\rightarrow$  (II) second order transition:

$$\Delta_{B,eff}^{crit} = \frac{-4\alpha d - \Delta_{0000}\ell_B - 2\Delta_{0011}\ell_B - \Delta_{1111}\ell_B + \ell_B X_{0000} + 2\ell_B X_{0011} + \ell_B X_{1111}}{\ell_B(z-2)}. \quad (\text{IV.49})$$

(II)  $\rightarrow$  (III) first order transition:

The ground state of phase (II) is lower in energy than the phase (III) ground state up to a critical bias

$$\Delta_{B,eff}^{crit} = \frac{1}{z}(\Delta_{0000} - 2\Delta_{0011} + 2\Delta_{01} - \Delta_{1111} + 2\Delta_Z). \quad (\text{IV.50})$$

### ★ Three Electrons: $\nu = -1$

When there are three electrons in the system, we find the following ground state structure:

#### Unbiased case $\Delta_B \equiv 0$ ; Evolution as a Function of $B$

At zero bias, the ground state is a fully polarised spin ferromagnet, while its valley isospin lies in the  $\{x-y\}$ -plane, and the orbital isospin is canted in an orbital coher-

ent phase.

The ground state configuration for the three electrons is given by

$$\begin{aligned}
 |v_1\rangle &= -\frac{1}{\sqrt{2}} \left[ |1, \uparrow, +\rangle + |1, \uparrow, -\rangle \right], \\
 |v_2\rangle &= \frac{1}{\sqrt{2}} \left[ |0, \uparrow, +\rangle + |0, \uparrow, -\rangle \right], \\
 |v_3\rangle &= -\frac{1}{\sqrt{2}} \sin \theta_0 \left[ |1, \uparrow, +\rangle - |1, \uparrow, -\rangle \right] - \frac{1}{\sqrt{2}} \cos \theta_0 \left[ |0, \uparrow, +\rangle - |0, \uparrow, -\rangle \right], \quad (\text{IV.51})
 \end{aligned}$$

where the optimal angle in orbital space  $\theta_0$ , as shown in figure IV.15, varies as a function of  $B$  between  $\theta_0 \rightarrow \frac{\pi}{4}$  at vanishing magnetic field  $B \rightarrow 0$  and  $\theta_0 = \frac{\pi}{2}$  at sufficiently high magnetic field strengths above a certain critical value  $B_{crit} \approx 11.3$  T. This angle fulfils the relation

$$\cos 2\theta_0 = \frac{-3\Delta_{0000} - 4\Delta_{01} + 3\Delta_{1111} + X_{0000} - X_{1111}}{\Delta_{0000} - 2(\Delta_{0011} + \Delta_{1001}) + \Delta_{1111} + X_{0000} - 2(X_{0011} + X_{1001}) + X_{1111}}. \quad (\text{IV.52})$$

The state exhibits the properties

$$\begin{aligned}
 S_z &\equiv \frac{3}{2}, \quad S_x \equiv S_y \equiv 0, \\
 T_z &= 0, \quad T_x \equiv \frac{1}{2}, \quad T_y \equiv 0, \\
 L_z &= -\cos 2\theta, \quad L_x = \sin 2\theta, \quad L_y \equiv 0. \quad (\text{IV.53})
 \end{aligned}$$

Along the line of zero bias, as a function of the magnetic field strength  $B$ , the ground state hence undergoes a transition from a canted state in the orbital isospin to a partially polarised state  $\mathbf{L} = \frac{1}{2}\mathbf{e}_z$ .

### Phases (I) and (II): Rotation of the Valley Isospin at either Canted or Partially Aligned Orbital Isospin

In the regime of very small bias  $\Delta_B$ , we find a rotation of the valley isospin at either canted or partially aligned orbital isospin, respectively. In both, phases (I) and (II), the ground state is a fully polarised spin ferromagnet. The valley isospin assumes non-trivial configurations  $0 \leq T_x, T_z \leq 1, T_y \equiv 0$ . Phase (I) occurs for sufficiently small values of the magnetic field,  $B < B_{crit}$ ; the corresponding ground state is given by an involved superposition of different single particle states which leads to a non-trivial isospin configuration. In phase (II), however, *i.e.*, at field values above the critical magnetic field, we can describe the valley isospin in simple

terms with the valley canting angle  $\theta$  as the only parameter.

These phases are characterised by the non-trivial combinations

Phase (I):

$$\begin{aligned}
 |v_1\rangle &= -a_1|1, \uparrow, +\rangle - a_2|1, \uparrow, -\rangle + b_1|0, \uparrow, +\rangle + b_2|0, \uparrow, -\rangle, \\
 |v_2\rangle &= b_1|1, \uparrow, +\rangle + b_2|1, \uparrow, -\rangle + a_1|0, \uparrow, +\rangle + a_2|0, \uparrow, -\rangle, \\
 |v_3\rangle &= c_1|1, \uparrow, +\rangle - c_2|1, \uparrow, -\rangle - c_3|0, \uparrow, +\rangle + c_4|0, \uparrow, -\rangle,
 \end{aligned} \tag{IV.54}$$

Phase (II):

$$\begin{aligned}
 |v_1\rangle &= -a_1|1, \uparrow, +\rangle - a_2|1, \uparrow, -\rangle, \\
 |v_2\rangle &= a_1|0, \uparrow, +\rangle + a_2|0, \uparrow, -\rangle, \\
 |v_3\rangle &= a_2|1, \uparrow, +\rangle - a_1|1, \uparrow, -\rangle,
 \end{aligned} \tag{IV.55}$$

with coefficients  $a_i, b_i, c_i > 0$  varying as functions of  $\Delta_B$  and  $B$ .

In phase (II), we can set  $a_1 = \cos \theta$  and  $a_2 = \sin \theta$  and determine the optimal angle to be

$$\cos 2\theta_{(II)} = \frac{\Delta_{B,eff}\ell_B}{\alpha d + \ell_B(\Delta_{0000} - X_{0000})}. \tag{IV.56}$$

For the phases (I) and (II) we find the following spin and isospin structure, respectively:

Phase (I):

$$\begin{aligned}
 S_z &= \frac{3}{2}, \quad S_x \equiv S_y \equiv 0, \\
 T_z &= a_1^2 - a_2^2 + b_1^2 - b_2^2 + \frac{1}{2}(c_1^2 - c_2^2 + c_3^2 - c_4^2), \\
 T_x &= 2a_1a_2 + 2b_1b_2 - (c_1c_2 + c_3c_4), \\
 T_y &\equiv 0, \\
 L_z &= \frac{1}{2}(c_1^2 + c_2^2 - c_3^2 - c_4^2), \\
 L_x &= -(c_1c_3 + c_2c_4), \\
 L_y &\equiv 0,
 \end{aligned} \tag{IV.57}$$

and phase (II):

$$\begin{aligned} S_z &= \frac{3}{2}, S_x \equiv S_y \equiv 0, \\ T_z &= a_1^2 - a_2^2 = \cos 2\theta, T_x = a_1 a_2 = \sin 2\theta, T_y \equiv 0, \\ L_z &= \frac{1}{2}, L_x \equiv L_y \equiv 0. \end{aligned}$$

The orbital isospin in phase (I) is in a canted configuration,  $0 \leq L_x, L_z \leq 1, L_y \equiv 0$ , whereas phase (II) is partially polarized in orbital space.

Hence, in phase (I) and (II), cuts along lines of increasing bias  $\Delta_B$  for any strength of the magnetic field  $B$  correspond to a rotation of the valley isospin vector from a configuration in the  $\{x-y\}$ -plane to a state fully aligned along the  $z$ -axis. At the same time, increasing  $B$  at a fixed value of the bias  $\Delta_B$  corresponds to rotating the orbital isospin from a canted configuration in phase (I) to a partly polarised configuration,  $\mathbf{L} = \frac{1}{2}\mathbf{e}_z$ , in phase (II).

### Phase (III) and (IV): Spin and Valley Ferromagnet, Rotation in the Orbital Isospin

At larger values of the bias  $\Delta_B$  we find pendants of phase (I) and (II), now at polarised configurations of the valley isospin: in this case, the ground state is a fully polarised spin ferromagnet and a partially polarised valley isospin, while the orbital isospin degree of freedom again varies as function of the bias  $\Delta_B$  and the magnetic field strength  $B$ .

The ground state of phase (III) is given by state vectors of the form

$$\begin{aligned} |v_1\rangle &= |1, \uparrow, +\rangle, \\ |v_2\rangle &= |0, \uparrow, +\rangle, \\ |v_3\rangle &= \cos \theta |1, \uparrow, -\rangle + \sin \theta |0, \uparrow, -\rangle, \end{aligned} \quad (\text{IV.58})$$

with the optimal angle determined by

$$\cos 2\theta_{(\text{III})} = \frac{\Delta_{0000} + 2\Delta_{01} - \Delta_{1111} + z\Delta_{B,eff}}{\Delta_{0000} - 2(\Delta_{0011} + \Delta_{1001}) + \Delta_{1111}}. \quad (\text{IV.59})$$

Therefore, the the following spin and isospin properties characterise phase (III):

$$\begin{aligned} S_z &\equiv \frac{3}{2}, S_x \equiv S_y \equiv 0, \\ T_z &= \frac{1}{2}, T_x \equiv T_y \equiv 0, \\ L_z &= \frac{1}{2} \cos 2\theta, L_x = \frac{1}{2} \sin 2\theta, L_y \equiv 0. \end{aligned} \quad (\text{IV.60})$$

This optimal canting angle of the orbital isospin varies as function of the bias  $\Delta_B$  and the magnetic field strength  $B$ ; at any value of  $\Delta_B$ , when  $B$  increases, the angle rotates until it reaches zero; this leads to a phase which is partially polarised in the orbital isospin.

Phase (IV):

$$\begin{aligned} |v_1\rangle &= |1, \uparrow, +\rangle, \\ |v_2\rangle &= |0, \uparrow, +\rangle, \\ |v_3\rangle &= |1, \uparrow, -\rangle, \end{aligned} \quad (\text{IV.61})$$

exhibiting the properties

$$\begin{aligned} S_z &\equiv \frac{3}{2}, \quad S_x \equiv S_y \equiv 0, \\ T_z &= \frac{1}{2}, \quad T_x \equiv T_y \equiv 0, \\ L_z &= \frac{1}{2}, \quad L_x \equiv L_y \equiv 0. \end{aligned} \quad (\text{IV.62})$$

Hence, increasing the magnetic field strength  $B$  corresponds to rotating the orbital isospin from a canted configuration in phase (III) to a partially polarised state  $\mathbf{L} = \frac{1}{2}\mathbf{e}_z$  in phase (IV). Both the spin and the valley isospin vectors remain constant in these phases for all values of  $\Delta_B$  and  $B$ .

### Phase (V): Evolution of all Spins and Isospins

A narrow transition regime is established with complex behaviour of the ground state configuration. All spin and isospin degrees of freedom take nontrivial values and evolve as functions of  $\Delta_B$  and  $B$ . In general, the ground state within this parameter regime is described by the vectors

$$\begin{aligned} |v_1\rangle &= |1, \uparrow, +\rangle \\ |v_2\rangle &= |0, \uparrow, +\rangle, \\ |v_3\rangle &= c_1|1, \uparrow, -\rangle + c_2|1, \downarrow, +\rangle - c_3|0, \uparrow, -\rangle - c_4|0, \downarrow, +\rangle, \end{aligned} \quad (\text{IV.63})$$

leading to spin and isospin properties

$$\begin{aligned} S_z &= 1 + \frac{1}{2}(c_1^2 - c_2^2 + c_3^2 - c_4^2), \quad S_x \equiv S_y \equiv 0, \\ T_z &= 1 - \frac{1}{2}(c_1^2 - c_2^2 + c_3^2 - c_4^2), \quad T_x \equiv T_y \equiv 0, \\ L_z &= \frac{1}{2}(c_1^2 + c_2^2 - c_3^2 - c_4^2), \quad L_x = -(c_1c_3 + c_2c_4), \quad L_y \equiv 0. \end{aligned} \quad (\text{IV.64})$$

Within the parameter range of phase (V) one can distinguish between the following regimes:

-Phase (Va):

For  $B < B_{crit}$ , all four entries  $c_i \neq 0$  evolve smoothly as functions of the bias  $\Delta_B$  and the magnetic field strength  $B$ . For increasing  $\Delta_B$  across phase (Va), this leads to smooth evolutions of the spin and valley isospins from  $S_z = \frac{3}{2}$  to  $S_z = \frac{1}{2}$  and from  $T_z = \frac{1}{2}$  to  $T_z = \frac{3}{2}$ , respectively, accompanied by kinks in the orbital isospin components which are nonzero within this range:  $0 < L_z < \frac{1}{2}$  and  $0 < L_x < \frac{1}{2}$ .

-Phases (Vb) and (Vc):

For  $B > B_{crit}$ , two competing transitions occur within the parameter range of phase (V): there is a smooth evolution of  $S_z$  and  $T_z$  as in the former case; It is governed by smoothly evolving entries  $c_1$  and  $c_2$  while  $c_3 \equiv c_4 \equiv 0$  (this entails within this regime  $L_x \equiv 0$  and  $L_z \equiv \frac{1}{2}$  fixed by normalisation). At a sufficiently high value of  $\Delta_B$ , eventually,  $c_4$  jumps to a nonzero value, thereby inducing nonzero values of  $L_z$  and  $L_x$  and nontrivial evolutions of all spin and isospin degrees of freedom.

### Phase (VI): Rotation of the Orbital Isospin

This phase occupies a wide parameter range including all magnetic field strengths and intermediate values of the bias  $\Delta_B$ . While the spin is partially polarised and the valley isospin is fully polarised, the orbital isospin is in a canted configuration.

The electrons occupy the states

$$\begin{aligned} |v_1\rangle &= |1, \uparrow, +\rangle \\ |v_2\rangle &= |0, \uparrow, +\rangle, \\ |v_3\rangle &= \cos \theta |1, \downarrow, +\rangle - \sin \theta |0, \downarrow, +\rangle, \end{aligned} \quad (\text{IV.65})$$

under the optimal angle

$$\cos 2\theta_{(\text{VI})} = \frac{\Delta_{0000} + 2\Delta_{01} - \Delta_{1111} - z\Delta_{B\text{eff}}}{\Delta_{0000} - 2(\Delta_{0011} + \Delta_{1001}) + \Delta_{1111}}, \quad (\text{IV.66})$$

resulting in the spin and isospin properties

$$\begin{aligned} S_z &\equiv \frac{1}{2}, \quad S_x \equiv S_y \equiv 0, \\ T_z &= \frac{3}{2}, \quad T_x \equiv T_y \equiv 0, \\ L_z &= \cos 2\theta, \quad L_x = \sin 2\theta, \quad L_y \equiv 0. \end{aligned} \quad (\text{IV.67})$$

Hence, for any value of the magnetic field  $B$ , with rising bias  $\Delta_B$ , the orbital isospin performs a rotation to a partially antiferromagnetically polarised configuration along the  $z$ -axis:  $\mathbf{L} \rightarrow -\frac{1}{2}\mathbf{e}_z$ .

### Phase (VII): Polarised in Spin and Valley, Partially Anti-Polarised Orbital Isospin

For sufficiently large values of the bias, the ground state phase eventually reaches a configuration which is partially polarised in spin, fully polarised in the valley isospin, and partially antiferromagnetically polarised in the orbital isospin degree of freedom.

The ground state phase is in the configuration

$$\begin{aligned} |v_1\rangle &= |1, \uparrow, +\rangle \\ |v_2\rangle &= |0, \uparrow, +\rangle, \\ |v_3\rangle &= |0, \downarrow, +\rangle, \end{aligned} \quad (\text{IV.68})$$

hence exhibiting

$$\begin{aligned} S_z &\equiv \frac{1}{2}, \quad S_x \equiv S_y \equiv 0, \\ T_z &\equiv \frac{3}{2}, \quad T_x \equiv T_y \equiv 0, \\ L_z &\equiv -\frac{1}{2}, \quad L_x \equiv L_y \equiv 0, \end{aligned} \quad (\text{IV.69})$$

which means phase (VII) eventually stabilised an aligned spin and valley isospin configuration, while the orbital isospin is anti-aligned along the  $z$ -axis.

### Analytic Description of the Phase Boundaries

Except for the transition regime of phase (V) described above, all phase transitions of the  $\nu = -1$  phase diagram go along with smooth rotations of the respective isospin vectors and therefore are of second order. The most prominent transitions occur at the following critical values of the bias:

(II)  $\longrightarrow$  (IV):

$$\Delta_{B,eff}^{crit} = \frac{\alpha d + \Delta_{0000}\ell_B - \ell_B X_{0000}}{\ell_B} \quad (\text{IV.70})$$

(III)  $\longrightarrow$  (IV):

$$\Delta_{B,eff}^{crit} = -\frac{2}{z}(\Delta_{0011} + \Delta_{01} + \Delta_{1001} - \Delta_{1111}) \quad (\text{IV.71})$$

(IV)  $\longrightarrow$  (Vb):

$$\Delta_{B,eff}^{crit} = \frac{-\alpha d + \Delta_{1111}\ell_B - \Delta_Z\ell_B - \ell_B X_{1111}}{\ell_B(z-1)} \quad (\text{IV.72})$$

(Vb)  $\longrightarrow$  (Vc):

$$\begin{aligned} \Delta_{B,eff}^{crit} = & \frac{1}{4\ell_B(2z \cos 2\theta_{Vb} - 2 \cos 2\theta_{Vb} + z \cos 2\theta_{Vc} + z - 2)} \\ & \left[ -18\alpha d - 16\alpha d \cos 2\theta_{Vb} + 2\alpha d \cos 4\theta_{Vb} - 3\Delta_{0000}\ell_B - 2\Delta_{0011}\ell_B \right. \\ & - 8\Delta_{01}\ell_B - 2\Delta_{1001}\ell_B + 3\Delta_{1111}\ell_B - 8\Delta_Z\ell_B + 2\Delta_{1111}\ell_B \cos 4t \\ & - 8\Delta_Z\ell_B \cos 2\theta_{Vb} - 2\ell_B X_{1111} \cos 4\theta_{Vb} + 4\Delta_{0000}\ell_B \cos 2\theta_{Vc} \\ & - \Delta_{0000}\ell_B \cos 4\theta_{Vc} + 2\Delta_{0011}\ell_B \cos 4\theta_{Vc} + 8\Delta_{01}\ell_B \cos 2\theta_{Vc} \\ & \left. + 2\Delta_{1001}\ell_B \cos 4\theta_{Vc} - 4\Delta_{1111}\ell_B \cos 2\theta_{Vc} - \Delta_{1111}\ell_B \cos 4\theta_{Vc} + 2\ell_B X_{1111} \right] \end{aligned} \quad (\text{IV.73})$$

(VI)  $\longrightarrow$  (VII):

$$\Delta_{B,eff}^{crit} = \frac{2}{z}(\Delta_{0000} - \Delta_{0011} + \Delta_{01} - \Delta_{1001}) \quad (\text{IV.74})$$

★ **Four Electrons:**  $\nu = 0$

The bilayer graphene system is charge neutral when there are four electrons per state occupying exactly half of the states within the octet. For this configuration of half filling we find the following different ground state phases:

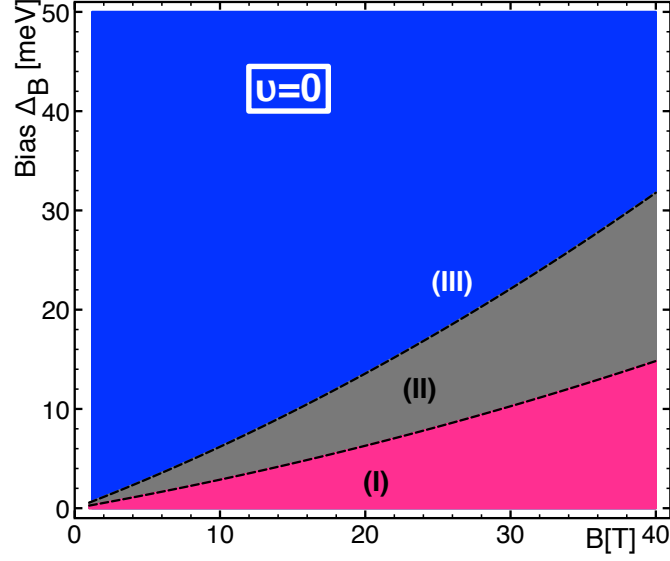
**Phase (I): Spin Ferromagnet**

For the unbiased scenario as well as for sufficiently small values of the bias  $\Delta_B$  the ground state is a fully polarised spin ferromagnet, while it is an antiferromagnet both in valley and in orbital space, leading to vanishing overall valley and orbital polarisation. The four electrons in the ground state occupy the states

$$\begin{aligned} |v_1\rangle &= |1, \uparrow, +\rangle, \\ |v_2\rangle &= |1, \uparrow, -\rangle, \\ |v_3\rangle &= |0, \uparrow, +\rangle, \\ |v_4\rangle &= |0, \uparrow, -\rangle. \end{aligned} \quad (\text{IV.75})$$

The total state is then a spin ferromagnet:

$$\begin{aligned} S_z &\equiv 2, \quad S_x \equiv S_y \equiv 0, \\ T_z &\equiv T_x \equiv T_y \equiv 0, \\ L_z &\equiv L_x \equiv L_y \equiv 0. \end{aligned} \quad (\text{IV.76})$$


**Figure IV.7**

Phase diagram of the  $\nu = 0$  ground state obtained from Hartree Fock analysis. There are three different phases, labelled (I), (II), and (III). Figure from reference [Knothe and Jolicœur, 2016] (edited).

### Phase (II): Evolution of Spin and Valley Isospin

For all magnetic field strengths and in an intermediate regime of the bias, the spin and the valley isospin undergo an evolution when varying  $\Delta_B$  and  $B$  as a function of one common angle  $\theta$ . The ground state of the phase is described by state vectors of the form

$$\begin{aligned}
 |v_1\rangle &= |1, \uparrow, +\rangle, \\
 |v_2\rangle &= \cos \theta |1, \uparrow, -\rangle + \sin \theta |1, \downarrow, +\rangle, \\
 |v_3\rangle &= |0, \uparrow, +\rangle, \\
 |v_4\rangle &= \cos \theta |0, \uparrow, -\rangle + \sin \theta |0, \downarrow, +\rangle.
 \end{aligned} \tag{IV.77}$$

The optimal angle is determined by

$$\cos 2\theta_{(II)} = \frac{4\alpha d + 2\Delta_Z \ell_B + \Delta_{B\text{eff}} \ell_B (z - 2)}{4\alpha d + \ell_B (\Delta_{0000} + 2\Delta_{0011} + \Delta_{1111} - X_{0000} - 2X_{0011} - X_{1111})}, \tag{IV.78}$$

yielding for the total spin and isospin properties

$$\begin{aligned}
 S_z &= 2 \cos^2 \theta, \quad S_x \equiv S_y \equiv 0, \\
 T_z &= 2 \sin^2 \theta, \quad T_x \equiv T_y \equiv 0, \\
 L_z &\equiv L_x \equiv L_y \equiv 0.
 \end{aligned} \tag{IV.79}$$

Hence, for a given value of the magnetic field  $B$ , upon increasing the bias  $\Delta_B$  over the parameter range of phase (II), the total spin evolves from a fully aligned state

to a state with zero total spin, while, contrarily, the total valley isospin evolves from zero to fully polarised valley ferromagnet state:  $\mathbf{S} = 2\mathbf{e}_z \rightarrow \mathbf{S} \equiv 0$ ,  $\mathbf{T} \equiv 0 \rightarrow \mathbf{T} = 2\mathbf{e}_z$ .

### Phase (III): Valley Isospin Ferromagnet

For sufficiently large values of the bias  $\Delta_B$  the ground state assumes antiferromagnetic order in both the spin space and in the space of the orbital isospin, while being a fully polarised ferromagnet in valley space. The ground state configuration of the single electrons turns into

$$\begin{aligned} |v_1\rangle &= |1, \uparrow, +\rangle, \\ |v_2\rangle &= |1, \downarrow, +\rangle, \\ |v_3\rangle &= |0, \uparrow, +\rangle, \\ |v_4\rangle &= |0, \downarrow, +\rangle, \end{aligned} \quad (\text{IV.80})$$

which represents a ferromagnetic state in valley space:

$$\begin{aligned} S_z &\equiv S_x \equiv S_y \equiv 0, \\ T_z &\equiv 2, \quad T_x \equiv T_y \equiv 0, \\ L_z &\equiv L_x \equiv L_y \equiv 0. \end{aligned} \quad (\text{IV.81})$$

### Analytic Description of the Phase Boundaries

The transitions between the different ground state phases of  $\nu = 0$  are all characterised by smooth rotations of the isospin degrees of freedom indicating continuous second order transitions.

We give the critical biases at which transitions between the different phases occur:

(I)  $\rightarrow$  (II):

$$\Delta_{B,eff}^{crit} = \frac{\Delta_{0000} + 2\Delta_{0011} + \Delta_{1111} - 2\Delta_Z - X_{0000} - 2X_{0011} - X_{1111}}{z - 2}. \quad (\text{IV.82})$$

(II)  $\rightarrow$  (III):

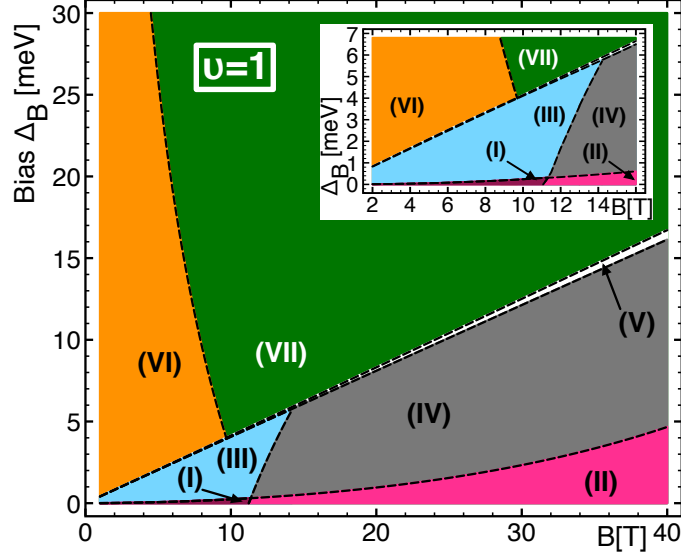
$$\Delta_{B,eff}^{crit} = \frac{\ell_B(-\Delta_{0000} - 2\Delta_{0011} - \Delta_{1111} - 2\Delta_Z + X_{0000} + 2X_{0011} + X_{1111}) - 8\alpha d}{\ell_B(z - 2)}. \quad (\text{IV.83})$$

### ★ Five Electrons: $\nu = 1$

For the case of five electrons we identify the following ground state structure:

**Figure IV.8**

Phase diagram of the  $\nu = 1$  ground state obtained from Hartree Fock analysis. There are different phases emerging, labelled (I)-(VII). Figure from reference [Knothe and Jolicœur, 2016].



#### Bias $\Delta_B \equiv 0$ ; Evolution as a Function of $B$

At zero bias, we find a ground state configuration in which the spin is partially polarised, while the valley isospin vector lies in the  $\{x-y\}$ -plane. The orbital isospin assumes a canted configuration, thus exhibiting non-trivial orbital coherence. The ground state structure for the five electrons is given by

$$\begin{aligned}
 |v_1\rangle &= |1, \uparrow, +\rangle, \\
 |v_2\rangle &= |1, \uparrow, -\rangle, \\
 |v_3\rangle &= |0, \uparrow, +\rangle, \\
 |v_4\rangle &= |0, \uparrow, -\rangle, \\
 |v_5\rangle &= \frac{1}{\sqrt{2}} \cos \theta_0 \left[ |1, \downarrow, +\rangle + |1, \downarrow, -\rangle \right] + \frac{1}{\sqrt{2}} \sin \theta_0 \left[ |0, \downarrow, +\rangle - |0, \downarrow, -\rangle \right], \quad (\text{IV.84})
 \end{aligned}$$

where the optimal angle  $\theta_0$ , as shown in figure IV.15, varies as a function of  $B$  between  $\theta_0 \rightarrow \frac{\pi}{4}$  at vanishing magnetic field  $B \rightarrow 0$  and  $\theta_0 = 0$  at sufficiently high magnetic field strengths above a certain critical value  $B_{crit} \approx 11$  T. This angle fulfils the relation

$$\cos \theta_0 = \frac{\sqrt{\Delta_{0000} - \Delta_{0011} + 2\Delta_{01} - \Delta_{1001} + X_{0000} - X_{0011} - X_{1001}}}{\sqrt{\Delta_{0000} - 2\Delta_{0011} - 2\Delta_{1001} + \Delta_{1111} + X_{0000} - 2X_{0011} - 2X_{1001} + X_{1111}}}. \quad (\text{IV.85})$$

The state exhibits the properties

$$\begin{aligned}
 S_z &\equiv \frac{3}{2}, \quad S_x \equiv S_y \equiv 0, \\
 T_z &= 0, \quad T_x \equiv \frac{1}{2}, \quad T_y \equiv 0, \\
 L_z &= \cos 2\theta, \quad L_x = \sin 2\theta, \quad L_y \equiv 0.
 \end{aligned} \tag{IV.86}$$

Along the line of zero bias, as a function of the magnetic field strength  $B$ , the ground state hence undergoes a transition from a canted state in the orbital isospin to a partially polarised state  $\mathbf{L} = \frac{1}{2}\mathbf{e}_z$ .

### Phases (I) and (II): Rotation of the Valley Isospin at either Canted or Partially Polarised Orbital Isospin

At small values of the bias  $\Delta_B$ , these phases are in a partially polarised spin state, while the valley isospin takes non-trivial values  $0 \leq T_x, T_z \leq 1$ . Meanwhile, the orbital isospin is either in canted configuration with  $0 \leq L_x, L_z \leq 1$  (phase I, for sufficiently small values of the magnetic field) or is partially polarised (phase II, above some critical magnetic field strength). The former case being more involved, in the latter phase (II) we find a single parameter dependence of the states' configuration with one optimal angle  $\theta$ . These phases are characterised by the non-trivial combinations

Phase (I):

$$\begin{aligned}
 |v_1\rangle &= |1, \uparrow, +\rangle, \\
 |v_2\rangle &= |1, \uparrow, -\rangle, \\
 |v_3\rangle &= |0, \uparrow, +\rangle, \\
 |v_4\rangle &= |0, \uparrow, -\rangle, \\
 |v_5\rangle &= a_1|1, \downarrow, +\rangle + a_2|1, \downarrow, -\rangle - a_3|0, \downarrow, +\rangle - a_4|0, \downarrow, -\rangle,
 \end{aligned} \tag{IV.87}$$

Phase (II):

$$\begin{aligned}
 |v_1\rangle &= |1, \uparrow, +\rangle, \\
 |v_2\rangle &= |1, \uparrow, -\rangle, \\
 |v_3\rangle &= |0, \uparrow, +\rangle, \\
 |v_4\rangle &= |0, \uparrow, -\rangle, \\
 |v_5\rangle &= a_1|1, \downarrow, +\rangle + a_2|1, \downarrow, -\rangle,
 \end{aligned} \tag{IV.88}$$

with coefficients  $a_i > 0$  varying as functions of  $\Delta_B$  and  $B$ .

In phase (II), we can set  $a_1 = \cos \theta$  and  $a_2 = \sin \theta$  and determine the optimal angle to be

$$\cos 2\theta_{(II)} = \frac{\Delta_{B,eff} \ell_B (z-1)}{\ell_B (X_{1111} - \Delta_{1111}) - \alpha d}, \quad (IV.89)$$

governing the canting in valley space.

For the phases (I) and (II) we find the following spin and isospin structure, respectively:

Phase (I):

$$\begin{aligned} S_z &= \frac{3}{2}, \quad S_x \equiv S_y \equiv 0, \\ T_z &= \frac{1}{2}(a_1^2 - a_2^2 + a_3^2 - a_4^2), \\ T_x &= a_1 a_2 + a_3 a_4, \\ T_y &\equiv 0, \\ L_z &= \frac{1}{2}(c_1^2 + c_2^2 - c_3^2 - c_4^2), \\ L_x &= -(c_1 c_3 + c_2 c_4), \\ L_y &\equiv 0, \end{aligned} \quad (IV.90)$$

Phase (II):

$$\begin{aligned} S_z &= \frac{3}{2}, \quad S_x \equiv S_y \equiv 0, \\ T_z &= \frac{1}{2}(a_1^2 - a_2^2) = \cos 2\theta, \quad T_x = a_1 a_2 = \sin 2\theta, \quad T_y \equiv 0, \\ L_z &= \frac{1}{2}, \quad L_x \equiv L_y \equiv 0. \end{aligned}$$

Hence, in phase (I) and (II), cuts along lines of increasing bias  $\Delta_B$  for any strength of the magnetic field  $B$  correspond to a rotation of the valley isospin vector from a configuration in the  $\{x-y\}$ -plane to a state aligned along the  $z$ -axis:  $\mathbf{T} = \frac{1}{2}\mathbf{e}_x \rightarrow \mathbf{T} = \frac{1}{2}\mathbf{e}_z$ . At the same time, increasing  $B$  at a fixed value of the bias  $\Delta_B$  corresponds to rotating the orbital isospin from a canted configuration in phase (I) to an partially polarised configuration,  $\mathbf{L} = \frac{1}{2}\mathbf{e}_z$ , in phase (II).

### Phase (III) and (IV): Spin and Valley Ferromagnet, Rotation of the Orbital Isospin

At larger values of the bias  $\Delta_B$ , similar behaviour as in phases (I) and (II) translates into valley polarised phases: we find the ground state to be partially polarised

both in spin space and in the space of the valley isospin, while the orbital isospin is either canted (below a critical magnetic field in phase III) or partially polarised (for sufficiently large magnetic field values in phase IV).

The ground state of phase (III) is given by state vectors of the form

$$\begin{aligned}
 |v_1\rangle &= |1, \uparrow, +\rangle, \\
 |v_2\rangle &= |1, \uparrow, -\rangle, \\
 |v_3\rangle &= |0, \uparrow, +\rangle, \\
 |v_4\rangle &= |0, \uparrow, -\rangle, \\
 |v_5\rangle &= \cos \theta |1, \downarrow, +\rangle + \sin \theta |0, \downarrow, +\rangle,
 \end{aligned} \tag{IV.91}$$

with the optimal angle determined by

$$\cos 2\theta_{\text{(III)}} = \frac{\Delta_{0000} + 2\Delta_{01} - \Delta_{1111} - z\Delta_{B,eff}}{\Delta_{0000} - 2(\Delta_{0011} + \Delta_{1001}) + \Delta_{1111}}. \tag{IV.92}$$

Therefore, the the following spin and isospin properties characterise phase (III):

$$\begin{aligned}
 S_z &\equiv \frac{3}{2}, \quad S_x \equiv S_y \equiv 0, \\
 T_z &= \frac{1}{2}, \quad T_x \equiv T_y \equiv 0, \\
 L_z &= \frac{1}{2} \cos 2\theta, \quad L_x = \frac{1}{2} \sin 2\theta, \quad L_y \equiv 0.
 \end{aligned} \tag{IV.93}$$

The optimal canting angle of the orbital isospin varies as a function of the bias  $\Delta_B$  and the magnetic field strength  $B$ ; at any value of  $\Delta_B$ , when  $B$  increases, the angle rotates until it reaches zero; this leads to a partially polarised phase in the orbital isospin:

Phase (IV):

$$\begin{aligned}
 |v_1\rangle &= |1, \uparrow, +\rangle, \\
 |v_2\rangle &= |1, \uparrow, -\rangle, \\
 |v_3\rangle &= |0, \uparrow, +\rangle, \\
 |v_4\rangle &= |0, \uparrow, -\rangle, \\
 |v_5\rangle &= |1, \downarrow, +\rangle,
 \end{aligned} \tag{IV.94}$$

exhibiting the properties

$$\begin{aligned}
 S_z &\equiv \frac{3}{2}, \quad S_x \equiv S_y \equiv 0, \\
 T_z &= \frac{1}{2}, \quad T_x \equiv T_y \equiv 0, \\
 L_z &= \frac{1}{2}, \quad L_x \equiv L_y \equiv 0.
 \end{aligned} \tag{IV.95}$$

Hence, increasing the magnetic field strength  $B$  corresponds to rotating the orbital isospin from a canted configuration in phase (III) to a partially polarised state  $\mathbf{L} = \frac{1}{2}\mathbf{e}_z$  in phase (IV). Both the spin and the valley isospin vectors remain constant in these phases for all values of  $\Delta_B$  and  $B$ .

### Phase (V): Evolution of all Spins and Isospins

Within a narrow range of the bias  $\Delta_B$ , there is an intermediate transition regime: we find a complex ground state structure in which all the spin and isospin degrees of freedom take non-trivial values and evolve as functions of  $\Delta_B$  and the magnetic field strength  $B$ . In general, the ground state within this parameter regime is described by the vectors

$$\begin{aligned}
 |v_1\rangle &= |1, \uparrow, +\rangle, \\
 |v_2\rangle &= a_1|1, \uparrow, -\rangle + a_2|1, \downarrow, +\rangle, \\
 |v_3\rangle &= |0, \uparrow, +\rangle, \\
 |v_4\rangle &= b_1|0, \uparrow, -\rangle + b_2|0, \downarrow, +\rangle, \\
 |v_5\rangle &= c_1|1, \uparrow, -\rangle + c_2|1, \downarrow, +\rangle + c_3|0, \uparrow, -\rangle + c_4|0, \downarrow, +\rangle,
 \end{aligned} \tag{IV.96}$$

leading to spin and isospin properties

$$\begin{aligned}
 S_z &= 1 + \frac{1}{2}(a_1^2 - a_2^2 + b_1^2 - b_2^2 + c_1^2 - c_2^2 + c_3^2 - c_4^2), \quad S_x \equiv S_y \equiv 0, \\
 T_z &= 1 - \frac{1}{2}(a_1^2 + a_2^2 - b_1^2 + b_2^2 - c_1^2 + c_2^2 - c_3^2 + c_4^2), \quad T_x \equiv T_y \equiv 0, \\
 L_z &= \frac{1}{2}(a_1^2 + a_2^2 - b_1^2 - b_2^2 + c_1^2 + c_2^2 - c_3^2 - c_4^2), \\
 L_x &= c_1c_3 + c_2c_4, \quad L_y \equiv 0.
 \end{aligned} \tag{IV.97}$$

Cuts of increasing bias  $\Delta_B$  at fixed  $B$  may exhibit one of three different types of behaviour, respectively, depending on the value of  $B$ :

- Phase (Va):

For small  $B$ , the phase (Va) is located between the phases (III) and (VI): in both these phases, the orbital isospin is neither zero nor fully polarised, exhibiting non-zero value  $L_x \neq 0$ . Phase (Va) now smoothly connects between these two phases with all four entries  $a_i \neq 0$ ,  $b_i \neq 0$ , and  $c_i \neq 0$  evolving smoothly as functions of the bias  $\Delta_B$  and the magnetic field strength  $B$ . For increasing  $\Delta_B$  across phase (Va), this leads to smooth evolutions of the spin and valley isospin from  $S_z = \frac{3}{2}$  to  $S_z = \frac{1}{2}$  and from  $T_z = \frac{1}{2}$  to  $T_z = \frac{3}{2}$ , respectively, accompanied by kinks in the orbital isospin components being nonzero  $0 < L_z < \frac{1}{2}$  and  $0 < L_x < \frac{1}{2}$ .

- Phase (Vb):

For an intermediate value of  $B$ , the phase (Vb) emerges between the phases (III) and (VII). In the former, the orbital isospin is not fully polarised, with  $L_x \neq 0$ , whereas in the latter only the x-component is nonzero:  $L_z = \frac{1}{2}$  and  $L_x \equiv L_y \equiv 0$ . This transition is accomplished within phase (Vb) by first a sudden jump of the orbital isospin  $L_x \rightarrow 0$ ,  $L_z \rightarrow \frac{1}{2}$ , as the coefficients  $c_3$  and  $c_4$  suddenly jump to zero; Subsequently, the smooth rotations of the spin and the valley isospin degrees of freedom are governed by the remaining coefficients  $a_i$  and  $b_i$  evolving smoothly.

-Phase (Vc):

For large enough values of the magnetic field, the phase (Vc) is located between the phases (IV) and (VII) — both these phases exhibit the same configuration of the orbital isospin degree of freedom:  $\mathbf{L} = \frac{1}{2}\mathbf{e}_z$ . Here, the coefficients  $c_i$  are zero throughout the phase (Vc):  $c_1 \equiv c_2 \equiv 0$ . The orbital isospin therefore remains constant within this regime. The remaining coefficients  $a_i$  and  $b_i$  evolve smoothly as functions of  $\Delta_B$  and  $B$ , entailing smooth rotations  $S_z = \frac{3}{2} \rightarrow S_z = \frac{1}{2}$   $T_z = \frac{1}{2} \rightarrow T_z = \frac{3}{2}$  across phase (Vc).

### Phase (VI) and (VII): Rotation of the Orbital Isospin to a Partially Polarised State

For sufficiently large values of the bias  $\Delta_B$ , we observe ground state structures akin to those of phases (III) and (IV), but here at full valley polarisation: at partially polarised spin and fully valley polarised isospin, the orbital isospin rotates from a canted position we call phase (VI) at sufficiently small magnetic fields to a partially polarised state, *i.e.*, phase (VII), above a certain critical magnetic field strength.

In phase (VI), the electrons occupy the states

$$\begin{aligned}
 |v_1\rangle &= |1, \uparrow, +\rangle, \\
 |v_2\rangle &= |1, \downarrow, +\rangle, \\
 |v_3\rangle &= |0, \uparrow, +\rangle, \\
 |v_4\rangle &= |0, \downarrow, +\rangle, \\
 |v_5\rangle &= \cos \theta |1, \uparrow, -\rangle - \sin \theta |0, \uparrow, -\rangle,
 \end{aligned} \tag{IV.98}$$

with the optimal angle

$$\cos 2\theta_{(VI)} = \frac{\Delta_{0000} + 2\Delta_{01} - \Delta_{1111} + \Delta_{B\text{eff}z}}{\Delta_{0000} - 2(\Delta_{0011} + \Delta_{1001}) + \Delta_{1111}}, \tag{IV.99}$$

resulting in the spin and isospin properties

$$\begin{aligned}
 S_z &\equiv \frac{1}{2}, \quad S_x \equiv S_y \equiv 0, \\
 T_z &= \frac{3}{2}, \quad T_x \equiv T_y \equiv 0, \\
 L_z &= \cos 2\theta, \quad L_x = \sin 2\theta, \quad L_y \equiv 0.
 \end{aligned} \tag{IV.100}$$

Hence, for any value of the magnetic field  $B$ , with rising bias  $\Delta_B$  the orbital isospin performs a rotation to a configuration aligned along the  $z$ -axis:  $\mathbf{L} \rightarrow \frac{1}{2}\mathbf{e}_z$ .

For sufficiently large values of the bias, phase (VII) is then given by the limiting case of phase (VI):

$$\begin{aligned}
 |v_1\rangle &= |1, \uparrow, +\rangle, \\
 |v_2\rangle &= |1, \downarrow, +\rangle, \\
 |v_3\rangle &= |0, \uparrow, +\rangle, \\
 |v_4\rangle &= |0, \downarrow, +\rangle, \\
 |v_5\rangle &= |1, \uparrow, -\rangle,
 \end{aligned} \tag{IV.101}$$

hence exhibiting

$$\begin{aligned}
 S_z &\equiv \frac{1}{2}, \quad S_x \equiv S_y \equiv 0, \\
 T_z &\equiv \frac{3}{2}, \quad T_x \equiv T_y \equiv 0, \\
 L_z &\equiv \frac{1}{2}, \quad L_x \equiv L_y \equiv 0,
 \end{aligned} \tag{IV.102}$$

which means phase (VII) eventually stabilises a configuration fully polarised along the  $z$ -axis in valley isospin, and partially polarised in spin and orbital isospin degree of freedom.

### Analytic Description of the Phase Boundaries

Except for the more complicated transition regime within phase (V), all phase transitions observed for the  $\nu = 1$  state are of continuous second order nature. We compute the critical values of the bias for these transitions, respectively:

(II)  $\longrightarrow$  (IV):

$$\Delta_{B,eff}^{crit} = \frac{-\alpha d - \Delta_{1111}\ell_B + \ell_B X_{1111}}{\ell_B(z-1)} \quad (\text{IV.103})$$

(III)  $\longrightarrow$  (IV):

$$\Delta_{B,eff}^{crit} = \frac{2(\Delta_{0011} + \Delta_{01} + \Delta_{1001} - \Delta_{1111})}{z} \quad (\text{IV.104})$$

(IV)  $\longrightarrow$  (Vc):

$$\Delta_{B,eff}^{crit} = \frac{\alpha d - \Delta_{0000}\ell_B + \Delta_Z\ell_B + \ell_B X_{0000}}{\ell_B} \quad (\text{IV.105})$$

(Vc)  $\longrightarrow$  (VII):

$$\Delta_{B,eff}^{crit} = \frac{3\alpha d + \Delta_{0000}\ell_B + \Delta_Z\ell_B - \ell_B X_{0000}}{\ell_B}$$

(VI)  $\longrightarrow$  (VII):

$$\Delta_{B,eff}^{crit} = -\frac{2(\Delta_{0011} + \Delta_{01} + \Delta_{1001} - \Delta_{1111})}{z} \quad (\text{IV.106})$$

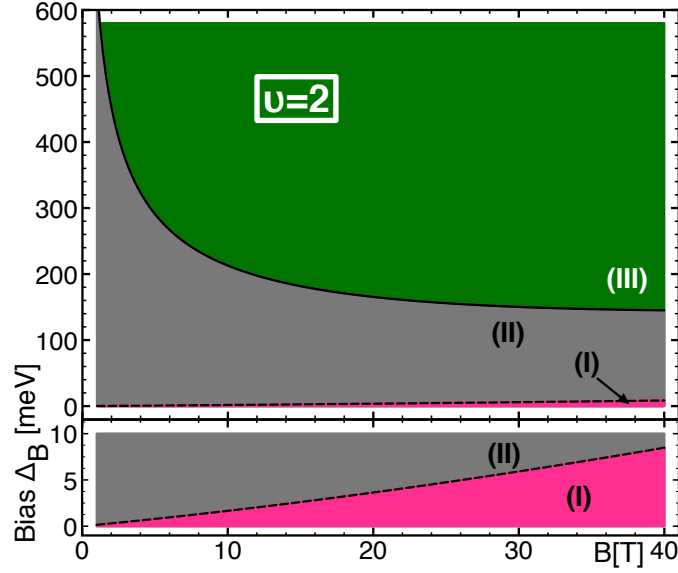
#### ★ Six Electrons: $\nu = 2$

If there are six electrons occupying octet states, the structure we find for the ground state is the one depicted in figure IV.9 with the following three different phases:

#### Phase (I): Valley Coherent Phase

In the regime of sufficiently small bias, we observe a ground state which is partially polarised in spin and exhibits valley coherence in a valley canted phase. This phase is characterised by the single electron states

$$\begin{aligned} |v_1\rangle &= |1, \uparrow, +\rangle, \\ |v_2\rangle &= |1, \uparrow, -\rangle, \\ |v_3\rangle &= |0, \uparrow, +\rangle, \\ |v_4\rangle &= |0, \uparrow, -\rangle, \\ |v_5\rangle &= \sin \theta |1, \downarrow, +\rangle + \cos \theta |1, \downarrow, -\rangle, \\ |v_6\rangle &= \sin \theta |0, \downarrow, +\rangle + \cos \theta |0, \downarrow, -\rangle, \end{aligned} \quad (\text{IV.107})$$


**Figure IV.9**

Phase diagram of the  $\nu = 2$  ground state as yielded by Hartree Fock analysis. Three different phases emerge, labelled (I), (II), (III). Figure from reference [Knothe and Jolicœur, 2016].

with the optimal canting angle

$$\cos 2\theta_{(I)} = -\frac{\Delta_{B,eff}\ell_B(z-2)}{\ell_B(-\Delta_{0000} - 2\Delta_{0011} - \Delta_{1111} + X_{0000} + 2X_{0011} + X_{1111}) - 4\alpha d}. \quad (\text{IV.108})$$

For the phase (I) we find the following spin and isospin structure:

$$\begin{aligned} S_z &= \frac{1}{2}, \quad S_x \equiv S_y \equiv 0, \\ T_z &= -\cos 2\theta, \quad T_x = \sin 2\theta, \quad T_y \equiv 0, \\ L_z &\equiv L_x \equiv L_y \equiv 0. \end{aligned}$$

The orbital order is antiferromagnetic, which leads to vanishing overall orbital polarisation.

Hence, in phase (I), cuts along lines of increasing bias  $\Delta_B$  for any strength of the magnetic field  $B$  correspond to a rotation of the valley-isospin vector from a configuration in the  $\{x-y\}$ -plane to a state partially polarised along the  $z$ -axis:  $\mathbf{T} = \mathbf{e}_x \rightarrow \mathbf{T} = \mathbf{e}_z$ .

### Phase (II): Partially Aligned Spin and Valley Ferromagnet

For larger values of the bias  $\Delta_B$ , we observe an intermediate regime, in which the ground state exhibits partial polarisation both in the spin and the valley isospin

degree of freedom and antiferromagnetic ordering in the orbital isospin.

The ground state of phase (II) is given by state vectors of the form

$$\begin{aligned}
 |v_1\rangle &= |1, \uparrow, +\rangle, \\
 |v_2\rangle &= |1, \uparrow, -\rangle, \\
 |v_3\rangle &= |0, \uparrow, +\rangle, \\
 |v_4\rangle &= |0, \uparrow, -\rangle, \\
 |v_5\rangle &= |1, \downarrow, +\rangle, \\
 |v_6\rangle &= |0, \downarrow, +\rangle.
 \end{aligned}
 \tag{IV.109}$$

Therefore, given the the spin and isospin properties of phase (II),

$$\begin{aligned}
 S_z &\equiv \frac{1}{2}, \quad S_x \equiv S_y \equiv 0, \\
 T_z &= \frac{1}{2}, \quad T_x \equiv T_y \equiv 0, \\
 L_z &\equiv L_x \equiv L_y \equiv 0,
 \end{aligned}
 \tag{IV.110}$$

the ground state stabilises a partially aligned spin and valley ferromagnet over a broad parameter range.

### Phase (III): Partially Aligned Valley and Orbital Ferromagnet

When the system is biased sufficiently strongly, we find the ground state to be a polarised state both for the valley and the orbital isospin. Meanwhile, due to antiferromagnetic ordering of the spin degree of freedom, the overall spin polarisation vanishes.

In phase (III), the ground state electron states are given by

$$\begin{aligned}
 |v_1\rangle &= |1, \uparrow, +\rangle, \\
 |v_2\rangle &= |1, \uparrow, -\rangle, \\
 |v_3\rangle &= |0, \uparrow, +\rangle, \\
 |v_4\rangle &= |1, \downarrow, -\rangle, \\
 |v_5\rangle &= |1, \downarrow, +\rangle, \\
 |v_6\rangle &= |0, \downarrow, +\rangle,
 \end{aligned}
 \tag{IV.111}$$

which reflects in the spin and isospin properties

$$\begin{aligned}
 S_z &\equiv S_x \equiv S_y \equiv 0, \\
 T_z &= \frac{1}{2}, \quad T_x \equiv T_y \equiv 0, \\
 L_z &= \frac{1}{2}, \quad L_x \equiv L_y \equiv 0.
 \end{aligned} \tag{IV.112}$$

The ground state stabilises a partially aligned valley and orbital ferromagnet for large values of the bias  $\Delta_B$  for all magnetic field strengths.

### Analytic Description of the Phase Boundaries

For the system at filling  $\nu = 2$  we identify two different types of phase transitions as functions of  $\Delta_B$  and  $B$ : the small bias transition (I) to (II) comes with a smooth rotation of the valley isospin and therefore is of continuous second order. For larger bias, however, the system jumps from phase (II) to phase (III) in a discontinuous fashion characterising a first order transition.

We give the values of the critical bias, at which these phase transitions occur:

Second order transition (I)  $\rightarrow$  (II):

$$\Delta_{B,eff}^{crit} = \frac{\ell_B(\Delta_{0000} - 2\Delta_{0011} - \Delta_{1111} + X_{0000} + 2X_{0011} + X_{1111}) - 4\alpha d}{\ell_B(z - 2)} \tag{IV.113}$$

First order transition (II)  $\rightarrow$  (III):

$$\Delta_{B,eff}^{crit} = \frac{-\Delta_{0000} - 2\Delta_{0011} - 2\Delta_{01} + \Delta_{1111} + 2\Delta_Z}{z} \tag{IV.114}$$

### ★ Seven Electrons: $\nu = 3$

With seven electrons, *i.e.*, only one hole in the octet, the ground state phases exhibit the structure shown in figure IV.10:

#### Bias $\Delta_B \equiv 0$ ; Evolution as a Function of $B$

At zero bias, we find a partially spin polarised ground state, while the valley isospin lies in the  $\{x-y\}$ -plane. The state exhibits orbital coherence as the orbital isospin is in a canted configuration.

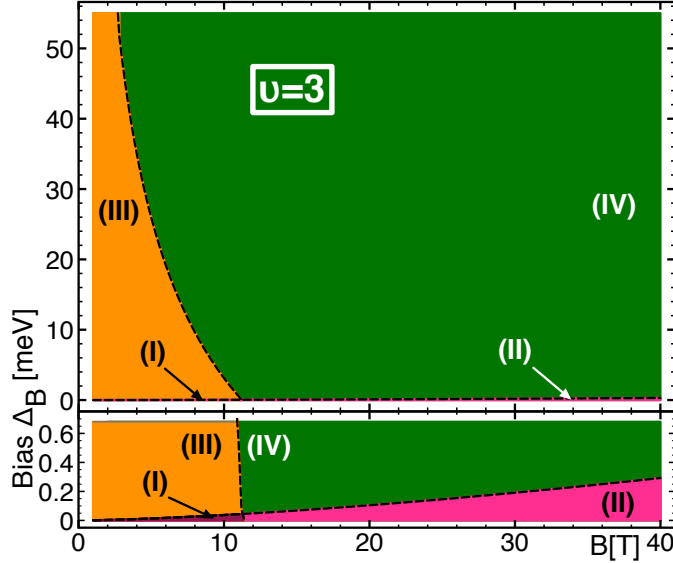


**Figure IV.10**  
Phase diagram of the  $\nu = 3$  ground state extracted from the Hartree Fock analysis. There are different phases emerging, labelled (I)-(IV). Figure from reference [Knothe and Jolicœur, 2016].

The ground state configuration for the seven electrons is given by

$$\begin{aligned}
 |v_1\rangle &= |1, \uparrow, +\rangle, \\
 |v_2\rangle &= |1, \uparrow, -\rangle, \\
 |v_3\rangle &= |0, \uparrow, +\rangle, \\
 |v_4\rangle &= |0, \uparrow, -\rangle, \\
 |v_5\rangle &= \frac{1}{\sqrt{2}} \cos \theta_0 \left[ |1, \downarrow, +\rangle + |1, \downarrow, -\rangle \right] + \frac{1}{\sqrt{2}} \sin \theta_0 \left[ |0, \downarrow, +\rangle + |0, \downarrow, -\rangle \right], \\
 |v_6\rangle &= \frac{1}{\sqrt{2}} \sin \theta_0 \left[ |1, \downarrow, +\rangle + |1, \downarrow, -\rangle \right] - \frac{1}{\sqrt{2}} \cos \theta_0 \left[ |0, \downarrow, +\rangle + |0, \downarrow, -\rangle \right], \\
 |v_7\rangle &= \frac{1}{\sqrt{2}} \sin \theta_0 \left[ |1, \downarrow, +\rangle - |1, \downarrow, -\rangle \right] + \frac{1}{\sqrt{2}} \cos \theta_0 \left[ |0, \downarrow, +\rangle - |0, \downarrow, -\rangle \right], \quad (\text{IV.115})
 \end{aligned}$$

where the optimal angle  $\theta_0$  varies as a function of  $B$  between  $\theta_0 \rightarrow \frac{\pi}{4}$  at vanishing magnetic field  $B \rightarrow 0$  and  $\theta_0 = 0$  at sufficiently high magnetic field strengths above a certain critical value  $B_{crit} \approx 11.3$  T. It fulfils the relation

$$\cos 2\theta_0 = \frac{-3\Delta_{0000} - 4\Delta_{01} + 3\Delta_{1111} + X_{0000} - X_{1111}}{\Delta_{0000} - 2\Delta_{0011} - 2\Delta_{1001} + \Delta_{1111} + X_{0000} - 2X_{0011} - 2X_{1001} + X_{1111}}. \quad (\text{IV.116})$$

The state exhibits the properties

$$\begin{aligned}
 S_z &\equiv \frac{1}{2}, \quad S_x \equiv S_y \equiv 0, \\
 T_z &= 0, \quad T_x \equiv \frac{1}{2}, \quad T_y \equiv 0, \\
 L_z &= -\cos 2\theta, \quad L_x = \sin 2\theta, \quad L_y \equiv 0.
 \end{aligned} \tag{IV.117}$$

Along the line of zero bias, as a function of the magnetic field strength  $B$ , the ground state hence undergoes a transition from a canted state in the orbital isospin to a partially aligned state  $\mathbf{L} = \frac{1}{2}\mathbf{e}_z$ .

### Phases (I) and (II): Rotation of the Valley Isospin at either Canted or Partially Aligned Orbital Isospin

In this regime of sufficiently weak bias  $\Delta_B$ , the ground state exhibits partial polarisation in spin space, while the valley isospin undergoes a rotation and therefore takes non-trivial values  $0 \leq T_x, T_z \leq \frac{1}{2}$ . Meanwhile, the orbital isospin is either canted with  $0 \leq L_x, L_z \leq \frac{1}{2}$  for small magnetic field strengths in phase (I), or partially polarised in phase (II) at sufficiently large magnetic fields. While the dependencies of the isospins in phase (I) being more involved, we can express the valley isospin in phase (II) in terms of one valley tilting angle.

These phases are characterised by the non-trivial combinations:

Phase (I):

$$\begin{aligned}
 |v_1\rangle &= |1, \uparrow, +\rangle, \\
 |v_2\rangle &= |1, \uparrow, -\rangle, \\
 |v_3\rangle &= |0, \uparrow, +\rangle, \\
 |v_4\rangle &= |0, \uparrow, -\rangle, \\
 |v_5\rangle &= -a_1|1, \downarrow, +\rangle + a_2|1, \downarrow, -\rangle - a_3|0, \downarrow, +\rangle + a_4|0, \downarrow, -\rangle, \\
 |v_6\rangle &= a_3|1, \downarrow, +\rangle - a_4|1, \downarrow, -\rangle - a_1|0, \downarrow, +\rangle + a_2|0, \downarrow, -\rangle, \\
 |v_7\rangle &= a_4|1, \downarrow, +\rangle + a_3|1, \downarrow, -\rangle + a_2|0, \downarrow, +\rangle + a_1|0, \downarrow, -\rangle,
 \end{aligned} \tag{IV.118}$$

with coefficients  $a_i > 0$  varying as functions of  $\Delta_B$  and  $B$ .

In phase (II), where  $a_1 \equiv 0$  and  $a_2 \equiv 0$ , we set  $a_3 = \cos \theta$  and  $a_4 = \sin \theta$ , and simplify above expression :

$$\begin{aligned}
 |v_1\rangle &= |1, \uparrow, +\rangle, \\
 |v_2\rangle &= |1, \uparrow, -\rangle, \\
 |v_3\rangle &= |0, \uparrow, +\rangle, \\
 |v_4\rangle &= |0, \uparrow, -\rangle, \\
 |v_5\rangle &= -\cos \theta |0, \downarrow, +\rangle + \sin \theta |0, \downarrow, -\rangle, \\
 |v_6\rangle &= \cos \theta |1, \downarrow, +\rangle - \sin \theta |1, \downarrow, -\rangle, \\
 |v_7\rangle &= \sin \theta |1, \downarrow, +\rangle + \cos \theta |1, \downarrow, -\rangle.
 \end{aligned} \tag{IV.119}$$

The optimal angle of phase (II) is then given by

$$\cos 2\theta_{(II)} = \frac{\Delta_{B,eff} \ell_B}{\alpha d + \ell_B (\Delta_{0000} - X_{0000})}. \tag{IV.120}$$

For the phases (I) and (II) we find the following spin and isospin structure, respectively:

Phase (I):

$$\begin{aligned}
 S_z &= \frac{1}{2}, \quad S_x \equiv S_y \equiv 0, \\
 T_z &= \frac{1}{2}(a_1^2 - a_2^2 + a_3^2 - a_4^2), \\
 T_x &= -(a_1 a_2 + a_3 a_4), \\
 T_y &\equiv 0, \\
 L_z &= -\frac{1}{2}(a_1^2 + a_2^2 - a_3^2 - a_4^2), \\
 L_x &= a_1 a_3 + a_2 a_4, \\
 L_y &\equiv 0,
 \end{aligned} \tag{IV.121}$$

Phase (II):

$$\begin{aligned}
 S_z &= \frac{3}{2}, \quad S_x \equiv S_y \equiv 0, \\
 T_z &= \frac{1}{2}(a_3^2 - a_4^2) = \cos 2\theta, \quad T_x = -a_3 a_4 = -\sin 2\theta, \quad T_y \equiv 0, \\
 L_z &= \frac{1}{2}, \quad L_x \equiv L_y \equiv 0.
 \end{aligned}$$

Hence, in phase (I) and (II), cuts along lines of increasing bias  $\Delta_B$  for any strength of the magnetic field  $B$  correspond to a rotation of the valley-isospin vector from a

configuration in the  $\{x-y\}$ -plane to a state aligned along the  $z$ -axis:  $\mathbf{T} = \frac{1}{2}\mathbf{e}_x \rightarrow \mathbf{T} = \frac{1}{2}\mathbf{e}_z$ . At the same time, increasing  $B$  at a fixed value of the bias  $\Delta_B$  corresponds to rotating the orbital isospin from a canted configuration in phase (I) to an aligned configuration,  $\mathbf{L} = \frac{1}{2}\mathbf{e}_z$ , in phase (II).

### Phase (III): Canted Orbital Isospin

At small magnetic fields and large values of the bias, the spin and the valley isospin degree of freedom are equally partially polarised, while the orbital isospin undergoes a rotation through a canted state, thereby exhibiting non-trivial orbital coherence.

The ground state of phase (III) is given by state vectors of the form

$$\begin{aligned}
 |v_1\rangle &= |1, \uparrow, +\rangle, \\
 |v_2\rangle &= |1, \uparrow, -\rangle, \\
 |v_3\rangle &= |0, \uparrow, +\rangle, \\
 |v_4\rangle &= |0, \uparrow, -\rangle, \\
 |v_5\rangle &= |1, \downarrow, +\rangle, \\
 |v_6\rangle &= |0, \downarrow, +\rangle, \\
 |v_7\rangle &= \cos\theta|1, \downarrow, -\rangle + \sin\theta|0, \downarrow, -\rangle,
 \end{aligned} \tag{IV.122}$$

with the optimal angle determined by

$$\cos 2\theta_{\text{(III)}} = -\frac{2(\Delta_{0011} + \Delta_{01} + \Delta_{1001} - \Delta_{1111})}{z}. \tag{IV.123}$$

Therefore, the following spin and isospin properties characterise phase (III):

$$\begin{aligned}
 S_z &\equiv \frac{1}{2}, \quad S_x \equiv S_y \equiv 0, \\
 T_z &= \frac{1}{2}, \quad T_x \equiv T_y \equiv 0, \\
 L_z &= \frac{1}{2} \cos 2\theta, \quad L_x = \frac{1}{2} \sin 2\theta, \quad L_y \equiv 0.
 \end{aligned} \tag{IV.124}$$

The optimal canting angle of the orbital isospin varies as function of the bias  $\Delta_B$  and the magnetic field strength  $B$ .

### Phase (IV): Partially Aligned Ferromagnet

When both magnetic field strength  $B$  and bias  $\Delta_B$  are sufficiently large, the ground state adopts a configuration in which all spin and isospin degrees of freedom are

equally partially polarised.

The ground state in this regime is described by the vectors

$$\begin{aligned}
 |v_1\rangle &= |1, \uparrow, +\rangle, \\
 |v_2\rangle &= |1, \uparrow, -\rangle, \\
 |v_3\rangle &= |0, \uparrow, +\rangle, \\
 |v_4\rangle &= |0, \uparrow, -\rangle, \\
 |v_5\rangle &= |1, \downarrow, +\rangle, \\
 |v_6\rangle &= |0, \downarrow, +\rangle, \\
 |v_7\rangle &= |1, \downarrow, -\rangle,
 \end{aligned}$$

where all the spins and isospins are partially aligned along the  $z$ -axis:

$$\begin{aligned}
 S_z &\equiv \frac{1}{2}, \quad S_x \equiv S_y \equiv 0, \\
 T_z &= \frac{1}{2}, \quad T_x \equiv T_y \equiv 0, \\
 L_z &= \frac{1}{2}, \quad L_x \equiv L_y \equiv 0.
 \end{aligned} \tag{IV.125}$$

### Analytic Description of the Phase Boundaries

All the phase transitions for filling factor  $\nu = 3$  are continuous second order transitions, which occur via smooth rotations of the respective isospin degrees of freedom.

We give the critical biases at which transitions between the different phases occur:

(I)  $\longrightarrow$  (III):

$$\Delta_{B,eff}^{crit} = \frac{\alpha d}{\ell_B} + \Delta_{0000} - X_{0000} \tag{IV.126}$$

(III)  $\longrightarrow$  (IV):

$$\Delta_{B,eff}^{crit} = -\frac{2(\Delta_{0011} + \Delta_{01} + \Delta_{1001} - \Delta_{1111})}{z} \tag{IV.127}$$

### IV.2.3 Properties of the Phases - Comparative Discussion

#### General Features

We start by discussing the common features shared by all the phase diagrams of figure IV.3 for the filling factors  $\nu \in [-3, 3]$ . In general, we observe a variety of different spin and isospin structures: among these, the valley and the orbital isospin

can be either fully or partially polarised, or in canted configurations, thus exhibiting non-trivial valley or orbital coherence. In figure IV.3, the regions where such valley or orbital coherent phases occur are drawn in bordeaux, pink, turquoise, yellow, or orange, respectively. Canting of the spin degree of freedom is observed for none of the configurations for any filling factor or any value of the system parameters. Hence, there is no coherence in the real spin and all the phases observed are either partially or fully spin polarised. The spin and isospin configurations for all the different possible phases are summarised in tables IV.9 and IV.10.

The unbiased system at  $\Delta_B \equiv 0$  is spin polarised for all values of the filling factor. This also remains true for sufficiently small values of the bias in every case. In figure IV.3, we refer to all phases except the blue or green ones at even filling factors. In the opposite limit of large bias, valley polarisation emerges for all  $\nu$ . These phases are coloured in blue or green in figure IV.3. Qualitatively, this is in accordance with experimental [Kim et al., 2011] as well as previous theoretical [Lambert and Côté, 2013] investigations which suggest an evolution towards a valley polarised state with increasing bias. The values of the critical bias and the critical magnetic field strength below which the system is spin polarised, while above these values valley polarisation can be observed, however, differ for different values of  $\nu$ . Furthermore, it depends on the filling factor whether the respective polarised phase formed in these two limits is partially polarised or fully polarised in spin or valley space.

### Odd versus Even Filling Factors

In the next step, we compare the behaviour of the ground state phase diagrams obtained at odd filling factors to the situation at even fillings. Special attention we pay to the properties of the orbital degree of freedom, as here we observe the following:

#### Odd fillings $\nu = -3, -1, 1, 3$

For the unbiased system, *i.e.*, along the line of zero bias  $\Delta_B \equiv 0$ , all the systems with  $\nu$  odd undergo a similar evolution of the orbital isospin: at small  $B$ , we find a orbitally canted configuration. Then, with rising  $B$ , the orbital isospin rotates smoothly until it reaches a polarised state above some critical magnetic field strength  $B_{crit}$ . For non-zero values of the bias this transition in the orbital configuration is translated into the upper half of each phase diagram: for every odd filling factor, we find a large phase exhibiting orbital coherence at any  $\Delta_B > 0$ . These regions of non-trivial orbital coherence are drawn in yellow or orange in figure IV.3. All the orbitally coherent phases

then, respectively, evolve into orbitally polarised configurations, marked in blue or green in figure IV.3, respectively, by smooth rotations of the orbital isospin when  $B$  is increased for any  $\Delta_B$  held fix.

**Even fillings  $\nu = -2, 0, 2$**

For even filling factors, however, we do not observe any phase with orbital coherence whatsoever. Furthermore, there is no phase transition as a function of  $B$  along the line of zero bias. In fact the ground state is in a configuration which is spin polarised at vanishing orbital isospin stable for all values of  $B$ . Some of the phases at  $\nu$  even do exhibit orbital polarisation, *i.e.*, the total orbital isospin is of the form  $\mathbf{L} \propto \mathbf{e}_z$ : these phases are drawn in blue at  $\nu = -2$ , and green at  $\nu = 2$  in figure IV.3. The remaining phases at even fillings show antiferromagnetic orbital order, *i.e.*, the overall orbital polarisation vanishes such that we find  $\mathbf{L} \equiv 0$ .

Furthermore, only for the cases  $\nu = -2$  and  $\nu = 2$  discontinuous phase transitions of first order are observed when entering the regime of very high bias. All other phase transitions in the bilayer graphene system correspond to smooth rotations of the respective isospin and are hence of second order.

#### IV.2.4 Negative against Positive Filling Factors

Finally let us compare the behaviour of the phases at negative filling factors  $\nu = -3, -2, -1, 0$ , table IV.9, to positive filling factors  $\nu = 1, 2, 3$ , table IV.10. Here, the most striking feature has to do with the appearance of orbital polarisation. In the limit of large values of the bias  $\Delta_B$ , the system exhibits orbital polarisation for all values of the filling factor: in figure IV.3 these phases are drawn in blue or in green. Differences, however, can be observed with respect to the question *in which direction* the system will be polarised in orbital space.

**Negative fillings  $\nu = -3, -2, -1, 0$**

For negative filling factors orbital polarisation is negative, *i.e.*, we find  $\mathbf{L} \propto -\mathbf{e}_z$ . This corresponds to the blue phases in figure IV.3. Physically, this indicates that at negative filling factors it is energetically favourable to populate predominantly the  $n = 0$  orbitals

**Positive fillings  $\nu = 1, 2, 3$**

The ground state for positive filling factors for sufficiently large bias turns out to be positively polarised:  $\mathbf{L} \propto +\mathbf{e}_z$ . These phases are indicated in green in figure IV.3. Hence, at positive filling factors the systems prefer to successively populate  $n = 1$  orbitals.

### IV.2.5 Phase Diagrams - Summary and Conclusion

In this section we analysed the ground state spin and isospin structure of bilayer graphene at different octet filling factors  $\nu$  under the influence of external electric and magnetic fields. Distinguishing the different phases by their different configurations of the spin, the valley isospin and the orbital isospin degree of freedom, within a Hartree Fock mean field treatment we derived the seven phase diagrams for  $\nu \in [-3, 3]$  in the plane spanned by the bias potential and the magnetic field. Concerning the nature of the individual phases we made the following observations:

#### Summary: Ground State Phase Diagrams for Different $\nu$

- Altogether, for all filling factors and all values of the external fields, we have identified a total of **32 different ground state phases**. Each phase is characterised by a different spin and isospin configuration. Among these phases, there are configurations which are either fully or partially polarised in the spin, the valley isospin, or the orbital isospin. Besides, both the valley isospin and the orbital isospin can be in canted configurations, carrying valley or orbital coherence. No canting is observed for the spin degree of freedom.
- For each individual filling factor, the largest absolute value of the total spin  $|\mathbf{S}|$  is assumed for the unbiased system, at  $\Delta_B \equiv 0$ , whereas the largest absolute value of the total valley isospin  $|\mathbf{T}|$  of that respective filling is favoured at large values of the bias  $\Delta_B \equiv 0$ .
- We observe **broad phases of non-trivial orbital coherence** for all odd values of the filling factors. These phases appear at intermediate strengths of the bias potential which might be potentially accessible in realistic experiments. No orbitally coherent phases are observed at even filling factors.
- For the unbiased system, *i.e.*, at  $\Delta_B \equiv 0$ , we observe a **novel phase transition as a function of an increasing magnetic field  $B$**  for all odd filling factors. It corresponds to a rotation from a phase canted in orbital space at small  $B$  to an orbitally polarised phase for sufficiently large  $B$  above a critical magnetic field strength  $B_{crit} \approx 11.3$  T. No such phase transition is observed for even filling factors.

In the following pages, we tabulate the the ground state configurations as well as the resulting spin and isospin properties corresponding to the Hartree Fock ground state phase diagrams of figure [IV.3](#).

Ground State Configurations for the Different Phases for Filling Factors  $\nu$ 

$\Delta_B \equiv 0$	$ v_1\rangle = \frac{1}{\sqrt{2}} \cos \theta [  1, \uparrow, +\rangle +  1, \uparrow, -\rangle ] + \frac{1}{\sqrt{2}} \sin \theta [  0, \uparrow, +\rangle +  0, \uparrow, -\rangle ]$
Phase (I)	$ v_1\rangle = a_1  1, \uparrow, +\rangle + a_2  1, \uparrow, -\rangle + a_5  0, \uparrow, +\rangle + a_6  0, \uparrow, -\rangle$
Phase (II)	$ v_1\rangle = \sin \theta  1, \uparrow, +\rangle + \cos \theta  1, \uparrow, -\rangle$
Phase (III)	$ v_1\rangle =  1, \uparrow, +\rangle$
Phase (IV)	$ v_1\rangle = \sin \theta  1, \uparrow, +\rangle + \cos \theta  0, \uparrow, +\rangle$
Phase (V)	$ v_1\rangle =  0, \uparrow, +\rangle$

**Table IV.2**

 Ground state configurations at  $\nu = -3$ .

$\Delta_B \equiv 0$	$ v_1\rangle = \frac{1}{\sqrt{2}} [  1, \uparrow, +\rangle +  1, \uparrow, -\rangle ],  v_2\rangle = \frac{1}{\sqrt{2}} [  0, \uparrow, +\rangle +  0, \uparrow, -\rangle ],$
Phase (I)	$ v_1\rangle = \cos \theta  1, \uparrow, +\rangle + \sin \theta  1, \uparrow, -\rangle,$ $ v_2\rangle = \cos \theta  0, \uparrow, +\rangle + \sin \theta  0, \uparrow, -\rangle,$
Phase (II)	$ v_1\rangle =  1, \uparrow, +\rangle,  v_2\rangle =  0, \uparrow, +\rangle.$
Phase (III)	$ v_1\rangle =  0, \uparrow, +\rangle,  v_2\rangle =  0, \downarrow, +\rangle,$

**Table IV.3**

 Ground state configurations at  $\nu = -2$ .

$\Delta_B = 0$	$ v_1\rangle = -\frac{1}{\sqrt{2}} [  1, \uparrow, +\rangle +  1, \uparrow, -\rangle ],  v_2\rangle = \frac{1}{\sqrt{2}} [  0, \uparrow, +\rangle +  0, \uparrow, -\rangle ],$ $ v_3\rangle = \frac{-1}{\sqrt{2}} \sin \theta [  1, \uparrow, +\rangle -  1, \uparrow, -\rangle ] - \frac{1}{\sqrt{2}} \cos \theta [  0, \uparrow, +\rangle -  0, \uparrow, -\rangle ],$
Phase (I)	$ v_1\rangle = -a_1  1, \uparrow, +\rangle - a_2  1, \uparrow, -\rangle + b_1  0, \uparrow, +\rangle + b_2  0, \uparrow, -\rangle,$ $ v_2\rangle = b_1  1, \uparrow, +\rangle + b_2  1, \uparrow, -\rangle + a_1  0, \uparrow, +\rangle + a_2  0, \uparrow, -\rangle,$ $ v_3\rangle = c_1  1, \uparrow, +\rangle - c_2  1, \uparrow, -\rangle - c_3  0, \uparrow, +\rangle + c_4  0, \uparrow, -\rangle,$
Phase (II)	$ v_1\rangle = -\cos \theta  1, \uparrow, +\rangle - \sin \theta  1, \uparrow, -\rangle,$ $ v_2\rangle = \cos \theta  0, \uparrow, +\rangle + \sin \theta  0, \uparrow, -\rangle,$ $ v_3\rangle = \sin \theta  1, \uparrow, +\rangle - \cos \theta  1, \uparrow, -\rangle,$
Phase (III)	$ v_1\rangle =  1, \uparrow, +\rangle,  v_2\rangle =  0, \uparrow, +\rangle,  v_3\rangle = \cos \theta  1, \uparrow, -\rangle + \sin \theta  0, \uparrow, -\rangle$
Phase (IV)	$ v_1\rangle =  1, \uparrow, +\rangle,  v_2\rangle =  0, \uparrow, +\rangle,  v_3\rangle =  1, \uparrow, -\rangle$
Phase (V)	$ v_1\rangle =  1, \uparrow, +\rangle,  v_2\rangle =  0, \uparrow, +\rangle,$ $ v_3\rangle = c_1  1, \uparrow, -\rangle + c_2  1, \downarrow, +\rangle - c_3  0, \uparrow, -\rangle - c_4  0, \downarrow, +\rangle$
Phase (VI)	$ v_1\rangle =  1, \uparrow, +\rangle,  v_2\rangle =  0, \uparrow, +\rangle,  v_3\rangle = \cos \theta  1, \downarrow, +\rangle + \sin \theta  0, \downarrow, +\rangle$
Phase (VII)	$ v_1\rangle =  1, \uparrow, +\rangle,  v_2\rangle =  0, \uparrow, +\rangle,  v_3\rangle =  0, \downarrow, +\rangle$

**Table IV.4**

 Ground state configurations at  $\nu = -1$ .

Phase (I)	$ v_1\rangle =  1, \uparrow, +\rangle,  v_2\rangle =  1, \uparrow, -\rangle,  v_3\rangle =  0, \uparrow, +\rangle,  v_4\rangle =  0, \uparrow, -\rangle$
Phase (II)	$ v_1\rangle =  1, \uparrow, +\rangle,  v_2\rangle = \cos\theta 1, \uparrow, -\rangle + \sin\theta 1, \downarrow, +\rangle,$ $ v_3\rangle =  0, \uparrow, +\rangle,  v_4\rangle = \cos\theta 0, \uparrow, -\rangle + \sin\theta 0, \downarrow, +\rangle$
Phase (III)	$ v_1\rangle =  1, \uparrow, +\rangle,  v_2\rangle =  1, \downarrow, +\rangle,  v_3\rangle =  0, \uparrow, +\rangle,  v_4\rangle =  0, \downarrow, +\rangle$

**Table IV.5**

 Ground state configurations at  $\nu = 0$ .

$\Delta_B = 0$	$ v_1\rangle =  1, \uparrow, +\rangle,  v_2\rangle =  1, \uparrow, -\rangle,  v_3\rangle =  0, \uparrow, +\rangle,  v_4\rangle =  0, \uparrow, -\rangle,$ $ v_5\rangle = \frac{1}{\sqrt{2}} \cos\theta [  1, \downarrow, +\rangle +  1, \downarrow, -\rangle ] - \frac{1}{\sqrt{2}} \sin\theta [  0, \downarrow, +\rangle +  0, \downarrow, -\rangle ]$
Phase (I)	$ v_1\rangle =  1, \uparrow, +\rangle,  v_2\rangle =  1, \uparrow, -\rangle,  v_3\rangle =  0, \uparrow, +\rangle,  v_4\rangle =  0, \uparrow, -\rangle,$ $ v_5\rangle = a_1 1, \downarrow, +\rangle + a_2 1, \downarrow, -\rangle - a_3 0, \downarrow, +\rangle - a_4 0, \downarrow, -\rangle$
Phase (II)	$ v_1\rangle =  1, \uparrow, +\rangle,  v_2\rangle =  1, \uparrow, -\rangle,  v_3\rangle =  0, \uparrow, +\rangle,$ $ v_4\rangle =  0, \uparrow, -\rangle,  v_5\rangle = \cos\theta 1, \downarrow, +\rangle + \sin\theta 1, \downarrow, -\rangle$
Phase (III)	$ v_1\rangle =  1, \uparrow, +\rangle,  v_2\rangle =  1, \uparrow, -\rangle,  v_3\rangle =  0, \uparrow, +\rangle,$ $ v_4\rangle =  0, \uparrow, -\rangle,  v_5\rangle = \cos\theta 1, \downarrow, +\rangle + \sin\theta 0, \downarrow, +\rangle$
Phase (IV)	$ v_1\rangle =  1, \uparrow, +\rangle,  v_2\rangle =  1, \uparrow, -\rangle,  v_3\rangle =  0, \uparrow, +\rangle,$ $ v_4\rangle =  0, \uparrow, -\rangle,  v_5\rangle =  1, \downarrow, +\rangle$
Phase (V)	$ v_1\rangle =  1, \uparrow, +\rangle,  v_2\rangle = a_1 1, \uparrow, -\rangle + a_2 1, \downarrow, +\rangle,  v_3\rangle =  0, \uparrow, +\rangle,$ $ v_4\rangle = b_1 0, \uparrow, -\rangle + b_2 0, \downarrow, +\rangle,$ $ v_5\rangle = c_1 1, \uparrow, -\rangle + c_2 1, \downarrow, +\rangle + c_3 0, \uparrow, -\rangle + c_4 0, \downarrow, +\rangle$
Phase (VI)	$ v_1\rangle =  1, \uparrow, +\rangle,  v_2\rangle =  1, \downarrow, +\rangle,  v_3\rangle =  0, \uparrow, +\rangle,$ $ v_4\rangle =  0, \downarrow, +\rangle,  v_5\rangle = \cos\theta 1, \uparrow, -\rangle + \sin\theta 0, \uparrow, -\rangle$
Phase (VII)	$ v_1\rangle =  1, \uparrow, +\rangle,  v_2\rangle =  1, \downarrow, +\rangle,  v_3\rangle =  0, \uparrow, +\rangle,$ $ v_4\rangle =  0, \downarrow, +\rangle,  v_5\rangle =  1, \uparrow, -\rangle$

**Table IV.6**

 Ground state configurations at  $\nu = 1$ .

$\Delta_B \equiv 0$	$ v_1\rangle =  1, \uparrow, +\rangle,  v_2\rangle =  1, \uparrow, -\rangle,  v_3\rangle =  0, \uparrow, +\rangle,  v_4\rangle =  0, \uparrow, -\rangle,$ $ v_5\rangle = \frac{1}{\sqrt{2}} [  1, \downarrow, +\rangle +  1, \downarrow, -\rangle ],  v_6\rangle = \frac{1}{\sqrt{2}} [  0, \downarrow, +\rangle +  0, \downarrow, -\rangle ]$
Phase (I)	$ v_1\rangle =  1, \uparrow, +\rangle,  v_2\rangle =  1, \uparrow, -\rangle,  v_3\rangle =  0, \uparrow, +\rangle,  v_4\rangle =  0, \uparrow, -\rangle,$ $ v_5\rangle = \sin\theta 1, \downarrow, +\rangle + \cos\theta 1, \downarrow, -\rangle,$ $ v_6\rangle = \sin\theta 0, \downarrow, +\rangle + \cos\theta 0, \downarrow, -\rangle$
Phase (II)	$ v_1\rangle =  1, \uparrow, +\rangle,  v_2\rangle =  1, \uparrow, -\rangle,  v_3\rangle =  0, \uparrow, +\rangle,$ $ v_4\rangle =  0, \uparrow, -\rangle,  v_5\rangle =  1, \downarrow, +\rangle,  v_6\rangle =  0, \downarrow, +\rangle$
Phase (III)	$ v_1\rangle =  1, \uparrow, +\rangle,  v_2\rangle =  1, \uparrow, -\rangle,  v_3\rangle =  0, \uparrow, +\rangle,$ $ v_4\rangle =  1, \downarrow, -\rangle,  v_5\rangle =  1, \downarrow, +\rangle,  v_6\rangle =  0, \downarrow, +\rangle$

**Table IV.7**

 Ground state configurations at  $\nu = 2$ .

$\Delta_B = 0$	$ v_1\rangle =  1, \uparrow, +\rangle,  v_2\rangle =  1, \uparrow, -\rangle,  v_3\rangle =  0, \uparrow, +\rangle,  v_4\rangle =  0, \uparrow, -\rangle,$ $ v_5\rangle = \frac{1}{\sqrt{2}} \cos \theta \left[  1, \downarrow, +\rangle +  1, \downarrow, -\rangle \right] + \frac{1}{\sqrt{2}} \sin \theta \left[  0, \downarrow, +\rangle +  0, \downarrow, -\rangle \right],$ $ v_6\rangle = \frac{1}{\sqrt{2}} \sin \theta \left[  1, \downarrow, +\rangle +  1, \downarrow, -\rangle \right] - \frac{1}{\sqrt{2}} \cos \theta \left[  0, \downarrow, +\rangle +  0, \downarrow, -\rangle \right],$ $ v_7\rangle = \frac{1}{\sqrt{2}} \sin \theta \left[  1, \downarrow, +\rangle -  1, \downarrow, -\rangle \right] + \frac{1}{\sqrt{2}} \cos \theta \left[  0, \downarrow, +\rangle -  0, \downarrow, -\rangle \right]$
Phase (I)	$ v_1\rangle =  1, \uparrow, +\rangle,  v_2\rangle =  1, \uparrow, -\rangle,  v_3\rangle =  0, \uparrow, +\rangle,  v_4\rangle =  0, \uparrow, -\rangle,$ $ v_5\rangle = -a_1 1, \downarrow, +\rangle + a_2 1, \downarrow, -\rangle - a_3 0, \downarrow, +\rangle + a_4 0, \downarrow, -\rangle,$ $ v_6\rangle = a_3 1, \downarrow, +\rangle - a_4 1, \downarrow, -\rangle - a_1 0, \downarrow, +\rangle + a_2 0, \downarrow, -\rangle,$ $ v_7\rangle = a_4 1, \downarrow, +\rangle + a_3 1, \downarrow, -\rangle + a_2 0, \downarrow, +\rangle + a_1 0, \downarrow, -\rangle$
Phase (II)	$ v_1\rangle =  1, \uparrow, +\rangle,  v_2\rangle =  1, \uparrow, -\rangle,  v_3\rangle =  0, \uparrow, +\rangle,  v_4\rangle =  0, \uparrow, -\rangle,$ $ v_5\rangle = -\cos \theta  0, \downarrow, +\rangle + \sin \theta  0, \downarrow, -\rangle,$ $ v_6\rangle = \cos \theta  1, \downarrow, +\rangle - \sin \theta  1, \downarrow, -\rangle,$ $ v_7\rangle = \sin \theta  1, \downarrow, +\rangle + \cos \theta  1, \downarrow, -\rangle$
Phase (III)	$ v_1\rangle =  1, \uparrow, +\rangle,  v_2\rangle =  1, \uparrow, -\rangle,  v_3\rangle =  0, \uparrow, +\rangle,  v_4\rangle =  0, \uparrow, -\rangle,$ $ v_5\rangle =  1, \downarrow, +\rangle,  v_6\rangle =  0, \downarrow, +\rangle,  v_7\rangle = \cos \theta  1, \downarrow, -\rangle + \sin \theta  0, \downarrow, -\rangle$
Phase (IV)	$ v_1\rangle =  1, \uparrow, +\rangle,  v_2\rangle =  1, \uparrow, -\rangle,  v_3\rangle =  0, \uparrow, +\rangle,  v_4\rangle =  0, \uparrow, -\rangle,$ $ v_5\rangle =  1, \downarrow, +\rangle,  v_6\rangle =  0, \downarrow, +\rangle,  v_7\rangle =  1, \downarrow, -\rangle$

**Table IV.8**

 Ground state configurations at  $\nu = 3$

Ground State Spin and Isospin Configurations for Different Filling Factors  $\nu$ 

Phase \ $\nu$	-3	-2	-1	0
$\Delta_B \equiv 0$	$\mathbf{S} = \frac{1}{2}\mathbf{e}_z$ $\mathbf{T} = \frac{1}{2}\mathbf{e}_x$ $\mathbf{L} = \frac{1}{2} \sin 2\theta \mathbf{e}_x + \frac{1}{2} \cos 2\theta \mathbf{e}_z$	$\mathbf{S} = \mathbf{e}_z$ $\mathbf{T} = \mathbf{e}_x$ $\mathbf{L} \equiv 0$	$\mathbf{S} = \frac{3}{2}\mathbf{e}_z$ $\mathbf{T} = \frac{1}{2}\mathbf{e}_z$ $\mathbf{L} = \frac{1}{2} \sin 2\theta \mathbf{e}_x - \frac{1}{2} \cos 2\theta \mathbf{e}_z$	$\mathbf{S} = 2\mathbf{e}_z$ $\mathbf{T} \equiv 0$ $\mathbf{L} \equiv 0$
I	$\mathbf{S} = \frac{1}{2}\mathbf{e}_z$ $0 \leq T_z, T_x \leq \frac{1}{2}, T_y \equiv 0$ $0 \leq L_z, L_x \leq \frac{1}{2}, L_y \equiv 0$	$\mathbf{S} = \mathbf{e}_z$ $\mathbf{T} = \sin 2\theta \mathbf{e}_x + \cos 2\theta \mathbf{e}_z$ $\mathbf{L} \equiv 0$	$\mathbf{S} = \frac{3}{2}\mathbf{e}_z$ $0 \leq T_z, T_x \leq \frac{1}{2}, T_y \equiv 0$ $0 \leq L_z, L_x \leq \frac{1}{2}, L_y \equiv 0$	$\mathbf{S} = 2\mathbf{e}_z$ $\mathbf{T} \equiv 0$ $\mathbf{L} \equiv 0$
II	$\mathbf{S} = \frac{1}{2}\mathbf{e}_z$ $\mathbf{T} = \frac{1}{2} \sin 2\theta \mathbf{e}_x - \frac{1}{2} \cos 2\theta \mathbf{e}_z$ $\mathbf{L} = \frac{1}{2}\mathbf{e}_z$	$\mathbf{S} = \mathbf{e}_z$ $\mathbf{T} = \mathbf{e}_z$ $\mathbf{L} \equiv 0$	$\mathbf{S} = \frac{3}{2}\mathbf{e}_z$ $\mathbf{T} = \frac{1}{2} \sin 2\theta \mathbf{e}_x + \frac{1}{2} \cos 2\theta \mathbf{e}_z$ $\mathbf{L} = \frac{1}{2}\mathbf{e}_z$	$\mathbf{S} = 2 \cos^2 \theta \mathbf{e}_z$ $\mathbf{T} = 2 \sin^2 \theta \mathbf{e}_z$ $\mathbf{L} \equiv 0$
III	$\mathbf{S} = \frac{1}{2}\mathbf{e}_z$ $\mathbf{T} = \frac{1}{2}\mathbf{e}_z$ $\mathbf{L} = \frac{1}{2}\mathbf{e}_z$	$\mathbf{S} \equiv 0$ $\mathbf{T} = \mathbf{e}_z$ $\mathbf{L} = -\mathbf{e}_z$	$\mathbf{S} = \frac{3}{2}\mathbf{e}_z$ $\mathbf{T} = \frac{1}{2}\mathbf{e}_z$ $\mathbf{L} = \frac{1}{2} \sin 2\theta \mathbf{e}_x + \frac{1}{2} \cos 2\theta \mathbf{e}_z$	$\mathbf{S} \equiv 0$ $\mathbf{T} = 2\mathbf{e}_z$ $\mathbf{L} \equiv 0$
IV	$\mathbf{S} = \frac{1}{2}\mathbf{e}_z$ $\mathbf{T} = \frac{1}{2}\mathbf{e}_z$ $\mathbf{L} = \frac{1}{2} \sin 2\theta \mathbf{e}_x - \frac{1}{2} \cos 2\theta \mathbf{e}_z$	-	$\mathbf{S} = \frac{3}{2}\mathbf{e}_z$ $\mathbf{T} = \frac{1}{2}\mathbf{e}_z$ $\mathbf{L} = \frac{1}{2}\mathbf{e}_z$	-
V	$\mathbf{S} = \frac{1}{2}\mathbf{e}_z$ $\mathbf{T} = \frac{1}{2}\mathbf{e}_z$ $\mathbf{L} = -\frac{1}{2}\mathbf{e}_z$	-	$\frac{1}{2} \leq S_z \leq \frac{3}{2}, S_x \equiv S_y \equiv 0$ $\frac{1}{2} \leq T_z \leq \frac{3}{2}, T_x \equiv T_y \equiv 0$ $0 \leq L_z, L_x \leq \frac{1}{2}, L_y \equiv 0$	-
VI	-	-	$\mathbf{S} = \frac{1}{2}\mathbf{e}_z$ $\mathbf{T} = \frac{3}{2}\mathbf{e}_z$ $\mathbf{L} = \frac{1}{2} \sin 2\theta \mathbf{e}_x + \frac{1}{2} \cos 2\theta \mathbf{e}_z$	-
VII	-	-	$\mathbf{S} = \frac{1}{2}\mathbf{e}_z$ $\mathbf{T} = \frac{3}{2}\mathbf{e}_z$ $\mathbf{L} = -\frac{1}{2}\mathbf{e}_z$	-

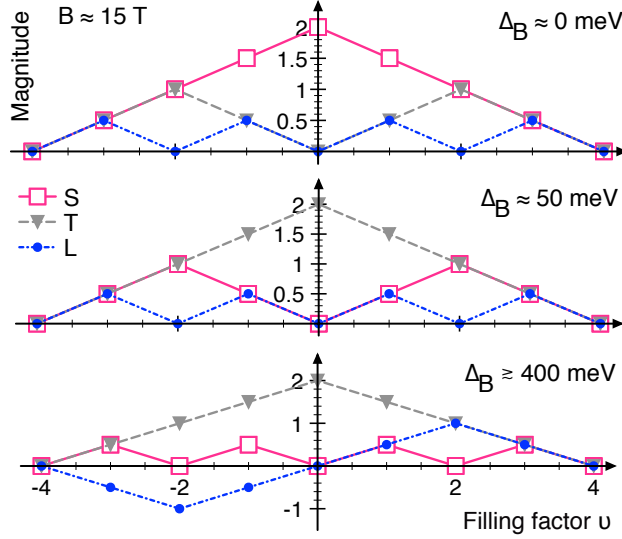
**Table IV.9**

Spin and isospin properties of the different phases observed for negative filling factors.

Phase \ $\nu$	1	2	3
$\Delta_B \equiv 0$	$\mathbf{S} = \frac{3}{2}\mathbf{e}_z$ $\mathbf{T} = \frac{1}{2}\mathbf{e}_x$ $\mathbf{L} = -\frac{1}{2}\sin 2\theta\mathbf{e}_x + \frac{1}{2}\cos 2\theta\mathbf{e}_z$	$\mathbf{S} = \mathbf{e}_z$ $\mathbf{T} = \mathbf{e}_x$ $\mathbf{L} \equiv 0$	$\mathbf{S} = \frac{1}{2}\mathbf{e}_z$ $\mathbf{T} = \frac{1}{2}\mathbf{e}_x$ $\mathbf{L} = \frac{1}{2}\sin 2\theta\mathbf{e}_x - \frac{1}{2}\cos 2\theta\mathbf{e}_z$
I	$\mathbf{S} = \frac{3}{2}\mathbf{e}_z$ $0 \leq T_z, T_x \leq \frac{1}{2}, T_y \equiv 0$ $0 \leq L_z, L_x \leq \frac{1}{2}, L_y \equiv 0$	$\mathbf{S} = \mathbf{e}_z$ $\mathbf{T} = \sin 2\theta\mathbf{e}_x - \cos 2\theta\mathbf{e}_z$ $\mathbf{L} \equiv 0$	$\mathbf{S} = \frac{1}{2}\mathbf{e}_z$ $0 \leq T_z, T_x \leq \frac{1}{2}, T_y \equiv 0$ $0 \leq L_z, L_x \leq \frac{1}{2}, L_y \equiv 0$
II	$\mathbf{S} = \frac{3}{2}\mathbf{e}_z$ $\mathbf{T} = \frac{1}{2}\sin 2\theta\mathbf{e}_x + \frac{1}{2}\cos 2\theta\mathbf{e}_z$ $\mathbf{L} = \frac{1}{2}\mathbf{e}_z$	$\mathbf{S} = \mathbf{e}_z$ $\mathbf{T} = \mathbf{e}_z$ $\mathbf{L} \equiv 0$	$\mathbf{S} = \frac{1}{2}\mathbf{e}_z$ $\mathbf{T} = -\frac{1}{2}\sin 2\theta\mathbf{e}_x + \frac{1}{2}\cos 2\theta\mathbf{e}_z$ $\mathbf{L} = \frac{1}{2}\mathbf{e}_z$
III	$\mathbf{S} = \frac{3}{2}\mathbf{e}_z$ $\mathbf{T} = \frac{1}{2}\mathbf{e}_z$ $\mathbf{L} = \frac{1}{2}\sin 2\theta\mathbf{e}_x + \frac{1}{2}\cos 2\theta\mathbf{e}_z$	$\mathbf{S} \equiv 0$ $\mathbf{T} = \mathbf{e}_z$ $\mathbf{L} = \mathbf{e}_z$	$\mathbf{S} = \frac{1}{2}\mathbf{e}_z$ $\mathbf{T} = \frac{1}{2}\mathbf{e}_z$ $\mathbf{L} = \frac{1}{2}\sin 2\theta\mathbf{e}_x + \frac{1}{2}\cos 2\theta\mathbf{e}_z$
IV	$\mathbf{S} = \frac{3}{2}\mathbf{e}_z$ $\mathbf{T} = \frac{1}{2}\mathbf{e}_z$ $\mathbf{L} = \frac{1}{2}\mathbf{e}_z$	-	$\mathbf{S} = \frac{1}{2}\mathbf{e}_z$ $\mathbf{T} = \frac{1}{2}\mathbf{e}_z$ $\mathbf{L} = \frac{1}{2}\mathbf{e}_z$
V	$\frac{1}{2} \leq S_z \leq \frac{3}{2}, S_x \equiv S_y \equiv 0$ $\frac{1}{2} \leq T_z \leq \frac{3}{2}, T_x \equiv T_y \equiv 0$ $0 \leq L_z, L_x \leq \frac{1}{2}, L_y \equiv 0$	-	-
VI	$\mathbf{S} = \frac{1}{2}\mathbf{e}_z$ $\mathbf{T} = \frac{3}{2}\mathbf{e}_z$ $\mathbf{L} = \frac{1}{2}\sin 2\theta\mathbf{e}_x + \frac{1}{2}\cos 2\theta\mathbf{e}_z$	-	-
VII	$\mathbf{S} = \frac{1}{2}\mathbf{e}_z$ $\mathbf{T} = \frac{3}{2}\mathbf{e}_z$ $\mathbf{L} = \frac{1}{2}\mathbf{e}_z$	-	-

**Table IV.10**

Spin and isospin properties of the different phases for the bilayer system at positive fillings


**Figure IV.11**

Octet polarisation: magnitude of the spin vector (pink solid line, empty squares), valley isospin vector (gray dashed line, filled triangles), and orbital isospin vector (blue dashed-dotted line, filled circles) as a function of the filling factor  $\nu$ , for different values of the bias potential  $\Delta_B$ . Figure from [Knothe and Jolicoeur, 2016].

### IV.3 Bilayer Graphene in the Zero-Energy Landau Level - Results (II): Physical Properties of the Phases

In this section we proceed by checking the many different ground states of bilayer graphene obtained in the previous section for their physical properties. The aim is to understand how different spin and isospin phases ground state configurations manifest itself and reflect, *e.g.*, in the polarisation properties, the electronic occupation of the two different layers, or scaling with the strength of the external fields. In a subsequent step, we discuss possible implications and consequences for experiments and compare our results to existing experimental and theoretical literature.

#### IV.3.1 Octet Polarisation and Hund's Rules

We analyse the spin and isospin polarisation properties within the octet. For the unbiased case  $\Delta_B \equiv 0$ , the dependence of the system's polarisation on the filling factor has been studied previously in reference [Barlas et al., 2008] in the frame of the effective two-band model of bilayer graphene. The authors establish *Hund's rules* for the single particle level occupation: in which order the single particle levels will be occupied when the states of the octet are gradually filled with electrons? What does the successive population of certain single particle levels imply for the values of the total spin and the total isospin at a certain electronic filling? Does the system prefer to balance out or to polarise a certain spin or isospin degree of freedom? In figure IV.11 we show the spin and isospin polarisation for  $B = 15$  T and three bias values  $\Delta_B = 0$  meV,  $\Delta_B = 50$  meV, and  $\Delta_B = 400$  meV. These val-

ues of  $B$  and  $\Delta_B$  are chosen as representative examples, similar behaviour occurs over a broad parameter range throughout the phase diagrams. Here, the *magnitude* of an isospin vector is to be understood as  $\text{magnitude}[\mathbf{e}_z]=\text{magnitude}[\mathbf{e}_x]=1$ .

Depending on the strength of the bias, we observe the following different behaviour:

**Unbiased case,  $\Delta_B \equiv 0$**

At zero bias we recover the results of Barlas et al. [Barlas et al., 2008]: First, the real spin degree of freedom is polarised. Second, under the restrictions imposed by the spin configuration, the polarisation of the valley isospin and, third, the polarisation of the orbital isospin is maximised to the greatest possible extent. This behaviour is shown in the upper plot of figure IV.11.

**$\Delta_B = 50 \text{ meV}$**

In the case of intermediate bias the role of real spin and valley isospin are reversed. Here, the valley degree of freedom is maximised first before maximising the remaining degrees of freedom: first, the real spin and, subsequently to the maximal possible extent, the orbital isospin.

**$\Delta_B = 400 \text{ meV}$**

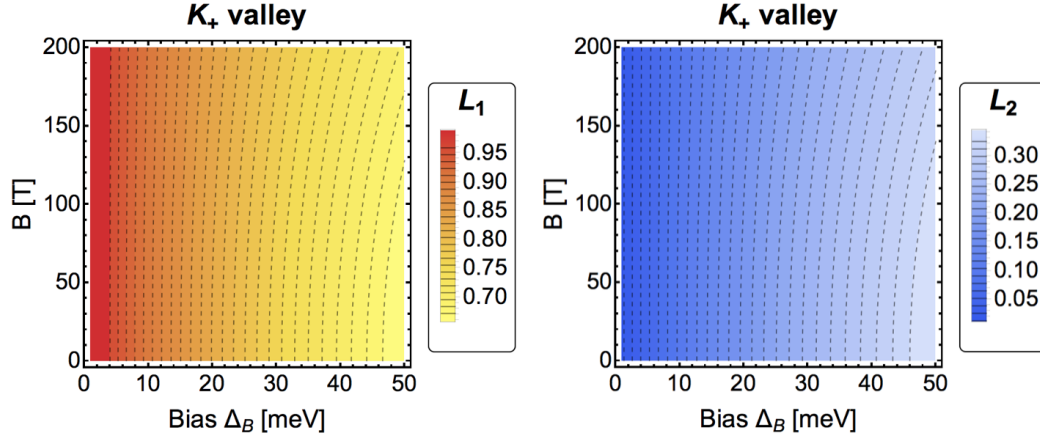
In the case of stronger bias the properties of the orbital isospin polarisation can be altered: At similar behaviour of the valley isospin, we observe states which are antiferromagnetically polarised in the orbital degree of freedom.

These examples at non-zero values of the bias,  $\Delta_B > 0$ , which we show in the central and lower plot of figure IV.11 demonstrate that the simple picture for the octet polarisation as drawn previously in reference [Barlas et al., 2008] may change if the system is biased.

A remark about the generality of these statements is in order: the three examples we show in figure IV.11 represent cuts through the broadest phases of the phase diagrams to be seen in figure IV.3 for all the different fillings  $\nu$ . Due to the rich structure apparent from figure IV.3, exhibiting a variety of different phases, many cuts through the phase diagrams are possible which may yield octet polarisation diagrams different from the ones shown as representative examples in figure IV.11.

### IV.3.2 Layer Polarisation

We discuss how the electrons distribute on the bilayer graphene lattice, given a certain filling factor and ground state phase. The electronic distribution between the two graphene layers has frequently been discussed in previous works, *e.g.*, [Côté

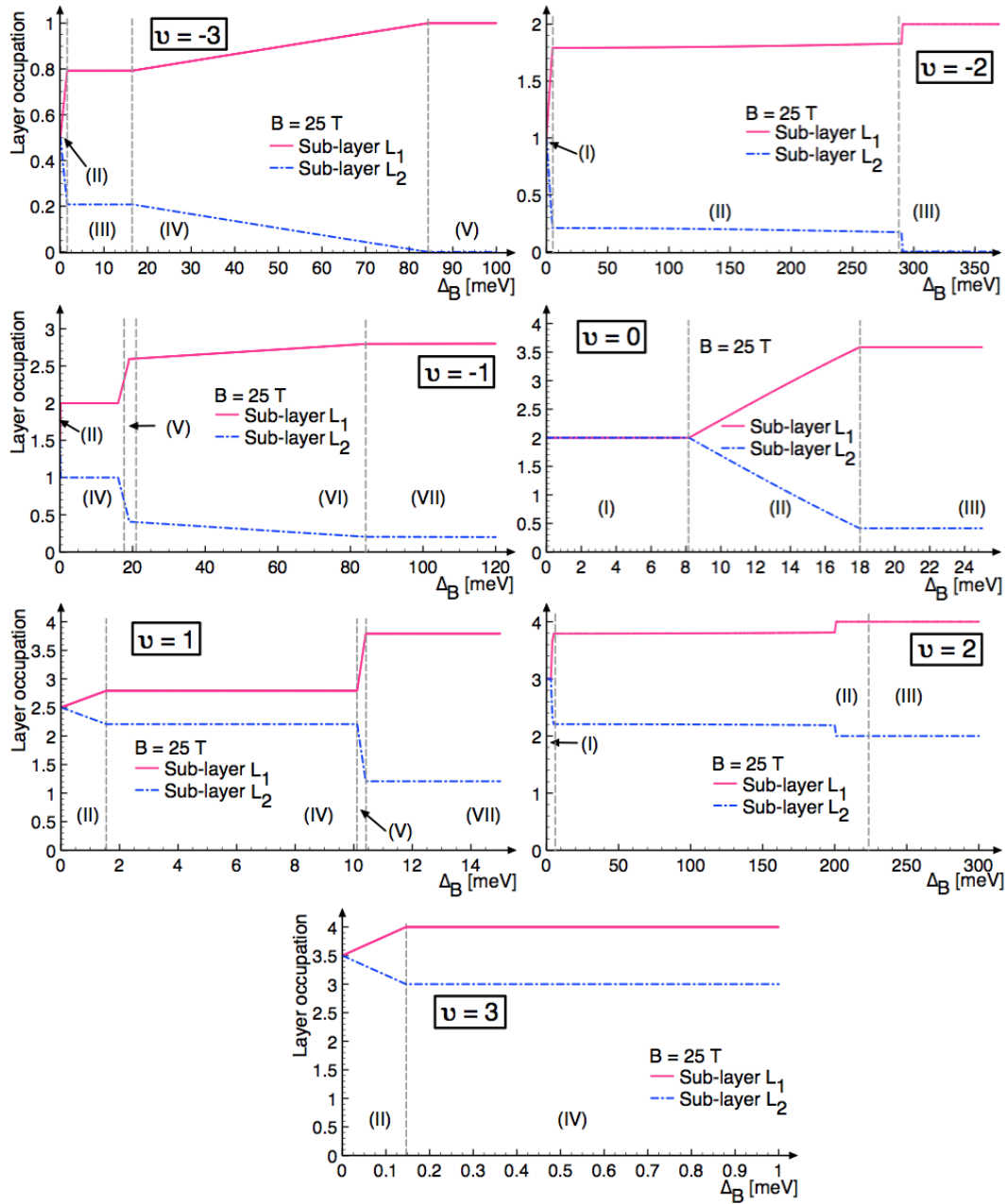


**Figure IV.12**

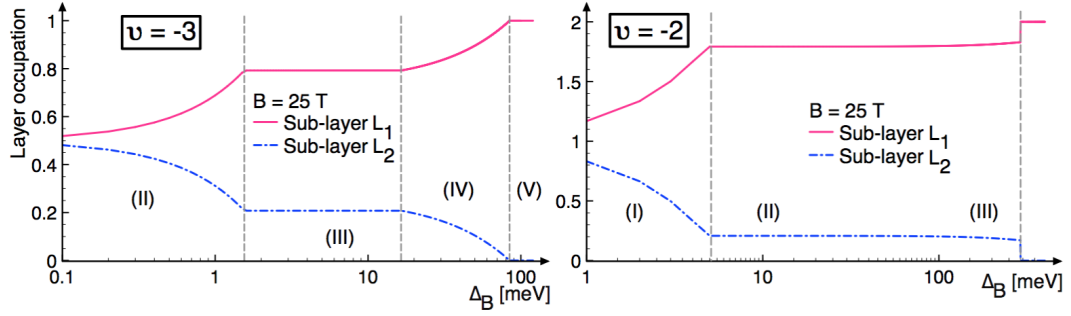
Electronic occupation of the sub-layer  $L_1^{K_+}$  (left) and sub-layer  $L_2^{K_+}$  (right) in the  $K_+$  valley as predicted by the four-band model as a function of magnetic field  $B$  and bias potential  $\Delta_B$ . Both plots use the same colour scale.

et al., 2010; Zhang and MacDonald, 2012; Min et al., 2008], investigating the formation of states exhibiting either interlayer coherence or being fully layer polarised. This is related to exotic properties such as the formation of electronic dipoles [Côté et al., 2010] or the anomalous condensation of excitons [Barlas et al., 2010]. These studies, however, have been carried out within the effective two-band model of bilayer graphene [McCann and Fal'ko, 2006]. As discussed in the introductory section II.1, as well as when deriving the model Hamiltonian of bilayer graphene, section IV.1.1, within this approximate description in terms of only two effective low-energy bands, there is a direct correspondence between the value of the valley index assigned to the electrons and the graphene layer. Therefore, this model automatically predicts a state which is valley polarised also to be *layer polarised*. This is not the case in the four-band model. As pointed out in section II.1 and again in section IV.1.1, it is clear from the form of the four-spinor states, equation (II.34), together with the behaviour of the coefficients for the respective entries given in equation (II.35) that the one-to-one correspondence between valley index and layer occupation is not exact in the description using all four bands. While for electrons occupying the  $n = 0$  orbital the identification valley  $\leftrightarrow$  layer can still be made, for electrons in the  $n = 1$  orbital also for a well-defined single valley index  $+$  or  $-$ , occupation of both layers is enforced as soon as the bias  $\Delta_B$  takes non-zero values.

We quote the notation of section II.1.1, where the coefficients of the state vectors


**Figure IV.13**

Electronic distribution between the two sub-layers, labeled as layer  $L_1$  and layer  $L_2$ , in the various ground state phases at different filling factors.


**Figure IV.14**

Electronic distribution as in figure IV.13 for the examples  $\nu = -3$  and  $\nu = -2$  in logarithmic scale to enhance the visibility of the low-bias regime. For zero bias  $\Delta_B = 0$ , for all filling factors the electrons are distributed equally between the two layers.

within the four-band model in the  $n$ th Landau level are denoted by  $b_{(n),i}$ . If we define the  $n = 0$  state to fully reside on the lower layer (on the atoms labelled by "A" in section II.1.1), for the  $n = 1$  Landau level in the  $K_+$ -valley, the occupation of the upper and the lower layer,  $L_1^{K_+}$  and  $L_2^{K_+}$ , as dictated by the coefficients in equation (II.35), is then given by  $L_1^{K_+} = |b_{(1),1}|^2 + |b_{(1),1}|^2$  and  $L_2^{K_+} = |b_{(1),3}|^2$ , respectively.

The layer occupations  $L_1^{K_+}$  and  $L_2^{K_+}$  in the the  $\{\Delta_B$ - $B$ \}-plane are- plotted in figure IV.12. It becomes evident that although the major weight of the electronic occupation is on sub-layer  $L_1$ , there is no full layer polarisation for the biased system:  $L_2 > 0 \forall \Delta_B \neq 0$ .

This implies important consequences for the properties of the phases we identified in the phase diagrams of figure IV.3. In general, valley polarised phases cannot be automatically identified with fully layer polarised states. In fact, as evident from the form of the state in equation (II.34), full layer polarisation can only be achieved if two conditions are met simultaneously: the electrons must form a state polarised in the valley degree of freedom and at the same time all of them exclusively occupy the  $n = 0$  orbital. We note that our explanations laid out here about the electronic layer occupation are not related to our Hartree Fock protocol or the explicit form of our model Hamiltonian. The behaviour of the electrons *in a given Hartree Fock spin and isospin phase* is rooted only in the properties of the four-band model and the form of the state vectors as detailed above. A solid understanding of the distribution of the electrons on the lattice, however, is vital for a proper understanding of experimental observations. There-

fore, we proceed by extracting the information about the electronic layer polarisation from our Hartree Fock results for each ground state phase at different filling factors  $\nu$ . The line of argumentation is easiest for the case  $\nu = -3$ , where there is only one single electron occupying states within the octet: If we consider the electronic state of an electron in the space  $\mathcal{H} = \mathcal{H}_{orb} \otimes \mathcal{H}_{spin} \otimes \mathcal{H}_{valley}$  written in the basis  $\{1 \uparrow +, 1 \uparrow -, 1 \downarrow +, 1 \downarrow -, 0 \uparrow +, 0 \uparrow -, 0 \downarrow +, 0 \downarrow -\}$  as  $\psi = (a_1, a_2, a_3, a_4, a_5, a_6, a_7, a_8)^t$ , we compute the occupation  $L_1^{K+}$  and  $L_2^{K+}$  of the upper and lower layer, respectively, as:

$$L_1^{K+} = |a_1|^2(|b_{(n),1}|^2 + |b_{(n),4}|^2) + |a_2|^2|b_{(n),3}|^2 + |a_3|^2(|b_{(n),1}|^2 + |b_{(n),4}|^2) \quad (\text{IV.128})$$

$$+ |a_4|^2|b_{(n),3}|^2 + |a_5|^2 + |a_7|^2,$$

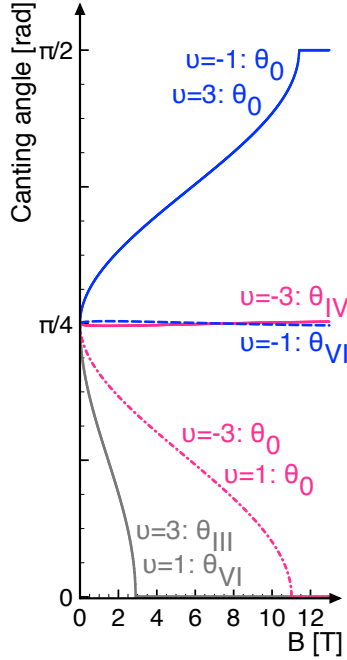
$$L_2^{K+} = |a_1|^2|b_{(n),3}|^2 + |a_2|^2(|b_{(n),1}|^2 + |b_{(n),4}|^2) + |a_3|^2|b_{(n),3}|^2 \quad (\text{IV.129})$$

$$+ |a_4|^2(|b_{(n),1}|^2 + |b_{(n),4}|^2) + |a_6|^2 + |a_8|^2.$$

We observe phases fulfilling the above two requirements for full layer polarisation in the large bias regime of the two lowest filling factors: For filling factor  $\nu = -3$  in phase (V) and for filling  $\nu = -2$  in phase (III). The other states at negative filling factors  $\nu = -1$  and  $\nu = 0$ , respectively, tend towards partially polarised states in the limit of large  $\Delta_B$ . Although the overall orbital isospin is partially negatively polarised along the  $z$ -axis, in these cases not only  $n = 0$ , but also  $n = 1$  orbitals are partially occupied. Therefore, the layer occupation does not tend towards exact layer polarisation. Nevertheless, in this regime we do find states in which the occupation of one of the two layers largely dominates over the occupation of the other layer. This, however, is not the case for the positive filling factors  $\nu = 1, 2, 3$ . In these cases, the states at large bias exhibit overall positive orbital polarisation, hence occupation of the  $n = 1$  orbital dominates over occupation of the  $n = 0$  state. As a consequence, no such thing as full layer polarisation can be seen. Even in the limit of large bias, the electrons will be distributed between both layers. Furthermore, for the unbiased system at  $\Delta_B \equiv 0$ , we observe the electrons to be equally distributed between both graphene layers for all values of the filling factor  $\nu \in [-3, 3]$ . We illustrate these different types of behaviour for the different filling factors  $\nu$  in figures IV.13 and IV.14.

### IV.3.3 Extrapolation to Zero Magnetic Field

We comment on the behaviour of bilayer graphene in the regime of very small magnetic field strengths. Experiments have studied in detail the limit of vanishing magnetic field for this system. It has been argued that in the absence of any magnetic field, there nevertheless emerges magnetic ordering of the spin and isospin degrees of freedom that spontaneously breaks underlying symmetries [Min et al., 2008; Zhang et al., 2010; Nandkishore and Levitov, 2010a; Jung et al., 2011]. This


**Figure IV.15**

Canting angles in orbital space at different filling factors at low magnetic field: blue lines for  $\nu = -1$  or  $\nu = 3$ : unbiased case,  $\theta_0$ , equations (IV.52), (IV.116) (solid) and phase (VI),  $\theta_{VI}$ , equation (IV.66) (dashed). pink curves at  $\nu = -3$  or  $\nu = 1$ : phase (IV),  $\theta_{IV}$ , equation (IV.35), (solid) and unbiased case,  $\theta_0$ , equations (IV.25), (IV.85) (dashed). gray curve at  $\nu = 3$  or  $\nu = 1$ : phase (III),  $\theta_{III}$ , equation (IV.123) and phase (VI),  $\theta_{VI}$ , equation (IV.99). For the angles at filling factors  $\nu = 2$  and  $\nu = -2$  we find  $\theta_0 \equiv \frac{\pi}{4} \forall B$ .

may lead to *spontaneous quantum Hall states* [Zhang et al., 2011; Zhang and MacDonald, 2012; Zhang et al., 2012]. The question arises how these spontaneous quantum Hall states might be related to the quantum Hall states at non-zero magnetic field [Nandkishore and Levitov, 2010b; Kharitonov, 2012a]. Recent experimental investigation draws the following picture: for charge neutral bilayer graphene, the existence of a gapped phase at zero magnetic field in sufficiently clean samples at sufficiently low temperatures is generally established [Freitag et al., 2012; Bao et al., 2012]. This phase is believed to continuously evolve into the gapped  $\nu = 0$  quantum Hall state as the magnetic field increases [Veligura et al., 2012; Velasco Jr et al., 2012; Weitz et al., 2010]. For filling factor  $\nu = 2$ , the observations of reference [Velasco Jr et al., 2014] suggest that the limiting behaviour with  $B \rightarrow 0$  depends on the bias potential applied: while for small bias  $\Delta_B$  the system extrapolates to a vanishing gap, for sufficiently large bias, when the system presumably has entered a phase different from the low bias phase, the gap remains finite as  $B$  goes to zero. Reference [Shi et al., 2016] reports for  $\nu = 1$  a vanishing gap with vanishing magnetic field independently of the bias potential, *e.g.*, for both of the two different phases observed in this study.

We analyse the limit  $B \rightarrow 0$  in our Hartree Fock mean field approach. The results we obtain from our Hartree Fock model Hamiltonian in this regime we present as follows: For each filling factor, we extract the properties of the unbiased case

$\Delta_B \equiv 0$ , as well as the phases that extend to the low magnetic field regime of the phase diagrams in figure IV.3. For the odd filling factors, these phases go along with canting of the orbital degree of freedom: This corresponds to phase (IV) at  $\nu = -3$ , to phase (VI) at  $\nu = -1$ , and to phase (VI) at  $\nu = 1$ . In order to obtain a better understanding of the behaviour at low magnetic fields, we show the evolution of the different canting angles in these respective phases as well as the orbital canting angles of the zero bias phases as functions of  $B$  in figure IV.15. The limiting states which follow from the naive extrapolation  $B \rightarrow 0$  are then summarised in Table IV.11.

From these states at vanishing magnetic fields, we read off the following crucial piece of information:

**Even filling factors**  $\nu = -2, 0, 2$

In the case of even filling of the octet the ground state configurations decompose into simple product states in the orbital degree of freedom. The ground states can be written in the form  $v_i = \sum_{n,\sigma,\tau,\tau'} a_{n,\sigma,\tau,\tau'} |n, \sigma, \tau, \tau'\rangle$  with coefficients  $a_i$ .

**Odd fillings**  $\nu = -3, -1, +1, +3$

For odd fillings, we find states with non-trivial orbital coherence in the limit  $B \rightarrow 0$ :  $v_i = \sum_{n,n',\sigma,\tau,\tau'} a_{n,n',\sigma,\tau,\tau'} |n, n', \sigma, \tau, \tau'\rangle$ . These orbitally coherent states explicitly rely on the quantisation of the Landau level modes by the external magnetic field and thus do not have an obvious counterpart in the zero-field case.

This means that the states at odd filling factors behave differently from the even filling factor states when the field is decreased to zero. While at even fillings the ground state might be connected smoothly to gapped spontaneous quantum Hall states at  $B = 0$ , such extrapolation is not obvious for odd filling factors. Here, the zero magnetic field ground state might be gapless. Indications for such behaviour have been seen experimentally, *e.g.*, in references [Veligura et al., 2012; Velasco Jr et al., 2012; Weitz et al., 2010], and [Shi et al., 2016]. We note, however, that the description of bilayer graphene in our model is valid really only in the limit of high magnetic fields as we rely on Landau level quantisation, on a continuous description and the assumption of sufficiently large Landau level splitting. Hence, Landau level mixing will be important at low fields. The states we extract for  $B \rightarrow 0$  in Table IV.11 can serve only as hints to connect the high magnetic field region and the case  $B = 0$  where spontaneous quantum Hall states have been predicted. We cannot exclude the existence of additional phases in the regime of small but non-zero magnetic field as conjectured, *e.g.*, in references [Weitz et al., 2010] or [Nandkishore and Levitov, 2010b].

$\nu$	Phase	Ground state in the limit $B \rightarrow 0$
-3	$\Delta_B \equiv 0$ (IV)	$ v_1\rangle = \frac{1}{2} \left[  1, \uparrow, +\rangle +  1, \uparrow, -\rangle +  0, \uparrow, +\rangle +  0, \uparrow, -\rangle \right]$ $ v_1\rangle = \frac{1}{\sqrt{2}} \left[  0, \uparrow, +\rangle +  1, \uparrow, +\rangle \right]$
-2	$\Delta_B \equiv 0$ (II)	$ v_1\rangle = \frac{1}{\sqrt{2}} \left[  1, \uparrow, +\rangle +  1, \uparrow, -\rangle \right],  v_2\rangle = \frac{1}{\sqrt{2}} \left[  0, \uparrow, +\rangle +  0, \uparrow, -\rangle \right]$ $ v_1\rangle =  1, \uparrow, +\rangle,  v_2\rangle =  0, \uparrow, +\rangle$
-1	$\Delta_B \equiv 0$ (VI)	$ v_1\rangle = -\frac{1}{\sqrt{2}} \left[  1, \uparrow, +\rangle +  1, \uparrow, -\rangle \right],  v_2\rangle = \frac{1}{\sqrt{2}} \left[  0, \uparrow, +\rangle +  0, \uparrow, -\rangle \right],$ $ v_3\rangle = -\frac{1}{2} \left[  1, \uparrow, +\rangle -  1, \uparrow, -\rangle +  0, \uparrow, +\rangle -  0, \uparrow, -\rangle \right]$ $ v_1\rangle =  1, \uparrow, +\rangle,  v_2\rangle =  0, \uparrow, +\rangle,  v_3\rangle = \frac{1}{\sqrt{2}} \left[  1, \downarrow, +\rangle +  0, \downarrow, +\rangle \right]$
0	$\Delta_B \equiv 0$ (III)	$ v_1\rangle =  1, \uparrow, +\rangle,  v_2\rangle =  1, \uparrow, -\rangle,  v_3\rangle =  0, \uparrow, +\rangle,  v_4\rangle =  0, \uparrow, -\rangle$ $ v_1\rangle =  1, \uparrow, +\rangle,  v_2\rangle =  1, \downarrow, +\rangle,  v_3\rangle =  0, \uparrow, +\rangle,  v_4\rangle =  0, \downarrow, +\rangle$
1	$\Delta_B \equiv 0$ (VI)	$ v_1\rangle =  1, \uparrow, +\rangle,  v_2\rangle =  1, \uparrow, -\rangle,  v_3\rangle =  0, \uparrow, +\rangle,  v_4\rangle =  0, \uparrow, -\rangle,$ $ v_5\rangle = \frac{1}{2} \left[  1, \downarrow, +\rangle +  1, \downarrow, -\rangle -  0, \downarrow, +\rangle -  0, \downarrow, -\rangle \right]$ $ v_1\rangle =  1, \uparrow, +\rangle,  v_2\rangle =  1, \downarrow, +\rangle,  v_3\rangle =  0, \uparrow, +\rangle,$ $ v_4\rangle =  0, \downarrow, +\rangle,  v_5\rangle = \frac{1}{\sqrt{2}} \left[  1, \uparrow, -\rangle +  0, \uparrow, -\rangle \right]$
2	$\Delta_B \equiv 0$ (II)	$ v_1\rangle =  1, \uparrow, +\rangle,  v_2\rangle =  1, \uparrow, -\rangle,  v_3\rangle =  0, \uparrow, +\rangle,  v_4\rangle =  0, \uparrow, -\rangle,$ $ v_5\rangle = \frac{1}{\sqrt{2}} \left[  1, \downarrow, +\rangle +  1, \downarrow, -\rangle \right],  v_6\rangle = \frac{1}{\sqrt{2}} \left[  0, \downarrow, +\rangle +  0, \downarrow, -\rangle \right]$ $ v_1\rangle =  1, \uparrow, +\rangle,  v_2\rangle =  1, \uparrow, -\rangle,  v_3\rangle =  0, \uparrow, +\rangle,$ $ v_4\rangle =  0, \uparrow, -\rangle,  v_5\rangle =  1, \downarrow, +\rangle,  v_6\rangle =  0, \downarrow, +\rangle$
3	$\Delta_B \equiv 0$ (III)	$ v_1\rangle =  1, \uparrow, +\rangle,  v_2\rangle =  1, \uparrow, -\rangle,  v_3\rangle =  0, \uparrow, +\rangle,  v_4\rangle =  0, \uparrow, -\rangle,$ $ v_5\rangle = \frac{1}{2} \left[  1, \downarrow, +\rangle +  1, \downarrow, -\rangle +  0, \downarrow, +\rangle +  0, \downarrow, -\rangle \right],$ $ v_6\rangle = \frac{1}{2} \left[  1, \downarrow, +\rangle +  1, \downarrow, -\rangle -  0, \downarrow, +\rangle -  0, \downarrow, -\rangle \right],$ $ v_7\rangle = \frac{1}{2} \left[  1, \downarrow, +\rangle -  1, \downarrow, -\rangle +  0, \downarrow, +\rangle -  0, \downarrow, -\rangle \right]$ $ v_1\rangle =  1, \uparrow, +\rangle,  v_2\rangle =  1, \uparrow, -\rangle,  v_3\rangle =  0, \uparrow, +\rangle,  v_4\rangle =  0, \uparrow, -\rangle,$ $ v_5\rangle =  1, \downarrow, +\rangle,  v_6\rangle =  0, \downarrow, +\rangle,  v_7\rangle = \frac{1}{\sqrt{2}} \left[  1, \downarrow, -\rangle +  0, \downarrow, -\rangle \right]$

**Table IV.11**

 Ground state configurations in the limit  $B \rightarrow 0$ .

### IV.3.4 Properties of the Phases - Summary

In this section we analysed several different aspects related to the physical properties of the many different possible ground state phases of bilayer graphene under external electric and magnetic fields identified in the previous section. The major aim was to understand how the individual phases might manifest itself in experiment and what might be features to distinguish them. We summarise the key findings of this section as follows:

#### Summary: Physical Properties of the Phases

- We analysed the octet polarisation properties when the eight single particle levels are successively populated with electrons. We saw that a non-zero bias potential can lead to **novel Hund's rules** compared to the unbiased system: depending on the value of the bias, either the spin or the valley isospin is polarised first or the direction of polarisation for the orbital isospin is reversed.
- When we studied the electronic distribution on the bilayer graphene lattice within the different phases within the frame of the four-band model, we saw that, generally, **no full layer polarisation**, with electrons residing on only one of the graphene lattices, is achieved, not even for the fully valley polarised configurations.
- For the regime of very small magnetic field strengths we observed that in the limit  $B \rightarrow 0$  the ground state configurations at even values of the filling factor tend to assume simple product states in the orbital degree of freedom. This suggests **smooth extrapolation to the zero field spontaneous quantum Hall states for  $\nu$  even**. At odd filling factors, however, this is not the case and the **limit states at vanishing magnetic field exhibit non-trivial orbital coherence for  $\nu$  odd**.

### IV.3.5 Relation to Experiment and to Theoretical Studies

In section IV.2 we saw that bilayer graphene in the quantum Hall regime exhibits a plethora of possible spin and isospin ground state phases for different octet filling factors and at different values of external electric and magnetic fields. In section IV.3 we gained insight in the behaviour and physical properties of the individual different phases. In a subsequent step, we now compare the predictions of our Hartree Fock mean field model treatment to the observations of experimental in-

vestigations as well as to earlier theoretical studies.

The effect of external magnetic and electric fields on graphene mono- and multilayers has been under intense experimental investigation [Weitz et al., 2010; Kim et al., 2011; Bao et al., 2012; Velasco Jr et al., 2012; Maher et al., 2013; Velasco Jr et al., 2014; Lee et al., 2014; Maher et al., 2014; Shi et al., 2016; Hunt et al., 2016]. We first briefly review the picture drawn by experiments and compare our work with experimental findings, before discussing similarities and differences compared to theoretical approaches [Castro et al., 2010; Côté et al., 2010; Lambert and Côté, 2013; Shizuya, 2012].

The fact that external fields influence the ordering of spin, valley, and orbital degrees of freedom, and that transitions between states of different spin and isospin order can be induced by tuning externally applied fields, has been realised several years ago [Weitz et al., 2010; Kim et al., 2011]. Recently, there has been tremendous improvement in the quality of the samples, and data became available in a much wider parameter range. This has led to detailed insights about the nature of the different phases at different filling factors. By carefully monitoring sudden changes in the conduction properties, one infers the number of phase transitions upon varying the bias potential at fixed magnetic field  $B$ :

- At  $\nu = \pm 3$ , a single phase transition has been seen [Weitz et al., 2010; Maher et al., 2013, 2014] at zero bias  $\Delta_B \equiv 0$ .
- For  $\nu = \pm 2$ , references [Weitz et al., 2010; Velasco Jr et al., 2014; Lee et al., 2014; Hunt et al., 2016; Maher et al., 2014] report multiple transitions at non-zero bias while there is no sign of phase transition at zero bias.
- Both types of transitions, at  $\Delta_B \equiv 0$  as well as at  $|\Delta_B| \neq 0$ , have been observed [Weitz et al., 2010; Shi et al., 2016; Hunt et al., 2016; Maher et al., 2014] at  $\nu = \pm 1$ .
- The properties at charge neutrality  $\nu = 0$  have been investigated in references [Weitz et al., 2010; Kim et al., 2011; Bao et al., 2012; Velasco Jr et al., 2012; Lee et al., 2014; Hunt et al., 2016; Maher et al., 2013]. While early investigations reported one transition at non-zero bias [Weitz et al., 2010; Kim et al., 2011], more recent studies report signatures of transitions at two different values of the bias potential implying at least three different phases.

It is common belief that for large bias potential the system will be in a spin and isospin configuration that maximises layer polarisation. Accordingly, in the opposite limit of very small or vanishing bias, the spin and isospin ordering is assumed

to be different from maximally possible layer polarisation.

We compare these experimental observations to the predictions of our calculations. In parameter ranges comparable to those of the respective experiments, we examine the different phases and the number of phase transitions at fixed magnetic field and increasing bias:

#### Filling factor $\nu = -3$

For filling factor  $\nu = -3$ , we see in our model two different possible scenarios, depending on the strength of the magnetic fields: for  $B < 11$  T we identify the sequence of transitions (I)  $\rightarrow$  (IV)  $\rightarrow$  (V), whereas for higher magnetic fields  $B > 11$  T the series of transitions (II)  $\rightarrow$  (III)  $\rightarrow$  (IV)  $\rightarrow$  (V) is observed.

Maher et al. [Maher et al., 2014] as well as Hunt et al. [Hunt et al., 2016] have studied the bilayer graphene system at  $\nu = \pm 3$  in the range of the bias  $|\Delta_B| \approx 0 - 34$  meV for magnetic fields  $B = 9$  T and  $B = 31$  T, respectively. We may attribute the single transition close to zero bias observed in both references to the transitions (I)  $\rightarrow$  (IV) at lower magnetic field or (II)  $\rightarrow$  (III) at higher magnetic field value, respectively. The values of the bias potential at which these transitions occur in our model are both small compared to the energy scales of the other phases of the phase diagram:  $\Delta_B \approx 0.185$  meV and  $\Delta_B \approx 2.5$  meV, respectively. The fact that no second phase transition is observed by Hunt et al. [Hunt et al., 2016] may imply that phase (IV) has not yet been reached at these values of the bias. If the zero-bias phases we find in the Hartree Fock treatment are destroyed by fluctuations beyond Hartree Fock, then this may explain a zero-bias transition between oppositely polarised states.

#### Filling factor $\nu = \pm 2$

For  $\nu = \pm 2$ , the sequence of transitions in our model is the same for all values of the magnetic field: (I)  $\rightarrow$  (II)  $\rightarrow$  (III) as a function of increasing bias. The second transition (II)  $\rightarrow$  (III), however, occurs at much higher values of the bias potential than ever shown in experimental data:  $\Delta_B \gtrsim 300$  meV in figure IV.3.

Our predictions are consistent with the observations at  $\nu = \pm 2$  of Velasco et al. [Velasco Jr et al., 2014], Maher et al. [Maher et al., 2014], Hunt et al. [Hunt et al., 2016], Lee et al. [Lee et al., 2014] identifying one phase transition at non-zero bias  $\Delta_B > 0$ . So the low-bias phase has valley coherence and this coherence is destroyed beyond a critical bias. The slope of the I/II transition

line in Velasco et al. is  $0.72 \text{ mV nm}^{-1} \text{ T}^{-1}$  while the Hartree Fock value is  $0.55 \text{ mV nm}^{-1} \text{ T}^{-1}$ .

#### Filling factor $\nu = \pm 1$

At fillings  $\nu = \pm 1$ , our model again suggests two different sequences of possible phase transitions depending on the value of the external magnetic field: for  $\nu = -1$  and magnetic fields  $B < 11.3 \text{ T}$ , we go through the sequence (I)  $\rightarrow$  (III)  $\rightarrow$  (VI)  $\rightarrow$  (VII). In the opposite case  $B > 11.3 \text{ T}$  we find (II)  $\rightarrow$  (IV)  $\rightarrow$  (V)  $\rightarrow$  (VI)  $\rightarrow$  (VII) when increasing  $\Delta_B$ . In the case  $\nu = +1$ , at small magnetic field  $B < 11.3 \text{ T}$ , the sequence is (I)  $\rightarrow$  (III)  $\rightarrow$  (VI) / (VII), whereas for larger field  $B > 11.3 \text{ T}$  it is (II)  $\rightarrow$  (IV)  $\rightarrow$  (V)  $\rightarrow$  (VI).

This may be compared to the experimental results of Shi et al. [Shi et al., 2016], Hunt et al. [Hunt et al., 2016], and Maher et al. [Maher et al., 2014], where the states  $\nu = \pm 1$  are probed for  $B = 28 \text{ T}$  in the range  $|\Delta_B| \approx 0 - 17 \text{ meV}$ , and in the range  $|\Delta_B| \approx 0 - 34 \text{ meV}$  at magnetic fields  $B = 31 \text{ T}$  and  $B = 9 \text{ T}$ , respectively. The observed transition near zero bias can be attributed to the phase transitions (I)  $\rightarrow$  (III) or (II)  $\rightarrow$  (IV), respectively, which occur in our model at relatively small values of  $\Delta_B$  compared to the range of the broadest phases of the phase diagram and to the overall range of the bias. The phase (II) carries valley coherence as proposed in Shi et al. A second transition observed in experiment at non-zero value of the bias might be identified with the transitions (III)  $\rightarrow$  (VI) or (IV)  $\rightarrow$  (V)/(VI) at  $\nu = -1$  and (III)  $\rightarrow$  (VI) / (VII) or (IV)  $\rightarrow$  (V)/(VII) at  $\nu = 1$ , respectively. In fact, Maher et al. have proposed that the finite bias transition they see at  $\nu = +1$  is the (IV)/(VII) transition.

#### Filling factor $\nu = 0$

In the  $\nu = 0$  case, the series of phases suggested by our model does not depend on the system parameters: for any value of the magnetic field, we observe two successive phase transitions (I)  $\rightarrow$  (II)  $\rightarrow$  (III) upon increasing bias potential. Here, phase (II) is a phase featuring intermediate values of the spin and the valley isospin, flanked by simpler, fully spin polarised (I) and fully valley polarised (III) phases.

This is consistent with recent experimental studies of the  $\nu = 0$  state by Lee et al. [Lee et al., 2014] and Hunt et al. [Hunt et al., 2016], where two transitions at two distinct non-zero values of the bias potential have been observed. The  $\nu = 0$  phase diagram shown in reference [Hunt et al., 2016] figure 2D also agrees well with the corresponding phase diagram predicted by our calculations. Furthermore, Maher et al. [Maher et al., 2013] have observed a critical

bias increasing as a function of the magnetic field, as it features in our model.

From this discussion we learn that our calculation reproduces several features observed experimentally in bilayer graphene at different filling factors. Notably, for every  $\nu$  we are able to identify phase transitions detected in experiment with transitions predicted by our model. However, the range of the bias in the data presented for the various different experimental studies only covers part of the phase diagrams of figure IV.3. We conjecture that in particular the phase of maximal orbital polarisation, corresponding to the phase with the highest number in each case, presumably has not been reached in experiments for the filling factors  $\nu = -3, \nu = -2, \nu = -1$ , and  $\nu = 2$ . As a consequence, according to the properties of the four-band model as discussed in sections II.1.1 and IV.3.2, maximal possible layer polarisation possibly has not been achieved experimentally. Furthermore, from the phase diagrams of figure IV.3, we conjecture that for example at fillings  $\nu = -3$  or  $\nu = 1$  a richer picture of different phases and phase transitions may emerge when studying the system in an extended parameter range for  $B$  and for  $\Delta_B$ .

We make the remark, however, that the individual experiments often differ in technical details such as gating or the way the sample is prepared: for example, references [Weitz et al., 2010; Velasco Jr et al., 2012, 2014; Shi et al., 2016] investigate the properties of suspended bilayer graphene, reference [Lee et al., 2014] uses double bilayer graphene heterostructures separated by a hexagonal boron nitride dielectric, while in references [Hunt et al., 2016; Maher et al., 2013, 2014] the bilayer graphene samples are encapsulated by hexagonal boron nitride. We have not tried to take into account the additional effects due to these different substrates, gatings, dielectrics, or encapsulations. These differences are likely to alter the physics of the phase competition [Hunt et al., 2016].

Let us now compare our results to previous theoretical investigations. Reference [Lambert and Côté, 2013] presents a detailed Hartree Fock study of bilayer graphene zero energy octet using the effective two-band model. They obtain the phase diagram of their model for all different filling factors  $\nu \in [-3, 3]$  for  $B = 10$  T as a function of the bias. The vast majority of states they deduce from their model is orbitally incoherent. Phases exhibiting orbital coherence emerge only at very large values of the bias. The authors do not take into account the presence of the Dirac sea in reference [Lambert and Côté, 2013]. It has become clear, however, that these electrons of the Dirac sea do play a non-silent role: as we discuss in section IV.1.1, Shizuya shows in reference [Shizuya, 2012] in a four-band model the importance of this effect. The ground state configurations identified in this treatment, *e.g.*, at

zero bias can be coherent superpositions of the  $n = 0$  and  $n = 1$  states. Moreover, in this analysis, the  $n = 1$  state lies lower in energy than the  $n = 0$  orbital while in reference [Lambert and Côté, 2013] generally the  $n = 0$  state is populated first. These results, however, were obtained from a somewhat simplified model with respect to Lambert and Côté in reference [Lambert and Côté, 2013].

Our treatment contains the ingredient of a realistic band structure, *i.e.*, four bands with all the  $\gamma_i$  couplings and we have included the Dirac sea exchange.

We further comment on the discussion of reference [Hunt et al., 2016] containing a detailed theoretical analysis of their experimental results. Using the four-band model, the authors take into account both, the splitting  $\Delta_{01}$  between  $n = 0$  and  $n = 1$  orbitals due to the presence of the Dirac sea electrons as discussed by Shizuya [Shizuya, 2012], as well as the  $\gamma_i$  couplings of the bilayer lattice. Furthermore, they incorporate the effect of screening due to the hexagonal boron nitride dielectric in their setup by a modified, phenomenological potential to model the effective, screened Coulomb interaction. This screening also effects the splitting  $\Delta_{01}$ . Investigating this screened model using Hartree Fock as well as density matrix renormalisation group techniques, they come to explain the phase transitions observed in their experiment in terms of solely incoherent phases.

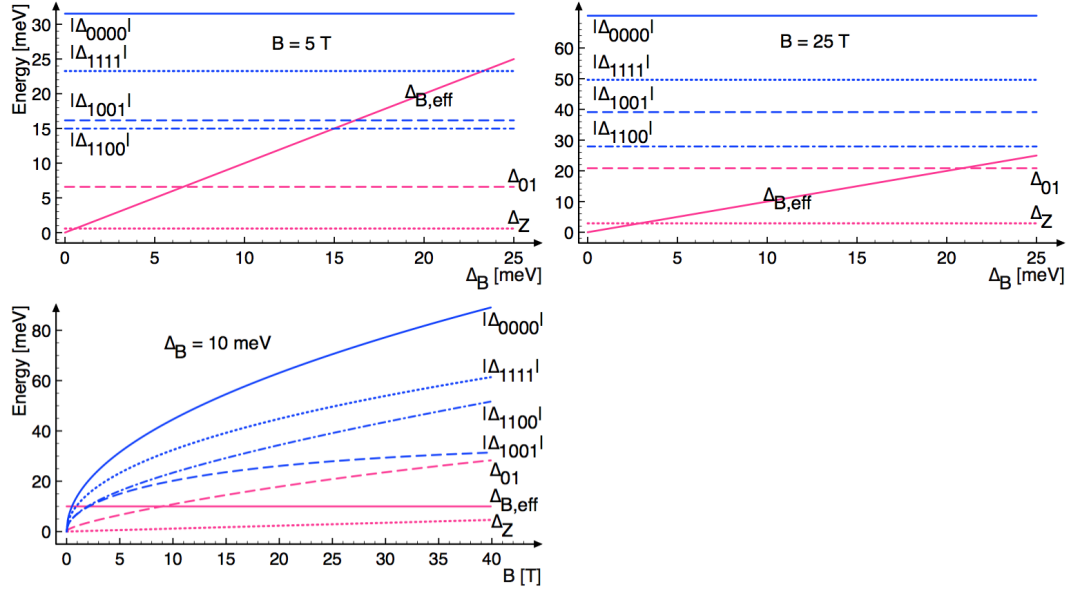
We note that in our model we do not account for any screening effects. Let us comment on the possible implications of screening corrections for our analysis. Polarisation effects in bilayer graphene have been discussed previously using the effective two-band model, when the bare Coulomb interaction between the electrons is replaced by an effective interaction potential  $V_{eff}$  [Nandkishore and Levitov, 2010a; Gorbar et al., 2010, 2011, 2012a,b; Papić and Abanin, 2014]. A static approximation, *i.e.*, neglecting the frequency dependence of the polarisation function, has been shown to overestimate the screening effects Gorbar et al. [2010, 2011, 2012b]. If the full frequency dependence is considered, the values for transport gaps in the quasiparticle spectrum are comparable to those observed in experiment and the experimentally observed linear scaling of these gaps with magnetic field is reproduced [Gorbar et al., 2012a,b]. Incorporating this time dependent dynamical correction, however, goes beyond the Hartree-Fock description chosen in our work. Instead, we renormalise the bare Coulomb potential by an effective dielectric constant  $\epsilon$  (*cf.* the discussion in section IV.1.1). This approximation has been used successfully in earlier works (*cf.*, *e.g.*, references [Shizuya, 2012; Lambert and Côté, 2013; Barlas et al., 2010; Côté et al., 2011, 2010]). In reference [Lambert and Côté, 2013], Lambert and Côté demonstrate within the two-band model that this approximation, while overestimating the transport gaps, qualitatively reproduces the behaviour of the ground state phases as compared to a treatment which accounts for

screening. Further justification comes from reference [Nandkishore and Levitov, 2010a], where the authors evaluate the generalised Haldane pseudopotentials for the electronic interaction using the effective two-band model and find them to be of comparable magnitude and behaviour, whether the screened or the unscreened Coulomb potential is used. It has to be noted additionally that the effect of screening should become weaker with increasing magnetic field at values where the descriptions within the two-band model are no longer valid. Another effect that may become important when comparing our results to experimental data is the screening of the external interlayer potential. It has been observed in density functional theory [Min et al., 2007] that the effective bias potential felt by the electrons might be reduced by screening effects. According to the results of reference [Min et al., 2007], this should lead to a simple linear relation between the external bias  $\Delta_{B,ext}$  and the screened potential felt by the electrons:  $\Delta_{B,screened} = a + b\Delta_{B,ext}$ , where the parameters in reference [Min et al., 2007] are approximately  $a = -0.5$  and  $b = 0.25$ .

#### IV.4 Bilayer Graphene in the Zero-Energy Landau Level - Conclusions and Remarks

In this chapter, we presented our studies on the spin and isospin properties of bilayer graphene under electric and magnetic external fields. We focused on the octet of quasi zero-energy levels near charge neutrality for which the filling factor is in the range  $[-3, +3]$  using a Hartree Fock method which is known to capture the main features of quantum Hall ferromagnetism. We have derived a microscopical model of bilayer graphene in the quantum Hall regime which retains all the four bands and which includes the tight-binding hopping parameters  $\gamma_0, \gamma_1, \gamma_3, \gamma_4$  that weakly break particle-hole symmetry. Furthermore, in the Hartree Fock calculation we have included the Coulomb exchange interaction with the occupied Dirac sea which restores the particle-hole symmetry in the absence of  $\gamma_4$ . The splitting between  $n = 0$  and  $n = 1$  orbitals is thus governed by the competition between band structure effects and Lamb-shift-like exchange interactions. The spin and isospin configuration then is determined by a careful balance between all these different symmetry breaking terms.

This is illustrated in figure IV.16, where we show the evolution of the energy splittings in spin space, valley isospin space, and orbital isospin space,  $\Delta_Z$ ,  $\Delta_{B,eff}$ , and  $\Delta_{01}$ , as well as the matrix elements of the Coulomb interaction as computed in section IV.1 as functions of the external magnetic and electric fields for different parameters. The curves for the valley breaking matrix elements,  $X_{1111}$ ,  $X_{0000}$ ,  $X_{1001}$ , and  $X_{1100}$  are slightly offset with respect to the valley conserving terms but comparable in their overall behaviour and are therefore not shown for the sake of vis-


**Figure IV.16**

Dependence on the external fields of the energy splittings in valley space, orbital space, and spin space,  $\Delta_{B,eff}$ ,  $\Delta_{01}$ , and  $\Delta_Z$ , respectively, as well of the valley conserving exchange matrix elements of the Coulomb interaction,  $\Delta_{1111}$ ,  $\Delta_{0000}$ ,  $\Delta_{1001}$ , and  $\Delta_{1100}$ , as computed from equation (IV.18). Figure from [Knothe and Jolicœur, 2016].

ibility. The explicit expressions for all the Coulomb matrix elements can be found in appendix C.

In the regime of small bias and large magnetic field,  $\Delta_{01}$  plays a pivotal role before being washed out at sufficiently strong bias by  $\Delta_{B,eff}$  acting as a "Zeeman-like" splitting in valley space.

In this regime of complex interplay between the various different symmetry breaking effects, we have studied the spin and isospin properties of this quantum Hall ferromagnetic system within Hartree Fock mean field theory:

## Summary: Graphene Bilayer in the Zero-Energy Landau Level

- In a first part, section IV.2, we have derived the **Hartree Fock ground state phase diagrams** in the plane spanned by the bias potential and the magnetic field for all the non-trivial filling factors  $[-3, +3]$  of the zero energy octet. We identified a total of **32 different phases**, where each phase is characterised by a unique spin and isospin configuration. Each of these phases was analysed in detail, yielding analytic expressions for the ground state wave functions, the values of the total spin and isospin degrees of freedom, as well as the critical parameters where transitions between the respective phases occur in our model.
- Subsequently, in section IV.3, we dwelled further on the **physical properties** of the individual phases: we analysed the **Hund's rules** for the spin and isospin polarisation upon successive population of the octet states, **electronic distribution** on the bilayer graphene lattice, and the possibility of layer polarisation in the different phases, as well as the **extrapolation to very small magnetic fields** of our model.
- Finally, we made the attempt to connect our results to existing experimental studies, by relating our ground state phases to phases observed in bilayer graphene in previous experimental investigations. When comparing to the various experimental results on bilayer graphene in the quantum Hall regime we find that our model can reproduce several features observed experimentally: most prominently, we are able to relate to the huge variety of different phases suggested by experiment by relating to the **number of ground state phases and phase transitions** predicted by our model.

We comment on possible implications of our results for future theoretical and experimental investigations:

For even filling factors  $\nu = 0, \pm 2$  our results are the same as the Hartree Fock treatment of Lambert and Côté [Lambert and Côté, 2013]. However for odd fillings  $\nu = \pm 1, \pm 3$  we find phases with non-trivial orbital coherence: see figure IV.3. These phases are thus of fundamentally different nature than those predicted in reference [Lambert and Côté, 2013]. As these orbital coherent phases appear at experimentally accessible values of the bias potential, it is plausible that they are among the phases actually observed in experiment. For fillings  $\nu = -3, -1$  they extend to all values of the magnetic field but require a specific range of bias. For

$\nu = +3, +1$  the orbital phases are restricted to the small-field regime which may be out of range of our approach due to Landau level mixing.

For odd filling factors we observe at small bias a transition from an orbital coherent phase to orbitally incoherent phases as a function of the magnetic field strength: the vector of orbital isospin rotates from a canted position at small magnetic field to a partially polarised configuration above a critical field strength  $B_{crit}$ . Such transitions with  $B$  have not been reported previously in the literature, as, *e.g.*, reference [Lambert and Côté, 2013] restricts its investigations of the ground state phases to the phase diagram at a single fixed value of the magnetic field. We conclude that varying the magnetic field can trigger the emergence of phase transitions for all odd  $\nu$ . We thus conjecture the existence of more phases and even richer phase diagrams when bilayer graphene is studied over a sufficiently large range of  $B$  values.

It remains to be mentioned that the fact that we observe a ferromagnetic state at charge neutrality  $\nu = 0$  for small values of the bias potential is at odds with the common belief that the  $\nu = 0$  bilayer graphene quantum Hall state is in a canted antiferromagnetic configuration. In analogy to the argumentation in the case of monolayer graphene, the canted antiferromagnetic phase is believed to explain the insulating state observed in this regime. We cannot explain insulating behaviour for the charge neutral state at low bias within our model. Therefore, it remains an intriguing question how our mean field Hartree Fock results would be influenced if analysed on the same footing as our study of monolayer graphene presented in chapter III [Knothe and Jolicœur, 2015]: considering a finite piece of bilayer graphene, in which way the phases might be influenced by short range symmetry breaking effects or the influence of a boundary potential? More precisely, the question arises whether and for which ground state phases in this scenario gapless, conducting edge states may be found. In the monolayer graphene case, we found the possibility for gapless edge states both in the canted antiferromagnetic and in the ferromagnetic phase due to the properties of the edge phases forming in the vicinity of the boundary of the sample. Whether the same phenomena might be observed in the case of bilayer graphene remains subject to future investigations.



---

## Valley Order of the Bi(111) Surface States in the Quantum Hall Regime

---

### V.1 Quantum Hall States on the (111) Surface of Bismuth - Introduction

This chapter presents preliminary results on the ground state structure of the Bi(111) surface states in the quantum Hall regime. Motivation stems from the recent insight that novel two-dimensional electron systems, as found on the two-dimensional surfaces of three dimensional materials, may exhibit unusual quantum Hall phenomena. For example, the class of topological crystalline insulators [Fu, 2011; Ando and Fu, 2015] has been arousing interest in the past years: in these kind of materials, the discrete point group symmetries of the crystal play a crucial role by inducing a particular topological nature for the electronic structure. We are interested in studying quantum Hall physics in similarly crystalline materials where we focus on the two-dimensional surfaces of three-dimensional crystals. A sample surface may break the crystalline symmetries. While low-symmetry surfaces of a crystal may not support robust surface states, for high-symmetry surfaces, *i.e.*, for surfaces where certain non-trivial symmetries are preserved, such surface states may be found [Fu, 2011; Hsieh et al., 2012]. These surface states at two-dimensional high-symmetry surfaces of three-dimensional crystals will be our object of interest in the following.

Studying these two-dimensional electron systems in the quantum Hall regime may be particularly promising thanks to the additional richness and complexity induced by the particular form of the electronic band structure in the respective

crystal under study. As exposed in the introductory chapter I, in the conventional two-dimensional (free) electron gas the dispersion of the electrons is simply quadratic. For materials of the graphene family we learned about the structure of two circular, linearly (monolayer graphene) or quadratically (bilayer graphene) dispersing cones, isolated within a low-energy description, and well separated in momentum space. The picture may become much richer when considering certain surfaces of crystalline materials. In these materials, for instance, multiple valleys may appear which may be of different than spherical shape. Examples include the three elliptical valleys of SnTe(001) [Hsieh et al., 2012; Ast and Höchst, 2001], the six approximately elliptical valleys of the (111) surface of elemental Bismuth [Du et al., 2016; Feldman et al., 2016], or the two valleys of half-moon shape of the (001) surface of  $\text{Sn}_{1-x}\text{Pb}_x\text{Se}$  mono crystals [Dziawa et al., 2012].

The presence of several valleys of unusual, anisotropic shape poses novel questions: one may ask for the *valley ordering*, *i.e.*, how a set of  $k$  valleys is populated when there are  $N < k$  electrons present in the system. This leads to the question of the electronic distribution both in reciprocal and in real space. Special interest has been devoted to the study of *nematic* phases that spontaneously lower the symmetry of the underlying Hamiltonian\* [Feldman et al., 2016; Li et al., 2016; Sodemann et al., 2017].

Quantum Hall systems with multiple valleys have been studied in the previous years in two-dimensional electron gases forming in quantum wells of pure Aluminium/Arsenic layers [Maezawa et al., 1992; Shayegan et al., 2007; Abanin et al., 2010]: in AlAs the band structure of the electronic dispersion forms several minima around the  $X$ -points, giving rise to six half-ellipsoid Fermi surfaces in the first Brillouin zone. Due to biaxial stress subject to the AlAs layer when grown on GaAs substrate, two of these valleys are generally occupied, giving rise to an anisotropic effective two-valley system. The similarity of the *which-valley* isospin has been realised and exploited to study the response of the system to in-plane strain [Shkolnikov et al., 2004] or formation of valley skyrmions, *i.e.*, configurations with a non-trivial modulation of the valley isospin in space, both in the integer and fractional quantum Hall regime [Shkolnikov et al., 2005; Padmanabhan et al., 2010].

The work presented here, however, focusses on a different kind of system: we are motivated by the recent insights about the quantum Hall physics of the (111) surface states of elemental Bismuth gained from the experimental results presented in the introductory chapter I: in reference [Feldman et al., 2016] conductance data

\* We define nematicity in chapter V.3.2, when discussing the physical properties of the phases we observe in our study.

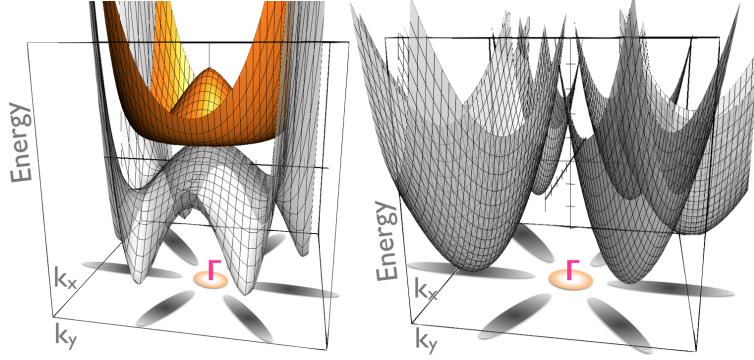


**Figure V.1** Bi(111) band structure (left) and our model in terms of six elliptical paraboloids (right), shown with the projection onto the  $\{k_x-k_y\}$ -plane.

directly reveals elliptical features of the underlying quantum Hall wave functions, reminiscence of the elliptical valleys of the Bi(111) Fermi surface. The orientation of the ellipses may differ within domains across the sample. These observations are interpreted as indicators for the formation of a nematic quantum Hall phase that breaks the underlying crystalline symmetry of the Bi(111) surface.

In this project we investigate the valley ordering of the (111) surface states of elemental bismuth. This represents work in progress.

### V.1.1 Theoretical Model of Bi(111) Quantum Hall States

#### Anisotropic Landau Level States of Bi(111)

The model for the (111) surface states of elemental Bismuth has been detailed in chapter I: as a model to the low-energy dispersion of these surface states in the vicinity of the  $\Gamma$ -point we describe six elliptical valleys arranged around  $\Gamma$  in a starlike order. A symbolic comparison between the band structure and our model is shown in figure V.1.

The way an external magnetic field induces anisotropic Landau level quantisation in one elliptical valley we demonstrated in chapter I. We consider a parabolic Hamiltonian  $H = -\hbar\omega_{c,\tau} a_\tau^\dagger a_\tau$  with  $a^\dagger = \frac{1}{\sqrt{2\hbar}}(\alpha_\tau \pi_x - i\beta_\tau \pi_y)$  and  $a = \frac{1}{\sqrt{2\hbar}}(\alpha_\tau \pi_x + i\beta_\tau \pi_y)$ , featuring the anisotropy parameters  $\alpha_\tau = \frac{1}{\sqrt{\lambda}} \cos \theta_\tau + i\sqrt{\lambda} \sin \theta_\tau$  and  $\beta_\tau = \sqrt{\lambda} \cos \theta_\tau + i\frac{1}{\sqrt{\lambda}} \sin \theta_\tau$ , and the squeezing parameter  $\lambda$ . In the Landau gauge, the anisotropic wavefunction of the  $n$ th Landau level is found to read

$$\phi_{n,\tau,k_y}(\mathbf{r}) = \langle \mathbf{r} | n, \tau, k_y \rangle = \frac{1}{L_y} e^{ik_y y} \frac{1}{\sqrt{2^n n! \sqrt{\pi} |\alpha_\tau| \ell}} e^{\alpha_\tau^* \beta_\tau \frac{(\xi_\tau)^2}{2}} H_n(\xi_\tau), \quad (\text{V.1})$$

in terms of  $k_y$  as the  $y$ -component of the Landau gauge momentum which labels the orbitals as  $k_y = \frac{2\pi}{L_y} |m|$  for a system of extension  $L_y$  in  $y$ -direction, and

$\xi_\tau = \frac{1}{|\alpha_\tau|\ell}(x - X_{k_y})$  with guiding centre coordinate  $X_{k_y} = k_y\ell^2$ . Further,  $H_n$  denotes the  $n$ th Hermite polynomial.

Generally it is assumed that due to strong spin-orbit coupling in Bismuth the ground state of the system will be fully spin polarised. Hence discarding the spin degree of freedom for this very reason, the state is consequently characterised by the valley index  $\tau \in \{1, \dots, 6\}$  labelling the six pockets.

### Interacting Many-Particle Hamiltonian

In this section, using the explicit form of the anisotropic wavefunctions of equation (V.1), we describe and derive the Hamiltonian we use to study interactions effects for the Bi(111) surface states.

Our aim is to describe the electrons on the (111) of elemental Bismuth in the presence of Coulomb interactions and local strain. The model Hamiltonian taking into account these two effects consists of two terms, correspondingly:

$$H = H_C + H_{strain}. \quad (\text{V.2})$$

Let us describe how we construct these two contributions microscopically.

#### *Coulomb Interaction: Different Scattering Processes*

We want to treat the Coulomb interaction between the electrons which we most generally write in the form

$$H_C = \frac{1}{2} \iint d\mathbf{r}d\mathbf{r}' \psi_1^\dagger(\mathbf{r}) \psi_2^\dagger(\mathbf{r}') V(\mathbf{r}, \mathbf{r}') \psi_3(\mathbf{r}') \psi_4(\mathbf{r}), \quad (\text{V.3})$$

where  $\psi_i(\mathbf{r}) = \sum_p \sum_{\mathbf{q}_i} \langle \mathbf{r} | \mathbf{q}_i; p \rangle c_{\mathbf{q}_i}(p)$  denotes the field operator of the electron with position  $\mathbf{r}$  and guiding centre coordinate  $p$ . In this sum, in principle, all values of the momentum  $\mathbf{q}$  are allowed. The spatial representation of the electronic wave function contains two parts, an slowly varying envelope function and a rapidly oscillating part:  $\langle \mathbf{r} | \mathbf{q}_i; p \rangle = f_{p;\mathbf{q}}^{env}(\mathbf{r}) e^{i\mathbf{q}\mathbf{r}}$ . In the next step, we decide to approximate equation (V.3) by keeping only those terms which contribute considerably to the sum. This corresponds to a truncation of the sum by explicit indices  $\tau = 1, \dots, 6$  labelling the six different valleys of Bi(111). We explicitly take into account inter-, as well as intra-valley interaction by allowing for processes which involve  $\tau_4 \neq \tau_1$  and  $\tau_3 \neq \tau_2$ . Note that this is in contrast to the case of monolayer and bilayer graphene discussed previously in chapter III and chapter IV, where the inter-valley scattering events transferring momenta between different valleys have

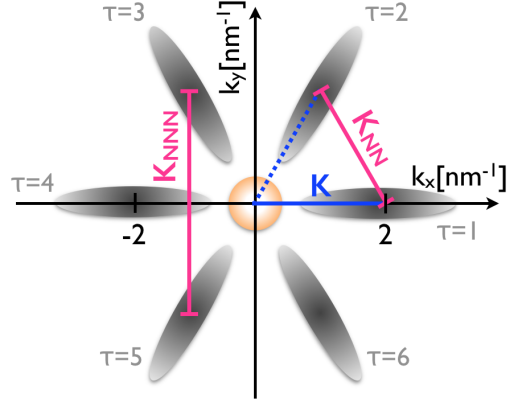
been omitted. In graphene systems this approximation to consider the Coulomb interaction as SU(2) valley symmetric is justified by the large distance in reciprocal space of the two valleys  $K_+$  and  $K_-$  in graphene compared to the inverse lattice spacing which causes these type of processes to be suppressed. This is further discussed in appendix D. Consequently, in other types of materials where the valleys are closer and momentum-transferring processes are thus facilitated, inter-valley scattering may play a crucial role.

Exploiting the conventions above the interaction Hamiltonian of equation (V.3) reads

$$\begin{aligned} H_C &= \sum_{p_i} \sum_{\tau_i} \frac{1}{2} \iint d\mathbf{r} d\mathbf{r}' \psi_{p_1, \tau_1}^*(\mathbf{r}) \psi_{p_2, \tau_2}^*(\mathbf{r}') \psi_{p_3, \tau_3}(\mathbf{r}') \psi_{p_4, \tau_4}(\mathbf{r}) \\ &\quad V(\mathbf{r}, \mathbf{r}') c_{\tau_1}^\dagger(p_1) c_{\tau_2}^\dagger(p_2) c_{\tau_3}(p_3) c_{\tau_4}(p_4) \\ &=: \sum_{p_i} \sum_{\tau_i} V_{\tau_1 \tau_2 \tau_3 \tau_4}^{p_1, p_2, p_3, p_4} c_{\tau_1}^\dagger(p_1) c_{\tau_2}^\dagger(p_2) c_{\tau_3}(p_3) c_{\tau_4}(p_4). \end{aligned} \quad (\text{V.4})$$

We separate the latter sum depending on the different combination of valley indices that may occur (suppressing the guiding centre index  $p_i$  for enhanced readability):

$$\begin{aligned} H_C &= \sum_{\substack{\tau_1 = \tau_4 \\ \tau_2 = \tau_3}} V_{\tau_1 \tau_2 \tau_3 \tau_4}^{\text{intra}} c_{\tau_1}^\dagger c_{\tau_2}^\dagger c_{\tau_3} c_{\tau_4} + \sum_{\substack{\tau_1 \neq \tau_4 \\ \text{and/or} \\ \tau_2 \neq \tau_3}} V_{\tau_1 \tau_2 \tau_3 \tau_4}^{\text{inter}} c_{\tau_1}^\dagger c_{\tau_2}^\dagger c_{\tau_3} c_{\tau_4} \\ &= \sum_{\tau_3, \tau_4} V_{\tau_4 \tau_3 \tau_3 \tau_4}^{\text{intra}} c_{\tau_4}^\dagger c_{\tau_3}^\dagger c_{\tau_3} c_{\tau_4} + \sum_{\substack{\tau_1 = \tau_3 \\ \tau_2 = \tau_4, \\ \tau_3 \neq \tau_4}} V_{\tau_3 \tau_4 \tau_3 \tau_4}^{\text{cons inter}} c_{\tau_3}^\dagger c_{\tau_4}^\dagger c_{\tau_3} c_{\tau_4} \\ &\quad + \sum_{\substack{\tau_1 \neq \tau_4 \\ \text{and/or} \\ \tau_2 \neq \tau_3}} V_{\tau_1 \tau_2 \tau_3 \tau_4}^{\text{nc inter}} c_{\tau_1}^\dagger c_{\tau_2}^\dagger c_{\tau_3} c_{\tau_4} \\ &= \begin{matrix} \text{[contribution} \\ \tau_3 = \tau_4] \end{matrix} \sum_{\tau_4} V_{\tau_4 \tau_4 \tau_4 \tau_4}^{\text{intra}} c_{\tau_4}^\dagger c_{\tau_4}^\dagger c_{\tau_4} c_{\tau_4} + \sum_{\substack{\tau_1 = \tau_2 \\ \tau_1 \neq \tau_3}} V_{\tau_1 \tau_1 \tau_3 \tau_3}^{\text{nc inter}} c_{\tau_1}^\dagger c_{\tau_1}^\dagger c_{\tau_3} c_{\tau_3} \\ &\quad + \sum_{\tau_1 \neq \tau_2} V_{\tau_1 \tau_2 \tau_3 \tau_3}^{\text{nc inter}} c_{\tau_1}^\dagger c_{\tau_2}^\dagger c_{\tau_3} c_{\tau_3} \\ &\quad \begin{matrix} \text{[contribution} \\ \tau_3 \neq \tau_4] \end{matrix} + \sum_{\tau_3 \neq \tau_4} V_{\tau_4 \tau_3 \tau_3 \tau_4}^{\text{intra}} c_{\tau_4}^\dagger c_{\tau_3}^\dagger c_{\tau_3} c_{\tau_4} + \sum_{\tau_3, \tau_4} V_{\tau_3 \tau_4 \tau_3 \tau_4}^{\text{cons inter}} c_{\tau_3}^\dagger c_{\tau_4}^\dagger c_{\tau_3} c_{\tau_4} \\ &\quad + \sum_{\tau_1 = \tau_2} V_{\tau_1 \tau_1 \tau_3 \tau_4}^{\text{nc inter}} c_{\tau_1}^\dagger c_{\tau_1}^\dagger c_{\tau_3} c_{\tau_4}. \end{aligned} \quad (\text{V.5})$$


**Figure V.2**

Arrangement of the valleys of Bi(111) in reciprocal space following reference [Ast and Höchst, 2001].

We distinguish between intra-valley ( $\tau_1 = \tau_4$  and  $\tau_2 = \tau_3$ ) and inter-valley ( $\tau_1 \neq \tau_4$  and/or  $\tau_2 \neq \tau_3$ ) scattering processes. For the inter-valley processes, we further split up into those cases where the total number of electrons per valley is conserved (cons:  $\tau_3 + \tau_4 = \tau_1 + \tau_2$ ) and non-conserving cases (nc:  $\tau_3 + \tau_4 \neq \tau_1 + \tau_2$ ). In the last step we split up between scattering processes where the two incoming particles have the same valley index ( $\tau_3 = \tau_4$ ) or a different valley index ( $\tau_3 \neq \tau_4$ ). Those terms which lead to an internal contradiction for the valley indices (such as *inter, cons* for  $\tau_3 = \tau_4$  or *inter, nc* for  $\tau_1 \neq \tau_2$ ) have been omitted.

As demonstrated in appendix D, different scattering processes show different scaling behaviour with  $K_{\tau,\tau'} = |\mathbf{K}_\tau - \mathbf{K}_{\tau'}|$  being the distance between two valleys  $\tau, \tau'$  in momentum space: processes which do not conserve the valley degrees of freedom, both inter-valley and intra-valley scatterings, are suppressed exponentially. We therefore safely neglect all valley-violating processes in the following analysis. Inter-valley scattering which conserves the valley isospin, on the other hand, scales like  $\frac{1}{K_{\tau,\tau'} \ell_B}$ . Usually, these processes likewise are neglected when studying graphene due to the large distance of the two valleys  $K_+$  and  $K_-$  in momentum space: this consequently gives rise to the approximate SU(4) symmetry of graphene. Processes of this second type, however, can have noticeable effects in other materials with different geometries of the energy dispersion, where the different valleys are less far separated in reciprocal space. We analyse their influence in the case of Bi(111).

We describe the intra- and inter-valley scattering processes with the following, effective interaction potentials:

**Intra-valley scattering:** Screened Coulomb potential

$$V^{intra}(\mathbf{q}) = \frac{2\pi e^2}{\epsilon(q + \kappa)}, \quad (\text{V.6})$$

with dielectric constant  $\epsilon$  and screening constant  $\kappa = 2\pi \frac{e^2 v_0}{\epsilon}$  in terms of the surface density of states  $v_0$ .

**Inter-valley scattering:** Constant effective potential

$$V_{\tau, \tau'}^{inter}(\mathbf{q}) = \frac{2\pi e^2}{\epsilon(K_{\tau, \tau'} + \kappa)} \quad (\text{V.7})$$

where  $K_{\tau, \tau'}$  denotes the distance between the valleys  $\tau$  and  $\tau'$  in momentum space.

We estimate the distances between valleys in momentum space for the geometry of the valley arrangement forming a star with six rays as sketched in figure V.2: when nearest neighbour valleys are separated by the distance  $K_{NN} = K_{\tau, \tau \pm 1} = K$ , we find for next nearest neighbours  $K_{NNN} = K_{\tau, \tau \pm 2} = \sqrt{3}K$ , and for the distance across the star  $K_{NNNN} = K_{\tau, \tau \pm 3} = 2K$ .

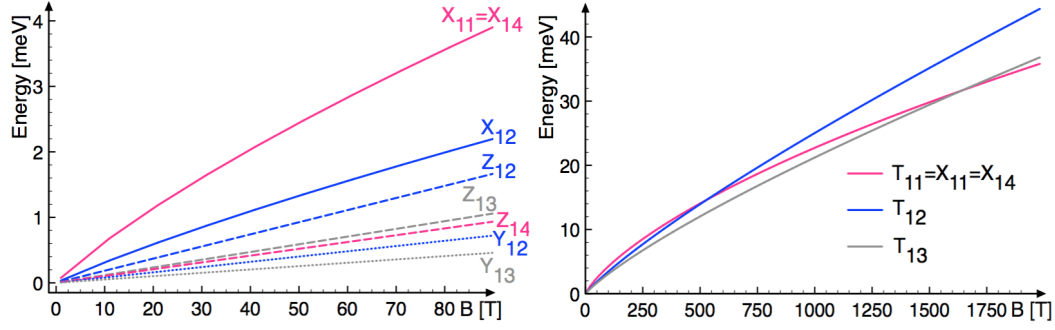
### *The Effect of Local Strain*

According to reference [Feldman et al., 2016] the six-fold valley degeneracy of the Landau levels in Bismuth is broken into two sets of valley degeneracy two and four, respectively. The authors attribute this to the effect of local strain leading to an energetic splitting  $\Delta_{strain} \approx -1.2$  meV between the two sets. We follow earlier considerations of strain effects on two-dimensional electron systems with elliptical Fermi surfaces in semiconductor systems [Shkolnikov et al., 2004; Maezawa et al., 1992] when describing strain for example along the (100) direction by the Hamiltonian

$$H_{strain} = \Delta_{strain(14)} \sum_{\tau} (\delta_{\tau,1} + \delta_{\tau,4}) c_{\tau}^{\dagger} c_{\tau}, \quad (\text{V.8})$$

where we use the index (14) to indicate that, without loss of generality, the (100) direction has been chosen as the axis of local strain, favouring the  $\tau = 1$  and the  $\tau = 4$  valleys energetically.

Strain along this axis hence favours occupation of the pair of opposite valleys aligned with the axis of strain as compared to the other four, rotated valleys. This mechanism creates a set of two valleys and a set of four valleys split energetically with respect to each other.


**Figure V.3**

Behaviour of the matrix elements  $X_{ij}$ ,  $Y_{ij}$ , and  $Z_{ij}$ , as well as the combinations  $T_{ij} = X_{ij} - Y_{ij} + Z_{ij}$  with  $B$ .

### Hartree Fock Decoupling

To study the above Hamiltonian  $H_C$  of equation (V.5) at the mean field level, we perform Hartree Fock decoupling according to  $h_{HF} = h_D - h_X$  with

$$\begin{aligned}
 h_{HF,D} &= h_{HF,D}^{intra} + h_{HF,D}^{inter} = \sum_{\substack{\tau_4=\tau_1 \\ \tau_2=\tau_3}} V_D^{intra} \langle c_{\tau_1}^\dagger c_{\tau_4} \rangle c_{\tau_2}^\dagger c_{\tau_3} + \sum_{\substack{\tau_4 \neq \tau_1 \\ \tau_2 \neq \tau_3}} V_D^{inter} \langle c_{\tau_1}^\dagger c_{\tau_4} \rangle c_{\tau_2}^\dagger c_{\tau_3} \\
 &= \sum_{\tau_4, \tau_3} V_D^{intra} \langle c_{\tau_4}^\dagger c_{\tau_4} \rangle c_{\tau_3}^\dagger c_{\tau_3} + \sum_{\tau_4 \neq \tau_3} V_D^{inter} \langle c_{\tau_3}^\dagger c_{\tau_4} \rangle c_{\tau_4}^\dagger c_{\tau_3},
 \end{aligned} \tag{V.9}$$

and

$$h_{HF,X} = h_{HF,X}^{intra} + h_{HF,X}^{inter} = \sum_{\tau_4, \tau_3} V_X^{intra} \langle c_{\tau_4}^\dagger c_{\tau_3} \rangle c_{\tau_3}^\dagger c_{\tau_4} + \sum_{\tau_4 \neq \tau_3} V_X^{inter} \langle c_{\tau_3}^\dagger c_{\tau_3} \rangle c_{\tau_4}^\dagger c_{\tau_4}. \tag{V.10}$$

In the following, we employ the notation  $V_H^{inter} \equiv Y$ ,  $V_X^{intra} \equiv X$ , and  $V_X^{inter} \equiv Z$ . The intra-valley Hartree term will be dropped as we assume it to be cancelled by a positive background charge.

### Anisotropic Matrix Elements

For the anisotropic valley system, we compute the lowest Landau level form fac-

tors of the Coulomb interaction as (see appendix D)

$$\begin{aligned}\mathfrak{F}_{00}^{\tau,\tau'}(\mathbf{q}) &= \langle \tau 0 | e^{-i\mathbf{q}\cdot\mathbf{r}_c} | 0\tau' \rangle \\ &= \mathcal{N}_{\tau\tau'} e^{\frac{\ell_B^2}{2\alpha_\tau\beta_{\tau'}^* + \alpha_{\tau'}^*\beta_\tau} [q_x^2\alpha_{\tau'}^*\alpha_\tau + q_y^2\beta_{\tau'}^*\beta_\tau - iq_xq_y(\alpha_{\tau'}^*\beta_\tau - \beta_{\tau'}^*\alpha_\tau)]}.\end{aligned}\quad (\text{V.11})$$

where  $\mathbf{r}_c = (x_c, y_c)$  is the guiding centre coordinate and  $n$  and  $\tau$  label the Landau level and the valley index, respectively. The anisotropy parameters  $\alpha_\tau$  and  $\beta_\tau$  are defined as in the introductory chapter II:  $\alpha_\tau = \frac{1}{\sqrt{\lambda}} \cos \theta_\tau + i\sqrt{\lambda} \sin \theta_\tau$ ,  $\beta_\tau = \sqrt{\lambda} \cos \theta_\tau + i\frac{1}{\sqrt{\lambda}} \sin \theta_\tau$  in terms of the squeezing parameter  $\lambda$ . The normalisation constant is given by

$$\mathcal{N}_{\tau\tau'} = \langle \tau | \tau' \rangle = \frac{\sqrt{2}}{\sqrt{|\alpha_\tau||\alpha_{\tau'}| \left( \frac{\beta_\tau}{\alpha_\tau} + \frac{\beta_{\tau'}^*}{\alpha_{\tau'}^*} \right)}} = \frac{\sqrt{2}}{\sqrt{|\alpha_\tau||\alpha_{\tau'}| (\gamma_\tau + \gamma_{\tau'}^*)}}, \quad (\text{V.12})$$

where we introduced the notation  $\gamma_\tau = \frac{\beta_\tau}{\alpha_\tau}$ .

Separating the real and the complex part, the latter equation can be cast into the convenient form

$$\begin{aligned}\mathfrak{F}_{00}^{\tau,\tau'}(\mathbf{q}) &= F_{00}^{\tau\tau'}(\mathbf{k}) e^{\frac{\ell_B^2}{2\alpha_\tau\beta_{\tau'}^* + \alpha_{\tau'}^*\beta_\tau} [-iq_xq_y(\alpha_{\tau'}^*\beta_\tau - \beta_{\tau'}^*\alpha_\tau)]}, \\ &= F_{00}^{\tau\tau'}(\mathbf{k}) e^{-\frac{iq_xq_y\ell_B^2}{2} [w_{\tau'\tau} - w_{\tau\tau'}]}\end{aligned}\quad (\text{V.13})$$

in terms of  $w_{\tau\tau'} = \frac{\beta_{\tau'}^*\alpha_\tau}{\beta_\tau\alpha_{\tau'}^* + \beta_{\tau'}^*\alpha_\tau} = \frac{\gamma_{\tau'}^*}{\gamma_\tau + \gamma_{\tau'}^*}$ .

In the equation above the reduced form factor reads

$$F_{00}^{\tau\tau'}(\mathbf{k}) = \mathcal{N}_{\tau,\tau'} e^{-\frac{1}{2} \frac{(q_x^2 + \gamma_\tau\gamma_{\tau'}^*q_y^2)\ell_B^2}{\gamma_\tau + \gamma_{\tau'}^*}}. \quad (\text{V.14})$$

Using this notation allows to compute the matrix elements according to

$$Y_{\tau,\tau'} = \frac{1}{2\pi\ell^2} V_{\tau,\tau'}^{inter} F_{00}^{\tau\tau'}(0) F_{00}^{\tau'\tau}(0), \quad (\text{V.15})$$

$$X_{\tau,\tau'} = \frac{1}{(2\pi)^2} \int d^2\mathbf{k} V_{\tau,\tau'}^{intra} F_{00}^{\tau\tau}(\mathbf{k}) F_{00}^{\tau'\tau'}(-\mathbf{k}) e^{ik_xk_y\ell^2 W_X^{\tau\tau'}}, \quad (\text{V.16})$$

$$Z_{\tau,\tau'} = \frac{1}{(2\pi)^2} V_{\tau,\tau'}^{inter} \int d^2\mathbf{k} F_{00}^{\tau\tau'}(\mathbf{k}) F_{00}^{\tau'\tau}(-\mathbf{k}) e^{ik_xk_y\ell^2 W_Z^{\tau\tau'}}, \quad (\text{V.17})$$

with  $W_X^{\tau\tau'} = 1 - w_{\tau\tau} - w_{\tau'\tau'}$ ,  $W_Z^{\tau\tau'} = 1 - w_{\tau\tau'} - w_{\tau'\tau}$ .

We note the following properties of the matrix elements:

$$\begin{aligned} X_{\tau,\tau} &= X_{\tau,\tau+3} = \text{constant} \forall \tau, \\ X_{\tau,\tau+1} &= X_{\tau,\tau+2} = \text{constant} \forall \tau, \end{aligned} \quad (\text{V.18})$$

with  $X_{\tau,\tau} > X_{\tau,\tau+1}$ .

For  $K = \text{constant}$ , all values of  $Z$  are equal and for  $Y$  we find  $Y_{\tau,\tau+1,2}$  are equal, but  $Y_{\tau,\tau+3} > Y_{\tau,\tau+1,2}$ . For  $K_{NN} = K$ ,  $K_{NNN} = \sqrt{3}K$ ,  $K_{across} = 2K$ , we find

$$\begin{aligned} Z_{\tau,\tau+1} &= Z_{\tau,\tau-1} \forall \tau, \\ Z_{\tau,\tau+2} &= Z_{\tau,\tau-2} = \text{constant} \forall \tau, \\ Z_{\tau,\tau+3} &= \text{constant} \forall \tau, \end{aligned} \quad (\text{V.19})$$

with  $Z_{\tau,\tau+1} > Z_{\tau,\tau+2} > Z_{\tau,\tau+3}$  and

$$\begin{aligned} Y_{\tau,\tau+1} &= Y_{\tau,\tau-1} \forall \tau, \\ Y_{\tau,\tau+2} &= Y_{\tau,\tau-2} = \text{constant} \forall \tau, \\ Y_{\tau,\tau+3} &= \text{constant} \forall \tau, \end{aligned} \quad (\text{V.20})$$

with  $Y_{\tau,\tau+1} > Z_{\tau,\tau+2}$  but  $Z_{\tau,\tau+3} > Y_{\tau,\tau+1}$ .

We compare the matrix elements  $X_{ij}$ ,  $Y_{ij}$ , and  $Z_{ij}$ , as well as the combinations  $T_{ij} = X_{ij} - Y_{ij} + Z_{ij}$  in figure V.3.

### *Full Hartree Fock Hamiltonian and Hartree Fock Energy Functional*

Combining the considerations about the Coulomb interactions and the effect of local strain, the full effective mean field Hamiltonian reads

$$\begin{aligned} h_{HF,tot} &= \sum_{\tau_4 \neq \tau_3} Y_{\tau_3,\tau_4} \langle c_{\tau_3}^\dagger c_{\tau_4} \rangle c_{\tau_4}^\dagger c_{\tau_3} + \sum_{\tau_4,\tau_3} X_{\tau_3,\tau_4} \langle c_{\tau_4}^\dagger c_{\tau_3} \rangle c_{\tau_3}^\dagger c_{\tau_4} \\ &+ \sum_{\tau_4 \neq \tau_3} Z_{\tau_3,\tau_4} \langle c_{\tau_3}^\dagger c_{\tau_3} \rangle c_{\tau_4}^\dagger c_{\tau_4} - \Delta_{strain(14)} \sum_{\tau} (\delta_{\tau,1} + \delta_{\tau,4}) c_{\tau}^\dagger c_{\tau}. \end{aligned} \quad (\text{V.21})$$

This entails the Hartree Fock energy functional

$$\begin{aligned}
E_{tot}^{HF} &= \frac{1}{2} \sum_{\tau_4 \neq \tau_3} Y_{\tau_3, \tau_4} \langle c_{\tau_3}^\dagger c_{\tau_4} \rangle \langle c_{\tau_4}^\dagger c_{\tau_3} \rangle + \frac{1}{2} \sum_{\tau_4, \tau_3} X_{\tau_3, \tau_4} \langle c_{\tau_4}^\dagger c_{\tau_3} \rangle \langle c_{\tau_3}^\dagger c_{\tau_4} \rangle \\
&+ \frac{1}{2} \sum_{\tau_4 \neq \tau_3} Z_{\tau_3, \tau_4} \langle c_{\tau_3}^\dagger c_{\tau_3} \rangle \langle c_{\tau_4}^\dagger c_{\tau_4} \rangle - \Delta_{strain(14)} \sum_{\tau} (\delta_{\tau,1} + \delta_{\tau,4}) \langle c_{\tau}^\dagger c_{\tau} \rangle \\
&= \frac{1}{2} \sum_{\tau_4 \neq \tau_3} Y_{\tau_3, \tau_4} P_{\tau_4, \tau_3} P_{\tau_3, \tau_4} + \frac{1}{2} \sum_{\tau_4, \tau_3} X_{\tau_3, \tau_4} P_{\tau_3, \tau_4} P_{\tau_4, \tau_3} \\
&+ \frac{1}{2} \sum_{\tau_4 \neq \tau_3} Z_{\tau_3, \tau_4} P_{\tau_3, \tau_3} P_{\tau_4, \tau_4} - \Delta_{strain(14)} \sum_{\tau} (\delta_{\tau,1} + \delta_{\tau,4}) P_{\tau, \tau}, \quad (V.22)
\end{aligned}$$

written in terms of the density matrix  $P_{\tau, \tau'} = \langle c_{\tau'}^\dagger c_{\tau} \rangle$ .

### V.1.2 Theoretical Treatment and Hartree Fock Routine

Our aim is to understand the quantum Hall ground state structure of the Bi(111) surface states within the theoretical model presented above. We exploit a mean field Hartree Fock description: the numerical self-consistent iteration scheme used to determine the Hartree Fock ground state is equivalent to the routine based on the Roothan algorithm we described in chapter IV for the case of bilayer graphene; after initialisation of a density matrix built from state vectors with random entries, an initial Hartree Fock Hamiltonian is computed from equation (V.21), and, subsequently, diagonalised. From its eigenvectors again the density matrix is formed, yielding an improved Hartree Fock Hamiltonian. The procedure is repeated until convergence is reached to a final Hartree Fock Hamiltonian  $h_{HF, tot}$  corresponding to equation (V.21). This numerical algorithm yields the Hartree Fock energy levels and eigenstates corresponding to  $h_{HF, tot}$ . Full knowledge of the state vectors and the corresponding density matrix in turn allows us to compute the Hartree Fock energy functional  $E_{tot}^{HF}$  from equation (V.22) and to understand its behaviour and the underlying physics by analytical means.

This procedure can be summarised as follows:

## Summary: Theoretical Treatment of Bi(111)

- Self-consistent numerical iteration routine to determine the Hartree Fock eigenstates and eigenenergies [cf. chapter IV]
- From the Hartree Fock ground state and the corresponding density matrix, determination of the Hartree Fock energy functional  $E_{tot}^{HF}$  [equation (V.22)]
- Analytical treatment of the energy functional

## V.2 Quantum Hall States on the (111) Surface of Bi - First Results: Ground State Valley Occupation

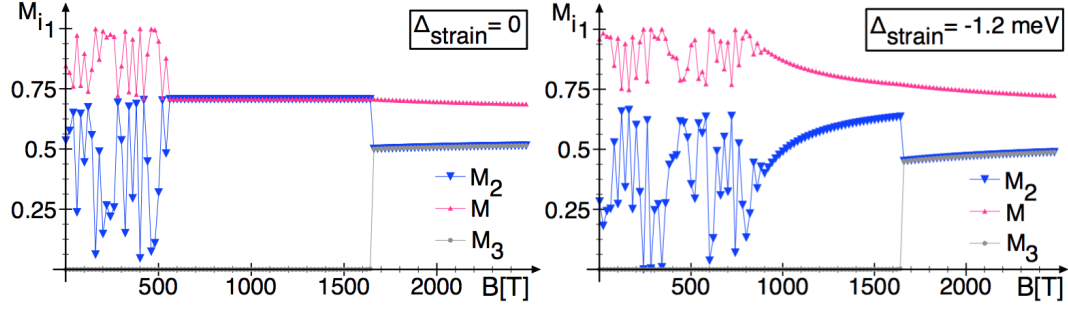
We study the Bi(111) system for different values of the filling factor  $\nu$ , *i.e.*, for different numbers of electrons in the system: while  $\nu = \frac{1}{6}$  corresponds to the case where there is one single electron occupying the six valley states,  $\nu = \frac{3}{6}$  indicates half-filling with three electrons in the sextet and  $\nu = \frac{5}{6}$  we write when there are five electrons or one hole present, respectively.

We use the numerical Hartree Fock iteration scheme described in the previous section section V.2 to determine the mean field ground state properties. We are interested in the *valley occupancy*, *i.e.*, the way the electrons distribute among the six valleys. In order to characterise this quantitatively, for a state vector  $v = (a_1, a_2, a_3, a_4, a_5, a_6)$  we introduce the *maximal valley occupancy*  $M = \max[a_1, a_2, a_3, a_4, a_5, a_6]$ .  $M = 1$  would indicate full valley polarisation into one single valley whereas  $M = \frac{1}{\sqrt{6}}$  would correspond to a fully valley coherent state where the electronic occupation is distributed homogeneously over all six valleys. To understand the structure of the state vectors in even more detail let us further consider the second largest occupancy  $M_2$  and the third largest occupancy  $M_3$ .

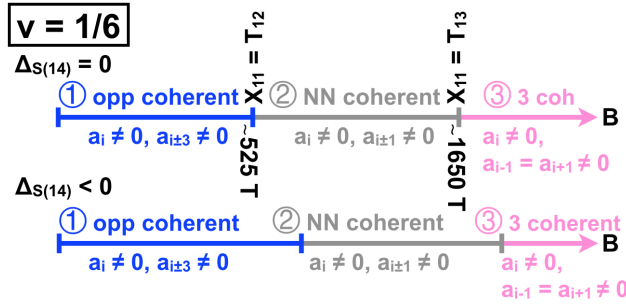
### V.2.1 Bi(111) at $\nu = \frac{1}{6}$

Let us discuss the case of filling factor  $\nu = \frac{1}{6}$ , *i.e.*, when there is one electron present in the system.

The plots shown in V.4 demonstrate the overall behaviour of the maximal occupancy  $M$  as well as  $M_2$  and  $M_3$  over a wide range of (hypothetical) magnetic


**Figure V.4**

Behaviour of the valley occupancies  $M, M_2, M_3$  with  $B$  for filling factor  $\nu = \frac{1}{6}$ .


**Figure V.5**

Different ground state phases at  $\nu = \frac{1}{6}$  in the strainless case  $\Delta_{strain} = 0$  (upper line) and for  $\Delta_{strain} < 0$  (lower line).

fields for the case of zero strain  $\Delta_{strain} \equiv 0$ , left plot, and in the strained case at  $\Delta_{strain} = -1.2$  meV, right plot. Let us describe the different regimes in both scenarios:

**Strainless Case:  $\Delta_{strain} = 0$**

① **Opposite coherent**

Within a wide range of the magnetic field  $B \lesssim 525$  T, the maximal occupancies  $M$  and  $M_2$  are scattered randomly between the configurations  $M = M_2 = \frac{1}{\sqrt{2}}$  and  $M = 1, M_2 = 0$ ; hence, there is condensation into two valleys, within which the distribution of the electron is degenerate. Close investigation of the corresponding Hartree Fock single particle state vector reveals that within this regime the electron may occupy any pair of *opposite valleys*  $\{\tau, \tau \pm 3\}$ . The corresponding ground state reads

$$|GS\rangle = a_\tau |0, \tau\rangle + a_{\tau \pm 3} |0, \tau \pm 3\rangle, \quad (\text{V.23})$$

where we denote with  $|n, \tau\rangle$  a state in the  $n$ th Landau level in valley  $\tau$ . Which of these opposite pairs will be singled out is not determined energetically. Also, any occupation of the two valleys of the opposite pair, *i.e.*, any pair

$a_\tau, a_{\tau+3}$  with  $a_\tau^2 + a_{\tau+3}^2 = 1$  is energetically degenerate.

Let us evaluate the energy functional of equation (V.24) for  $\nu = \frac{1}{6}$ :

The general energy functional for one electron in the state  $|v\rangle = (a_1, a_2, a_3, a_4, a_5, a_6)$ , hence  $\nu = \frac{1}{6}$ , reads

$$\begin{aligned}
 E_{tot,1/6}^{HF} &= - (a_1^4 + a_4^4) \Delta_{strain(14)} - \frac{1}{2} \sum_i a_i^4 X_{11} \\
 &\quad - (X_{12} - Y_{12} + Z_{12}) \Omega_{12} - (X_{13} - Y_{13} + Z_{13}) \Omega_{13} \\
 &\quad - (X_{14} - Y_{14} + Z_{14}) \Omega_{14}, \\
 &= - (a_1^4 + a_4^4) \Delta_{strain(14)} - \frac{1}{2} \sum_i a_i^4 X_{11} - T_{12} \Omega_{12} - T_{13} \Omega_{13} - T_{14} \Omega_{14},
 \end{aligned} \tag{V.24}$$

where

$$\begin{aligned}
 \Omega_{12} &= a_1^2 a_2^2 + a_2^2 a_3^2 + a_3^2 a_4^2 + a_4^2 a_5^2 + a_5^2 a_6^2 + a_6^2 a_1^2, \\
 \Omega_{13} &= a_1^2 a_3^2 + a_2^2 a_4^2 + a_1^2 a_5^2 + a_3^2 a_5^2 + a_2^2 a_6^2 + a_4^2 a_6^2, \\
 \Omega_{14} &= a_1^2 a_4^2 + a_2^2 a_5^2 + a_3^2 a_6^2,
 \end{aligned} \tag{V.25}$$

and

$$T_{ij} = X_{ij} - Y_{ij} + Z_{ij}. \tag{V.26}$$

We study the general functional for the special case of coherence between two opposite valleys:

- Condensation to a pair of opposite valleys, *i.e.*,  $\tau = 1, \tau' = 4$  without loss of generality:  $a_1 = a_4 = \frac{1}{\sqrt{2}}, a_2 = a_3 = a_5 = a_6 = 0$ . This entails  $\Omega_{12} = \Omega_{13} = 0$  and  $\Omega_{14} = a_1^2 a_4^2$  and therefore we have

$$E_{tot, \textcircled{1}}^{HF} = -\frac{1}{2} (a_1^4 + a_4^4) X_{11} - a_1^2 a_4^2 T_{14}. \tag{V.27}$$

- We use the properties of the matrix elements:  
 $X_{\tau, \tau} = X_{\tau, \tau \pm 3}$ , therefore  $X_{11} = X_{14}$ ,  
 $Y_{\tau, \tau \pm 3} = \text{constant } \forall \tau$  and  $Z_{\tau, \tau \pm 3} = \text{constant } \forall \tau$ ,  
 and, most importantly:  $Y_{\tau, \tau \pm 3} = Z_{\tau, \tau \pm 3} \forall \tau$ : direct and exchange interaction cancel each other in opposite valleys.

Therefore:

$$E_{tot,1/6,①}^{HF} = -\left[\frac{1}{\sqrt{2}}\underbrace{(a_1^2 + a_4^2)}_1\right]^2 X_{11} = -\frac{1}{2}X_{11}. \quad (\text{V.28})$$

Hence, the total energy in this case is independent of the coefficients  $a_1, a_4$ , i.e., of the distribution between the two occupied valleys.

### ② Nearest neighbour coherent

For sufficiently high fields  $525 \text{ T} \gtrsim B \gtrsim 1650 \text{ T}$ , maximal occupation gets pinned to  $M = \frac{1}{\sqrt{2}}$ . Hence, the electron is in a balanced superposition between two valleys. From the corresponding state vectors it can be seen that in this regime now pairs of *neighbouring valleys*  $\{\tau, \tau \pm 1\}$  are occupied:

$$|GS\rangle = \frac{1}{\sqrt{2}}|0, \tau\rangle + \frac{1}{\sqrt{2}}|0, \tau \pm 1\rangle, \quad (\text{V.29})$$

The energy functional for a state in this configuration with  $a_\tau = a_{\tau \pm 1} = \frac{1}{\sqrt{2}}$  reads

$$E_{tot,1/6,②}^{HF} = -\frac{1}{2}X_{11} - \frac{1}{4}T_{12}. \quad (\text{V.30})$$

### ③ Three-fold coherence

For even higher values of the magnetic field we observe a state in a coherent superposition between three different valleys:  $a_\tau \neq 0, a_{\tau-1} = a_{\tau+1} \neq 0$ :

$$|GS\rangle = a_1|0, \tau - 1\rangle + a_2|0, \tau\rangle + a_1|0, \tau + 1\rangle, \quad (\text{V.31})$$

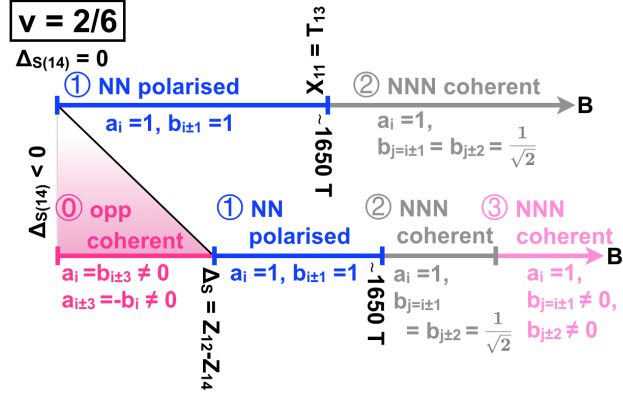
The three different phases of the  $\nu = \frac{1}{6}$  ground state at zero strain as a function of the magnetic field are summarised in the upper sketch of figure V.5. We find that the phase boundaries between the different phases are governed by the following conditions:

$$\begin{aligned} E_{tot,1/6,①}^{HF} > E_{tot,1/6,②}^{HF} &\Leftrightarrow T_{12} > X_{11} \\ \text{and } E_{tot,1/6,②}^{HF} > E_{tot,1/6,③}^{HF} &\Leftrightarrow T_{13} > X_{11}. \end{aligned} \quad (\text{V.32})$$

We see hence that the phase boundaries can be related to the crossing between the matrix elements and the quantities  $T_{ij}$  in the right panel of figure V.3.

**Figure V.6**

Different ground state phases at  $\nu = \frac{2}{6}$  in the strainless case  $\Delta_{strain} = 0$  (upper line) and for  $\Delta_{strain} < 0$  (lower line).



**Strained Case:**  $\Delta_{strain} < 0$

From the right panel of figure V.4 we see that this behaviour of the  $\nu = \frac{1}{6}$  state is not changed much qualitatively when including the effect of strain: as in the low-field regime opposite pairs, such as  $\tau = 1, \tau' = 4$ , are favoured already, besides singling out one particular pair, the strain term does not induce novel ground state configurations. It solely stabilises further this regime to even higher magnetic fields. In the high field regime, the ground state is influenced by the competition between the interaction which favours neighbouring or next nearest neighbour pairs and the strain potential favouring opposite pairs.

### V.2.2 Bi(111) at $\nu = \frac{2}{6}$

We discuss the situation at filling factor  $\nu = \frac{2}{6}$ , *i.e.*, when there are two electrons in the system.

**Strainless Case:**  $\Delta_{strain} = 0$

Depending on the value of the magnetic field, we find the following two different ground state configurations:

① **Nearest neighbour polarised**

For  $B \lesssim 1650$  T both electrons are fully polarised. They condense into two neighbouring valleys  $\{\tau, \tau \pm 1\}$ . The two electronic states read

$$|v_1\rangle = |0, \tau\rangle \quad \text{and} \quad |v_2\rangle = |0, \tau \pm 1\rangle. \quad (\text{V.33})$$

The energy functional for this case is given by

$$E_{tot,2/6,①}^{HF} = -X_{11} - Z_{12}. \quad (\text{V.34})$$

**② Next nearest neighbour coherent**

For  $B \gtrsim 1650$  T one electron remains fully polarised while the other electron is in a balanced coherent superposition between two next nearest neighbour valleys  $\tau, \tau \pm 2$ . We write the two state vectors as  $|v_1\rangle = (a_1, a_2, a_3, a_4, a_5, a_6)$  and  $|v_2\rangle = (b_1, b_2, b_3, b_4, b_5, b_6)$ . This case corresponds to two electronic states

$$|v_1\rangle = |0, \tau\rangle \quad \text{and} \quad |v_2\rangle = \frac{1}{\sqrt{2}}|0, \tilde{\tau} = \tau \pm 1\rangle + \frac{1}{\sqrt{2}}|0, \tau \pm 2\rangle. \quad (\text{V.35})$$

The Hartree Fock energy functional for this configuration is given by

$$E_{tot,2/6,②}^{HF} = -\frac{3}{4}X_{11} - Z_{12} - \frac{1}{4}T_{13}. \quad (\text{V.36})$$

From the competition of the energy functionals we compute the transition between the two above phases to occur at

$$E_{tot,2/6,②}^{HF} < E_{tot,2/6,①}^{HF} \Leftrightarrow T_{13} > X_{11}, \quad (\text{V.37})$$

dictated by the crossing between the matrix elements in figure V.3.

**Strained Case:  $\Delta_{strain} < 0$** 

Unlike the  $\nu = \frac{1}{6}$  case, at  $\nu = \frac{2}{6}$  the situation is dramatically changed as soon as non-zero strain is taken into account: the competition with an additional strain potential favouring two opposite valleys induces novel ground state phases which are not present in the strainless case.

Most prominently at low magnetic fields there is an additional phase:

**① Opposite coherent**

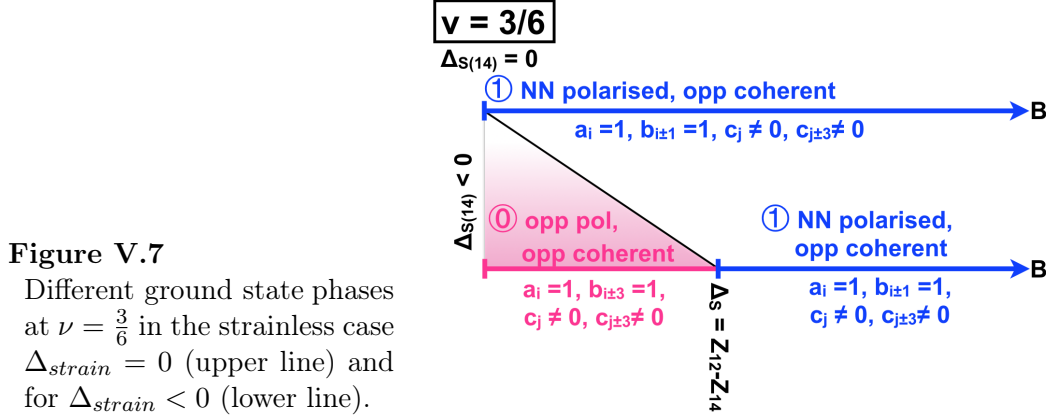
This phase features  $a_i = b_{i\pm 3} \neq 0$  and  $a_{i\pm 3} = -b_i \neq 0$  and state vectors

$$|v_1\rangle = a_\tau|0, \tau\rangle + a_{\tau\pm 3}|0, \tau \pm 3\rangle \quad \text{and} \quad |v_2\rangle = -a_{\tau\pm 3}|0, \tau\rangle + a_\tau|0, \tau \pm 3\rangle. \quad (\text{V.38})$$

The corresponding energy functional, similar to the  $\nu = \frac{1}{6}$  low-field phase without strain, is again independent of the actual values of the coefficients  $a_i$  and  $b_i$ :

$$E_{tot,2/6,①}^{HF} = -2\Delta_{strain(14)} - X_{11} - Z_{14}, \quad (\text{V.39})$$

which entails that here again the ground state energy is independent of the actual distribution of the electrons among the valleys occupied.



In the presence of strain, the nearest neighbour polarised phase features  $E_{tot,2/6,\textcircled{1}}^{HF} = -\Delta_{strain} - X_{11} - Z_{12}$ . The phase transition between the novel, opposite coherent phase at low magnetic fields and the nearest neighbour polarised phase is now governed by the interplay between the inter-valley exchange matrix elements and the strain potential:

$$E_{tot,2/6,\textcircled{1}}^{HF} < E_{tot,2/6,\textcircled{0}}^{HF} \Leftrightarrow \Delta_{strain} < -Z_{14} + Z_{12}. \quad (\text{V.40})$$

The situation for  $\frac{2}{6}$  with and without including the effect of strain is summarised in the sketches of figure V.6.

### V.2.3 Bi(111) at $\nu = \frac{3}{6}$

Next we consider the system at half filling of the sextet, *i.e.*, at  $\nu = \frac{3}{6}$  when there are three electrons present.

**Strainless Case:**  $\Delta_{strain} = 0$

In the absence of strain we observe one single, stable Hartree Fock ground state phase for all values of the magnetic field:

#### ① Nearest neighbour polarised and opposite coherent

While two of the electrons are fully polarised into two neighbouring valleys, the third electron assumes a superposition between two opposite valleys. Writing the three electronic states as  $|v_1\rangle = (a_1, a_2, a_3, a_4, a_5, a_6)$ ,  $|v_2\rangle = (b_1, b_2, b_3, b_4, b_5, b_6)$  and  $|v_3\rangle = (c_1, c_2, c_3, c_4, c_5, c_6)$  this corresponds to states with  $a_i = b_{i\pm 1} = 1$  and  $c_j, c_{j\pm 3} \neq 0$ :

$$|v_1\rangle = |0, \tau\rangle, \quad |v_2\rangle = |0, \tau \pm 1\rangle, \quad \text{and} \quad |v_3\rangle = c_{\tilde{\tau}}|0, \tilde{\tau}\rangle + c_{\tilde{\tau}\pm 3}|0, \tilde{\tau} \pm 3\rangle. \quad (\text{V.41})$$

The energy functional for this phase can be computed to read

$$E_{tot,3/6,\textcircled{1}}^{HF} = -\frac{3}{2}X_{11} - 2Z_{12} - Z_{13}. \quad (\text{V.42})$$

**Strained Case:**  $\Delta_{strain} < 0$

As in the case of  $\nu = \frac{2}{6}$ , also at filling  $\nu = \frac{3}{6}$  a novel ground state phase is induced at low magnetic fields once a non-zero strain potential is taken into account.

We identify the additional configuration:

**⓪ Opposite polarised and opposite coherent**

Driven by the additional strain potential lowering the energy of a pair of two opposite valleys, the system now prefers to fully occupy these two valleys in the low-field regime. Thereby the third electron maintains coherence between a different pair of opposite valleys:  $a_i = b_{i\pm 3} = 1$  and  $c_j, c_{j\pm 3} \neq 0$ :

$$|v_1\rangle = |0, \tau\rangle, \quad |v_2\rangle = |0, \tau \pm 3\rangle, \quad \text{and} \quad |v_3\rangle = c_{\tilde{\tau}}|0, \tilde{\tau}\rangle + c_{\tilde{\tau}\pm 3}|0, \tilde{\tau} \pm 3\rangle. \quad (\text{V.43})$$

We identify the ground state energy functional for this phase as

$$E_{tot,3/6,\textcircled{0}}^{HF} = -2\Delta_{strain(14)} - \frac{3}{2}X_{11} - 2Z_{12} - Z_{13} - Z_{14}. \quad (\text{V.44})$$

At higher values of the magnetic field the system goes back to the nearest neighbour polarised / opposite coherent phase observed for the strainless case, which now in the presence of strain exhibits the energy  $E_{tot,3/6,\textcircled{1}}^{HF} = -\Delta_{strain(14)} - \frac{3}{2}X_{11} - 2Z_{12} - Z_{13}$ .

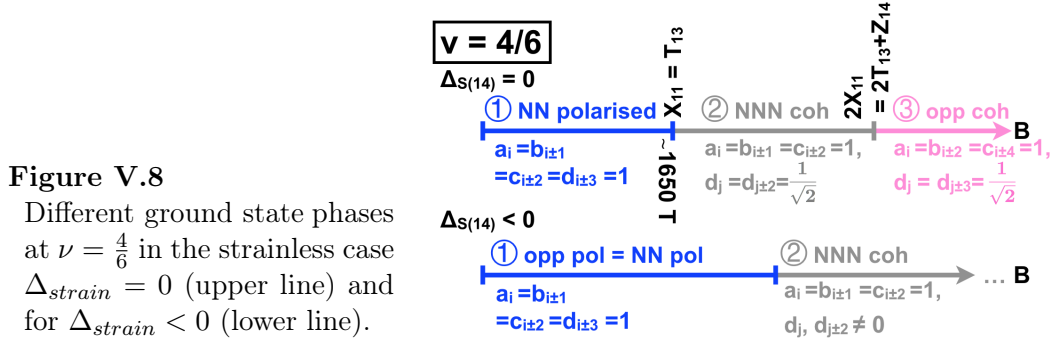
Just as for filling  $\nu = \frac{2}{6}$ , we find that the transition between the two phases occurs when the effects of inter-valley exchange matrix elements overcomes the local strain potential:

$$E_{tot,3/6,\textcircled{1}}^{HF} < E_{tot,3/6,\textcircled{0}}^{HF} \Leftrightarrow \Delta_{strain(14)} < -Z_{14} + Z_{12}. \quad (\text{V.45})$$

The different phases for  $\frac{3}{6}$  with and without a strain potential are sketched in figure [V.7](#).

#### V.2.4 Bi(111) at $\nu = \frac{4}{6}$

We consider the situation for four electrons occupying the valley sextet states, *i.e.*, for filling factor  $\nu = \frac{4}{6}$ .



**Strainless Case:**  $\Delta_{strain} = 0$

We identify three different ground state configurations for the four electronic states  $|v_1\rangle = (a_1, a_2, a_3, a_4, a_5, a_6)$ ,  $|v_2\rangle = (b_1, b_2, b_3, b_4, b_5, b_6)$ ,  $|v_3\rangle = (c_1, c_2, c_3, c_4, c_5, c_6)$  and  $|v_4\rangle = (d_1, d_2, d_3, d_4, d_5, d_6)$ , depending on the value of the magnetic field:

① Nearest neighbour polarised

For  $B \lesssim 1650 \text{ T}$  we observe a fully polarised configuration in which the four electrons fully occupy four neighbouring valleys:  $a_i = b_{i\pm 1} = c_{i\pm 2} = d_{i\pm 3} = 1$ . The four electron states can hence be written as

$$\begin{aligned} |v_1\rangle &= |0, \tau\rangle, & |v_2\rangle &= |0, \tau \pm 1\rangle, \\ |v_3\rangle &= |0, \tau \pm 2\rangle, & |v_4\rangle &= |0, \tau \pm 3\rangle. \end{aligned} \quad (\text{V.46})$$

The energy functional for this case is given by

$$E_{tot,4/6, \textcircled{1}}^{HF} = -2X_{11} - 3Z_{12} - 2Z_{13} - Z_{14}. \quad (\text{V.47})$$

② Next nearest neighbour coherent

At values of the magnetic field  $B \gtrsim 1650 \text{ T}$ , while three electrons remain polarised in neighbouring valleys, the fourth electron assumes a balanced superposition between two next nearest neighbour valleys  $\{\tau, \tau \pm 2\}$ :  $a_i = b_{i\pm 1} = c_{i\pm 2} = 1$  and  $d_j = d_{j\pm 2} = \frac{1}{\sqrt{2}}$ . The four electron single particle states hence read:

$$\begin{aligned} |v_1\rangle &= |0, \tau\rangle, & |v_2\rangle &= |0, \tau \pm 1\rangle, & |v_3\rangle &= |0, \tau \pm 2\rangle, \\ |v_4\rangle &= \frac{1}{\sqrt{2}}|0, \tilde{\tau}\rangle + \frac{1}{\sqrt{2}}|0, \tilde{\tau} \pm 2\rangle. \end{aligned} \quad (\text{V.48})$$

We find an energy functional according to

$$E_{tot,4/6, \textcircled{2}}^{HF} = -\frac{7}{4}X_{11} - \frac{1}{4}T_{13} - 3Z_{12} - 2Z_{13} - Z_{14}. \quad (\text{V.49})$$

### ③ Opposite coherent

For even higher values of the magnetic field the system assumes a configuration in which three electrons fully condense into single valleys while the fourth electron is in a balanced superposition between a pair of opposite valleys  $\{\tau, \tau \pm 3\}$ :  $a_i = b_{i\pm 1} = c_{i\pm 3} = 1$  and  $d_j = d_{j\pm 3} = \frac{1}{\sqrt{2}}$ . We write the corresponding electron states as

$$\begin{aligned} |v_1\rangle &= |0, \tau\rangle, \quad |v_2\rangle = |0, \tau \pm 1\rangle, \quad |v_3\rangle = |0, \tau \pm 3\rangle, \\ |v_4\rangle &= \frac{1}{\sqrt{2}}|0, \tilde{\tau}\rangle + \frac{1}{\sqrt{2}}|0, \tilde{\tau} \pm 3\rangle. \end{aligned} \quad (\text{V.50})$$

The corresponding energy functional for this phase reads

$$E_{tot,4/6,③}^{HF} = -\frac{5}{2}X_{11} - 3Z_{12} - 2Z_{13} - \frac{1}{2}Z_{14}. \quad (\text{V.51})$$

We identify the conditions for the phase boundaries between the respective phases as induced by the crossing between the matrix elements in figure V.3 as

$$\begin{aligned} E_{tot,4/6,①}^{HF} > E_{tot,4/6,②}^{HF} &\Leftrightarrow T_{13} > X_{11} \\ \text{and } E_{tot,4/6,②}^{HF} > E_{tot,4/6,③}^{HF} &\Leftrightarrow X_{11} > T_{13} + \frac{1}{2}Z_{14}. \end{aligned} \quad (\text{V.52})$$

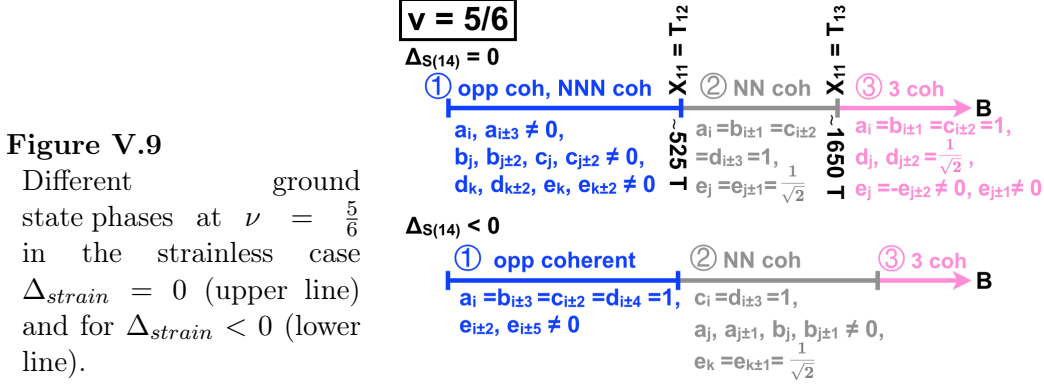
**Strained Case:**  $\Delta_{strain} < 0$

The picture for filling factor  $\nu = \frac{4}{6}$  is not altered much qualitatively by the influence of a local strain potential. The first phase ① already features a fully occupied pair of opposite valleys. The strain potential lowering the energy for one particular pair simply dictates which pair will be occupied but does not change the configuration as such. Higher-field phases are influenced by driving the degree of coherence away from the perfectly balanced case with equal occupation  $\frac{1}{\sqrt{2}}$ .

We sketch the different phases for  $\frac{4}{6}$  with and without strain in the two lines of figure V.8.

#### V.2.5 Bi(111) at $\nu = \frac{5}{6}$

Next, let us study the case of filling factor  $\nu = \frac{5}{6}$ , *i.e.*, the scenario when there are five electrons in the system or one hole in the valley sextet, respectively.



**Strainless Case:**  $\Delta_{strain} = 0$

Without strain the system assumes the following different ground state phases for the five electronic states  $|v_1\rangle = (a_1, a_2, a_3, a_4, a_5, a_6)$ ,  $|v_2\rangle = (b_1, b_2, b_3, b_4, b_5, b_6)$ ,  $|v_3\rangle = (c_1, c_2, c_3, c_4, c_5, c_6)$ ,  $|v_4\rangle = (d_1, d_2, d_3, d_4, d_5, d_6)$  and  $|v_5\rangle = (e_1, e_2, e_3, e_4, e_5, e_6)$  depending on the value of the magnetic field:

① **Next nearest neighbour and opposite coherent**

At fields  $B \lesssim 525$  T the ground state assumes a complex structure in which both, coherence between next nearest neighbour valley pairs  $\{\tau, \tau \pm 2\}$ , and pairs of opposite valleys  $\{\tau, \tau \pm 3\}$  can be observed:  $a_i, a_{i\pm 3} \neq 0$  as well as  $b_j, b_{j\pm 2}, c_j, c_{j\pm 2}, d_k, d_{k\pm 2}, e_k, e_{k\pm 2} \neq 0$ . We write these electronic states as

$$\begin{aligned} |v_1\rangle &= a_\tau |0, \tau\rangle + a_{\tau\pm 3} |0, \tau \pm 3\rangle, \\ |v_2\rangle &= b_{\tilde{\tau}} |0, \tilde{\tau}\rangle + b_{\tilde{\tau}\pm 2} |0, \tilde{\tau} \pm 2\rangle, \quad |v_3\rangle = c_{\tilde{\tau}} |0, \tilde{\tau}\rangle + c_{\tilde{\tau}\pm 2} |0, \tilde{\tau} \pm 2\rangle, \\ |v_4\rangle &= d_{\tilde{\tau}} |0, \tilde{\tau}\rangle + c_{\tilde{\tau}\pm 2} |0, \tilde{\tau} \pm 2\rangle \quad |v_5\rangle = e_{\tilde{\tau}} |0, \tilde{\tau}\rangle + e_{\tilde{\tau}\pm 2} |0, \tilde{\tau} \pm 2\rangle. \end{aligned} \quad (\text{V.53})$$

The energy functional of this state can be found to be independent of the actual values of the entries:

$$E_{tot, 5/6, \textcircled{1}}^{HF} = -\frac{5}{2} X_{11} - 4(Z_{12} + 2Z_{13}) - 2Z_{14}. \quad (\text{V.54})$$

Hence, as observed already for the cases  $\nu = \frac{1}{6}$ ,  $\nu = \frac{2}{6}$ , and  $\nu = \frac{3}{6}$ , the electronic distribution in each respective valley pair is left undetermined as the manifold of all possible configurations is energetically degenerate.

② **Nearest neighbour coherent**

For  $525 \text{ T} \lesssim B \lesssim 1650$  T four electrons fully polarise into nearest neighbouring valleys while the fifth electron assumes a balanced coherent state between two next nearest neighbour valleys  $\{\tau, \tau \pm 2\}$ :  $a_i = b_{i\pm 1} = c_{i\pm 2} =$

$$d_{i\pm 3} = 1, e_j = e_{j\pm 2} = \frac{1}{\sqrt{2}}.$$

The five electrons hence occupy the states

$$\begin{aligned} |v_1\rangle &= |0, \tau\rangle, |v_2\rangle = |0, \tau \pm 1\rangle, |v_3\rangle = |0, \tau \pm 2\rangle, |v_4\rangle = |0, \tau \pm 3\rangle, \\ |v_5\rangle &= \frac{1}{\sqrt{2}}|0, \tilde{\tau}\rangle + \frac{1}{\sqrt{2}}|0, \tilde{\tau} \pm 2\rangle. \end{aligned} \quad (\text{V.55})$$

The corresponding Hartree Fock energy functional reads

$$E_{tot,5/6, \textcircled{2}}^{HF} = \frac{9}{4}X_{11} - \frac{1}{4}T_{12} - 4(Z_{12} + Z_{12} + \frac{1}{2}Z_{14}). \quad (\text{V.56})$$

### ③ Three-fold coherence

For higher values of the magnetic field  $B \gtrsim 1650$  T, a complex ground state structure with coherence between three valleys is observed:  $a_i = b_{\pm 1} = c_{\pm 2} = 1$ ,  $d_j = d_{j\pm 2} = \frac{1}{\sqrt{2}}$ , and  $e_j = -e_{j\pm 2} \neq 0, e_{j\pm 1} \neq 0$ . The corresponding electronic states are given by

$$\begin{aligned} |v_1\rangle &= |0, \tau\rangle, |v_2\rangle = |0, \tau \pm 1\rangle, |v_3\rangle = |0, \tau \pm 2\rangle, \\ |v_4\rangle &= \frac{1}{\sqrt{2}}|0, \tilde{\tau}\rangle + \frac{1}{\sqrt{2}}|0, \tilde{\tau} \pm 2\rangle, |v_5\rangle = e_1|0, \tilde{\tau} - 1\rangle + e_2|0, \tilde{\tau}\rangle - e_1|0, \tilde{\tau} + 1\rangle. \end{aligned} \quad (\text{V.57})$$

As in the previous cases, the phase boundaries are induced by the crossing of the matrix elements shown in figure V.3:

$$E_{tot,5/6, \textcircled{2}}^{HF} < E_{tot,5/6, \textcircled{1}}^{HF} \Leftrightarrow T_{12} > X_{11} \text{ and } E_{tot,5/6, \textcircled{3}}^{HF} < E_{tot,5/6, \textcircled{2}}^{HF} \Leftrightarrow T_{13} > X_{11} \quad (\text{V.58})$$

**Strained Case:**  $\Delta_{strain} < 0$

The picture for the  $\nu = \frac{5}{6}$  ground state is altered as follows when local strain is taken into account: the strain potential by lowering the energy for a pair of opposite valleys favours full polarisation of one electron into each of this valleys, respectively. At low fields, the resulting nearest neighbour polarised and opposite coherent configuration with  $a_i = c_{i\pm 1} = b_{i\pm 3} = d_{i\pm 4} = 1$  and  $e_{i\pm 2}, e_{i\pm 5} \neq 0$  and states

$$\begin{aligned} |v_1\rangle &= |0, \tau\rangle, |v_2\rangle = |0, \tau \pm 1\rangle, |v_3\rangle = |0, \tau \pm 3\rangle, |v_4\rangle = |0, \tau \pm 4\rangle, \\ |v_5\rangle &= \frac{1}{\sqrt{2}}|0, \tilde{\tau}\rangle + \frac{1}{\sqrt{2}}|0, \tilde{\tau} \pm 3\rangle. \end{aligned} \quad (\text{V.59})$$

is still a subclass of phase ①.

We illustrate the evolution of the different phases for  $\frac{5}{6}$  with and without strain as functions of the magnetic field in the sketches of figure V.9.

### V.3 Quantum Hall States on the (111) Surface of Bi - Discussion and Preliminary Conclusion

Let us summarise our preliminary findings on the ground state properties of the Bi(111) surface states.

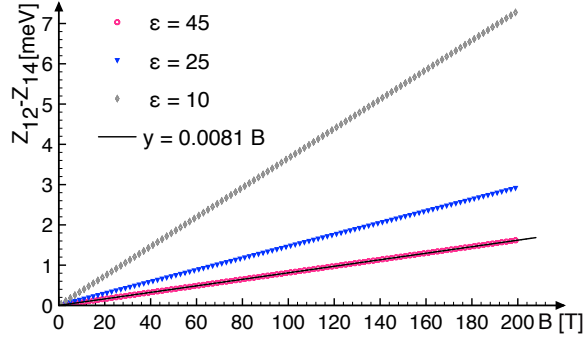
#### V.3.1 General Behaviour of the Model

In a scenario without strain,  $\Delta_{strain} \equiv 0$ , at accessible values of the magnetic field the system for all filling factors except  $\nu = \frac{5}{6}$  tends to polarise involving next nearest valleys  $\{\tau, \tau \pm 1\}$  for any even number of electrons, while in the case of an odd electron number it is preferred to establish a coherent superposition between two opposite valleys  $\{\tau, \tau \pm 3\}$  for the reminiscent single electron. Filling  $\nu = \frac{5}{6}$  represents a special case that will be discussed separately. The rotational symmetry of the system is lowered as certain valleys are singled out spontaneously.

The ground state of filling factor  $\nu = \frac{5}{6}$  at zero strain represents an exception as here coherence is established not only between pairs of opposite valleys  $\{\tau, \tau \pm 3\}$  but also between next nearest neighbour valleys  $\{\tau, \tau \pm 2\}$ .

We observe for the strainless case that states with different valley combinations are induced at very high values of the magnetic fields  $B > 500$  T. In this field regime for all fillings except  $\nu = \frac{3}{6}$ , next nearest neighbour coherent states or even coherent superpositions between three valleys can be found. An interesting exception is provided by the half-filled case  $\nu = \frac{3}{6}$ , where the ground state at zero strain with two electrons fully polarised into a pairs of nearest neighbour valleys and one electron in a coherent superposition between two opposite valleys proves to be especially stable and unchanged for all values of the magnetic field.

Phenomena akin to the phase transitions we see at such high values of the magnetic field,  $B \approx 525$  T and  $B \approx 1650$  T, which are driven by the interplay between intra- and inter-valley scattering processes, have been observed before in other multivalley systems such as SnTe [Li et al., 2016]. Here we prove the existence of such phase transitions for an SU(6) ferromagnet and demonstrate the nature of the possible phases at higher fields. However, in Bi(111), for the parameters chosen, any effect or phase transition induced by this competition between the inter- and intra valley interactions happens at such high values of the magnetic field that they are beyond the reach of experimental investigations.

**Figure V.10**

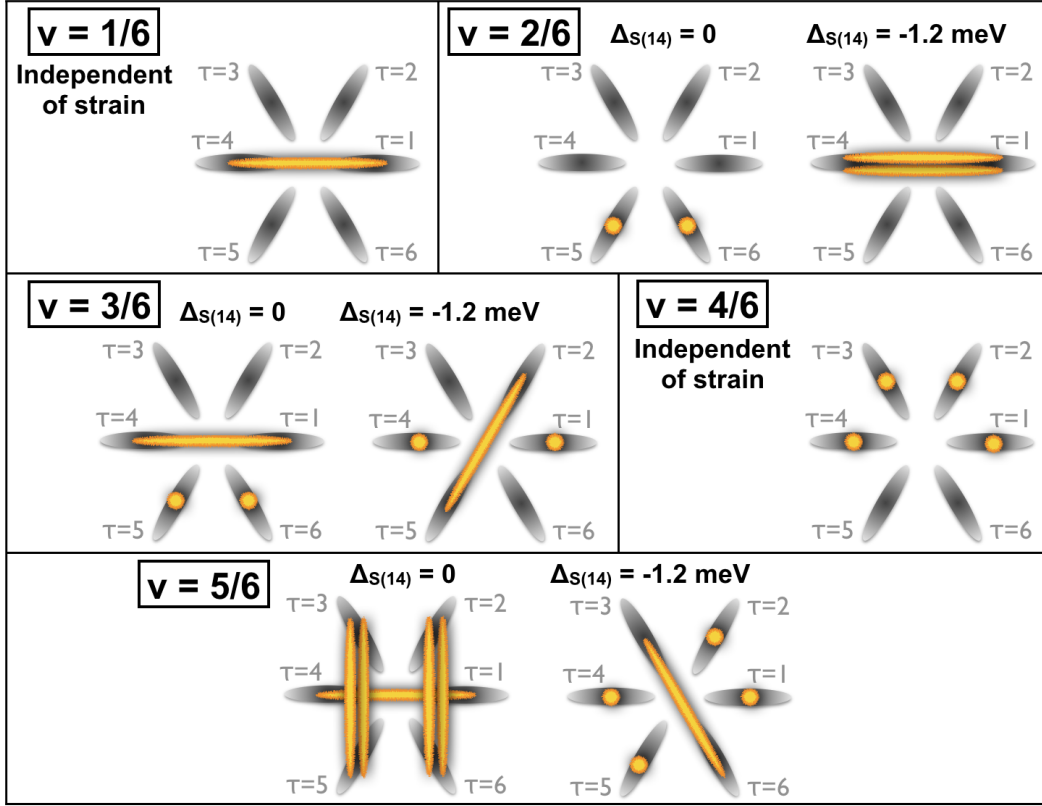
The quantity  $Z_{12} - Z_{14}$  as a function of the magnetic field for different values of the dielectric constant  $\epsilon$  (numerical data is represented by symbols: magenta open circles  $\epsilon = 45$ , blue filled triangles  $\epsilon = 25$ , gray open diamonds  $\epsilon = 10$ ).

The picture changes for several of the filling factors, however, once the effects of local strain are taken into account: now, there is a competition between the inter-valley exchange interaction and the influence of the strain potential. For filling factors  $\nu = \frac{2}{6}$ ,  $\nu = \frac{3}{6}$ , and  $\nu = \frac{5}{6}$  the predicted Hartree Fock ground state changes; configurations involving coherences between two opposite valleys  $\{\tau, \tau \pm 3\}$  are induced. Moreover, for the cases of filling  $\nu = \frac{2}{6}$  or  $\nu = \frac{3}{6}$  the possibility emerges to drive a transition as a function of the magnetic field strength between the newly induced low-field phase in the presence of strain and the phase which would be the ground state phase in the absence of strain. We repeat above results by saying that this transition should occur once the following relation between the strain potential and the inter-valley exchange elements is fulfilled:  $\Delta_{strain} = Z_{12} - Z_{14}$ .

In order to analyse further the possibility of inducing a phase transition in the Bi(111) system, we plot the behaviour of the quantity  $Z_{12} - Z_{14}$  as a function of the magnetic field for several different system parameters in figure V.10. Let us start by describing the case of screening parameter  $\epsilon = 45$  that we have been discussing so far: we find that  $Z_{12} - Z_{14}$  behaves linearly and is very well approximated by a straight line following  $f(B) = 0.0081 \text{ B[T]}$ . This predicts the phase transitions to occur around  $B \approx 148 \text{ T}$ , which lies well beyond the experimentally accessible regime. The slope of the curve, however, can be manipulated, *e.g.*, by changing the value of the screening parameter, without changing its linear nature: we observe in figure V.10 much steeper curves, *e.g.*, for  $\epsilon = 25$  or  $\epsilon = 10$ . This suggests that phase transitions within a realistic range of magnetic field values become possible when effecting the dielectric constant  $\epsilon$ , *e.g.*, by substrate engineering.

### V.3.2 Discussion of the Physically Relevant Regime

Let us discuss the results for our model of Bi(111) asking to what extent they may provide a realistic description of Bismuth and what might be possible implications for experimental investigations of this system.


**Figure V.11**

Summary of the phases observed within the physically relevant parameter regime within our model for all filling factors  $\nu \in \{\frac{1}{6}, \dots, \frac{5}{6}\}$  of the Bi(111) sextet.

### Physically Relevant Parameter Range

Obviously, magnetic field ranges as those discussed for the numerical data are not realistic values. In this section we therefore limit the discussion to the phases that appear below  $B < 50$  T. Concerning the influence of local strain, reference [Feldman et al., 2016] claims a splitting between orbitals of about  $\Delta_{strain} \approx -1.2$  meV. We therefore compare the phases of the strainless case to those which emerge at  $\Delta_{strain} = -1.2$  meV.

### Physically Relevant Phases

The different phases which we observe within this physically relevant parameter range are summarised in figure V.11: we see that all the phase involve either full polarisation into single valleys or coherence between pairs of opposite valleys.

Hence, all the phases lower the full  $C_6$  symmetry of the Bi(111) Fermi surface to a lower rotational symmetry class. In this sense<sup>†</sup>, all the phases in figure V.11 can be called *nematic*. While the system is symmetric under a particle-hole transformation in the strainless case, this particle-hole symmetry is broken by the strain potential favouring one particular pair of opposite valleys.

### Discussion: Relevance of Undetermined Coherence

For several filling factors and system parameters in the Bi(111) system we observe that minimising the Hartree Fock energy yields as ground state a coherent superposition between two opposite valleys  $\{\tau, \tau \pm 3\}$ , where the actual degree of coherence is left undetermined by the Hartree Fock equations. In other words, both, the fully balanced coherent state with equal weight in both valleys, as well as the incoherent state fully polarised into only one of the valleys is contained in this class of states. Let us elucidate further this kind of states to understand their origin in our model as well as their physical significance.

We exemplarily discuss the simplest case of one electron in the sextet,  $\nu = \frac{1}{6}$ . As explained in section V.2.1, we observe the undetermined opposite coherent state at this filling factor at low fields both with or without strain. We repeat equation (V.27) when saying the Hartree Fock energy functional of this phase is given by

$$E_{tot, \textcircled{1}}^{HF} = -\frac{1}{2}(a_1^4 + a_4^4)X_{11} - a_1^2 a_4^2 T_{14}. \quad (\text{V.60})$$

In the remainder of section V.2.1, we argued that due to the properties of the matrix elements  $X_{11} = X_{14}$ , and  $Y_{\tau, \tau \pm 3} = Z_{\tau, \tau \pm 3} \forall \tau$ , the energy functional (here in the absence of strain) simply reduces to  $E_{tot, 1/6, \textcircled{1}}^{HF} = -\frac{1}{2}X_{11}$ . It hence does not depend on the coefficients  $a_1, a_4$  and is therefore independent of the actual degree of coherence.

The degeneracy of the matrix elements, crucial to above line of argumentation as it leads to the mutual perfect cancellation of terms, is related to our model of the valleys in the Bi(111) Fermi surface as *perfect ellipses*: therefore, due to the mirror symmetry of the electronic dispersion implied by this geometry, opposite valleys are *exactly equivalent*, yielding identical matrix elements. The existence of such degenerate manifolds of states including all possible degrees of coherence ranging between full valley polarisation to the balanced case of equal distribution between the two valleys, has been observed before, e.g., in SU(4) symmetric, cross-like valley arrangements with perfectly elliptic valleys [Sodemann et al., 2017]. For the

---

<sup>†</sup> We here employ the following definition of *nematicity*: a phase is called *nematic*, if it spontaneously breaks a symmetry of the underlying Hamiltonian which interchanges two axes of the system [Fradkin et al., 2010].

case of the Bi(111) Fermi surface it has been argued, however, that in a more realistic description of the Bi(111) valleys, the ellipses should be slightly deformed to reflect the valleys real "tadpole"-like shape [Ohtsubo et al., 2012; Sodemann et al., 2017]. This breaking of the mirror symmetry would alter the matrix elements  $X_{ij}, Y_{ij}, Z_{ij}$  and lift the degeneracies. From equation (V.60) we see that in the energy functional there is a competition between the term  $E_1 = -\frac{1}{2}(a_1^4 + a_4^4)X_{11}$  favouring polarisation into one single valley and  $E_2 = -a_1^2 a_4^2 T_{14}$  which is minimised for the case of equally balanced opposite coherence with  $a_1 = a_2 = \frac{1}{\sqrt{2}}$ . The phase boundary between the polarised and the opposite coherent state would then be determined by  $X_{11} = T_{14}$ . Recalling that  $T_{14} = X_{14} - Y_{14} + Z_{14}$  we see that the competition between polarisation or opposite valley coherence will be decided by what is affected more by a deformation of the orbitals, the intra-valley interaction  $X_{ij}$ , or the inter-valley interaction term  $Z_{ij} - Y_{ij}$ . To determine the exact outcome for deformed orbitals is beyond the scope of our simple approximation in terms of identical, perfectly symmetric ellipses. We note, however, that the actual physical behaviour of the systems is expected to be determined by an interesting interplay between intra- and inter-valley scattering processes.

### V.3.3 Preliminary Summary

We have analysed quantum Hall ferromagnetism of the quantum Hall states on the Bi(111) surface within a model description in the framework of Hartree Fock mean field theory. Let us summarise our preliminary results so far:

#### Summary: Quantum Hall States of Bi(111)

- The occupation of the six anisotropic valleys of the Bi(111) Fermi surface is governed by a subtle interplay between **intravalley scattering**, **intervalley scattering** and the effect of **local strain**.
- For different numbers of electrons in the system and upon varying the strength of the external magnetic field, we observe **different ground state phases** characterised by **different occupation of the six valleys**. All the ground state configurations lower the rotational symmetry of the system and therefore represent **nematic phases**.

More work will be needed to obtain more precise insights about the properties of this system as well as about possible implications for experimental investigations.

### Final Discussion

---

We have employed mean field Hartree Fock theory on microscopic model Hamiltonians to analyse several aspects of quantum Hall ferromagnetism in the different two-dimensional materials *monolayer graphene*, *bilayer graphene*, and *the (111) surface of elemental Bismuth*. The main results on either of the three materials are detailed in itemised summary boxes at the end of the respective chapters, [III](#), [IV](#), [V](#).

This final chapter serves to put these novel insights obtained in each of the projects into context and to discuss common aspects, implications, and consequences. Furthermore, we want to give an outlook to possible future experimental and theoretical investigations.

#### VI.1 Conclusion

In the introductory chapter [I](#) we presented the results of existing experimental investigations. Based on these observations made in experiments, we formulated key questions that piqued our interest in the matter and stimulated the research presented in these projects: in our opinion, concerning the aspects addressed by these questions, theoretical work beyond the existing treatises was needed in order to obtain fully coherent, satisfying theoretical pictures of the respective system. Let us now see to what extent these initiatory questions have been answered in the course of this work and at which points maybe novel, exciting questions and possibilities arose instead.

### VI.1.1 Monolayer Graphene - From the Bulk, can we understand the Edges?

In chapter III we studied how a terminating edge of a finite piece of monolayer graphene influences the states and properties of the system when approaching this boundary from the bulk. We saw that the presence of an edge by no means leaves the bulk state invariant: on the contrary, novel states are induced in the vicinity of the boundary which exhibit different features both in the ground state, as well as in the spectrum of excited states compared to the bulk. Therefore, when considering a finite sample of monolayer graphene no unambiguous assignment can be made *which state* or *which phase* the total system is in — rather, the bulk of the system is in one particular phase, while undergoing an evolution as a function of the spatial distance to the edge towards an *edge phase* close enough to the boundary. This edge phase may very well be different from the bulk phase. Most importantly, in the picture drawn by our results there is no clear one-to-one correspondence between the bulk state of the system and the conductance properties seen in experiments as [Young et al., 2014]. Our results from the detailed model taking into account the explicit presence of an edge suggest that the transitions between regimes of insulating and conducting behaviour seen experimentally may not necessarily correspond to transitions of the bulk phase. In fact, they may correspond to *pure edge phenomena* where the changes in the system's conductance properties are induced by transitions of the edge phases rather than the bulk phases. The behaviour of these edge regimes is of much more subtle and complex nature than that of the translationally invariant bulk. Therefore, we conclude that in order to truly understand the properties of monolayer graphene and the behaviour observed in experiment, one needs to thoroughly understand not only the bulk of the system, but it is of crucial important to develop a complete picture including the boundaries and the different kinds of edge phenomena induced by them.

### VI.1.2 Bilayer Graphene - How many Different Phases are there?

In chapter IV we analysed the ground state structure of bilayer graphene in the presence of external electric and magnetic fields. The set of system parameters which can be tuned in experiment consists in the field strengths of either the magnetic and the electric field applied, as well as the number of electrons that may occupy the eight states of the zero energy octet of bilayer graphene. As a function of these parameters we observed a total of 32 different phases, where each phase is characterised by a different configuration of the discrete spin and isospin degrees of freedom of bilayer graphene. We studied in depth the dependency of the ground state configuration on the system parameters which allows predictions for the total

number of phases, the parameter range for a certain phase, as well as the number and nature of phase transitions. This information can be compared to the experimental results on transitions between different phases in bilayer graphene we presented in chapter I. It has to be noted, however, that with our model Hamiltonian we describe a translational invariant system of infinite bilayer graphene — direct comparison to data from conductance measurements therefore is hampered by the fact that we do not have any information about edge regimes or the behaviour of possible current carrying edge states in the respective phases.

### VI.1.3 Bismuth(111) - Does the Ground State break Symmetries?

In chapter V we presented first, preliminary results on the quantum Hall states on the (111) surface of elemental Bismuth. We analysed a microscopic model accounting for the six anisotropic valleys of the Bi(111) Fermi surface as well as the effect of local strain to determine the ground state valley occupation for different numbers of electrons in the system or for different strengths of the external magnetic field. For all values of the tuneable parameters we observe the ground state to spontaneously lower the rotational symmetry of the system. This we take as evidence for the ground state of Bi(111) to generally represent a nematic phase, in accordance with recent experiments [Feldman et al., 2016]. This project, however, represents work in progress. More work will be needed to fully understand the properties of the Bi(111) quantum Hall states.

### VI.1.4 Summary: Understanding a Material - Bulk versus Edge Phenomena

Let us conclude the picture drawn by our investigations: in the case of monolayer graphene we saw the material's properties to be strongly influenced by the presence of atomic edges in a finite sample. In fact, our results suggest that the changes of conductance properties with changing magnetic field may be explained by *pure edge phenomena* related only to the behaviour of the system induced within a spatially narrow regime close enough to the edges. This idea to take into account carefully possible edge effects in atomic lattices, however, is of course not limited to the case of monolayer graphene.

Concerning bilayer graphene we chose to investigate the translationally invariant, infinite case. While in some aspects we find good agreement between our model and experimental findings, as elucidated in detail in chapter IV, in other regards our model suggests behaviour different from that observed experimentally. Maybe the most prominent point of disagreement is the charge neutral  $\nu = 0$  state of bi-

layer graphene at small values of the bias potential: in this regime, the ground state of our model assumes a fully polarised, ferromagnetic phase. Leaning on the correspondence between bulk phases and the number of crossings of the edge states in monolayer graphene suggested by a simplified, translational invariant treatment (see chapter III for more details), a ferromagnetic ground state is generally believed to exhibit gapless edge states and therefore to lead to conducting behaviour. The  $\nu = 0$  state of bilayer graphene, however, is observed to be an insulator [Maher et al., 2013]. By the same argumentation as above, because the canted antiferromagnetic phase (in monolayer graphene) is believed to have gapless edge states, this insulating phase is thus generally identified as most probably being a canted phase in the spin degree of freedom. This line of argumentation may, however, be challenged by our results. We saw in monolayer graphene that a ferromagnetic ground state phase does not necessarily yield gapless edge states due to edge effects. It is reasonable to conjecture similar phenomena to occur in bilayer graphene. In order to properly understand the conductance properties of bilayer graphene as observed in real world experiments, where forcibly always a finite sample is investigated, it would be necessary to carefully take into account the edge effects.

The situation becomes even more rich and complex when moving away from the graphene family towards other classes of two-dimensional materials. Within this work, we turned our attention towards the (111) surface of elemental Bismuth where we investigated the effects of valley-breaking interaction processes and local strain. The electronic surface states living on the two-dimensional surfaces of three-dimensional crystals offer a variety of possibilities for novel quantum Hall physics. But also here, just as in the case of bilayer graphene explained above, at the point when one ultimately tries to understand conductance properties, it will be necessary to understand the edge regimes of the material and to this end take into account terminating boundaries in the description, eventually. In general, whenever studying any kind of quantum Hall phenomena in a novel type of two-dimensional material, a careful consideration has to be made in order to mutually weigh against each other all the different kinds of effects induced by this particular material, including possible edge effects.

## VI.2 Outlook

Based on the above discussion, especially of the shortcomings and insufficiencies of our work we would like to give an outlook on possible directions for future research: let us say that there is a lot to be learned in the field of quantum Hall physics. Studying quantum Hall effects in novel two-dimensional materials

offers a wide and rich playground as basically any new material holds the possibility for novel phenomena to be added to the picture. Especially the family of three-dimensional crystal materials hosting two dimensional surface states seems a promising class for new, exciting quantum Hall physics. Long after Klaus von Klitzing made the seminal discovery of the integer quantum Hall effect, the field still does not fail to offer surprises. We hope that our humble contribution helps to stimulate research facing the many interesting questions that remain to be answered.



---

## Monolayer Graphene: The Kinetic Energy effective Edge Potential

---

### A.1 Landau Levels in the Presence of a Boundary

We aim at understanding the energy levels near the edges of a finite piece of monolayer graphene subject to a magnetic field. To this end we consider Landau level quantisation of a finite piece of monolayer graphene. We explicitly discuss the different boundary condition imposed by zigzag and armchair edges. The ideas sketched here closely follow the derivations in references [Abanin et al., 2006] and [Brey and Fertig, 2006b].

#### A.1.1 Low-Energy Dirac Hamiltonian

We work in the low-energy approximation of the tight-binding framework in the quantum Hall regime laid out in the introductory section II.1.1. In the presence of a magnetic field, the Hamiltonian of monolayer graphene in the vicinity of the Dirac points can be represented in terms of the creation and annihilation operators  $a = \frac{\ell_B}{\sqrt{2}\hbar}(\pi_x - i\pi_y)$  and  $a^\dagger = \frac{\ell_B}{\sqrt{2}\hbar}(\pi_x + i\pi_y)$  as

$$H_B^{eff} = v_F \sqrt{2} \frac{\hbar}{\ell_B} \begin{bmatrix} \begin{pmatrix} 0 & a \\ a^\dagger & 0 \end{pmatrix} & 0 \\ 0 & \begin{pmatrix} 0 & -a^\dagger \\ -a & 0 \end{pmatrix} \end{bmatrix}. \quad (\text{A.1})$$

In above formulae, we used the notation of the canonical momentum  $\pi = \mathbf{p} - \frac{e}{c}\mathbf{A}(\mathbf{r})$ , where  $\mathbf{A}(\mathbf{r})$  denotes the vector potential generating the magnetic field. The

above representation of the Hamiltonian implies the four-component spinor of the states on the lattice to be ordered as

$$\psi = \begin{pmatrix} \psi^{A,+} \\ \psi^{B,+} \\ -\psi^{A,-} \\ -\psi^{B,-} \end{pmatrix}, \quad (\text{A.2})$$

where the indices  $A$  and  $B$  refer to the two triangular sub-lattices and the degenerate Dirac points are labeled by  $K_+$  and  $K_-$ , respectively.

For the wave functions  $\phi_A$  on the sub-lattice  $A$  and  $\phi_B$  on sub-lattice  $B$  we write within an expansion around the two Dirac points  $K_+$  and  $K_-$ :

$$\phi_A(\mathbf{r}) = e^{i\mathbf{K}_+\cdot\mathbf{r}}\psi^{A,+} - e^{-i\mathbf{K}_-\cdot\mathbf{r}}\psi^{A,-}, \quad (\text{A.3a})$$

$$\phi_B(\mathbf{r}) = e^{i\mathbf{K}_+\cdot\mathbf{r}}\psi^{B,+} - e^{-i\mathbf{K}_-\cdot\mathbf{r}}\psi^{B,-}. \quad (\text{A.3b})$$

The eigenvalue equation  $H_B^{eff} \psi = E\psi$  yields the following conditioning equations for the individual components:

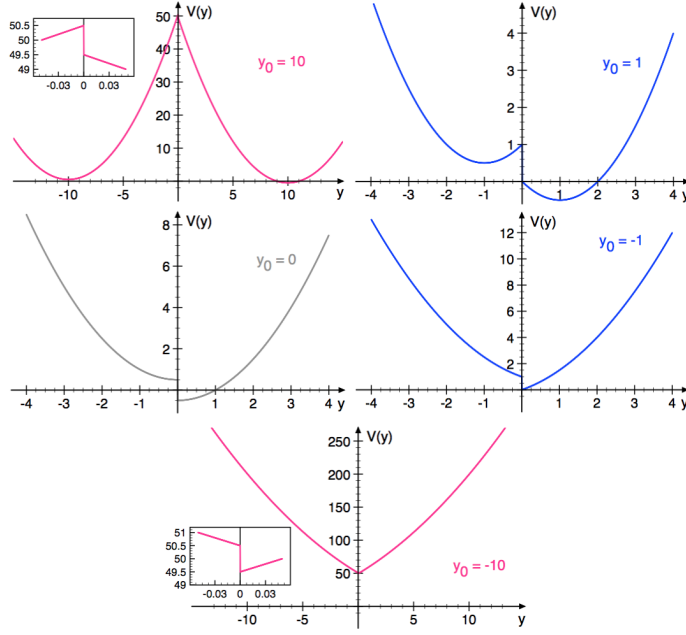
$$\begin{aligned} v_F\sqrt{2}\frac{\hbar}{\ell_B} \mathbf{a} \psi^{B,+} &= E \psi^{A,+}, \\ v_F\sqrt{2}\frac{\hbar}{\ell_B} \mathbf{a}^\dagger \psi^{A,+} &= E \psi^{B,+} \\ \Rightarrow \mathbf{a} \mathbf{a}^\dagger \psi^{A,+} &= E^2 \frac{\ell_B^2}{v_F^2 2\hbar^2} \psi^{A,+}, \end{aligned} \quad (\text{A.4a})$$

$$\begin{aligned} v_F\sqrt{2}\frac{\hbar}{\ell_B} \mathbf{a}^\dagger \psi^{B,-} &= E \psi^{A,-}, \\ v_F\sqrt{2}\frac{\hbar}{\ell_B} \mathbf{a} \psi^{A,-} &= E \psi^{B,-} \\ \Rightarrow \mathbf{a}^\dagger \mathbf{a} \psi^{A,-} &= E^2 \frac{\ell_B^2}{v_F^2 2\hbar^2} \psi^{A,-} \end{aligned} \quad (\text{A.4b})$$

Using Landau gauge, *i.e.*,  $A_x = -B y$  and  $A_y = 0$ , we expand the product of annihilation and creation operators in equations (A.4a) and (A.4b) in terms of the components of the kinetic momentum  $\mathbf{p}$ :

$$\mathbf{a} \mathbf{a}^\dagger = \frac{\ell_B^2}{2\hbar^2} \left( \pi_x^2 - i[\pi_y, \pi_x] + \pi_y^2 \right) = \frac{1}{2} \left( \frac{\ell_B^2}{\hbar^2} p_y^2 + \frac{\ell_B^2}{\hbar^2} (p_x + B \frac{e}{c} y)^2 + 1 \right), \quad (\text{A.5a})$$

$$\mathbf{a}^\dagger \mathbf{a} = \frac{\ell_B^2}{2\hbar^2} \left( \pi_x^2 + i[\pi_y, \pi_x] + \pi_y^2 \right) = \frac{1}{2} \left( \frac{\ell_B^2}{\hbar^2} p_y^2 + \frac{\ell_B^2}{\hbar^2} (p_x + B \frac{e}{c} y)^2 - 1 \right), \quad (\text{A.5b})$$


**Figure A.1**

Plot of the function  $V(y) = \frac{1}{2}(|y| - y_0)^2 - \frac{1}{2}\text{sgn}(y)$  for different values of  $y_0$  yielding the (rescaled) effective potential in equation (A.6).

where we exploited the commutation relation of the components of the canonical momentum:  $[\pi_y, \pi_x] = -i\frac{\hbar^2}{\ell_B^2}$ .

Hence, combining equation (A.4) and (A.5), we can summarise the condition on the wave function on sub-lattice A as

$$\left(p_y^2 + V(y)\right) \tilde{\psi}_A = \tilde{E} \tilde{\psi}_A, \quad (\text{A.6})$$

where we require the state  $\tilde{\psi}_A$  to fulfil

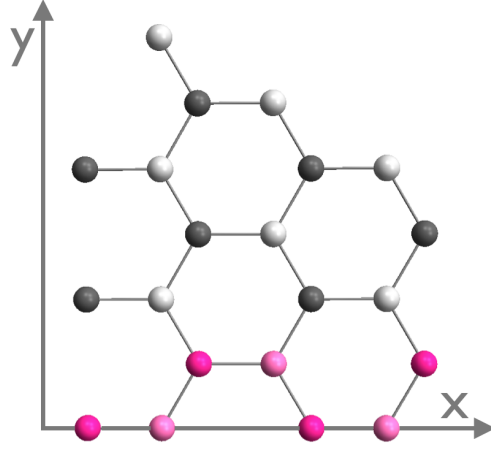
$$\tilde{\psi}_A(x, y) = \begin{cases} \psi^{A,+}, & \text{if } y < 0 \\ \psi^{A,-}, & \text{if } y > 0. \end{cases} \quad (\text{A.7})$$

Further, in equation (A.6), we defined the effective potential  $V(y) = (B_c^e |y| - y_0)^2 - \frac{\hbar^2}{\ell_B^2} \text{sgn}(y)$  with  $y_0 = -p_x$ , as well as the rescaled effective energy  $\tilde{E} = \frac{E^2}{v_F^2}$ . Note that the quadratic relation for the energy implies that every solution for equation (A.6) results in a positive and a negative energy solution, respectively.

The shape of the potential at different values of  $y_0$  is shown in figure A.1.

**Figure A.2**

Semi-infinite monolayer graphene lattice with an armchair edge (magenta atoms) along the line  $y = 0$ .



### A.1.2 Terminating Edge: Boundary Conditions

We discuss the case of a finite piece of monolayer graphene: different ways to terminate the lattice require imposing different boundary conditions.

#### Armchair Edge: Boundary Conditions

The geometry of an armchair edge is shown in figure A.2: The hexagonal graphene lattice extends infinitely in the  $x$ -direction, but in  $y$  exhibits infinite extension to plus infinity in the upper half plane, only. Along the line  $y = 0$  it exhibits an atomically sharp edge, where the final atoms are of the  $A$  and  $B$  sub-lattice type, in an alternating way. Therefore, the proper boundary conditions to impose require both, the wave functions of the  $A$  and of the  $B$  sub-lattice, to vanish at  $y = 0$ :

$$\phi_A(x, y = 0) = \phi_B(x, y = 0) = 0. \quad (\text{A.8})$$

Requiring these boundary conditions to be fulfilled by the wave functions  $\phi_A(\mathbf{r})$  and  $\phi_B(\mathbf{r})$  as written in equation (A.3) yields the following conditions on the envelope functions:

$$\psi^{A,+}(x, y = 0) = \psi^{A,-}(x, y = 0), \quad \psi^{B,+}(x, y = 0) = \psi^{B,-}(x, y = 0). \quad (\text{A.9})$$

Note that this requires valley mixing of the states of the two different Dirac points.

#### Armchair Edge: Discussion of the Energy Levels

Let us translate the conditions of equation (A.9) imposed by the armchair boundary along  $y = 0$  into the context of the description of the problem in terms of the

effective eigenvalue equation (A.6): The requirements are continuity of  $\psi^{A,+}$ , evaluated on the negative half-axis  $y < 0$ , and  $\psi^{A,-}$ , evaluated on the positive half-axis  $y > 0$ , along the line  $y = 0$ . It further implies continuity of the derivative of the wave function, which, by virtue of the relations in equations A.4, is associated with the functions  $\psi^{B,+}$  and  $\psi^{B,-}$ .

We are hence confronted with the one-dimensional problem of solving for the eigenfunctions in the presence of the potential  $V(y)$ , where the solutions for  $y < 0$  represent  $\psi^{A,-}$  and for  $y > 0$  in turn we obtain  $\psi^{A,+}$ . Considering the shape of the potential for different values of  $y_0$  as displayed in figure A.1, we gain the following qualitative insights about the structure of the energy levels:

**Deep in the bulk:**  $y_0 \rightarrow +\infty$

The potential  $V(y)$  takes the shape of two well separated harmonic potentials, shifted by one unit in energy with respect to each other (upper left panel of figure A.1). Thus, for the energetic level structure we expect quantisation similar to the harmonic oscillator separately for each well:

$$\text{Left well: } E_{\text{left},m}^{\infty} = (m + \frac{1}{2}) + \frac{1}{2} = 1, 2, 3, 4, \dots$$

$$\text{Right well: } E_{\text{right},m}^{\infty} = (m + \frac{1}{2}) - \frac{1}{2} = 0, 1, 2, 3, \dots$$

The energies are given here in units of the characteristic energy  $\hbar\omega$  where the frequency  $\omega$  is the same for both wells as it does not change with a mere shift of the harmonic potential in  $y$ .

We hence obtain a two-fold degeneracy between the left and the right well  $E_{\text{left},m}^{\infty} = E_{\text{right},m+1}^{\infty}$ . Only the zero-energy ground state  $E_{\text{right},m=0}^{\infty} = 0$  appears as a singlet state.

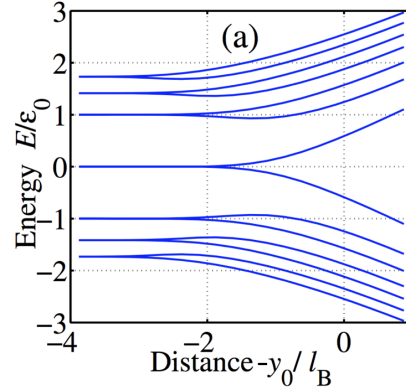
This implies two-fold degeneracy between the Dirac points  $K_+$  and  $K_-$  within the bulk for all but the zero-energy ground state.

**Close to the edge:**  $y_0 \rightarrow -\infty$

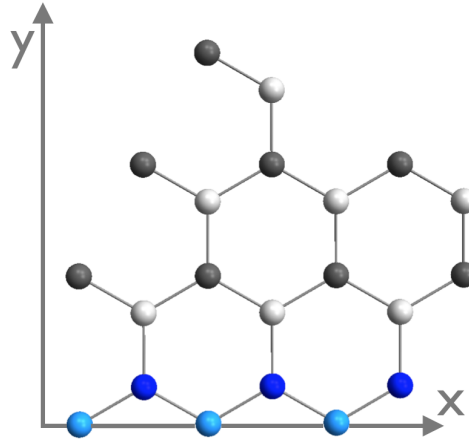
In this limit, as in the lowest panel of figure A.1, the potential resembles a triangular potential well, staggered at  $y = 0$  by one unit of energy with respect to each other. The eigenenergies are neither equidistant nor multiples of integer energy units. Therefore, no degenerate states are found between the left and the right well. With  $y_0$  becoming more and more negative, the

**Figure A.3**

Sketch of the energy spectrum of monolayer graphene near an armchair boundary. The boundary condition of equation (A.9) lifts the degeneracy of the  $K_+$  and  $K_-$  valley. Figure from reference [Abanin et al., 2006] (edited).


**Figure A.4**

Semi-infinite graphene lattice with a zigzag edge (blue atoms) along the line  $y = 0$ .



steepness of the triangles effectively grows; therefore, the energy of the levels becomes higher and higher as we approach the edge.

Hence, the degeneracy between the  $K_+$  and the  $K_-$  point which is established in the bulk is lifted more and more as we approach the edge of the system. Furthermore, the levels bend increasingly towards higher energies.

The characteristic behaviour of the energy levels in the bulk and near the edge can be seen in figure A.3.

### Zigzag Edge: Boundary Conditions

As we show in figure A.4, in the case of the zigzag configuration, the edge is formed by atoms of but one sub-lattice type,  $A$  or  $B$ , respectively. Therefore, the boundary condition of vanishing wave function applies to one of the sub-lattice

states of equation (A.3), only (which we label with  $A$  without loss of generality):

$$\begin{aligned} \phi_A(x, y = 0) &= 0 \\ \Leftrightarrow \psi^{A,+}(x, y = 0) &= \psi^{A,-}(x, y = 0) = 0. \end{aligned} \quad (\text{A.10})$$

Hence, we obtain two independent conditions decoupling the problems for the Dirac points  $K_+$  and  $K_-$  on sub-lattice  $A$ . Furthermore, the states on the  $B$  sub-lattice remain unaffected by the zigzag boundary edge. The problem thus resembles that of two semi-harmonic oscillators, mirrored with respect to each other, and bounded by an infinite wall potential at  $y = 0$ .

### Zigzag Edge: Discussion of the Energy Levels

The problem of a one-dimensional harmonic oscillator with an infinite potential barrier at one side is solvable by analytical means as has been demonstrated in reference [Mei and Lee, 1983]. We briefly review the derivation given within this reference. For a potential which is harmonic with eigenfrequency  $\omega$  for  $x > -r$  and infinite for  $x < -r$  as

$$V_{hHO} = \begin{cases} \frac{1}{2}\mu\omega^2x^2, & \text{if } x > -r \\ +\infty, & \text{if } x < -r, \end{cases} \quad (\text{A.11})$$

where  $\mu$  denotes the mass of the particle. The eigenfunctions are non-zero only in the region  $x > -r$  and we obtain quantisation of the energies as

$$E_m = \hbar\omega\left(m + \frac{1}{2}\right), \quad (\text{A.12})$$

where the corresponding eigenfunctions for  $x > -r$  are given by the *Weber functions*  $D_m(x)$

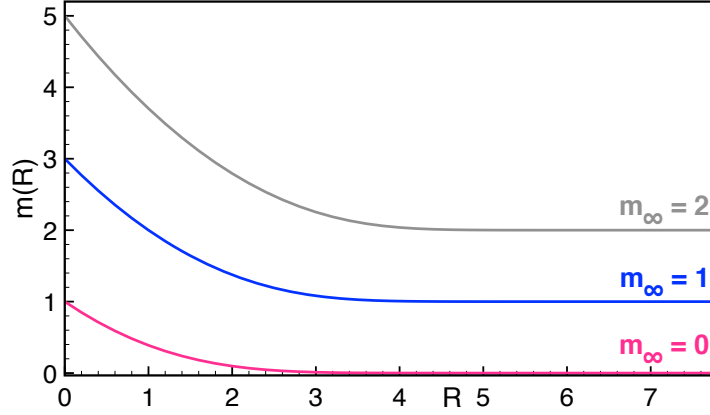
$$D_m(x) = 2^{\frac{m}{2}} e^{-\frac{z^2}{4}} \left( \frac{\sqrt{\pi}}{\Gamma[\frac{1}{2} - \frac{1}{2}m]} F\left[-\frac{1}{2}; \frac{1}{2}; \frac{1}{2}z^2\right] - \frac{\sqrt{2\pi}z}{\Gamma[-\frac{1}{2}m]} F\left[\frac{1}{2} - \frac{1}{2}m; \frac{3}{2}; \frac{1}{2}z^2\right] \right). \quad (\text{A.13})$$

Note that we require  $m \in \mathbb{R}$ , but not necessarily to be integer.

In equation (A.13) we used the notation  $\Gamma$  to denote the Gamma function  $\Gamma(z) = \int_0^\infty t^{z-1} e^{-t} dt$  for  $\Re(z) > 0$  as well as  $F$  for the confluent hypergeometric function defined by its polynomial expansion as

$$F(a; b; x) = 1 + \frac{a}{b}x + \frac{a(a+1)}{2!b(b+1)}x^2 + \frac{a(a+1)(a+2)}{3!b(b+1)(b+2)}x^3 + \dots \quad (\text{A.14})$$

Exact, analytical solutions exist for the limits  $r \rightarrow \infty$  (unperturbed harmonic oscillator) and  $r \rightarrow 0$  (half-harmonic oscillator), which lead to quantisation at values of


**Figure A.5**

Quantum numbers  $m$  defined by equation (A.15) characterising the energy levels  $E_m = \hbar\omega(m + \frac{1}{2})$  of the harmonic oscillator with an infinite potential barrier as a function of the barrier distance  $R$ . The limit  $R \rightarrow \infty$  corresponds to the unperturbed harmonic oscillator (equidistant levels with level spacing  $\Delta m = 1$ , existing zero-energy mode), whereas  $R = 0$  gives the half harmonic oscillator, where only odd values of  $m$  are supported (equidistant levels with level spacing  $\Delta m = 2$ , no zero-energy mode).

$m$  being exactly integer, where in the first case any  $m \in \mathbb{N}$  renders a valid solution, where in the second case only odd values of  $m$  are allowed.

In general, requiring the wave function to vanish at a generic point  $x = -r$  entails the following condition on the values of  $m$

$$\frac{F[-\frac{1}{2}m; \frac{1}{2}; \frac{1}{2}R^2]}{\Gamma[\frac{1}{2} - \frac{1}{2}m]} = -\sqrt{2}R \frac{F[\frac{1}{2} - \frac{1}{2}m; \frac{3}{2}; \frac{1}{2}R^2]}{\Gamma[-\frac{1}{2}m]}, \quad (\text{A.15})$$

where we rescaled the distance of the barrier as  $R = \sqrt{\frac{2\mu\omega}{\hbar}}r$ .

We show the solutions for the allowed quantum numbers  $m$  as a function of the distance  $R$  from the barrier in figure A.5 as obtained numerically as the solutions to equation A.15. We discuss the qualitative behaviour of the energy levels for  $K_+$  and  $K_-$  below.

The level structure of the problem as shown in equation (A.5) dictated by equation (A.15) entails the following consequences for the behaviour of the energy levels in the graphene sample:

**Deep in the bulk:**  $y_0 \rightarrow +\infty$ 

We recover the case of the ordinary harmonic oscillators which hardly feel the influence of the infinite wall at  $y = 0$ . As in the case of the armchair edge, the potential  $V(y)$  takes the shape of two well-separated harmonic potentials, shifted by one unit in energy with respect to each other as shown in the upper left panel of figure A.1. The boundary condition that forces the wave functions to vanish at  $y = 0$  are compatible with the usual condition  $\psi \rightarrow 0$  for  $y \rightarrow \pm\infty$  of the ordinary treatment of the harmonic oscillator problem. Thus, also in the zigzag case, for the energy level structure we approximately obtain quantisation similar to the harmonic oscillator separately for each well:

$$\text{Left well: } E_{\text{left},m}^{\infty} = (m + \frac{1}{2}) + \frac{1}{2} = 1, 2, 3, 4, \dots$$

$$\text{Right well: } E_{\text{right},m}^{\infty} = (m + \frac{1}{2}) - \frac{1}{2} = 0, 1, 2, 3, \dots$$

The energies are given again in units of the characteristic energy  $\hbar\omega$  where the frequency  $\omega$  is the same for both wells as it does not change with a mere shift of the harmonic potential in  $y$ .

Again, we obtain a two-fold degeneracy between the left and the right well  $E_{\text{left},m}^{\infty} = E_{\text{right},m+1}^{\infty}$ . Only the zero-energy ground state  $E_{\text{right},m=0}^{\infty} = 0$  appears as a singlet state.

Thus, also in the case of a zigzag boundary, we recover two-fold degeneracy between the Dirac points  $K_+$  and  $K_-$  within the bulk for all but the zero-energy ground state.

**Special case**  $y_0 = 0$ 

Here, the potential  $V(y)$  appears as two half-harmonic oscillators, mirrored along  $y = 0$  with respect to each other as in the centre left panel of figure A.1, and shifted by one unit in energy. This problem is solvable analytically, supporting only the eigenfunctions of the harmonic oscillator which vanish at  $y = 0$  thus leading to quantisation in terms of odd quantum numbers, only. We therefore obtain the energy level structure:

$$\text{Left well: } E_{\text{left},m}^0 = (m + \frac{1}{2}) + \frac{1}{2} \Bigg|_{m \text{ odd}} = 2, 4, 6, 8, \dots$$

$$\text{Right well: } E_{\text{right},m}^0 = (m + \frac{1}{2}) - \frac{1}{2} \Big|_{m \text{ odd}} = 1, 3, 5, 7, \dots$$

We observe that there is no degeneracy within the two wells anymore. Besides, as the half-harmonic oscillator does not support a  $m = 0$  mode, there is no zero-energy state in this case.

**Close to the edge:**  $y_0 \rightarrow -\infty$

In this limit, shown in the lowest panel of figure A.1, the potential resembles two triangular potential wells, mirrored and shifted by one unit of energy with respect to each other. The eigenenergies are neither equidistant nor multiples of integer energy units. Therefore, no degenerate states are found between the left and the right well. With  $y_0$  becoming more and more negative, the steepness of the triangles effectively grows. We compare the case of the triangular potential well with steepness  $F$ , where the eigenfunctions are given by the Airy-functions and the eigenenergies are proportional to  $(\frac{\hbar^2 F^2}{2\mu})^{\frac{1}{3}}$ , hence grow with growing  $F$ . We thus expect similar behaviour, *i.e.*, the energy to become higher and higher with growing steepness as we approach the edge.

Hence, the degeneracy between the  $K_+$  and the  $K_-$  point found in the bulk is lifted more and more as we approach the edge of the system. Furthermore, the levels bend increasingly towards higher energies.

The structure of the energy levels for  $K_+$  and  $K_-$  resulting from these considerations we show in figure A.6.

In our study of a finite piece of monolayer graphene in the quantum Hall regime presented in chapter III we use the bulk zero energy level, marked in magenta in figure A.6, as a model of the kinetic energy effective edge potential describing the change of the  $n = 0$  Landau level dispersion induced by the presence of the boundary. We obtain  $m_0(R)$  by numerically evaluating equation (A.15) from which we then proceed to calculate the lowest Landau level energy as a function of the distance to the boundary.

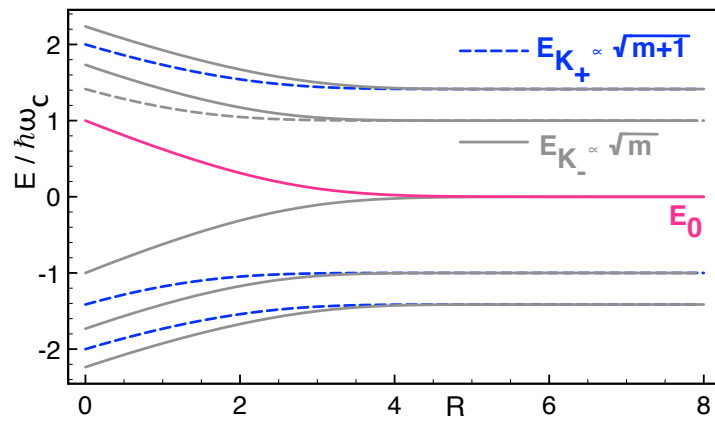


**Figure A.6**

Energetic level structure in the zigzag case as a result of the calculations with the harmonic oscillator plus the infinite barrier. We highlight in magenta the bulk zero-energy level  $E_0(R)$ .



---

## Monolayer Graphene: Parametrisation of the Ground State Wave Function

---

### B.1 The Minimal Set of Parameters

We are interested in the analysis of the two-electron state introduced in section [III.1.1](#)

$$|\psi_{GS}\rangle = \prod_p \left( \frac{1}{2} \sum_{\mu, \nu} g_{\mu\nu} c_{\mu}^{\dagger}(p) c_{\nu}^{\dagger}(p) |0\rangle \right), \quad (\text{B.1})$$

where  $p$  indicates the Landau gauge momentum, whereas the indices  $\mu, \nu$  label the different spin and isospin configurations  $\{|\uparrow +\rangle, |\uparrow -\rangle, |\downarrow +\rangle, |\downarrow -\rangle\}$  in the Hilbert space  $\mathcal{H} = \mathcal{H}_{\text{spin}} \otimes \mathcal{H}_{\text{valley}}$ . As  $|\psi_{GS}\rangle$  describes an fermionic two particle state, we require the characterising  $4 \times 4$  matrix  $g$  to be antisymmetric:  $g_{\mu\nu} = -g_{\nu\mu}$ . It therefore generally contains six independent complex entries and hence twelve real parameters.

This appendix is devoted to the problem of finding a suitable parametrisation of the entries of the matrix  $g$ . By fully exploiting the symmetries of the underlying Hamiltonian as well as making use of all constraints and requirements for the wave functions of interest and thereby reducing step by step the number of free parameters in the problem will lead us to a representation of  $g$  in terms of but three real independent parameters  $\alpha, \beta, \chi$ . The calculation presented here is closely related to the parametrisation of the state of a double layer electron gas quantum Hall system derived in reference [[Ezawa et al., 2005](#)].

### B.1.1 Parametrising a General Antisymmetric Matrix

Any generic antisymmetric  $4 \times 4$  matrix  $g$  is characterised by six complex entries, hence by twelve real parameters. The six matrices of the set  $\mathcal{B}_M = \{\tau_\alpha \tau_y \sigma_y, \sigma_\alpha \tau_y \sigma_y\}$  span the space of antisymmetric  $4 \times 4$  matrices, where  $\sigma_j = \sigma_j^{2 \times 2} \otimes \mathbb{1}^{2 \times 2}$  denotes the  $j$ -th Pauli matrix acting in spin space, and  $\tau_j = \mathbb{1}^{2 \times 2} \otimes \sigma_j^{2 \times 2}$  denotes the corresponding Pauli matrix acting in valley space, respectively. The index  $\alpha$  runs over the spacial coordinates  $x, y, z$ :  $\alpha \in \{x, y, z\}$ . We therefore expand  $g$  in this basis  $\mathcal{B}_M$  in the form

$$g = -\frac{i}{2}[(\mathbf{a} + i\mathbf{b}) \cdot \mathcal{T} + (\mathbf{c} + i\mathbf{d}) \cdot \mathcal{S}] \tau_y \sigma_y, \quad (\text{B.2})$$

where we understand  $\mathcal{T}_j = \tau_j$  and  $\mathcal{S}_j = \sigma_j$  while  $i$  denotes the imaginary unit.

The twelve parameters are now encoded in the four real three-dimensional vectors  $\mathbf{a}, \mathbf{b}, \mathbf{c}, \mathbf{d} \in \mathbb{R}^3$ . We therefore translated the problem of parametrising the entire of  $g$  to the equivalent one to find a suitable parametrisation of these four vectors.

Directly from the definitions of the expectation values of the different observables we obtain the following conditions for the components (*cf.* equations III.25 in chapter III):

$$S_\alpha = \frac{1}{2} \langle \psi_{GS} | \mathbf{c}^\dagger(p) \sigma_\alpha \mathbf{c}(p) | \psi_{GS} \rangle = \frac{1}{2} \text{Tr}[\sigma_\alpha g g^\dagger] = \sum_{ij} c_i d_j \epsilon_{ij\alpha} = (\mathbf{c} \times \mathbf{d})_\alpha, \quad (\text{B.3a})$$

$$T_\alpha = \frac{1}{2} \langle \psi_{GS} | \mathbf{c}^\dagger(p) \tau_\alpha \mathbf{c}(p) | \psi_{GS} \rangle = \frac{1}{2} \text{Tr}[\tau_\alpha g g^\dagger] = \sum_{ij} a_i b_j \epsilon_{ij\alpha} = (\mathbf{a} \times \mathbf{b})_\alpha, \quad (\text{B.3b})$$

$$R_{\alpha\beta} = \frac{1}{2} \langle \psi_{GS} | \mathbf{c}^\dagger(p) \sigma_\alpha \tau_\beta \mathbf{c}(p) | \psi_{GS} \rangle = \frac{1}{2} \text{Tr}[\sigma_\alpha \tau_\beta g g^\dagger] = a_\beta c_\alpha + b_\beta d_\alpha, \quad (\text{B.3c})$$

which implies the following interrelations:

$$R_{\alpha\beta} S_\beta = 0, \quad (\text{B.4a})$$

$$T_\alpha R_{\alpha\beta} = 0, \quad (\text{B.4b})$$

$$2S_\alpha T_\beta = \epsilon_{abc} \epsilon_{bhe} R_{ch} R_{de}. \quad (\text{B.4c})$$

We now aim at constructing the most general tensor  $\underline{R}$  that fulfils the conditions imposed by equations (B.4a) - (B.4c).

To this end, we choose the orthonormal basis of  $\mathbb{R}^3$  given by

$$\mathcal{B}_{\mathbb{R}^3} = \{\mathbf{u}_T, \mathbf{u}_S, \mathbf{q}\}, \quad (\text{B.5})$$

where we understand

$$u_{T\alpha} = \frac{T^2 S_\alpha - (\mathbf{T} \cdot \mathbf{S}) T_\alpha}{TQ}, \quad (\text{B.6a})$$

$$u_{S\beta} = \frac{S^2 T_\beta - (\mathbf{T} \cdot \mathbf{S}) S_\beta}{SQ}, \quad (\text{B.6b})$$

$$q_\gamma = \frac{Q_\gamma}{Q}, \quad (\text{B.6c})$$

with  $\mathbf{Q} = \mathbf{T} \times \mathbf{S}$ .

For these basis vectors, the following relations hold:

$$\mathbf{u}_T \perp \mathbf{T} : \mathbf{u}_T \cdot \mathbf{T} = 0, \quad (\text{B.7a})$$

$$\mathbf{u}_S \perp \mathbf{S} : \mathbf{u}_S \cdot \mathbf{S} = 0, \quad (\text{B.7b})$$

$$\mathbf{u}_T \perp \mathbf{q} : \mathbf{u}_T \cdot \mathbf{q} = 0, \quad (\text{B.7c})$$

$$\mathbf{u}_S \perp \mathbf{q} : \mathbf{u}_S \cdot \mathbf{q} = 0, \quad (\text{B.7d})$$

$$\mathbf{u}_T \perp \mathbf{u}_S : \mathbf{u}_S \cdot \mathbf{u}_T = 0, \quad (\text{B.7e})$$

$$\mathbf{u}_S \times \mathbf{q} = -\frac{\mathbf{S}}{S}, \quad (\text{B.7f})$$

$$\mathbf{u}_T \times \mathbf{q} = -\frac{\mathbf{T}}{T}. \quad (\text{B.7g})$$

Furthermore, they allow to expand the tensor  $\underline{\underline{R}}$  as

$$R_{\alpha\beta} = u_{S\alpha} u_{T\beta} R_{TS} + u_{T\beta} q_\alpha R_{TQ} + q_\beta u_{S\alpha} R_{QS} + q_\alpha q_\beta, \quad (\text{B.8})$$

with the four expansion coefficients  $R_{TS}, R_{TQ}, R_{QS}, R_{QQ} \in \mathbb{R}$  due to equation (B.4c) as

$$R_{TQ} R_{QS} - R_{TS} R_{QQ} = TS. \quad (\text{B.9})$$

We now construct the four vectors  $\mathbf{a}, \mathbf{b}, \mathbf{c}, \mathbf{d}$  in the basis  $\mathcal{B}_{\mathbb{R}^3}$  as defined in equation (B.5), thereby requiring the relations of equations (B.3a)-(B.3c) to hold.

We write

$$a_i = \theta_a u_{Ti} + \xi_a q_i, \quad (\text{B.10a})$$

$$b_i = \theta_b u_{Ti} + \xi_b q_i, \quad (\text{B.10b})$$

$$c_i = \theta_c u_{Si} + \xi_c q_i, \quad (\text{B.10c})$$

$$d_i = \theta_d u_{Si} + \xi_d q_i, \quad (\text{B.10d})$$

where equations (B.3a), (B.3b) impose the following conditions on the expansion coefficients

$$\theta_a \xi_b - \xi_a \theta_b = T, \quad (\text{B.11a})$$

$$\xi_c \theta_d - \theta_c \xi_d = S, \quad (\text{B.11b})$$

whereas from equation (B.3c) we infer

$$\begin{aligned} R_{TS} &= \theta_c \theta_a + \theta_d \theta_b, & R_{TQ} &= \xi_c \theta_a + \xi_d \theta_b, \\ R_{QS} &= \theta_c \xi_a + \theta_d \xi_b, & R_{QQ} &= \xi_c \xi_a + \xi_d \xi_b. \end{aligned} \quad (\text{B.12})$$

Using the condition of equation (B.11a), we solve the system of equations in B.12 for the coefficients  $\theta_{c/d}$  and  $\xi_{c/d}$  as

$$\begin{aligned} \theta_c &= \frac{1}{T}(R_{TS}\xi_b - R_{QS}\theta_b), & \xi_c &= \frac{1}{T}(R_{TQ}\xi_b - R_{QQ}\theta_b), \\ \theta_d &= \frac{1}{T}(R_{QS}\theta_a - R_{TS}\xi_a), & \xi_d &= \frac{1}{T}(R_{QQ}\theta_a - R_{TQ}\xi_a). \end{aligned} \quad (\text{B.13})$$

These solutions automatically fulfil the condition of equation (B.11b).

The twelve free parameters identified beforehand to parametrise the most general matrix  $g$  as given in equation (B.2) and hence the ground state  $|\psi_{GS}\rangle$  of equation (B.1), now are encoded in the components of the observables which we count as:

Parametrisation: Step 1

$$\begin{aligned} \mathbf{S} &: S_x, S_y, S_z \rightarrow 3 \text{ parameters,} \\ \mathbf{T} &: T_x, T_y, T_z \rightarrow 3 \text{ parameters,} \\ \mathbf{R} &: R_{TS}, R_{TQ}, R_{QS}, R_{QQ} \rightarrow 4 - 1 = 3 \text{ parameters,} \\ &\quad \text{(with one condition of eqn. (B.9))} \\ \text{Coefficients} &: \theta_a, \theta_b, \xi_a, \xi_b \rightarrow 4 - 1 = 3 \text{ parameters.} \\ &\quad \text{(with one condition of eqn. (B.11a))} \end{aligned} \quad (\text{B.14})$$

In the next paragraph, we formulate the physical conditions on the ground state  $|\psi_{GS}\rangle$  in terms of the set of parameters given in equation (B.14). We aim at exploiting these conditions in order to reduce the number of free parameters as far as possible.

### Normalisation

The condition for the two-particle ground state  $|\psi_{GS}\rangle$  to be properly normalised, *i.e.*,  $\text{Tr}[gg^\dagger] = 2$ , allows to reduced the number of parameters by

one. We rewrite the normalisation condition to fulfil as

$$\begin{aligned} \text{Tr}[gg^\dagger] = 2 &\Leftrightarrow \mathbf{a}^2 + \mathbf{b}^2 + \mathbf{c}^2 + \mathbf{d}^2 = 2 \\ &\Leftrightarrow \frac{1}{2}(\theta_a^2 + \theta_b^2) (T^2 + R_{QS}^2 + R_{QQ}^2) + \frac{1}{2}(\xi_a^2 + \xi_b^2) (T^2 + R_{TS}^2 + R_{TQ}^2) \\ &\quad - (\theta_b \xi_b + \theta_a \xi_a) (R_{TS} R_{QS} + R_{QQ} R_{TQ}) = T^2 \end{aligned} \quad (\text{B.15})$$

### Global phase

We express the vectors  $\Theta = (\theta_a, \theta_b)^T$ ,  $\Xi = (\xi_a, \xi_b)^T$  in terms of the angle  $\gamma$  enclosed, *i.e.*,  $\gamma = \sphericalangle(\Theta, \Xi)$  and omit the overall phase:

$$\Theta = \theta \begin{pmatrix} \cos \frac{\gamma}{2} \\ -\sin \frac{\gamma}{2} \end{pmatrix}, \quad \Xi = \xi \begin{pmatrix} \cos \frac{\gamma}{2} \\ \sin \frac{\gamma}{2} \end{pmatrix}. \quad (\text{B.16})$$

The vector properties of  $\Theta$  and  $\Xi$  imply the following relations:

$$\begin{aligned} \theta_a^2 + \theta_b^2 &= \theta^2, \\ \xi_a^2 + \xi_b^2 &= \xi^2, \\ \theta_a \xi_a + \theta_b \xi_b &= \theta \xi \cos \gamma. \end{aligned} \quad (\text{B.17})$$

We reformulate the conditions of equations (B.11a) and (B.15) in this notation to read

$$\theta \xi \sin \gamma = T, \quad (\text{B.18a})$$

$$\begin{aligned} \frac{1}{2}(T^2 + R_{QS}^2 + R_{QQ}^2) + \frac{1}{2}(T^2 + R_{TS}^2 + R_{TQ}^2) \\ - \theta \xi \cos \gamma (R_{TS} R_{QS} + R_{QQ} R_{TQ}) = T^2. \end{aligned} \quad (\text{B.18b})$$

Furthermore, we introduce the variables  $x, y$  as

$$\begin{aligned} x &= \theta^2 \left(1 + \frac{R_{QS}^2 + R_{QQ}^2}{T^2}\right) + \xi^2 \left(1 + \frac{R_{TS}^2 + R_{TQ}^2}{T^2}\right) \\ y &= \theta^2 \left(1 + \frac{R_{QS}^2 + R_{QQ}^2}{T^2}\right) - \xi^2 \left(1 + \frac{R_{TS}^2 + R_{TQ}^2}{T^2}\right), \end{aligned} \quad (\text{B.19})$$

allows to combine the conditions of equations (B.18) using the relation  $\cos^2 \gamma + \sin^2 \gamma = 1$  to read

$$(ax - 2)^2 + a(1 - a)y^2 = 4(1 - a)[1 - (S^2 + T^2 + R^2)], \quad (\text{B.20})$$

where we defined

$$a = \frac{T^2(T^2 + S^2 + R^2)}{(T^2 + R_{QS}^2 + R_{QQ}^2)(T^2 + R_{TS}^2 + R_{TQ}^2)}. \quad (\text{B.21})$$

The relation of equation (B.20) defines an ellipse equation. In the present case, where  $S^2 + T^2 + R^2 \equiv 1$ , due to the vanishing of the right hand side, equation (B.20) only permits one singular solution:  $x = \frac{2}{a}, y = 0$ .

The conditions of equations (B.18) thus translate into conditions on  $x$  and  $y$ , which can be solved straightforwardly as

$$\theta^2 = T^2 + R_{TS}^2 + R_{TQ}^2, \quad \xi^2 = T^2 + R_{QS}^2 + R_{QQ}^2, \quad (\text{B.22})$$

and translated back into the angle  $\gamma$  via

$$\sin \gamma = \frac{T}{\theta \xi}, \quad \cos \gamma = \frac{\sqrt{\theta^2 \xi^2 - T^2}}{\theta \xi}. \quad (\text{B.23})$$

This, in turn, allows to obtain  $\theta_a, \theta_b, \xi_a, \xi_b$  via equation (B.16) as well as  $\theta_c, \theta_d, \xi_c, \xi_d$  via equation (B.12).

Thus, dropping the overall normalisation constant as well as the global phase and exploiting the ground state condition  $S^2 + T^2 + R^2 \equiv 1$ , we have reduced the number of free variables parametrising the matrix  $g$  to a total of nine parameters, encoded as

Parametrisation: Step 2

$$\begin{aligned} \mathbf{S} : S_x, S_y, S_z &\rightarrow 3 \text{ parameters,} \\ \mathbf{T} : T_x, T_y, T_z &\rightarrow 3 \text{ parameters,} \\ \mathbf{R} : R_{TS}, R_{TQ}, R_{QS}, R_{QQ} &\rightarrow 4 - 1 = 3 \text{ parameters,} \\ &\text{(with one condition of eqn. (B.9)).} \end{aligned} \quad (\text{B.24})$$

### B.1.2 Parametrising the Energy Functional

We proceed the reduction of the number of free parameters needed by exploiting the symmetries of the Hamiltonian under consideration.

The energy functional  $E_{tot} = \langle H_{tot} \rangle$  computed from the Hamiltonian of equation (III.4) reads

$$E_{tot} = -2E_{kin}T_x - 2E_ZS_z + \frac{1}{2} \sum_{\alpha} u_{\alpha} \left( \text{Tr}[\tau_{\alpha}gg^{\dagger}]^2 - \text{Tr}[\tau_{\alpha}gg^{\dagger}\tau_{\alpha}gg^{\dagger}] \right), \quad (\text{B.25})$$

where the traces in above equation (B.25) can be evaluated as

$$\text{Tr}[\tau_{\alpha}gg^{\dagger}]^2 = 4T_{\alpha}^2 \quad (\text{B.26a})$$

$$\text{Tr}[\tau_{\alpha}gg^{\dagger}\tau_{\alpha}gg^{\dagger}] = 1 - \sum_i (S_i^2 + T_i^2 + \sum_j R_{ij}^2) + 2 \left( \sum_i S_i^2 + T_{\alpha}^2 + \sum_i R_{i\alpha} \right). \quad (\text{B.26b})$$

Exploiting the ground state condition  $\mathbf{S}^2 + \mathbf{T}^2 + R^2 = 1$ , we find the energy functional  $E_{tot}$  hence to read

$$\begin{aligned} E_{tot} &= -2(E_{kin}T_x + E_ZS_z) + \sum_{\alpha} (T_{\alpha}^2 - S_{\alpha}^2 - \sum_i R_{i\alpha}^2) \\ &= -2(E_{kin}T_x + E_ZS_z) + u_z T_z^2 + u_{\perp} (T_x^2 + T_y^2) \\ &\quad - u_z S_z^2 - u_{\perp} (S_x^2 + S_y^2) - u_z \sum_i R_{iz}^2 - 2u_{\perp} \left( \sum_i R_{ix}^2 + \sum_i R_{iy}^2 \right), \end{aligned} \quad (\text{B.27})$$

where we agreed on  $u_x = u_y = u_{\perp}$ .

We exploit the symmetries of above energy functional of equation (B.27). We note that  $\mathbf{S}$  and  $R_{ix}, R_{iy}, R_{iz} \forall i$  rotate as vectors in spin space and  $\mathbf{T}$  and  $R_{ix}, R_{iy}, R_{iz} \forall i$  rotate as vectors in valley isospin space. Hence, in order to minimise  $E_{tot}$  of equation (B.27), we can perform rotations of  $\mathbf{S}$  ( $\mathbf{T}$ ) in spin (valley isospin) space, without affecting  $\mathbf{S}^2$  or  $R_{ix}^2, R_{iy}^2$ , or  $R_{iz}^2$  ( $\mathbf{T}^2$  or  $R_{ix}^2, R_{iy}^2$ , or  $R_{iz}^2$ ):

Orientation of the spin:  $E_{tot}$  of equation (B.27) is minimised for the maximal value of  $S_z$ . We therefore chose the total spin  $\mathbf{S}$  to be aligned along the  $z$ -axis in spin space:  $S_x = S_y = 0$ .

Orientation of the valley isospin:  $E_{tot}$  of equation (B.27) depends on the projection of the total isospin  $\mathbf{T}$  on the  $x$ - $y$ -plane. Therefore, we chose  $\mathbf{T}$  to be oriented along the  $x$ -axis in isospin space:  $T_y = 0$ .

The aim of the next step is to express in energy functional  $E_{tot}$  of equation (B.27) in terms of the observables  $\mathbf{T}$  and  $\mathbf{S}$ . To this end, we start by relating the components of the tensor  $R_{\alpha\beta}$  to  $\mathbf{S}$  and  $\mathbf{T}$ . As only three of the four coefficients

$R_{TS}, R_{TQ}, R_{QS}, R_{QQ}$  are independent, we parametrise in terms of three free parameters  $\omega, \chi,$  and  $\lambda$  as

$$R_{TS} + iR_{TQ} = e^{i\omega} \left( \frac{T}{\chi} - i\lambda \right), \quad (\text{B.28a})$$

$$R_{QS} + iR_{QQ} = -ie^{i\omega} \chi S, \quad (\text{B.28b})$$

which ensures the condition of equation (B.9) on the coefficients to be fulfilled and further entails the following relations:

$$R_{TS}R_{QS} + R_{TQ}R_{QQ} = \chi S \lambda, \quad (\text{B.29a})$$

$$R_{TS}^2 + R_{TQ}^2 = \frac{T^2}{\chi^2} + \lambda^2, \quad (\text{B.29b})$$

$$R_{QS}^2 + R_{QQ}^2 = \chi^2 S^2. \quad (\text{B.29c})$$

Using above equations (B.29), the parts of equations (B.27) containing entries of  $R_{\alpha\beta}$  are found to read in terms of  $\omega, \lambda$  and  $\chi$ :

$$\begin{aligned} R^2 &= \sum_{ij} R_{ij}^2 = R_{TS}^2 + R_{TQ}^2 + R_{QS}^2 + R_{QQ}^2 \\ &= \frac{T^2}{\chi^2} + \lambda^2 + \chi^2 S^2, \end{aligned} \quad (\text{B.30a})$$

$$\begin{aligned} \sum_i R_{i\alpha}^2 &= u_{T\alpha}^2 (R_{TS}^2 + R_{TQ}^2) + q_\alpha^2 (R_{QS}^2 + R_{QQ}^2) \\ &\quad + 2u_{T\alpha} q_\alpha (R_{TS}R_{QS} + R_{TQ}R_{QQ}) \\ &= u_{T\alpha}^2 \left( \frac{T^2}{\chi^2} + \lambda^2 \right) + q_\alpha^2 \chi^2 S^2 + 2u_{T\alpha} q_\alpha \chi S \lambda. \end{aligned} \quad (\text{B.30b})$$

From the form of the  $R_{\alpha\beta}$ -dependent terms as they are given in equation (B.30) we draw the following conclusions for the parameters:

#### Freedom of $\omega$

As the expressions of equation (B.30) do not depend on the parameter  $\omega$ , the energy functional  $E_{tot}$  of equation (B.27) in turn does not depend on  $\omega$ , either. The total energy therefore is independent of the choice of  $\omega$  which hence can be chosen freely at any convenient value.

### Minimising $\lambda$

From the identity

$$\begin{aligned} S^2 + R^2 + T^2 &= 1 \\ \Leftrightarrow S_z^2 + T^2 + \frac{T^2}{\chi^2} + \chi^2 S_z^2 + \lambda^2 &= 1, \end{aligned} \quad (\text{B.31})$$

we observe that decreasing  $\lambda$  can be compensated by increasing  $S_z$  accordingly in order to maintain above equality. As the total energy  $E_{tot}$  as in equation (B.27) is minimised by the maximal value of  $S_z$ , we infer reversely that the minimum value of  $E_{tot}$  is obtained for the minimum absolute value of  $\lambda$ , *i.e.*, for  $\lambda \equiv 0$ .

The coefficients which appear in equation (B.30) we compute directly from their definitions of equation (B.6) by inserting straightforwardly the explicit expressions for  $\mathbf{S}$  and  $\mathbf{T}$ :

$$\begin{aligned} u_{Tx} &= \frac{-T_z}{\sqrt{T_x^2 + T_z^2}}, & q_x &= 0, \\ u_{Ty} &= 0, & q_y &= -1, \\ u_{Tz} &= \frac{T_x}{\sqrt{T_x^2 + T_z^2}}, & q_z &= 0. \end{aligned} \quad (\text{B.32})$$

Applying this parametrisation as developed above, the ground state energy of equation (B.30) reads in terms of the variables  $S_z, T_x, T_y$  and  $\chi$ :

$$\begin{aligned} E_{tot} &= -2(E_{kin}T_x + E_Z S_z) - u_z \left( \frac{T_x^2}{\chi^2} - T_z^2 + S_z^2 \right) \\ &\quad - u_{\perp} \left( \frac{T_z^2}{\chi^2} - T_x^2 + 2S_z^2 + \chi^2 S_z^2 \right) \end{aligned} \quad (\text{B.33})$$

One further parameter can be eliminated by making use of the condition  $S^2 + R^2 + T^2 = 1$  and rewriting with the help of equation (B.30)

$$\begin{aligned} S^2 + R^2 + T^2 &= 1 \\ \Leftrightarrow S_z^2(1 + \chi^2) + T^2(1 + \frac{1}{\chi^2}) &= 1 \\ \Leftrightarrow S_z^2 &= \frac{1}{1 + \chi^2} \left[ 1 - T^2(1 + \frac{1}{\chi^2}) \right], \end{aligned} \quad (\text{B.34})$$

when introducing the parametrisation

$$S_z^2 = \frac{1}{1 + \chi^2} (1 - \alpha^2), \quad (\text{B.35})$$

with  $\alpha^2 = (T_x^2 + T_z^2) \frac{\chi^2 + 1}{\chi^2}$ . For the isospin components this representation entails parametrisation as

$$T_x = \alpha \sqrt{1 - \beta^2} \frac{\chi}{\sqrt{\chi^2 + 1}}, \quad T_z = \alpha \beta \frac{\chi}{\sqrt{\chi^2 + 1}}. \quad (\text{B.36})$$

#### Parametrisation: Final Representation

As a consequence, the functional of the total energy finally can be expressed in terms of the three variational parameters  $-1 \leq \alpha \leq 1$ ,  $-1 \leq \beta \leq 1$  and  $\chi \in \mathbb{R}$ :

$$E_{tot} = -2(E_{kin} \alpha \sqrt{1 - \beta^2} \frac{\chi}{\sqrt{\chi^2 + 1}} + E_Z \frac{\sqrt{1 - \alpha^2}}{\sqrt{1 - \chi^2}}) - u_z \left( \frac{1}{\chi^2 + 1} - \alpha^2 \beta^2 \right) - u_{\perp} \left( \alpha^2 (\beta^2 - 2) + \frac{2 + \chi^2}{1 + \chi^2} \right). \quad (\text{B.37})$$

The representation of  $E_{tot}$  in terms of but three parameters as in equation B.37 allows convenient handling such as numerical minimisation. We exploit this fact in In chapter III when studying a finite piece of monolayer graphene in a space dependent treatment.

---

## Bilayer Graphene: Exchange Interaction Matrix Elements

---

### C.1 Explicit Form of the Exchange Integrals

This appendix is devoted to providing the explicit expressions for the matrix elements of the Coulomb exchange interaction calculated within the four-band model.

Repeating the formula given in section IV.1, the exchange integrals are given by

$$\mathfrak{X}_{\substack{n_1, n_2 \\ n_3, n_4}}^{\xi, \xi'}(\mathbf{q}) = \alpha \int \frac{d\mathbf{p} \ell_B^2}{2\pi} \frac{1}{p \ell_B} e^{-pd(1-\delta_{\xi, \xi'})} \mathfrak{K}_{n_1, n_4}(p) \mathfrak{K}_{n_3, n_2}(-p) e^{i\mathbf{p} \times \mathbf{q} \ell_B^2}, \quad (\text{C.1})$$

in terms of the generalised form factors  $\mathfrak{K}_{n, n'}$  of the four-band model of bilayer graphene as defined in equation (IV.12):

$$\begin{aligned} \mathfrak{K}_{n, n'}(\mathbf{q}) &= b_{(n'), 1}^* b_{(n), 1} K_{n, n'}(\mathbf{q}) + b_{(n'), 2}^* b_{(n), 2} K_{n-2, n'-2}(\mathbf{q}) \\ &+ (b_{(n'), 3}^* b_{(n), 3} + b_{(n'), 4}^* b_{(n), 4}) K_{n-1, n'-1}(\mathbf{q}). \end{aligned} \quad (\text{C.2})$$

We are interested in the properties of the zero-energy states of bilayer graphene carrying Landau level quantum numbers  $n = 0$  or  $n = 1$ . For convenience, we list some of the properties for the cases  $n, n' = 0, 1$  which are used in the calculation of the form factors (*cf.* the definition of the  $n, n' = 0, 1$  states of the four-band model as

given in II.35):

$$n = 0, n' = 0 :$$

$$F_{0,0}(\mathbf{q}) = e^{-\frac{\ell_B^2 q^2}{4}},$$

$$b_{(0),1}^* b_{(0),1} = 1, b_{(0),2}^* b_{(0),2} = 0, b_{(0),3}^* b_{(0),3} = 0, b_{(0),4}^* b_{(0),4} = 0,$$

$$n = 1, n' = 0 :$$

$$F_{1,0}(\mathbf{q}) = e^{-\frac{\ell_B^2 q^2}{4}} \left( \frac{\ell_B}{\sqrt{2}} \right) (iq_x + q_y),$$

$$b_{(1),1}^* b_{(0),1} = c_1, b_{(1),2}^* b_{(0),2} = 0, b_{(1),3}^* b_{(0),3} = 0, b_{(1),4}^* b_{(0),4} = 0,$$

$$n = 0, n' = 1 :$$

$$F_{0,1}(\mathbf{q}) = e^{-\frac{\ell_B^2 q^2}{4}} \left( \frac{\ell_B}{\sqrt{2}} \right) (iq_x - q_y),$$

$$b_{(0),1}^* b_{(1),1} = c_1, b_{(0),2}^* b_{(1),2} = 0, b_{(0),3}^* b_{(1),3} = 0, b_{(0),4}^* b_{(1),4} = 0,$$

$$n = 1, n' = 1 :$$

$$F_{1,1}(\mathbf{q}) = e^{-\frac{\ell_B^2 q^2}{4}} \left( 1 - \frac{q^2 \ell_B^2}{2} \right),$$

$$b_{(1),1}^* b_{(1),1} = c_1^2, b_{(1),2}^* b_{(1),2} = 0,$$

$$b_{(1),3}^* b_{(1),3} = c_1^2 \frac{(1 - M^2 z^2)^2}{g_1^2}, b_{(1),4}^* b_{(1),4} = c_1^2 |zM|^2. \quad (\text{C.3})$$

From these, the corresponding generalised form factors are obtained straightforwardly

$$\begin{aligned} \mathfrak{K}_{0,0}(\mathbf{p}) &= K_{0,0}(\mathbf{p}) = e^{-\frac{\ell_B^2 p^2}{4}} \\ \mathfrak{K}_{0,1}(\mathbf{p}) &= c_1 K_{0,1}(\mathbf{p}) = e^{-\frac{\ell_B^2 p^2}{4}} \frac{c_1 \ell_B}{\sqrt{2}} (ip_x + p_y) \\ \mathfrak{K}_{1,0}(\mathbf{p}) &= c_1 K_{1,0}(\mathbf{p}) = e^{-\frac{\ell_B^2 p^2}{4}} \frac{c_1 \ell_B}{\sqrt{2}} (ip_x - p_y) \\ \mathfrak{K}_{1,1}(\mathbf{p}) &= e^{-\frac{\ell_B^2 p^2}{4}} \left( 1 - c_1 \frac{\ell_B^2 p^2}{2} \right), \end{aligned} \quad (\text{C.4})$$

where we used the definition of  $c_1$  as  $c_1 = \frac{1}{\sqrt{1 + \frac{1}{g_1^2} (1 - M^2 z^2)^2 + z^2 M^2}}$  as introduced in chapter II.

For the simplified case of  $\mathbf{q} \equiv 0$ , the matrix elements of equation (C.1) can be evaluated analytically, following the definition of the form factors of as in equation (IV.10) and using the properties listed in equation (C.3). As in the main part, section IV.1, we use the notation  $\Delta_{n_1 n_2 n_3 n_4} := \mathfrak{X}_{n_3, n_4}^{\xi, \xi}$  for the terms conserving the valley index and  $X_{n_1 n_2 n_3 n_4} := \mathfrak{X}_{n_3, n_4}^{\xi, \xi'}$  in the case  $\xi \neq \xi'$  for the valley index non-conserving terms.

Valley conserving terms:

$$\begin{aligned}
 \Delta_{0000} &= \alpha \sqrt{\frac{\pi}{2}}, \\
 \Delta_{1111} &= \frac{\alpha}{4} \sqrt{\frac{\pi}{2}} [4 + c_1(3c_1 - 4)], \\
 \Delta_{1001} &= \alpha \sqrt{\frac{\pi}{2}} \frac{c_1^2}{2}, \\
 \Delta_{0011} &= -\alpha \sqrt{\frac{\pi}{2}} \frac{(c_1 - 2)}{2}.
 \end{aligned} \tag{C.5}$$

Valley breaking terms:

$$\begin{aligned}
 X_{0000} &= \alpha \sqrt{\frac{\pi}{2}} e^{\frac{1}{2} \frac{d^2}{\ell_B^2}} \text{Erf}\left[\frac{1}{\sqrt{2}} \frac{d}{\ell_B}\right], \\
 X_{1111} &= \frac{\alpha}{8\ell_B^4} \left[ -2c_1 d \ell_B (c_1 d^2 + (5c_1 - 4)\ell^2), \right. \\
 &\quad \left. + \sqrt{2\pi} e^{\frac{1}{2} \frac{d^2}{\ell_B^2}} (c_1^2 d^4 + 2c_1(3c_1 - 2)d^2 \ell_B^2 + (4 + (3c_1 - 4)\ell^4) \text{Erf}\left[\frac{1}{\sqrt{2}} \frac{d}{\ell_B}\right]) \right], \\
 X_{1001} &= c_1^2 \frac{\alpha}{4\ell^2} \left[ -2d \ell_B + e^{\frac{1}{2} \frac{d^2}{\ell_B^2}} (d^2 + \ell_B^2) \sqrt{2\pi} \text{Erf}\left[\frac{1}{\sqrt{2}} \frac{d}{\ell_B}\right] \right], \\
 X_{0011} &= \frac{\alpha}{4\ell^2} \left[ 2c_1 d \ell_B - \sqrt{2\pi} e^{\frac{1}{2} \frac{d^2}{\ell_B^2}} (c_1 d^2 + (c_1 - 2)\ell_B^2) \text{Erf}\left[\frac{1}{\sqrt{2}} \frac{d}{\ell_B}\right] \right].
 \end{aligned} \tag{C.6}$$

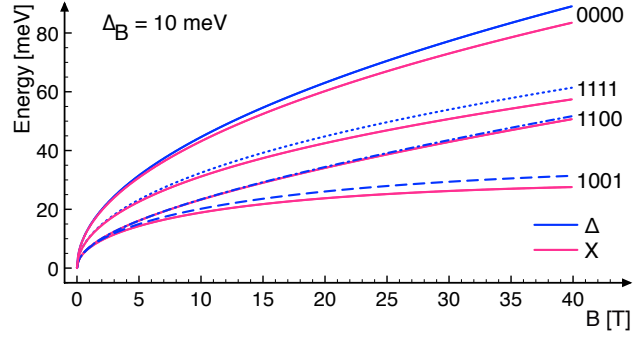
In the above formulae, Erf denotes the error function.

## C.2 Energetic Scales

In order to grasp the energetic scales in our calculations we provide numbers for the energetic splittings and the matrix elements for some system parameters.

**Figure C.1**

Matrix elements  $\Delta$  and  $X$  as functions of the magnetic field  $B$  for fixed bias. The numbers correspond to the subindices indicating the Landau level quantum numbers.



Energetic splittings at  $B = 10$  T:

$\Delta_C$	44.5874 meV	$\Delta_{01}$	$\frac{1}{8}\Delta_C c_1^2(4 - 3c_1^2)$	(C.7)
$\Delta_Z$	1.158 meV	$\Delta_B$	$0.34 E_{\perp} [\frac{\text{mV}}{\text{nm}}]$ meV	

Matrix elements for the values  $M = 0$  and  $B = 10$  T, *i.e.*, for  $c_1(B = 10 \text{ T}, M = 0) = 0.9534$ :

$\Delta_{0000}$	44.5874 meV	$\Delta_{1111}$	32.4746 meV	(C.8)
$\Delta_{1001}$	20.265 meV	$\Delta_{0011}$	23.333 meV	
$X_{0000}$	44.4407 meV	$X_{1111}$	31.191 meV	
$X_{1001}$	18.9782 meV	$X_{0011}$	23.2481 meV	

We demonstrate the behaviour the matrix elements as functions of  $B$  for fixed bias  $\Delta_B = 10$  meV in figure C.1.

---

## Bismuth(111): Decomposition of the Coulomb Interaction

---

### D.1 Coulomb Interaction for Anisotropic Quantum Hall States

We start generally from the Coulomb interaction for electrons in two spatial dimensions

$$H_C = \frac{1}{2} \sum_{\mathbf{q}} V(\mathbf{q}) \rho(-\mathbf{q}) \rho(\mathbf{q}), \quad (\text{D.1})$$

in terms of the Fourier transformed electronic density  $\rho(\mathbf{q}) = \int d^2r e^{-i\mathbf{q}\mathbf{r}} \psi^\dagger(\mathbf{r})\psi(\mathbf{r})$  and the Coulomb potential  $V(\mathbf{q}) = \frac{2\pi e^2}{\epsilon|\mathbf{q}|}$ .

We decompose the density operators in the basis of the spinor wave functions of electrons depending on a set of quantum numbers  $\{\xi\}$ :

$$\rho(\mathbf{q}) = \sum_{\xi;\xi'} \psi_\xi^\dagger \psi_{\xi'} e^{-i\mathbf{q}\mathbf{r}} c_\xi^\dagger c_{\xi'}. \quad (\text{D.2})$$

For single particle wave functions  $\psi_\xi$  in the latter equation we assume the following:

We describe the low-energy situation of Bi(111) as six copies of an anisotropic, elliptical valley formed by one single parabolic band. The six valleys are identical among each other modulo rotation. Hence, after Landau level quantisation of this energetic structure by a magnetic field, the electronic single particle wave function is characterised by three quantum numbers:  $n$  and  $m$  denote the Landau

level quantisation indices and  $\tau = 1 \dots 6$  labels the valleys. We write the electronic single particle states explicitly as

$$\psi_{nm;\tau} = |nm;\tau\rangle e^{i\mathbf{K}_\tau \mathbf{r}}, \quad (\text{D.3})$$

where  $|nm;\tau\rangle$  is the slowly varying envelope function in the  $\tau$ th valley and  $e^{i\mathbf{K}_\tau \mathbf{r}}$  denotes the rapidly oscillating part. The vector  $\mathbf{K}_\tau$  defines the position of the  $\tau$ th valley in momentum space.

Now we express the interaction Hamiltonian in terms of this basis:

$$H_C = \frac{1}{2} \sum_{\mathbf{q}} \sum_{n_i;\tau_i} V_{n_i;\tau_i}(\mathbf{q}) \tilde{\rho}_{n_1,n_3}^{\tau_1,\tau_3}(-\mathbf{q}) \tilde{\rho}_{n_2,n_4}^{\tau_2,\tau_4}(\mathbf{q}), \quad (\text{D.4})$$

featuring the reduced density operators

$$\tilde{\rho}_{n,n'}^{\tau,\tau'}(\mathbf{q}) = \sum_{m,m'} \langle \tau; m | e^{-i[\mathbf{q}+(\mathbf{K}_\tau-\mathbf{K}_{\tau'})]\mathbf{R}} | m'; \tau' \rangle, \quad (\text{D.5})$$

and the matrix elements

$$V_{n_i;\tau_i}(\mathbf{q}) = \frac{2\pi e^2}{\epsilon|\mathbf{q}|} \mathcal{F}_{n_1,n_3}^{\tau_1,\tau_3}(-\mathbf{q}) \mathcal{F}_{n_2,n_4}^{\tau_2,\tau_4}(\mathbf{q}), \quad (\text{D.6})$$

in terms of the form factors

$$\mathcal{F}_{n,n'}^{\tau,\tau'}(\mathbf{q}) = \langle \tau; n | e^{-i[\mathbf{q}+(\mathbf{K}_\tau-\mathbf{K}_{\tau'})]\mathbf{r}_c} | n'; \tau' \rangle, \quad (\text{D.7})$$

where we used the decomposition  $\mathbf{r} = \mathbf{R} + \mathbf{r}_c$  of the spatial coordinate into the coordinate of the guiding centre and the cyclotron orbit, respectively.

### D.1.1 Form Factors for Lowest Landau Level Interaction

We want to compute the form factor of equation (D.7) for electrons in the lowest Landau level, that is, for the special case  $n = n' = 0$ . The expression of interest hence reads

$$\mathcal{F}_{0,0}^{\tau,\tau'}(\mathbf{Q}) = \langle \tau; 0 | e^{-i[\mathbf{Q}\mathbf{r}_c]} | 0; \tau' \rangle. \quad (\text{D.8})$$

We exploit the following armamentarium in order tackle the latter equation (D.8):

- Anisotropy parameters

$$\alpha_\tau = \eta \cos \theta_\tau + i \frac{1}{\eta} \sin \theta_\tau, \quad \beta_\tau = \frac{1}{\eta} \cos \theta_\tau + i \eta \sin \theta_\tau, \quad (\text{D.9})$$

which fulfil

$$\alpha_\tau \beta_\tau^* + \alpha_\tau^* \beta_\tau = 2. \quad (\text{D.10})$$

- Anisotropic ladder operators

$$\mathbf{a}_\tau^\dagger = \frac{\ell_B}{\sqrt{2}\hbar}(\alpha_\tau \Pi_x - i\beta_\tau \Pi_y), \quad \mathbf{a}_\tau = \frac{\ell_B}{\sqrt{2}\hbar}(\alpha_\tau^* \Pi_x + i\beta_\tau^* \Pi_y), \quad (\text{D.11})$$

which fulfil the commutation relations:  $[\mathbf{a}_\tau, \mathbf{a}_\tau^\dagger] = 1$  and  $[\mathbf{a}_{\tau'}, \mathbf{a}_\tau^\dagger] = \frac{1}{2}(\alpha_\tau \beta_{\tau'}^* + \alpha_{\tau'}^* \beta_\tau)$ . They act on the number states in the  $\tau$ th valley as

$$\mathbf{a}_\tau \psi_{n,\tau} = -i \frac{\alpha_\tau^*}{|\alpha_\tau|} \sqrt{n} \psi_{n-1,\tau}, \quad \mathbf{a}_\tau^\dagger \psi_{n,\tau} = -i \frac{|\alpha_\tau|}{\alpha_\tau^*} \sqrt{n+1} \psi_{n+1,\tau}, \quad (\text{D.12})$$

and annihilate the vacuum of the corresponding valley as  $\mathbf{a}_\tau \psi_{0,\tau} = 0$ .

- The anisotropic momenta can be expanded in terms of the ladder operators.

For equal indices:

$$\Pi_x = \frac{\hbar c}{\sqrt{2}\ell_B}(\beta_\tau^* \mathbf{a}_\tau^\dagger + \beta_\tau \mathbf{a}_\tau), \quad \Pi_y = i \frac{\hbar c}{\sqrt{2}\ell_B}(\alpha_\tau^* \mathbf{a}_\tau^\dagger - \alpha_\tau \mathbf{a}_\tau) \quad (\text{D.13})$$

For mixed indices:

$$\begin{aligned} \Pi_x &= \frac{\sqrt{2}}{\alpha_\tau \beta_{\tau'}^* + \alpha_{\tau'}^* \beta_\tau} \frac{\hbar c}{\ell_B} (\beta_{\tau'}^* \mathbf{a}_\tau^\dagger + \beta_\tau \mathbf{a}_{\tau'}), \\ \Pi_y &= i = \frac{\sqrt{2}}{\alpha_\tau \beta_{\tau'}^* + \alpha_{\tau'}^* \beta_\tau} \frac{\hbar c}{\ell_B} (\alpha_{\tau'}^* \mathbf{a}_\tau^\dagger - \alpha_\tau \mathbf{a}_{\tau'}) \end{aligned} \quad (\text{D.14})$$

- Guiding centre coordinates in terms of the ladder operators:

For equal indices:

$$x_c = \frac{\Pi_y}{eB} = \frac{i}{\sqrt{2}} \ell_B (\alpha_\tau^* \mathbf{a}_\tau^\dagger - \alpha_\tau \mathbf{a}_\tau), \quad y_c = -\frac{\Pi_x}{eB} = -\frac{1}{\sqrt{2}} \ell_B (\beta_\tau^* \mathbf{a}_\tau^\dagger + \beta_\tau \mathbf{a}_\tau), \quad (\text{D.15})$$

For mixed indices:

$$\begin{aligned} x_c &= i \frac{\sqrt{2}}{\alpha_\tau \beta_{\tau'}^* + \alpha_{\tau'}^* \beta_\tau} \ell_B (\alpha_{\tau'}^* \mathbf{a}_\tau^\dagger - \alpha_\tau \mathbf{a}_{\tau'}), \\ y_c &= -\frac{\sqrt{2}}{\alpha_\tau \beta_{\tau'}^* + \alpha_{\tau'}^* \beta_\tau} \ell_B (\beta_{\tau'}^* \mathbf{a}_\tau^\dagger + \beta_\tau \mathbf{a}_{\tau'}), \end{aligned} \quad (\text{D.16})$$

- with which we can write the expansion in term of the mixed coordinates expressions:

$$\mathbf{Q} \cdot \mathbf{r}_c^\tau = \Omega_{\tau'} \mathbf{a}_\tau^\dagger + \bar{\Omega}_\tau \mathbf{a}_{\tau'}, \quad (\text{D.17})$$

in terms of the generalised momenta  $\Omega_{\tau'} = i \frac{\sqrt{2}}{\alpha_\tau \beta_{\tau'}^* + \alpha_{\tau'}^* \beta_\tau} \ell_B (\alpha_{\tau'}^* Q_x + i \beta_{\tau'}^* Q_y)$ , and  $\bar{\Omega}_\tau = -i \frac{\sqrt{2}}{\alpha_\tau \beta_{\tau'}^* + \alpha_{\tau'}^* \beta_\tau} \ell_B (\alpha_\tau Q_x - i \beta_\tau Q_y)$ .

The latter relations allow us to perform the following computation:

$$\begin{aligned} \mathcal{F}_{0,0}^{\tau,\tau'}(\mathbf{Q}) &= \langle \tau; 0 | e^{-i[\Omega_{\tau'} \mathbf{a}_\tau^\dagger + \bar{\Omega}_\tau \mathbf{a}_{\tau'}]} | 0; \tau' \rangle \\ &\stackrel{BCH}{=} \langle \tau; 0 | e^{-i\Omega_{\tau'} \mathbf{a}_\tau^\dagger} e^{-i\bar{\Omega}_\tau \mathbf{a}_{\tau'}} e^{-i\frac{1}{2}[-i\Omega_{\tau'} \mathbf{a}_\tau^\dagger, -i\bar{\Omega}_\tau \mathbf{a}_{\tau'}]} | 0; \tau' \rangle \\ &= e^{\frac{1}{2}\Omega_{\tau'} \bar{\Omega}_\tau [\mathbf{a}_\tau^\dagger, \mathbf{a}_{\tau'}]} \langle \tau; 0 | e^{-i\Omega_{\tau'} \mathbf{a}_\tau^\dagger} e^{-i\bar{\Omega}_\tau \mathbf{a}_{\tau'}} | 0; \tau' \rangle \\ &= e^{-\frac{1}{4}\Omega_{\tau'} \bar{\Omega}_\tau (\alpha_\tau \beta_{\tau'}^* + \alpha_{\tau'}^* \beta_\tau)} \underbrace{\langle \tau; 0 | 0; \tau' \rangle}_{=:\mathcal{N}_{\tau\tau'}} \\ &= \mathcal{N}_{\tau\tau'} e^{\frac{\ell_B^2}{2\alpha_\tau \beta_{\tau'}^* + \alpha_{\tau'}^* \beta_\tau} [Q_x^2 \alpha_\tau^* \alpha_\tau + Q_y^2 \beta_{\tau'}^* \beta_\tau - i Q_x Q_y (\alpha_{\tau'}^* \beta_\tau - \beta_{\tau'}^* \alpha_\tau)]}. \end{aligned} \quad (\text{D.18})$$

The latter expression for  $\mathcal{F}_{0,0}^{\tau,\tau'}$  can be symmetrised to read

$$\mathcal{F}_{0,0}^{\tau,\tau'} = \mathcal{N}_{\tau\tau'} e^{\frac{\ell_B^2}{2\alpha_\tau \beta_{\tau'}^* + \alpha_{\tau'}^* \beta_\tau} [\frac{1}{2}(A_{\tau,\tau'} + B_{\tau,\tau'})(Q_x^2 + Q_y^2) + \frac{1}{2}(A - B)(Q_x^2 - Q_y^2) - i C_{\tau,\tau'} Q_x Q_y]} \quad (\text{D.19})$$

where we used the abbreviations  $A_{\tau,\tau'} = \alpha_\tau^* \alpha_{\tau'}$ ,  $B_{\tau,\tau'} = \beta_{\tau'}^* \beta_\tau$ , and  $C_{\tau,\tau'} = \alpha_{\tau'}^* \beta_\tau - \beta_{\tau'}^* \alpha_\tau$ .

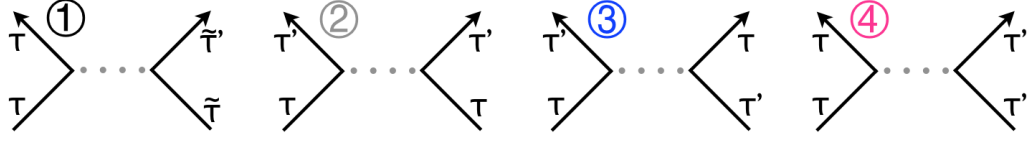
By means of the triangular inequality\* we deduce that  $\mathcal{F}_{0,0}^{\tau,\tau'}$  is to be dominated by the first term in the exponent as  $|(A + B)(Q_x^2 + Q_y^2)| \geq |(A - B)(Q_x^2 - Q_y^2)|$  and the absolute value of the oscillatory term is bounded by unity. We will therefore carefully examine the behaviour of the expression  $e^{\frac{\ell_B^2}{2\alpha_\tau \beta_{\tau'}^* + \alpha_{\tau'}^* \beta_\tau} [\frac{1}{2}(A+B)(Q_x^2 + Q_y^2)]}$  in order to estimate the contributions of different types of scattering processes to the from factor  $\mathcal{F}_{0,0}^{\tau,\tau'}$ .

### D.1.2 Estimation of Different Scattering Processes

We abbreviate  $S_{\tau,\tau'} = \alpha_\tau \beta_{\tau'}^* + \alpha_{\tau'}^* \beta_\tau$  and  $\Omega_{\tau,\tau'} = A_{\tau,\tau'} + B_{\tau,\tau'}$  to write the relation

$$\mathcal{F}_{0,0}^{\tau,\tau'} \propto e^{-\frac{\ell_B^2}{4S_{\tau,\tau'}} \Omega_{\tau,\tau'} |\mathbf{Q}|^2}. \quad (\text{D.20})$$

\* More precisely, we use  $\|x - y\| \leq \|x + y\|$  for any pair of numbers  $x, y \in \mathbb{C}$ .


**Figure D.1**

Different types of valley scattering processes for the Coulomb interaction: ① Momentum non-conserving process, ② Umklapp process, ③ Backscattering process, ④ Valley symmetric process.

We estimate the contributions to the Coulomb interactions from the different possible valley scattering processes sketched in figure D.1:

**① Momentum non-conserving processes**

Valley scattering process:  $\tau \rightarrow \tau$ ,  $\tilde{\tau} \rightarrow \tilde{\tau}' \neq \tilde{\tau}$

Here, the matrix element of equation (D.6) is proportional to

$$\begin{aligned}
 V_{0;\tau_i}(\mathbf{q}) &\propto \mathcal{F}_{0,0}^{\tau,\tau}[-\mathbf{q}] \mathcal{F}_{0,0}^{\tilde{\tau},\tilde{\tau}'}[\mathbf{q} + (\mathbf{K}_{\tilde{\tau}} - \mathbf{K}_{\tilde{\tau}'})] \\
 &\propto e^{-\frac{\ell_B^2}{4S_{\tau,\tau}} \Omega_{\tau,\tau} |\mathbf{q}|^2} e^{-\frac{\ell_B^2}{4S_{\tilde{\tau},\tilde{\tau}'}} \Omega_{\tilde{\tau},\tilde{\tau}'} |\mathbf{q} + (\mathbf{K}_{\tilde{\tau}} - \mathbf{K}_{\tilde{\tau}'})|^2} \\
 &\sim e^{-\frac{\ell_B^2}{8S_{\tilde{\tau},\tilde{\tau}'}} \Omega_{\tilde{\tau},\tilde{\tau}'} |\mathbf{K}_{\tilde{\tau}} - \mathbf{K}_{\tilde{\tau}'}|^2}.
 \end{aligned} \tag{D.21}$$

Hence we understand this type of process to be exponentially suppressed in the distance of the two valleys  $\tilde{\tau}$  and  $\tilde{\tau}'$  in momentum space.

**② Umklapp processes**

Valley scattering process:  $\tau \rightarrow \tau'$ ,  $\tau \rightarrow \tau'$

Here, the matrix element of equation (D.6) is proportional to

$$\begin{aligned}
 V_{0;\tau_i}(\mathbf{q}) &\propto \mathcal{F}_{0,0}^{\tau,\tau'}[-\mathbf{q} + (\mathbf{K}_{\tau} - \mathbf{K}_{\tau'})] \mathcal{F}_{0,0}^{\tau,\tau'}[\mathbf{q} + (\mathbf{K}_{\tau} - \mathbf{K}_{\tau'})] \\
 &\propto e^{-\frac{\ell_B^2}{4S_{\tau,\tau'}} \Omega_{\tau,\tau'} |\mathbf{q} - (\mathbf{K}_{\tau} - \mathbf{K}_{\tau'})|^2} e^{-\frac{\ell_B^2}{4S_{\tau,\tau'}} \Omega_{\tau,\tau'} |\mathbf{q} + (\mathbf{K}_{\tau} - \mathbf{K}_{\tau'})|^2} \\
 &\sim e^{-\frac{\ell_B^2}{4S_{\tau,\tau'}} \Omega_{\tau,\tau'} (2|\mathbf{q}|^2 + 2|\mathbf{K}_{\tau} - \mathbf{K}_{\tau'}|^2)} \sim e^{-\frac{\ell_B^2}{2S_{\tilde{\tau},\tilde{\tau}'}} \Omega_{\tilde{\tau},\tilde{\tau}'} |\mathbf{K}_{\tau} - \mathbf{K}_{\tau'}|^2}.
 \end{aligned} \tag{D.22}$$

Therefore, as this type of process also violates conservation of momentum, we find it equally to be suppressed exponentially.

**③ Backscattering processes**

Valley scattering process:  $\tau \rightarrow \tau'$ ,  $\tau' \rightarrow \tau$

Here, the matrix element of equation (D.6) is proportional to

$$\begin{aligned}
 V_{0;\tau_i}(\mathbf{q}) &\propto \mathcal{F}_{0,0}^{\tau,\tau'}[-\mathbf{q} + (\mathbf{K}_\tau - \mathbf{K}_{\tau'})] \mathcal{F}_{0,0}^{\tau',\tau}[\mathbf{q} + (\mathbf{K}_{\tau'} - \mathbf{K}_\tau)] \\
 &\propto e^{-\frac{\ell_B^2}{4S_{\tau,\tau'}} \Omega_{\tau,\tau'} |\mathbf{q} - (\mathbf{K}_\tau - \mathbf{K}_{\tau'})|^2} e^{-\frac{\ell_B^2}{4S_{\tau',\tau}} \Omega_{\tau',\tau} |\mathbf{q} + (\mathbf{K}_{\tau'} - \mathbf{K}_\tau)|^2} \\
 &\propto e^{-\frac{\ell_B^2}{4S_{\tau,\tau'}} \Omega_{\tau,\tau'} |\mathbf{q} - (\mathbf{K}_\tau - \mathbf{K}_{\tau'})|^2} e^{-\frac{\ell_B^2}{4S_{\tau',\tau}} \Omega_{\tau',\tau} |\mathbf{q} - (\mathbf{K}_\tau - \mathbf{K}_{\tau'})|^2}. \quad (\text{D.23})
 \end{aligned}$$

Hence, after transformation  $\mathbf{q}' = \mathbf{q} - (\mathbf{K}_\tau - \mathbf{K}_{\tau'})$  we see by virtue of equation (D.6) that this process gives rise to the following contribution to the interaction

$$\begin{aligned}
 V_{0;\tau_i}(\mathbf{q}') &= \frac{2\pi e^2}{\epsilon |\mathbf{q}' + (\mathbf{K}_\tau - \mathbf{K}_{\tau'})|} e^{-\frac{\ell_B^2}{4S_{\tau,\tau'}} \Omega_{\tau,\tau'} |\mathbf{q}'|^2} e^{-\frac{\ell_B^2}{4S_{\tau',\tau}} \Omega_{\tau',\tau} |\mathbf{q}'|^2} \\
 &\sim \frac{2\pi e^2}{\epsilon |\mathbf{K}_\tau - \mathbf{K}_{\tau'}|} e^{-\frac{\ell_B^2}{4S_{\tau,\tau'}} \Omega_{\tau,\tau'} |\mathbf{q}'|^2} e^{-\frac{\ell_B^2}{4S_{\tau',\tau}} \Omega_{\tau',\tau} |\mathbf{q}'|^2}. \quad (\text{D.24})
 \end{aligned}$$

Consequently, we see this scattering process to give rise to a contribution that scales like one over the distance of the two valleys  $\tilde{\tau}$  and  $\tilde{\tau}'$  in momentum space.

#### ④ Valley symmetric processes

Valley scattering process:  $\tau \rightarrow \tau, \tilde{\tau} \rightarrow \tilde{\tau}$

In this case, the matrix element of equation (D.6) is proportional to

$$V_{0;\tau_i}(\mathbf{q}) \propto \mathcal{F}_{0,0}^{\tau,\tau}[-\mathbf{q}] \mathcal{F}_{0,0}^{\tilde{\tau},\tilde{\tau}}[\mathbf{q}] \propto e^{-\frac{\ell_B^2}{4S_{\tau,\tau}} \Omega_{\tau,\tau} |\mathbf{q}|^2} e^{-\frac{\ell_B^2}{4S_{\tilde{\tau},\tilde{\tau}}} \Omega_{\tilde{\tau},\tilde{\tau}} |\mathbf{q}|^2}.$$

This type of processes will thus yield the leading contribution to the interaction as all oscillating terms leading to suppression for large absolute values of  $\mathbf{K}$  are cancelled.

---

## List of Publications

---

The following publications are based on this thesis:

- Phase diagram of a graphene bilayer in the zero-energy Landau level  
Angelika Knothe, Thierry Jolicœur  
Phys. Rev. B 94, 235149 (2016), arXiv:1609.04983
- Edge structure of graphene monolayers in the  $\nu = 0$  quantum Hall state  
Angelika Knothe, Thierry Jolicœur  
Phys. Rev. B 92, 165110 (2015), arXiv:1507.05866

Other publications of the author which are not related to this thesis:

- Frequency correlations in reflection from random media  
Angelika Knothe, Thomas Wellens  
J. Opt. Soc. Am. A 32, 305-313 (2015), arXiv:1501.07792
- Flux conservation in coherent backscattering and weak localization of light  
Angelika Knothe, Thomas Wellens  
J. Phys. A: Math. Theor. 46, 315101 (2013), arXiv:1304.0893



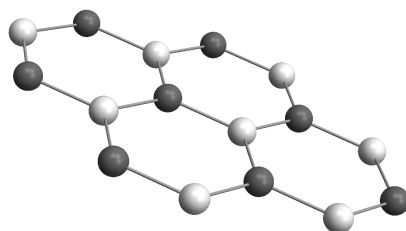
---

## Synthèse en Français

---

Plusieurs ingrédients de cette thèse proviennent des révolutions récentes dans le monde de la physique moderne. D'une part, la découverte de "l'Effet Hall quantique" par Klaus von Klitzing en 1980 (v. [Klitzing \[1985\]](#), prix Nobel 1985), la quantification de la conductivité dans des gaz des électrons en deux dimensions sous champs magnétique a lieu à des températures suffisamment basses. Cette découverte a été reconnue comme un des tous premiers exemples d'un système "topologique". De l'autre part, la réalisation de graphène, un réseau bi-dimensionnel d'atomes de carbone, par Novoselov and Geim ([Geim and Novoselov \[2007\]](#), prix Nobel 2010). Cette découverte des réseaux atomiques vraiment bi-dimensionnels qui peuvent être réalisés dans le monde réel a constitué la naissance d'un vrai zoo de systèmes nouveaux et palpitants en deux dimensions. En principe, les effets Hall quantiques sont attendus pour tout système dans lequel les électrons sont confinés en deux dimensions spatiales sous champs fort magnétique. Donc, en réunissant ces deux concepts fondamentaux de la physique de la matière condensée moderne, les effets Hall quantiques dans les réseaux atomiques en deux dimensions forment un champs abondant pour explorer des nouveaux phénomènes fascinants.

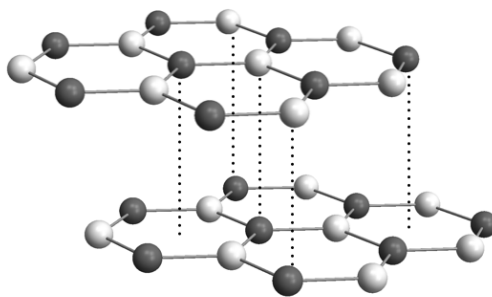
Cette thèse traite des systèmes de Hall quantiques en deux dimensions, dans lesquels les électrons peuvent porter plusieurs degrés de liberté discrets différents. Le ferromagnétisme de Hall quantique fournit une manière élégante et efficace de traiter ces degrés de liberté électroniques comme des spins et isospins effectifs des électrons. Les différentes phases du système correspondent alors à différents ordres de spin ou d'isospin. En exploitant cette analogie, nous explorons différents aspects des systèmes bi-dimensionnels dans le régime de Hall quantique en étudiant la structure correspondante des spins et isospins.

**FIGURE D.2**

Matériau étudié dans le premier projet : les monocouches de graphène. Des atomes de carbone sont arrangés dans un réseau hexagonal. Ceci fournit un système vraiment bi-dimensionnel dans lequel les électrons sont confinés en deux dimensions spatiales.

Ce travail consiste en trois parties qui analysent chacune des matériaux différents bi-dimensionnels dans le régime de l'effet Hall quantique. Dans chaque projet, nous utilisons la théorie de Hartree-Fock pour étudier le système à plusieurs composantes de spin et d'isospin dans l'approximation de champ moyen. Toutes nos considérations sont directement stimulées par des résultats expérimentaux. Notre motivation principale est d'obtenir une compréhension plus profonde des processus physiques et des mécanismes qui déterminent les propriétés des matériaux à partir d'investigations exclusivement théoriques de modèles abstraits. Nous espérons que cela permettra par la suite de tirer des conclusions sur les expériences, de donner des explications aux phénomènes observés ainsi que de donner des perspectives pour des investigations futures.

Le premier projet est consacré à un échantillon fini d'une monocouche de graphène comme celle montrée dans la figure D.2 : nous étudions les propriétés de spin et d'isospin des électrons en présence d'un bord qui brise la symétrie de translation dans l'espace. Dans les monocouches de graphène, les électrons portent, en plus du spin réel, un degré de liberté supplémentaire qui s'appelle «l'isospin de vallée». Cet isospin tient compte d'une manière élégante de la dégénérescence de la dispersion des électrons dans le graphène dans les deux "vallées" situés à deux points de haute symétrie dans la première zone de Brillouin. Le diagramme de phase dans un système de graphène infini avait été analysé auparavant par Kharitonov sous la référence [Kharitonov \[2012c\]](#) : Il identifie quatre phases différents possibles dont chacune présente un ordre différent de spin et d'isospin de vallée. Néanmoins, pour toute investigation expérimentale dans le monde réel, l'échantillon de graphène forcément est toujours de taille finie. Donc, les propriétés du système près du bord de l'échantillon sont essentielles pour comprendre le comportement

**FIGURE D.3**

Matériau étudié dans le deuxième projet : les bicouches de graphène. Deux monocouches de graphènes (comme ceux de la figure D.2) sont empilées l'un au-dessus de l'autre avec l'arrangement de Bernal, donc dans l'arrangement des atomes de carbone montré dans cette image.

du graphène vu dans les expériences. Pour toutes les phases possibles dans le graphène infini nous analysons en utilisant la méthode de Hartree-Fock comment la structure de l'état fondamental ainsi que celle des états excités est influencée par la présence du bord, en comparaison avec les propriétés de l'intérieur du système qui conserve la symétrie de translation. Nous trouvons que les phases dans l'intérieur, et en conséquence tous les propriétés du système, se transforment en fonction de la distance au bord. Près du bord nous observons des états nouveaux qui ne peuvent pas être trouvés dans l'intérieur. En particulier les états fondamentaux peuvent être d'une structure plus complexes que ceux de l'intérieur en comportant, par exemple, de l'intrication non-triviale entre les degrés de liberté du spin et de vallée. Nous discutons les propriétés de la structure des états de bord ainsi que leurs relations éventuelles avec des mesures de conductivité. En particulier nous remettons en question l'explication habituelle des transitions entre régimes de conductivités différentes observées dans des études expérimentales d'une couche simple de graphène, qui est fondée sur des transitions entre des différentes phases dans l'intérieur du système. Nous proposons une explication alternative basée uniquement sur des transitions entre différentes phases près du bord. Les résultats de ce projet ont été publiés sous la référence [Knothe and Jolicoeur \[2015\]](#).

Dans la deuxième partie de la thèse, nous nous intéressons aux bicouches de graphène, donc deux couches de graphène empilées l'un au-dessus de l'autre avec l'arrangement de Bernal comme nous montrons dans la figure D.3. Nous analysons, pour des systèmes infinis sans bords, la dépendance des propriétés de spin et d'isospin sur les champs magnétiques et électriques extérieurs. Dans les bicouches

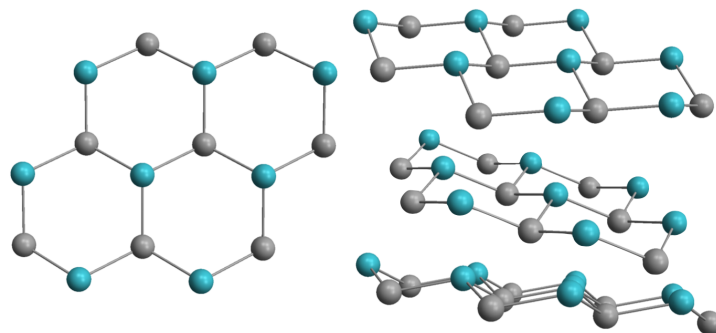


**FIGURE D.4**

Matériau étudié dans le troisième projet : la surface (111) de bismuth élémentaire (orientations différentes). Les électrons dans les états des surfaces d'un cristal trois-dimensionnel également sont confinés en deux dimensions spatiales.

de graphène, il existe un degré de liberté «orbital» supplémentaire à cause d'une dégénérescence entre les niveaux de Landau avec les nombres quantiques  $n = 0$  et  $n = 1$ . Dans notre modèle nous incorporons, à part du couplage avec les champs magnétiques et électriques extérieurs, l'interaction coulombienne des électrons dans les niveaux  $n = 0$  et  $n = 1$  entre eux, ainsi que l'interaction avec les électrons qui constituent la mer de Dirac dans le graphène. Dans une étude champ moyen de Hartree-Fock nous identifions les multiples états fondamentaux différents en fonction des intensités des champs électrique et magnétique et nous présentons les diagrammes de phases correspondants. Nous analysons les propriétés des phases et des transitions entre elles. Notamment notre modèle prédit pour certains régimes des paramètres suffisamment larges et accessible dans des expériences des états fondamentaux pour lesquelles les degrés de liberté d'isospin présentent une cohérence non-triviale. La phase qui porte de la cohérence non-triviale entre les niveaux de Landau  $n = 0$  et  $n = 1$  est particulièrement intéressante car cette propriété existe que dans les bicouches de graphène. Nous faisons la comparaison avec la littérature expérimentale ainsi que les traitements théoriques antérieurs sur les transitions de phase dans les bicouches de graphène pour faire des suggestions pour associer les prédictions des phases de notre modèle aux phases observées aux expériences. Les résultats que nous avons obtenus dans cette partie ont été publiés sous la référence [Knothe and Jolicoeur \[2016\]](#).

Enfin, dans notre projet le plus récent, nous donnons un aperçu de la possibilité d'étendre les idées précédentes pour analyser des surfaces bi-dimensionnelles de cristaux en trois dimensions dans le régime de Hall quantique. Sous certaines

conditions ces surfaces peuvent supporter des états de surface stables. Des électrons qui sont dans ces états de surface se trouvent confinés en deux dimensions spatiales. Nous discutons l'exemple d'une surface (111) de bismuth élémentaire qui est montré dans la figure D.4 : dans ce cas, en considérant la dispersion de basse énergie des états de surface, on est confronté à un système de plusieurs vallées dégénérées et anisotropes. Nous essayons de trouver un modèle de dispersion dans ce système en approximant les vallées par des bandes elliptiques et en considérant l'effet de contraintes locales. On présente des résultats préliminaires sur l'ordre du degré de liberté de vallée des états fondamentaux. Le travail présenté sur ce sujet dans cette thèse est encore en cours.

En résumant nous constatons que nous avons fait des études de certaines propriétés des réseaux atomiques différents dans le régime de l'effet Hall quantique. Nous espérons que ce travail va contribuer à avancer cette domaine de la physique moderne de la matière condensée. Mais ce n'est que le début ! Déjà aujourd'hui beaucoup d'autres réseaux atomiques bi-dimensionnels sont connus qui sont stables et qui ont été réalisés dans les expériences. Comme c'est un champs en pleine évolution, dans les années à venir, cette famille va croître encore. Ça donne la perspective palpitante d'explorer les propriétés nouvelles et inconnues d'un pléiade de matériaux originaux, ainsi que leur combinaisons comme des empilements des couches pareilles ou différentes ou des hétérostructures. Nous espérons que cette direction de recherche actuelle va mener à de nouvelles découvertes physiques fondamentales ainsi qu'à des idées originales en vue d'applications.



---

## Bibliography

---

- D. A. Abanin, S. A. Parameswaran, S. A. Kivelson, and S. L. Sondhi. Nematic valley ordering in quantum Hall systems. *Physical Review B*, 82(3):035428, 2010. doi: 10.1103/PhysRevB.82.035428.
- Dmitry A. Abanin, Patrick A. Lee, and Leonid S. Levitov. Spin-Filtered Edge States and Quantum Hall Effect in Graphene. *Physical Review Letters*, 96(17):176803, 2006. doi: 10.1103/PhysRevLett.96.176803.
- A. R. Akhmerov and C. W. J. Beenakker. Boundary conditions for Dirac fermions on a terminated honeycomb lattice. *Physical Review B*, 77(8):085423, 2008. doi: 10.1103/PhysRevB.77.085423.
- I. L. Aleiner, D. E. Kharzeev, and A. M. Tsvelik. Spontaneous symmetry breaking in graphene subjected to an in-plane magnetic field. *Physical Review B*, 76(19):195415, 2007. doi: 10.1103/PhysRevB.76.195415.
- Jason Alicea and Matthew P. A. Fisher. Graphene integer quantum Hall effect in the ferromagnetic and paramagnetic regimes. *Physical Review B*, 74(7):075422, 2006. doi: 10.1103/PhysRevB.74.075422.
- Jason Alicea and Matthew P. A. Fisher. Interplay between lattice-scale physics and the quantum Hall effect in graphene. *Solid State Communications*, 143(11–12):504–509, 2007. ISSN 0038-1098. doi: 10.1016/j.ssc.2007.06.035.
- Yoichi Ando and Liang Fu. Topological Crystalline Insulators and Topological Superconductors: From Concepts to Materials. *Annual Review of Condensed Matter Physics*, 6(1):361–381, 2015. doi: 10.1146/annurev-conmatphys-031214-014501.
- Christian R. Ast and Hartmut Höchst. Fermi Surface of Bi(111) Measured by Photoemission Spectroscopy. *Physical Review Letters*, 87(17):177602, 2001. doi: 10.1103/PhysRevLett.87.177602.

- W. Bao, L. Jing, J. Velasco Jr, Y. Lee, G. Liu, D. Tran, B. Standley, M. Aykol, S. B. Cronin, D. Smirnov, M. Koshino, E. McCann, M. Bockrath, and C. N. Lau. Stacking-dependent band gap and quantum transport in trilayer graphene. *Nature Physics*, 7(12):948–952, 2011. ISSN 1745-2473. doi: 10.1038/nphys2103.
- Wenzhong Bao, Jairo Velasco, Fan Zhang, Lei Jing, Brian Standley, Dmitry Smirnov, Marc Bockrath, Allan H. MacDonald, and Chun Ning Lau. Evidence for a spontaneous gapped state in ultraclean bilayer graphene. *Proceedings of the National Academy of Sciences*, 109(27):10802–10805, 2012. ISSN 0027-8424, 1091-6490. doi: 10.1073/pnas.1205978109.
- Yafis Barlas, R. Côté, K. Nomura, and A. H. MacDonald. Intra-Landau-Level Cyclotron Resonance in Bilayer Graphene. *Physical Review Letters*, 101(9):097601, 2008. doi: 10.1103/PhysRevLett.101.097601.
- Yafis Barlas, R. Côté, J. Lambert, and A. H. MacDonald. Anomalous Exciton Condensation in Graphene Bilayers. *Physical Review Letters*, 104(9):096802, 2010. doi: 10.1103/PhysRevLett.104.096802.
- Yafis Barlas, Kun Yang, and A. H. MacDonald. Quantum Hall effects in graphene-based two-dimensional electron systems. *Nanotechnology*, 23:052001, 2012. ISSN 0957-4484. doi: 10.1088/0957-4484/23/5/052001.
- Kirill I. Bolotin, Fereshte Ghahari, Michael D. Shulman, Horst L. Stormer, and Philip Kim. Observation of the fractional quantum Hall effect in graphene. *Nature*, 462(7270):196–199, 2009. ISSN 0028-0836. doi: 10.1038/nature08582.
- L. Brey and H. A. Fertig. Electronic states of graphene nanoribbons studied with the Dirac equation. *Physical Review B*, 73(23):235411, 2006a. doi: 10.1103/PhysRevB.73.235411.
- Luis Brey and H. A. Fertig. Edge states and the quantized Hall effect in graphene. *Physical Review B*, 73(19):195408, 2006b. doi: 10.1103/PhysRevB.73.195408.
- Eduardo V. Castro, K. S. Novoselov, S. V. Morozov, N. M. R. Peres, J. M. B. Lopes dos Santos, Johan Nilsson, F Guinea, A. K. Geim, and A. H. Castro Neto. Electronic properties of a biased graphene bilayer. *Journal of Physics: Condensed Matter*, 22(17):175503, 2010. ISSN 0953-8984. doi: 10.1088/0953-8984/22/17/175503.
- A. H. Castro Neto, F. Guinea, N. M. R. Peres, K. S. Novoselov, and Geim A. K. The electronic properties of graphene. *Reviews of Modern Physics*, 81(1):109–162, 2009. doi: 10.1103/RevModPhys.81.109.

- C. de C. Chamon and X. G. Wen. Sharp and smooth boundaries of quantum Hall liquids. *Physical Review B*, 49(12):8227–8241, 1994. doi: 10.1103/PhysRevB.49.8227.
- A. M. Chang, L. N. Pfeiffer, and K. W. West. Observation of Chiral Luttinger Behavior in Electron Tunneling into Fractional Quantum Hall Edges. *Physical Review Letters*, 77(12):2538–2541, 1996. doi: 10.1103/PhysRevLett.77.2538.
- D. B. Chklovskii, B. I. Shklovskii, and L. I. Glazman. Electrostatics of edge channels. *Physical Review B*, 46(7):4026–4034, 1992. doi: 10.1103/PhysRevB.46.4026.
- R. Côté and Manuel Barrette. Validity of the two-component model of bilayer and trilayer graphene in a magnetic field. *Physical Review B*, 88(24):245445, 2013. doi: 10.1103/PhysRevB.88.245445.
- R. Côté, Jules Lambert, Yafis Barlas, and A. H. MacDonald. Orbital order in bilayer graphene at filling factor  $\nu = -1$ . *Physical Review B*, 82(3):035445, 2010. doi: 10.1103/PhysRevB.82.035445.
- R. Côté, J. P. Fouquet, and Wenchen Luo. Biased bilayer graphene as a helical quantum Hall ferromagnet. *Physical Review B*, 84(23):235301, 2011. doi: 10.1103/PhysRevB.84.235301.
- J. R. M. de Nova and I. Zapata. Symmetry characterization of the collective modes of the phase diagram of the  $\nu = 0$  quantum Hall state in graphene: Mean-field and spontaneously broken symmetries. *arXiv:1701.03278 [cond-mat]*, 2017.
- C. R. Dean, A. F. Young, P. Cadden-Zimansky, L. Wang, H. Ren, K. Watanabe, T. Taniguchi, P. Kim, J. Hone, and K. L. Shepard. Multicomponent fractional quantum Hall effect in graphene. *Nature Physics*, 7(9):693–696, 2011. ISSN 1745-2473. doi: 10.1038/nphys2007.
- Hongjian Du, Xia Sun, Xiaogang Liu, Xiaojun Wu, Jufeng Wang, Mingyang Tian, Aidi Zhao, Yi Luo, Jinlong Yang, Bing Wang, and J. G. Hou. Surface Landau levels and spin states in bismuth (111) ultrathin films. *Nature Communications*, 7: 10814, 2016. ISSN 2041-1723. doi: 10.1038/ncomms10814.
- P. Dziawa, B. J. Kowalski, K. Dybko, R. Buczko, A. Szczerbakow, M. Szot, E. Łusakowska, T. Balasubramanian, B. M. Wojek, M. H. Berntsen, O. Tjernberg, and T. Story. Topological crystalline insulator states in  $\text{Pb}_{1-x}\text{Sn}_x\text{Se}$ . *Nature Materials*, 11(12):1023–1027, 2012. ISSN 1476-1122. doi: 10.1038/nmat3449.
- Motohiko Ezawa. Quantum Hall Effects in Silicene. *Journal of the Physical Society of Japan*, 81(6):064705, 2012. ISSN 0031-9015. doi: 10.1143/JPSJ.81.064705.

- Z. F. Ezawa, M. Eliashvili, and G. Tsitsishvili. Ground-state structure in  $\nu = 2$  bilayer quantum Hall systems. *Physical Review B*, 71(12):125318, 2005. doi: 10.1103/PhysRevB.71.125318.
- Zyun F. Ezawa. *Quantum Hall Effects: Field Theoretical Approach and Related Topics*. World Scientific Publishing Company, Hackensack, N.J. ; London, 2nd edition edition, 2008. ISBN 978-981-270-032-2.
- Benjamin E. Feldman, Mallika T. Randeria, András Gyenis, Fengcheng Wu, Huiwen Ji, R. J. Cava, Allan H. MacDonald, and Ali Yazdani. Observation of a nematic quantum Hall liquid on the surface of bismuth. *Science*, 354:316–321, 2016. ISSN 0036-8075, 1095-9203. doi: 10.1126/science.aag1715.
- H. A. Fertig and L. Brey. Luttinger Liquid at the Edge of Undoped Graphene in a Strong Magnetic Field. *Physical Review Letters*, 97(11):116805, 2006. doi: 10.1103/PhysRevLett.97.116805.
- Eduardo Fradkin, Steven A. Kivelson, Michael J. Lawler, James P. Eisenstein, and Andrew P. Mackenzie. Nematic Fermi Fluids in Condensed Matter Physics. *Annual Review of Condensed Matter Physics*, 1(1):153–178, 2010. doi: 10.1146/annurev-conmatphys-070909-103925.
- F. Freitag, J. Trbovic, M. Weiss, and C. Schönenberger. Spontaneously Gapped Ground State in Suspended Bilayer Graphene. *Physical Review Letters*, 108(7):076602, 2012. doi: 10.1103/PhysRevLett.108.076602.
- Liang Fu. Topological Crystalline Insulators. *Physical Review Letters*, 106(10):106802, 2011. doi: 10.1103/PhysRevLett.106.106802.
- A. K. Geim and K. S. Novoselov. The rise of graphene. *Nature Materials*, 6(3):183–191, 2007. ISSN 1476-1122. doi: 10.1038/nmat1849.
- M. O. Goerbig. Electronic properties of graphene in a strong magnetic field. *Reviews of Modern Physics*, 83(4):1193–1243, 2011. doi: 10.1103/RevModPhys.83.1193.
- E. V. Gorbar, V. P. Gusynin, and V. A. Miransky. Energy gaps at neutrality point in bilayer graphene in a magnetic field. *JETP Letters*, 91(6):314–318, 2010. ISSN 0021-3640, 1090-6487. doi: 10.1134/S0021364010060111.
- E. V. Gorbar, V. P. Gusynin, Junji Jia, and V. A. Miransky. Broken-symmetry states and phase diagram of the lowest Landau level in bilayer graphene. *Physical Review B*, 84(23):235449, 2011. doi: 10.1103/PhysRevB.84.235449.

- E. V. Gorbar, V. P. Gusynin, A. B. Kuzmenko, and S. G. Sharapov. Magneto-optical and optical probes of gapped ground states of bilayer graphene. *Physical Review B*, 86(7):075414, 2012a. doi: 10.1103/PhysRevB.86.075414.
- E. V. Gorbar, V. P. Gusynin, V. A. Miransky, and I. A. Shovkovy. Broken symmetry  $\nu = 0$  quantum Hall states in bilayer graphene: Landau level mixing and dynamical screening. *Physical Review B*, 85(23):235460, 2012b. doi: 10.1103/PhysRevB.85.235460.
- M. Grayson, D. C. Tsui, L. N. Pfeiffer, K. W. West, and A. M. Chang. Continuum of Chiral Luttinger Liquids at the Fractional Quantum Hall Edge. *Physical Review Letters*, 80(5):1062–1065, 1998. doi: 10.1103/PhysRevLett.80.1062.
- E. H. Hall. On a New Action of the Magnet on Electric Currents. *American Journal of Mathematics*, 2(3):287–292, 1879. ISSN 0002-9327. doi: 10.2307/2369245.
- M. Z. Hasan and C. L. Kane. *Colloquium* : Topological insulators. *Reviews of Modern Physics*, 82(4):3045–3067, 2010. doi: 10.1103/RevModPhys.82.3045.
- Paul-Henri Heenen and Michel R. Godefroid. The Hartree-Fock method. *Scholarpedia*, 7(10):10545, 2012. ISSN 1941-6016. doi: 10.4249/scholarpedia.10545.
- Timothy H. Hsieh, Hsin Lin, Junwei Liu, Wenhui Duan, Arun Bansil, and Liang Fu. Topological crystalline insulators in the SnTe material class. *Nature Communications*, 3:982, 2012. ISSN 2041-1723. doi: 10.1038/ncomms1969.
- Zi-Xiang Hu, R. N. Bhatt, Xin Wan, and Kun Yang. Realizing Universal Edge Properties in Graphene Fractional Quantum Hall Liquids. *Physical Review Letters*, 107(23):236806, 2011. doi: 10.1103/PhysRevLett.107.236806.
- B. M. Hunt, J. I. A. Li, A. A. Zibrov, L. Wang, T. Taniguchi, K. Watanabe, J. Hone, C. R. Dean, M. Zaletel, R. C. Ashoori, and A. F. Young. Direct measurement of discrete valley and orbital quantum numbers in a multicomponent quantum Hall system. *arXiv:1607.06461 [cond-mat]*, 2016.
- Jainendra K. Jain. *Composite Fermions by Jainendra K. Jain*. Cambridge University Press, 2007.
- Martin Janssen, Olaf Viefweger, Ulrich Fastenrath, and Janos Hajdu. *Introduction to the Theory of the Integer Quantum Hall Effect*. Wiley-VCH, Weinheim ; New York, 427 s. edition, 1994. ISBN 978-3-527-29209-7.
- G. Jezequel, Y. Petroff, R. Pinchaux, and Félix Yndurain. Electronic structure of the Bi(111) surface. *Physical Review B*, 33(6):4352–4355, 1986. doi: 10.1103/PhysRevB.33.4352.

- J. Jung and A. H. MacDonald. Theory of the magnetic-field-induced insulator in neutral graphene sheets. *Physical Review B*, 80(23):235417, 2009. doi: 10.1103/PhysRevB.80.235417.
- Jeil Jung, Fan Zhang, and Allan H. MacDonald. Lattice theory of pseudospin ferromagnetism in bilayer graphene: Competing interaction-induced quantum Hall states. *Physical Review B*, 83(11):115408, 2011. doi: 10.1103/PhysRevB.83.115408.
- Maxim Kharitonov. Canted Antiferromagnetic Phase of the  $\nu = 0$  Quantum Hall State in Bilayer Graphene. *Physical Review Letters*, 109(4):046803, 2012a. doi: 10.1103/PhysRevLett.109.046803.
- Maxim Kharitonov. Edge excitations of the canted antiferromagnetic phase of the  $\nu = 0$  quantum Hall state in graphene: A simplified analysis. *Physical Review B*, 86(7):075450, 2012b. doi: 10.1103/PhysRevB.86.075450.
- Maxim Kharitonov. Phase diagram for the  $\nu = 0$  quantum Hall state in monolayer graphene. *Physical Review B*, 85(15):155439, 2012c. doi: 10.1103/PhysRevB.85.155439.
- Seyoung Kim, Kayoung Lee, and E. Tutuc. Spin-Polarized to Valley-Polarized Transition in Graphene Bilayers at  $\nu = 0$  in High Magnetic Fields. *Physical Review Letters*, 107(1):016803, 2011. doi: 10.1103/PhysRevLett.107.016803.
- Youngwook Kim, Jaesung Park, Intek Song, Jong Mok Ok, Younjung Jo, Kenji Watanabe, Takashi Taniguchi, Hee Cheul Choi, Dong Su Lee, Suyong Jung, and Jun Sung Kim. Broken-Symmetry Quantum Hall States in Twisted Bilayer Graphene. *Scientific Reports*, 6:38068, 2016. ISSN 2045-2322. doi: 10.1038/srep38068.
- Angelika Knothe and Thierry Jolicoeur. Edge structure of graphene monolayers in the  $\nu = 0$  quantum Hall state. *Physical Review B*, 92:165110, 2015. doi: 10.1103/PhysRevB.92.165110.
- Angelika Knothe and Thierry Jolicoeur. Phase diagram of a graphene bilayer in the zero-energy Landau level. *Physical Review B*, 94:235149, 2016. doi: 10.1103/PhysRevB.94.235149.
- Yu. M. Koroteev, G. Bihlmayer, J. E. Gayone, E. V. Chulkov, S. Blügel, P. M. Echenique, and Ph. Hofmann. Strong Spin-Orbit Splitting on Bi Surfaces. *Physical Review Letters*, 93(4):046403, 2004. doi: 10.1103/PhysRevLett.93.046403.
- Willis E. Lamb and Robert C. Retherford. Fine structure of the hydrogen atom by a microwave method. *Physical Review*, 72(3):241–243, 1947. doi: 10.1103/PhysRev.72.241.

- J. Lambert and R. Côté. Quantum Hall ferromagnetic phases in the Landau level  $n=0$  of a graphene bilayer. *Physical Review B*, 87(11):115415, 2013. doi: 10.1103/PhysRevB.87.115415.
- Jules Lambert. Ferro-aimants de Hall dans la bicouche de graphène. *Thèse de Doctorat*, 2013. doi: <http://hdl.handle.net/11143/6552>.
- Dong Su Lee, Christian Riedl, Thomas Beringer, A. H. Castro Neto, Klaus von Klitzing, Ulrich Starke, and Jurgen H. Smet. Quantum Hall Effect in Twisted Bilayer Graphene. *Physical Review Letters*, 107(21):216602, 2011. doi: 10.1103/PhysRevLett.107.216602.
- Kayoung Lee, Babak Fallahazad, Jiamin Xue, David C. Dillen, Kyoungwan Kim, Takashi Taniguchi, Kenji Watanabe, and Emanuel Tutuc. Chemical potential and quantum Hall ferromagnetism in bilayer graphene. *Science*, 345(6192):58–61, 2014. ISSN 0036-8075, 1095-9203. doi: 10.1126/science.1251003.
- Guohong Li, Adina Luican-Mayer, Dmitry Abanin, Leonid Levitov, and Eva Y. Andrei. Evolution of Landau levels into edge states in graphene. *Nature Communications*, 4:1744, 2013. doi: 10.1038/ncomms2767.
- Xiao Li, Fan Zhang, and H. MacDonald, A. SU(3) Quantum Hall Ferromagnetism in SnTe. *Physical Review Letters*, 116(2):026803, 2016. doi: 10.1103/PhysRevLett.116.026803.
- Cheng-Cheng Liu, Wanxiang Feng, and Yugui Yao. Quantum Spin Hall Effect in Silicene and Two-Dimensional Germanium. *Physical Review Letters*, 107(7):076802, 2011. doi: 10.1103/PhysRevLett.107.076802.
- Zheng Liu, Kazu Suenaga, Peter J. F. Harris, and Sumio Iijima. Open and Closed Edges of Graphene Layers. *Physical Review Letters*, 102(1):015501, 2009. doi: 10.1103/PhysRevLett.102.015501.
- J. M. B. Lopes dos Santos, N. M. R. Peres, and A. H. Castro Neto. Graphene Bilayer with a Twist: Electronic Structure. *Physical Review Letters*, 99(25):256802, 2007. doi: 10.1103/PhysRevLett.99.256802.
- Chun Hung Lui, Zhiqiang Li, Kin Fai Mak, Emmanuele Cappelluti, and Tony F. Heinz. Observation of an electrically tunable band gap in trilayer graphene. *Nature Physics*, 7(12):944–947, 2011. ISSN 1745-2473. doi: 10.1038/nphys2102.
- A. Luican, Guohong Li, A. Reina, J. Kong, R. R. Nair, K. S. Novoselov, A. K. Geim, and E. Y. Andrei. Single-Layer Behavior and Its Breakdown in Twisted Graphene Layers. *Physical Review Letters*, 106(12):126802, 2011. doi: 10.1103/PhysRevLett.106.126802.

- A. H. MacDonald. Introduction to the Physics of the Quantum Hall Regime. *arXiv:cond-mat/9410047*, 1994.
- Koichi Maezawa, Takashi Mizutani, and Syoji Yamada. Effective mass and ground state of AlAs quantum wells studied by magnetoresistance measurements. *Journal of Applied Physics*, 71(1):296–299, 1992. ISSN 0021-8979. doi: 10.1063/1.350704.
- P. Maher, C. R. Dean, A. F. Young, T. Taniguchi, K. Watanabe, K. L. Shepard, J. Hone, and P. Kim. Evidence for a spin phase transition at charge neutrality in bilayer graphene. *Nature Physics*, 9(3):154–158, 2013. ISSN 1745-2473. doi: 10.1038/nphys2528.
- Patrick Maher, Lei Wang, Yuanda Gao, Carlos Forsythe, Takashi Taniguchi, Kenji Watanabe, Dmitry Abanin, Zlatko Papić, Paul Cadden-Zimansky, James Hone, Philip Kim, and Cory R. Dean. Tunable fractional quantum Hall phases in bilayer graphene. *Science*, 345(6192):61–64, 2014. ISSN 0036-8075, 1095-9203. doi: 10.1126/science.1252875.
- Edward McCann and Vladimir I. Fal’ko. Landau-Level Degeneracy and Quantum Hall Effect in a Graphite Bilayer. *Physical Review Letters*, 96(8):086805, 2006. doi: 10.1103/PhysRevLett.96.086805.
- Edward McCann and Mikito Koshino. The electronic properties of bilayer graphene. *Reports on Progress in Physics*, 76(5):056503, 2013. ISSN 0034-4885. doi: 10.1088/0034-4885/76/5/056503.
- J. W. McClure. Band Structure of Graphite and de Haas-van Alphen Effect. *Physical Review*, 108(3):612–618, 1957. doi: 10.1103/PhysRev.108.612.
- W. N. Mei and Y. C. Lee. Harmonic oscillator with potential barriers-exact solutions and perturbative treatments. *Journal of Physics A: Mathematical and General*, 16(8):1623, 1983. ISSN 0305-4470. doi: 10.1088/0305-4470/16/8/010.
- E. J. Mele. Commensuration and interlayer coherence in twisted bilayer graphene. *Physical Review B*, 81(16):161405, 2010. doi: 10.1103/PhysRevB.81.161405.
- Hongki Min, Bhagawan Sahu, Sanjay K. Banerjee, and A. H. MacDonald. *Ab initio* theory of gate induced gaps in graphene bilayers. *Physical Review B*, 75(15):155115, 2007. doi: 10.1103/PhysRevB.75.155115.
- Hongki Min, Giovanni Borghi, Marco Polini, and A. H. MacDonald. Pseudospin magnetism in graphene. *Physical Review B*, 77(4):041407, 2008. doi: 10.1103/PhysRevB.77.041407.

- Florian Mintert, André R. R. Carvalho, Marek Kuś, and Andreas Buchleitner. Measures and dynamics of entangled states. *Physics Reports*, 415(4):207–259, 2005. ISSN 0370-1573. doi: 10.1016/j.physrep.2005.04.006.
- M. Mucha-Kruczyński, O. Tsypliyev, A. Grishin, E. McCann, Vladimir I. Fal’ko, Aaron Bostwick, and Eli Rotenberg. Characterization of graphene through anisotropy of constant-energy maps in angle-resolved photoemission. *Physical Review B*, 77(19):195403, 2008. doi: 10.1103/PhysRevB.77.195403.
- M. Mucha-Kruczyński, D. S. L. Abergel, E. McCann, and V. I. Fal’ko. On spectral properties of bilayer graphene: The effect of an SiC substrate and infrared magneto-spectroscopy. *Journal of Physics: Condensed Matter*, 21(34):344206, 2009. ISSN 0953-8984. doi: 10.1088/0953-8984/21/34/344206.
- Marcin Mucha-Kruczyński. *Theory of Bilayer Graphene Spectroscopy*. Springer Theses. Springer Berlin Heidelberg, Berlin, Heidelberg, 2013. ISBN 978-3-642-30935-9 978-3-642-30936-6.
- Ganpathy Murthy, Efrat Shimshoni, and H. A. Fertig. Collective edge modes near the onset of a graphene quantum spin Hall state. *Physical Review B*, 90(24):241410, 2014. doi: 10.1103/PhysRevB.90.241410.
- K. Nakada, M. Fujita, G. Dresselhaus, and M. S. Dresselhaus. Edge state in graphene ribbons: Nanometer size effect and edge shape dependence. *Physical Review B, Condensed Matter*, 54(24):17954–17961, 1996. doi: 10.1103/PhysRevB.54.17954.
- Rahul Nandkishore and Leonid Levitov. Quantum anomalous Hall state in bilayer graphene. *Physical Review B*, 82(11):115124, 2010a. doi: 10.1103/PhysRevB.82.115124.
- Rahul Nandkishore and Leonid Levitov. Flavor Symmetry and Competing Orders in Bilayer Graphene. *arXiv:1002.1966 [cond-mat]*, 2010b.
- A. J. Niemi and G. W. Semenoff. Quantum Holonomy and the Chiral Gauge Anomaly. *Physical Review Letters*, 55(9):927–930, 1985. doi: 10.1103/PhysRevLett.55.927.
- Kentaro Nomura and Allan H. MacDonald. Quantum Hall Ferromagnetism in Graphene. *Physical Review Letters*, 96(25):256602, 2006. doi: 10.1103/PhysRevLett.96.256602.
- K. S. Novoselov, A. K. Geim, S. V. Morozov, D. Jiang, Y. Zhang, S. V. Dubonos, I. V. Grigorieva, and A. A. Firsov. Electric Field Effect in Atomically Thin Carbon

- Films. *Science*, 306(5696):666–669, 2004. ISSN 0036-8075, 1095-9203. doi: 10.1126/science.1102896.
- Y. Ohtsubo, J. Mauchain, J. Faure, E. Papalazarou, M. Marsi, P. Le Fèvre, F. Bertran, A. Taleb-Ibrahimi, and L. Perfetti. Giant Anisotropy of Spin-Orbit Splitting at the Bismuth Surface. *Physical Review Letters*, 109(22):226404, 2012. doi: 10.1103/PhysRevLett.109.226404.
- Yoshiyuki Ohtsubo and Shin-ichi Kimura. Topological phase transition of single-crystal Bi based on empirical tight-binding calculations. *New Journal of Physics*, 18(12):123015, 2016. ISSN 1367-2630. doi: 10.1088/1367-2630/18/12/123015.
- Medini Padmanabhan, T. Gokmen, and M. Shayegan. Ferromagnetic Fractional Quantum Hall States in a Valley-Degenerate Two-Dimensional Electron System. *Physical Review Letters*, 104(1):016805, 2010. doi: 10.1103/PhysRevLett.104.016805.
- Z. Papić and D. A. Abanin. Topological Phases in the Zeroth Landau Level of Bilayer Graphene. *Physical Review Letters*, 112(4):046602, 2014. doi: 10.1103/PhysRevLett.112.046602.
- R. Peierls. On the Theory of the Diamagnetism of Conduction Electrons. In *Selected Scientific Papers of Sir Rudolf Peierls*, volume Volume 19 of *World Scientific Series in 20th Century Physics*, pages 97–120. CO-PUBLISHED BY IMPERIAL COLLEGE PRESS AND WORLD SCIENTIFIC PUBLISHING CO., 1933. ISBN 978-981-02-2692-3. doi: 10.1142/9789812795779\_0010.
- Rudolf A. Römer and Christoph Sohrmann. Hartree–Fock interactions in the integer quantum Hall effect. *physica status solidi (b)*, 245(2):336–343, 2008. ISSN 1521-3951. doi: 10.1002/pssb.200743321.
- C. C. J. Roothaan. New Developments in Molecular Orbital Theory. *Reviews of Modern Physics*, 23(2):69–89, 1951. doi: 10.1103/RevModPhys.23.69.
- Riichiro Saito, G. Dresselhaus, and M. S. Dresselhaus. *Physical Properties of Carbon Nanotubes*. Imperial College Press, 1998. ISBN 978-1-86094-093-4. Google-Books-ID: w5oHCWhA2EQC.
- Elton J. G. Santos and Efthimios Kaxiras. Electric-Field Dependence of the Effective Dielectric Constant in Graphene. *Nano Letters*, 13(3):898–902, 2013. ISSN 1530-6984. doi: 10.1021/nl303611v.
- Sankar Das Sarma and Aron Pinczuk. *Perspectives in Quantum Hall Effects: Novel Quantum Liquids in Low-Dimensional Semiconductor Structures*. John Wiley & Sons, New York, 1. auflage edition, 1996. ISBN 978-0-471-11216-7.

- M. Shayegan, E. P. De Poortere, O. Gunawan, Y. P. Shkolnikov, E. Tutuc, and K. Vakili. Quantum hall effect in a multi-valley two-dimensional electron system. *International Journal of Modern Physics B*, 21(08n09):1388–1397, 2007. ISSN 0217-9792. doi: 10.1142/S0217979207042884.
- Yanmeng Shi, Yongjin Lee, Shi Che, Ziqi Pi, Timothy Espiritu, Petr Stepanov, Dmitry Smirnov, Chun Ning Lau, and Fan Zhang. Energy Gaps and Layer Polarization of Integer and Fractional Quantum Hall States in Bilayer Graphene. *Physical Review Letters*, 116(5):056601, 2016. doi: 10.1103/PhysRevLett.116.056601.
- K. Shizuya. Structure and the Lamb-shift-like quantum splitting of the pseudo-zero-mode Landau levels in bilayer graphene. *Physical Review B*, 86(4):045431, 2012. doi: 10.1103/PhysRevB.86.045431.
- Y. P. Shkolnikov, K. Vakili, E. P. De Poortere, and M. Shayegan. Giant low-temperature piezoresistance effect in AlAs two-dimensional electrons. *Applied Physics Letters*, 85(17):3766–3768, 2004. ISSN 0003-6951. doi: 10.1063/1.1808883.
- Y. P. Shkolnikov, S. Misra, N. C. Bishop, E. P. De Poortere, and M. Shayegan. Observation of Quantum Hall “Valley Skyrmions”. *Physical Review Letters*, 95(6):066809, 2005. doi: 10.1103/PhysRevLett.95.066809.
- J. C. Slonczewski and P. R. Weiss. Band Structure of Graphite. *Physical Review*, 109(2):272–279, 1958. doi: 10.1103/PhysRev.109.272.
- Inti Sodemann, Zheng Zhu, and Liang Fu. Quantum Hall ferroelectrics and nematics in multivalley systems. *arXiv:1701.07836 [cond-mat]*, 2017.
- C. Sohrmann and R. A. Römer. Compressibility stripes for mesoscopic quantum Hall samples. *New Journal of Physics*, 9(4):97, 2007. ISSN 1367-2630. doi: 10.1088/1367-2630/9/4/097.
- So Takei, Amir Yacoby, Bertrand I. Halperin, and Yaroslav Tserkovnyak. Spin Superfluidity in the  $\nu = 0$  Quantum Hall State of Graphene. *Physical Review Letters*, 116(21):216801, 2016. doi: 10.1103/PhysRevLett.116.216801.
- D. C. Tsui. Interplay of Disorder and Interaction in Two-Dimensional Electron Gas in Intense Magnetic Fields, 1998.
- D. C. Tsui, H. L. Stormer, and A. C. Gossard. Two-Dimensional Magnetotransport in the Extreme Quantum Limit. *Physical Review Letters*, 48(22):1559–1562, 1982. doi: 10.1103/PhysRevLett.48.1559.
- K. v. Klitzing. THE QUANTIZED HALL EFFECT. *Nobel lecture*, 1985.

- K. v. Klitzing, G. Dorda, and M. Pepper. New Method for High-Accuracy Determination of the Fine-Structure Constant Based on Quantized Hall Resistance. *Physical Review Letters*, 45(6):494–497, 1980. doi: 10.1103/PhysRevLett.45.494.
- J. Velasco Jr, L. Jing, W. Bao, Y. Lee, P. Kratz, V. Aji, M. Bockrath, C. N. Lau, C. Varma, R. Stillwell, D. Smirnov, Fan Zhang, J. Jung, and A. H. MacDonald. Transport spectroscopy of symmetry-broken insulating states in bilayer graphene. *Nature Nanotechnology*, 7(3):156–160, 2012. ISSN 1748-3387. doi: 10.1038/nnano.2011.251.
- J. Velasco Jr, Y. Lee, F. Zhang, K. Myhro, D. Tran, M. Deo, D. Smirnov, A. H. MacDonald, and C. N. Lau. Competing ordered states with filling factor two in bilayer graphene. *Nature Communications*, 5:4550, 2014. doi: 10.1038/ncomms5550.
- A. Veligura, H. J. van Elferen, N. Tombros, J. C. Maan, U. Zeitler, and B. J. van Wees. Transport gap in suspended bilayer graphene at zero magnetic field. *Physical Review B*, 85(15):155412, 2012. doi: 10.1103/PhysRevB.85.155412.
- P. R. Wallace. The Band Theory of Graphite. *Physical Review*, 71(9):622–634, 1947. doi: 10.1103/PhysRev.71.622.
- R. T. Weitz, M. T. Allen, B. E. Feldman, J. Martin, and A. Yacoby. Broken-Symmetry States in Doubly Gated Suspended Bilayer Graphene. *Science*, 330(6005):812–816, 2010. ISSN 0036-8075, 1095-9203. doi: 10.1126/science.1194988.
- Fengcheng Wu, Inti Sodemann, Yasufumi Araki, Allan H. MacDonald, and Thierry Jolicoeur. SO(5) symmetry in the quantum Hall effect in graphene. *Physical Review B*, 90(23):235432, 2014. doi: 10.1103/PhysRevB.90.235432.
- Kun Yang. Field Theoretical Description of Quantum Hall Edge Reconstruction. *Physical Review Letters*, 91(3):036802, 2003. doi: 10.1103/PhysRevLett.91.036802.
- Daijiro Yoshioka. *The Quantum Hall Effect*. Springer, softcover reprint of hardcover 1st ed. 2002 edition, 2010.
- A. F. Young, J. D. Sanchez-Yamagishi, B. Hunt, S. H. Choi, K. Watanabe, T. Taniguchi, R. C. Ashoori, and P. Jarillo-Herrero. Tunable symmetry breaking and helical edge transport in a graphene quantum spin Hall state. *Nature*, 505(7484):528–532, 2014. ISSN 0028-0836. doi: 10.1038/nature12800.
- Fan Zhang and A. H. MacDonald. Distinguishing Spontaneous Quantum Hall States in Bilayer Graphene. *Physical Review Letters*, 108(18):186804, 2012. doi: 10.1103/PhysRevLett.108.186804.

Fan Zhang, Hongki Min, Marco Polini, and A. H. MacDonald. Spontaneous inversion symmetry breaking in graphene bilayers. *Physical Review B*, 81(4):041402, 2010. doi: 10.1103/PhysRevB.81.041402.

Fan Zhang, Jeil Jung, Gregory A. Fiete, Qian Niu, and Allan H. MacDonald. Spontaneous Quantum Hall States in Chirally Stacked Few-Layer Graphene Systems. *Physical Review Letters*, 106(15):156801, 2011. doi: 10.1103/PhysRevLett.106.156801.

Fan Zhang, Hongki Min, and A. H. MacDonald. Competing ordered states in bilayer graphene. *Physical Review B*, 86(15):155128, 2012. doi: 10.1103/PhysRevB.86.155128.

**Titre :** Ferromagnétisme de Hall quantique dans les systèmes multicomposantes

**Mots clés :** Physique Mathématique, L'Effet Hall quantique, Graphène, Électrons fortement corrélés, Isospin

**Résumé :** Cette thèse traite des systèmes de Hall quantiques en deux dimensions, dans lesquels les électrons peuvent porter plusieurs degrés de liberté discrets différents. Le ferromagnétisme de Hall quantique fournit une manière de traiter ces degrés de liberté électroniques comme des spins et isospins effectifs des électrons. Les différentes phases du système correspondent alors à différents ordres de spin ou d'isospin. En exploitant cette analogie, nous explorons différents aspects des systèmes bi-dimensionnels dans le régime de Hall quantique en étudiant la structure correspondante des spins et isospins.

Ce travail consiste en trois parties qui analysent différents matériaux bi-dimensionnels dans le régime de l'effet Hall quantique. Dans chaque projet, nous utilisons la théorie de Hartree-Fock pour étudier le système à plusieurs composantes de spin et d'isospin dans l'approximation de champ moyen. Toutes nos considérations sont directement stimulées par des résultats expérimentaux. Notre motivation principale est d'obtenir une compréhension plus profonde des processus physiques et des mécanismes qui déterminent les propriétés des matériaux à partir d'investigations exclusivement théoriques de modèles abstraits. Nous espérons que cela permettra par la suite de tirer des conclusions sur les expériences, de donner des explications aux phénomènes observés ainsi que de donner des perspectives pour des investigations futures.

**Title :** Quantum Hall Ferromagnetism in Multicomponent Systems

**Keywords :** Mathematical Physics, Quantum Hall Effect, Graphene, Strongly Correlated Electrons, Isospin

**Abstract :** The present thesis deals with two-dimensional quantum Hall systems in which the electrons may be endowed with multiple discrete degrees of freedom. Quantum Hall ferromagnetism provides a framework to treat these electronic degrees of freedom as effective spins and isospins of the electrons. Different orderings of the electronic spins and isospins then characterise different possible phases of the system. Using this analogy, various aspects of the two-dimensional systems in the quantum Hall regime are explored theoretically by studying the corresponding spin and isospin structure.

The work consists of three parts in which different two-dimensional materials are investigated in the quantum Hall regime. In any of the three projects presented within this thesis, Hartree Fock theory is employed to study the multicomponent spin and isospin system at the mean field level. All our considerations are stimulated directly by experimental results. We draw our main motivation from the key idea that purely theoretical investigations of abstract models may allow us to obtain deeper insights into the physical processes and mechanisms that determine the properties of the materials. This, in turn, we hope to allow conclusions about the experiments by providing possible explanations of the phenomena observed, as well as prospects for future investigations.

